Onderzoek naar de reksnelheidsafhankelijkheid
van de trek-, mode-I-delaminatie- en lagesnelheidsimpacteigenschappen
van koolstof/epoxy- en glas/polyamide-6-composieten

Investigation of the Rate-Dependency
of Carbon/Epoxy and Glass/Polyamide-6 Composites
in Tension, Mode-I Delamination and Low-Velocity Impact

Siebe Willem Frank Spronk

Promotoren: prof. dr. ir. W. Van Paepegem, prof. dr. F. A. Gilabert Villegas
Proefschrift ingediend tot het behalen van de graad van
Doctor in de ingenieurswetenschappen: materiaalkunde

UNIVERSITEIT
GENT

Vakgroep Materialen, Textiel en Chemische Proceskunde
Voorzitter: prof. dr. P. Kiekens
Faculteit Ingenieurswetenschappen en Architectuur
Academiejaar 2018 - 2019

ISBN 978-94-6355-157-1
NUR 971, 978
Wettelijk depot: D/2018/10.500/75

Promotors

prof. dr. ir. W. Van Paepegem
Ghent University
Faculty of Engineering and Architecture
Department of Materials, Textiles and Chemical Engineering

prof. dr. F.A. Gilabert
Ghent University
Faculty of Engineering and Architecture
Department of Materials, Textiles and Chemical Engineering

Examination Committee

prof. G. De Cooman (Chair)	Ghent University, Belgium
prof. S. Hertelé (Secretary)	Ghent University, Belgium
prof. W. Van Paepegem (Promotor)	Ghent Universtiy, Belgium
prof. F.A. Gilabert (Promotor)	Ghent University, Belgium
prof. M. Kersemans	Ghent University, Belgium
dr. L. Farkas	Siemens SISW, Belgium
prof. C. Kassapoglou	Lockheed Martin, The Netherlands; Delft University of Technology, The Netherlands
prof. F. Meraghni	École Nationale Supérieure d'Arts et Métiers, France

Research Institute

Ghent University
Department of Materials, Textiles and Chemical Engineering
Tech Lane Ghent Science Park - Campus A
Technologiepark-Zwijnaarde 903
B-9052 Zwijnaarde, Belgium

The work leading to this dissertation was funded by the strategic basic research (SBO) project M3Strength, which fits in the MacroModelMat (M3) program funded by the Strategic Initiative Materials in Flanders (SIM) and the Flemish government agency for Innovation and Entrepeneurship (VLAIO).

Preface

It was one of my former Master's thesis supervisors dr. Thomas Beumler who shared me his experience that a PhD is more a personal challenge rather than a technical one. I had just received the news that I was accepted at Ghent University a while after I had decided to apply for a PhD at the Mechanics of Materials and Structures group, after stumbling on the vacancy on their website (thanks Dimi!). At the time I took him for a fool and expected that this would be like any other job with just some tougher technical hurdles to overcome. Little did I know that I was the fool, and Thomas was absolutely right. After almost 4,5 years of intense, difficult, and at times pointless labour, I feel like I indeed evolved strongly on the personal side, and that the technical challenges were just the easy ones.

Would I still choose for this PhD if I had had the current knowledge back then? Definitely. I would advise anyone the great experience to dive in completely into the depths of a scientific subject and to get the time to choose one's own preferred route to discover where one could provide a valuable contribution to the body of knowledge. Especially when there is adequate guidance along the way.

And what an adequate guidance I have received. First and foremost, I thank my promotor Prof. Wim Van Paepegem. Thank you for finding a slot in your maximally optimised schedule for each and every time I felt the need to discuss anything. Thank you for providing adequate commentary to every single slide or page I intended to make public. Thanks for your positivism, and your trust. It has been an absolute pleasure for me to be able to operate under your wings and to be enriched by your vast knowledge about any subject you have touched upon in your career (including political tactics!). Also many thanks go out to my copromotor Prof. Francisco Gilabert for his extensive guidance for any modelling-related matter, for his careful reads of my papers and for his answers to my more practical questions. And of course to Prof. Joris Degrieck, who proved to possess a seemingly inexhaustible stream of creative ideas to tackle experimental challenges.

Apart from the guidance above, I was blessed to be part of a group of researchers who all worked on the M3Strength project. Ruben, David, of course again Fran, and later also Mohammad: thanks for all the weekly, bi-weekly, monthly and Joint meetings we had together. It was pleasant to have a fixed moment of reflection, to discuss plans of attack, and to bounce ideas around to see if they make any sense. The slides and minutes of these gatherings were an essential source of

information for my papers, presentations and especially my dissertation.

I need to thank Siemens Industry Software N.V. and Honda R&D Co. Ltd. for their assistance and advice that helped lead towards the completion of this project. Also, I am grateful to Honda R&D Co. Ltd., Mitsubishi Chemical Corporation and Ten Cate Advanced Composites for supplying the material for the M3Strength project that I purposefully destroyed again during the course of this research. A special thanks goes out to Naito-san and Kevin Kaiser for replying to the countless e-mails that I sent their way. Thanks also to the guys at Teijin Aramid in Arnhem, The Netherlands, for their help in getting us a hydraulic pulse test bench.

Of course there were also colleagues outside of M3Strength whose help cannot go without mentioning. I acknowledge Prof. Mathias Kersemans and dr. Erik Verboven for their essential assistance in this research regarding anything that has to do with ultrasound. Thanks to Luc and Pascal for translating ideas to reality in the workshop, and especially Pascal for getting up at 4 AM for an exhaustive day of machine-haulage. Thanks to all those, especially Ives, who took the time to explain how things work. Thanks to Line for taking good care of the organizational side of things. I am also grateful to my intern and thesis students for their hard work: Thomas Michielsen, Lucie Merceron, Jori De Baerdemaeker, Mattijs Dolphen, Nikodem Szymański, Guillaume Mulliez and Sanjay Gothivarekar.

Then there is the psychological aid in the form of much-appreciated distraction. Thanks to Ruben, a.k.a. 'the Belgian guy from Delft who got the fatigue modelling position just before you applied for it,' (luckily, because high-speed experiments are so much cooler), for the many conferences, courses and project meetings together. Thanks Frederik (and Mathijs, Jori and yes, also Gabriele) for the swimming sessions with necessary post-swim-Rodenbachs. A big thank you to Ruben, Frederik, Mathijs and Gabriele for the great hikes in Italy, Montenegro and Scotland. Thank you Sam, Mathias, Joren and Joachim for the daily office escapades, Mathias and Mathijs (and various worthy opponents) for the game nights, Joanna and Inge for the insane cakes, Matthias for the anecdotes and Mate, Lode for the pleasant discussions over a Gageleer, Klaas for the numerous lab moments, and everybody else for contributing in their way to the fantastic atmosphere in our wing at 903. Thanks also to the members of the Ghent University Choir (GUK) for making my time in Ghent unforgettable. Thanks to all my friends in the Netherlands to remain in contact, especially Heini for the impressive cover.

Finally, thanks to my family back in the Netherlands for their love, support, and teaching me the values and giving me the opportunities that brought me this far. And especially to Maria, who put up with all my PhD-related complaints, who remained beside me even though I paid more attention to my screen and who brought light to my darkest moments.

Siebe
Ixelles, September 2018

SIEMENS HONDA Honda R&D Co., Ltd. MITSUBISHI CHEMICAL TENCATE materials that make a difference

Summary

For an effective design process of composite automotive structures that keep the passengers safe in a crash, the use of an accurate predictive finite-element model is essential. Without such a tool, every design iteration would require an experimental validation, which would make the development costs rise too much for composites to be cost-effective for application in consumer vehicles.

A model relies on accurate input data to realistically describe a crash. In the case of composites, this data needs to be acquired at representative test speeds, because the mechanical behaviour of these materials depends on strain rate.

The goal of the current research is therefore twofold. First, experimental methodologies are developed which allow the extraction of reliable test data of composites tested at a range of test speeds. Second, a large test programme is executed which produces results from which the variation of relevant composite mechanical properties with speed is determined.

Three load cases are considered. The first two are tension and mode-I delamination. These tests aim mostly to provide input data for predictive models. It needs to be noted that using a tensile load on a composite with its reinforcements at 45° with the loading direction, also information about the shear behaviour can be obtained. The third load case is out-of-plane impact, which serves to generate validation data. This data allows for an evaluation of the prediction accuracy of the models that use data from the first two test types to simulate the experimental conditions of the impact tests.

Two material systems are investigated: carbon/epoxy and glass/polyamide-6. They are both relevant for the automotive industry, and intentionally chosen very different in type in order to create as robust as possible test methods.

A hydraulic pulse test bench is employed for the dynamic tensile tests, which relies on a piezoelectric cell to measure the load. Strain is acquired using both strain gauges and digital image correlation with a high-speed camera. It is established in literature that the material in automotive structures experiences strain rates of approximately up to $200\,\mathrm{s}^{-1}$ during a crash. The aim of this part of the test campaign is thus to obtain tensile composite stress-strain data in the range of quasi-static strain-rate up to $200\,\mathrm{s}^{-1}$.

To make sure the correct values of stress and strain are correlated to each other, the data streams are synchronized by analysing the delay of each component in the measurement chain. Synchronization is found to be of utmost importance at the higher rates, because an incorrect synchronization can lead to a false sense of rate-(in)dependency.

Five limiting factors of the dynamic tensile experimental set-up are identified, which bound the obtainable tensile strain rate to a maximum value. The first limit depends on the test bench capabilities and specimen length, the second on ringing of the load cell, the third on the frame rate of the image acquisition, the fourth on the bandwidth of the strain gauge amplifier and the fifth on the requirement for an approximate equilibrium to exist within the sample. The ringing of the load cell poses the most stringent limit here. There is currently no robust solution to overcome this limit for dynamic tensile testing in a hydraulic pulse test bench.

Based on only valid data below the limiting strain rates, conclusions are drawn on the rate-dependency of the tested composites. The strongest dependency on rate is seen in the pure polymers. No rate-dependency is seen in the literature for carbon fibres, and this makes the overall dependency on test speed of any fibre-dominated laminate of carbon/epoxy practically absent. The 0° unidirectional glass/polyamide-6 shows an expected clear rate-dependency which is also seen for the other laminates of this material, even though the percentile change with rate is reduced. The macroscopic rate-dependency of woven composites with cross-ply or quasi-isotropic lay-ups mostly follow the behaviour of the 0° unidirectional laminates (or fibres) of the same material system, albeit that the differences become even smaller. For laminates with fibres only oriented in the ± 45 directions, woven or UD, the rate-dependency is strongest on maximum stress and Young's modulus: the stress-strain curves appear to be 'pulled upwards.'

Dynamic mode-I delamination is attempted using both a drop-weight set-up and the hydraulic pulse machine. The drop tower method is able to delaminate the carbon/epoxy at different delamination rates, and optical acquisition successfully tracks the position and orientation of the bottom block. The position signal, however, is not smooth enough to use it to compute the force acting on the bottom leg of the double cantilever beam specimen. Extracting the fracture toughness using a finite-element model, moreover, depends on an ill-defined contact condition between the impactor and the bottom block to introduce energy into the system, which prevents the model from converging on mesh refinements

It is thus decided to continue using the hydraulic pulse machine, which successfully pulls specimens apart while recording a useful load history. Finite element analysis proves that the actuation speed is limited to about $3\,\mathrm{m\,s^{-1}}$. Above this speed, firstly, the equations used for the quasi-static data reduction are no longer valid, due to the absence of equilibrium in the specimen. Secondly, the current experimental set-up causes the curvature of both legs not to be equal at the highest speeds, resulting in a crack propagation which is not pure mode-I.

The glass/polyamide-6 system shows a strong stepwise crack progression behaviour which is only partially resolved by stiffening the specimens. Nevertheless, a conclusion can be drawn based on the obtained data in the range of valid testing speeds. All the successfully tested laminates show a reduction of the mode-I fracture toughness with testing speed.

Finally, the rate-dependency to out-of-plane impact is investigated by comparing the damage due to low-velocity impact to that due to quasi-static indentation. To this end, a new drop-weight impact tower is developed to allow the execution of

impact tests with only a small variation on impact velocity within a test scenario. The indentation tests are performed on an electromechanical test bench. The dent depth and the damage area are measured ultrasonically in a post-mortem study to characterise the amount of damage done to the specimens. Additionally, the damage in several specimens is studied in detail using optical microscopy.

The impact damage in both carbon/epoxy and glass/polyamide-6 depends on the impact speed. For glass/polyamide-6, the force-displacement response is completely different at the higher displacement values, and widespread matrix cracking in impacted specimens, in contrast to the local damage zones for the indented ones. For carbon/epoxy, the difference between low-velocity impact and quasi-static indentation is significantly smaller. The force-displacement curves for carbon/epoxy show an underestimation of the load prior to the first significant stiffness loss for quasi-static indentation, while the C-scans show that the damaged area and dent depth are larger when using indentation instead of low-velocity impact. Optical microscopy reveals significant differences in the distribution of matrix cracks and delaminations. For both materials, the energy dissipation does not show a significant change with test speed, and it is therefore not a suitable value to characterise the rate dependency of laminates under out-of-plane loading.

From a design perspective, the rate-dependency of carbon/epoxy is concluded to be limited enough to allow the use of quasi-static indentation to obtain a conservative estimation of the damage due to low-velocity impact. This is not the case for glass/polyamide-6, for which the differences in damage resulting from both test methods are too large. The validation of a finite element model, however, requires the right test conditions to be reproduced for both materials.

In conclusion, the goals of the research have been met. Experimental methodologies have been developed and their ranges of reliability quantified. The methodologies have been applied to the two material systems in an experimental programme in which in total over a thousand tests have been executed. This programme has resulted in a large, consistent database of dynamic test results, capable of supporting the development of composite material models that predict impact with both input and validation data.

Samenvatting

Om een effectief ontwerpproces te verkrijgen voor composietstructuren in automobiele toepassingen, die de passagiers moeten beschermen tijdens een botsing, is het essentieel een accuraat voorspellend eindige-elementenmodel toe te passen. Zonder een dergelijk model zou elke ontwerpiteratie namelijk een experimentele validatie nodig hebben, hetgeen de ontwerpkosten dusdanig doet stijgen dat de toepassing van composieten niet langer kosteneffectief zou zijn voor consumentenvoertuigen.

Voor een realistische weergave van de werkelijkheid is een model afhankelijk van de invoer van accurate data. In het geval van composietmaterialen dienen deze data te zijn vergaard door middel van testen op representatieve snelheden, aangezien het mechanisch gedrag van deze materialen afhangt van de reksnelheid.

Het doel van dit onderzoek is daarom tweeledig. Enerzijds worden er experimentele methoden ontwikkeld. Deze maken de extractie van betrouwbare data mogelijk uit testen aan verschillende snelheden op composieten. Anderzijds wordt er een groot experimenteel programma uitgevoerd van waaruit de variatie van relevante mechanische eigenschappen van composieten met snelheid kan worden bepaald.

Drie belastingssituaties worden behandeld in het onderzoek. De eerste twee betreffen trek en mode-I-delaminatie. De testen met deze belasting zijn vooral bedoeld om gegevens te voorzien die als invoer kunnen dienen voor voorspellende numerieke modellen. Het dient overigens vermeld te worden dat ook schuifeigenschappen te verkrijgen zijn met een trektest door de vezelversterking onder een hoek van $45°$ met de belasting te plaatsen. De derde belastingssituatie is een stoot uit het vlak, die vooral voor validatie dient. De verkregen data uit deze derde test maken het namelijk mogelijk de voorspellingsprecisie te evalueren, doordat de modellen de data van de twee eerdere testen gebruiken om de gevolgen van de stoot op het composiet te simuleren.

In dit onderzoek worden twee materiaalsystemen behandeld: koolstof/epoxy en glas/polyamide-6. Beide zijn relevant voor de automobielindustrie en beide zijn intentioneel erg verschillend gekozen zodat de testmethoden die erop ontwikkeld worden zo robuust mogelijk worden.

De dynamische trektesten worden uitgevoerd met behulp van een hydraulische pulsmachine, die voor de krachtmetingen een piëzo-elektrische krachtopnemer gebruikt. Rek wordt gemeten door middel van zowel rekstrookjes als digitale beeldcorrelatie met een hogesnelheidscamera. In de literatuur staat vermeld dat het materiaal van constructieve elementen in auto's reksnelheden tot ongeveer

$200\,\mathrm{s}^{-1}$ ervaart in een botsing. Het doel van dit gedeelte van het testprogramma is dan ook om rek-trek-krommen van de composieten te vergaren in het bereik van quasi-statische reksnelheid tot aan $200\,\mathrm{s}^{-1}$.

Om er zeker van te zijn dat de juiste rek met de juiste trek gecorreleerd wordt, wordt de synchronisatie van beide gegevensstromen verzekerd door een analyse van de signaalvertraging van elk component in de ketting van meetinstrumenten. De synchronisatie is uiterst belangrijk, aangezien een onzorgvuldige alignering van rek met trek tot een foutief beeld van de reksnelheidsafhankelijkheid kan leiden.

Er zijn vijf limiterende factoren voor de dynamische trekopstelling geïdentificeerd die de verkrijgbare reksnelheid tot een maximumwaarde beperken. De eerste factor hangt af van de snelheid die de machine kan produceren en de proefstuklengte, de tweede van de eigentrilling van het krachtmeetsysteem, de derde van de snelheid waarmee de beelden voor de digitale beeldcorrelatie worden opgenomen, de vierde van de bandbreedte van de versterker van het rekstrooksignaal en de vijfde van het vereiste dat het proefstuk ongeveer in evenwicht moet zijn. Het trillen van de krachtmeter vormt momenteel de meest strikte beperking en er is op dit moment geen robuuste oplossing om deze op te heffen voor dynamische trek in een hydraulische pulsmachine.

Op basis van alleen geldige gegevens beneden de reksnelheidslimieten worden er conclusies getrokken over de reksnelheidsafhankelijkheid van de geteste composieten. De pure polymeren tonen de sterkste afhankelijkheid van reksnelheid. De literatuur toont aan dat koolstofvezels geen reksnelheidsafhankelijkheid bezitten. Dit zorgt ervoor dat elk willekeurig laminaat van koolstof/epoxy waarin de vezels het gedrag domineren in het algemeen ook geen reksnelheidsafhankelijkheid toont. Het pure 0° unidirectionele glas/polyamide-6-laminaat toont de verwachte duidelijke afhankelijkheid met reksnelheid. Deze afhankelijkheid is ook present is in de andere laminaten van dit materiaal, echter is voor deze laminaten de hoeveelheid verandering met reksnelheid minder dan voor het unidirectionele laminaat. De macroscopische reksnelheidsafhankelijkheid van geweven composieten met een kruislingse of quasi-isotrope stapeling volgt het gedrag van de 0° unidirectionele laminaten (of dat van de droge vezels) van hetzelfde materiaalsysteem, hoewel de invloed van reksnelheid nog kleiner is. Alle laminaten met de vezelversterking in de ± 45-richting, geweven of unidirectioneel, tonen weer een duidelijke reksnelheidsafhankelijkheid die het sterkst zichtbaar is voor de maximumspanning en de Young's modulus: de rek-trek-krommen lijken 'omhooggetrokken' te worden.

Zowel een valtoren als de hydraulische pulsmachine is gebruikt in een poging dynamische mode-I-delaminatie uit te voeren. De valtoren slaagt erin verschillende delaminatiesnelheden te veroorzaken in het koolstof/epoxy en door middel van optische data-acquisitie worden zowel de positie als de oriëntatie accuraat gevolgd. Het positiesignaal is echter niet glad genoeg om gebruikt te kunnen worden voor de berekening van de kracht op het onderste been van het proefstuk. Daarbij komt dat de bepaling van de breuktaaiheid met behulp van de eindige-elementenmethode afhangt van een slecht definieerbare contactconditie tussen de

impactor en het onderste blok die de energie in het systeem moet brengen, waardoor er geen vermazingsconvergentie van het model is.

De keuze is daarom gemaakt om verder te werken met de hydraulische pulsmachine, die in staat is met succes de proefstukken uiteen te trekken en daarbij een bruikbaar krachtsignaal te meten. Met behulp van de eindige-elementenmethode is vastgesteld dat de testsnelheid tot een maximum van ongeveer $3\,\mathrm{m\,s^{-1}}$ beperkt is. Bij hogere snelheden zijn enerzijds de vergelijkingen voor de quasi-statische dataverwerking niet meer geldig, omdat het proefstuk niet langer in evenwicht is. Anderzijds zorgt de huidige opstelling ervoor dat de kromming in beide delen van het proefstuk niet langer gelijk is bij de hoogste snelheden, hetgeen resulteert in een scheurgroei die niet zuiver mode-I is.

Het glas/polyamide-6 toont een sterk stapsgewijze scheurgroei, die slechts gedeeltelijk te verbeteren is door de proefstukken te verstijven. Desalniettemin kan er op basis van de gegevens in het geldige snelheidsbereik geconcludeerd worden dat de breuktaaiheid voor alle laminaten, waarvan de testen geslaagd zijn, afneemt met toenemende testsnelheid.

Tot slot is de snelheidsafhankelijkheid van stoten uit het vlak onderzocht door de schade als gevolg van een lagesnelheidsimpact te vergelijken met die van een quasi-statische indrukking. Voor dit doeleinde is er een nieuwe valtoren ontwikkeld die in staat stelt stootproeven uit te voeren met slechts een kleine variatie op de impactsnelheid binnen een getest scenario. De indrukkingstesten zijn uitgevoerd op een elektromechanische trekbank. De diepte van de deuk en de schadeoppervlakte zijn gemeten met ultrageluid om zo de mate van schade in een proefstuk te bepalen. Daarnaast is de schade in een aantal proefstukken in detail bestudeerd met behulp van optische microscopie.

De inslagschade in zowel koolstof/epoxy als glas/polyamide-6 hangt af van de impactsnelheid. In het geval van het glas/polyamide-6 is het kracht-verplaatsingsgedrag volledig anders bij de hogere verplaatsingen en ontstaan er tijdens een stoot wijdverspreide matrixscheuren terwijl er na quasi-statische indrukking slechts een lokale zone met schade is. Het verschil tussen het materiaalgedrag tijdens een lagesnelheidsimpact of dat tijdens een quasi-statische indrukking is significant kleiner voor koolstof/epoxy. De kracht-verplaatsingscurves tonen dat de kracht net voor het eerste duidelijke stijfheidsverlies lager uitvalt voor de quasi-statische indrukking, terwijl de ultrasone metingen aantonen dat de schadeoppervlakte en deukdiepte juist groter zijn voor de indrukking dan voor de lagesnelheidsimpact. Door middel van de optische microscopie zijn er significante verschillen in de verdeling van de matrixscheuren en delaminaties aan het licht gebracht. De energiedissipatie verandert voor beide materiaalsystemen nauwelijks met testsnelheid, hetgeen aantoont dat het geen geschikte waarde is om de snelheidsafhankelijkheid van uit het vlak belaste laminaten mee te bepalen.

De snelheidsafhankelijkheid van koolstof/epoxy wordt beperkt genoeg bevonden om voor ontwerpdoeleinden quasi-statische indrukking te kunnen gebruiken om een conservatieve schatting te maken van de schade die ontstaat door een lagesnelheidsimpact. Dit is echter niet het geval voor glas/polyamide-6, aangezien in dat geval het verschil in schade tussen beide testmethoden te groot is. Voor van

de validering van een eindige-elementenmodel dienen echter voor beide materiaalsystemen de juiste experimentele condities gereproduceerd te worden.

Tot slot wordt er geconcludeerd dat de doelen van het onderzoek bereikt zijn. Er zijn experimentele methoden ontwikkeld waarvoor de maximumsnelheden voor een betrouwbare data-acquisitie zijn bepaald. De methoden zijn toegepast op zowel koolstof/epoxy- als glas/polyamide-6-composieten in een experimenteel programma waarin totaal meer dan duizend testen zijn uitgevoerd. Dit programma heeft geresulteerd in een grote en consistente database aan resultaten, waarmee de ontwikkeling van materiaalmodellen voor composieten in impactsituaties ondersteund kan worden in de vorm van zowel invoer- als validatiedata.

About the author

Siebe Willem Frank Spronk was born at 10:10 on August 15th, 1988 in Doetinchem, The Netherlands. After having finished his university preparatory education (VWO), he moved to Delft to study Aerospace Engineering at the Delft University of Technology in 2006. He obtained his BSc degree in the minimum of three years, and subsequently he spent one year as full-time Vice-President of the Delftsche Studenten Bond, a fraternity with at the time just under 300 members. He was responsible for the maintenance on the monumental building they resided, as well as for the financial administration of the student restaurant.

In September 2010, Siebe continued to pursue a MSc degree Aerospace Structures and Design Methodologies with a supplementary Honours Track on composite materials. This addition allowed him to perform two internships instead of one, which were carried out at the A350 Manufacturing Engineering group of Airbus in Stade, Germany, and the Core Engineering group of Bombardier Aerospace in Toronto, Canada. Siebe performed his MSc thesis in cooperation with Airbus for the A400M program. He combined the work of several researchers to create an analytical tool that can predict the crack initiation and subsequent propagation of a glass-reinforced aluminium (Glare) panel with variable layer thicknesses under uni-axial variable-amplitude fatigue loading. Siebe obtained his MSc degree mid 2013, after which he started his career as a researcher in the Aerospace Structures and Materials department under the wings of his former thesis supervisor.

On April 1st, 2014, he started his PhD on the dynamic material characterization of automotive composites at the Mechanics of Materials and Structures research group of Ghent University within the SBO project M3Strength. This research has allowed him to combine his passions for experimentation, numerical analysis and composite materials, while maintaining a necessary link with reality through frequent contact with the industrial partners in the project.

Siebe is currently first author of three publications in peer-reviewed international scientific journals (A1) of which two are relevant to this dissertation, and he is first author of six publications in proceedings of international scientific conferences.

Publications

Publications in peer-reviewed international journals indexed in the Science Citation Index (A1)

S.W.F. Spronk, I Şen, R.C. Alderliesten. *Predicting fatigue crack initiation in fibre metal laminates based on metal fatigue test data.* International Journal of Fatigue, 70:428-439, 2015.

R.D.B. Sevenois, D. Gomez, F.A. Gilabert, S.W.F. Spronk, S. Fonteyn, M. Heyndrickx, L. Pyl, D. Van Hemelrijck, J. Degrieck, W. Van Paepegem. *Avoiding interpenetrations and the importance of nesting in analytic geometry construction for Representative Unit Cells of woven composite laminates.* Composites Science and Technology, 136:119-132, 2016.

L. Daelemans, A. Cohades, T. Meireman, J. Beckx, S.W.F. Spronk, M. Kersemans, I. De Baere, H. Rahier, V. Michaud, W. Van Paepegem, K. De Clerck. *Electrospun nanofibrous interleaves for improved low velocity impact resistance of glass fibre reinforced composite laminates.* Materials & Design, 141(5):170-184, 2016.

R.D.B. Sevenois, D. Gomez, F.A. Gilabert, S.W.F. Spronk, W. Van Paepegem. *Microscale based prediction of matrix crack initiation in UD composite plies subjected to multiaxial fatigue for all stress ratios and load levels.* Composites Science and Technology, 142:124-138, 2017.

D. Garoz, F.A. Gilabert, R.D.B. Sevenois, S.W.F. Spronk, W. Van Paepegem. *Material parameter identification of the elementary ply damage mesomodel using virtual micro-mechanical tests of a carbon fiber epoxy system.* Composite Structures, 181:391-404, 2017.

S.W.F. Spronk, M. Kersemans, J.C.A. De Baerdemaeker, F.A. Gilabert, R.D.B. Sevenois, D. Garoz, C. Kassapoglou, W. Van Paepegem. *Comparing damage from low-velocity impact and quasi-static indentation in automotive carbon/epoxy and glass/polyamide-6 laminates.* Polymer Testing, 65:231-241, 2018.

S.W.F. Spronk, E. Verboven, F.A. Gilabert, R.D.B. Sevenois, D. Garoz, M. Kersemans, W. Van Paepegem. *Stress-strain synchronization for high strain rate tests on brittle composites.* Polymer Testing, 67:477-486, 2018.

R.D.B. Sevenois, D. Garoz, E. Verboven, F.A. Gilabert, L. Pyl, M. Kersemans, S.W.F. Spronk, W. Van Paepegem. *Multiscale Approach for Identification of Transverse Isotropic Carbon Fibre Properties and Prediction of Woven Elastic Properties using Ultrasonic Identification.* Submitted to Composite Science and Technology, June 2018.

Full papers in proceedings of international scientific conferences (C1)

S.W.F. Spronk, J. Degrieck, F.A. Gilabert, F. Allaeys, W. Van Paepegem. *New test set-up for measuring rate-dependent mode-I delamination properties of unidirectional and woven composites.* In: ECCM17 - 17th European Conference on Composite Materials, Munich, Germany, June 2016.

D. Garoz, F.A. Gilabert, R.D.B. Sevenois, S.W.F. Spronk, A. Rezaei, W. Van Paepegem. *Definition of periodic boundary conditions in explicit dynamic simulations of micro- or meso-scale unit cells with conformal and non-conformal meshes.* In: ECCM17 - 17th European Conference on Composite Materials, Munich, Germany, June 2016.

F.A. Gilabert, D. Gomez, R.D.B. Sevenois, S.W.F. Spronk, A. Rezaei, W. Van Paepegem. *Composite micro-scale model accounting for debonding, strain-rate dependence and damage under impact using an explicit finite element solver.* In: ECCM17 - 17th European Conference on Composite Materials, Munich, Germany, June 2016.

S.W.F. Spronk, M. Dolphen, I. De Baere, F.A. Gilabert, R.D.B. Sevenois, D. Garoz, W. Van Paepegem, J. Degrieck. *Testing for tensile rate-dependence in composite laminates.* In: SAMPE Europe 2016, Liège, Belgium, September 2016.

R.D.B. Sevenois, S.W.F. Spronk, J.C.A. De Baerdemaeker, I. De Baere, D. Garoz, F.A. Gilabert, M. Kersemans, C. Kassapoglou, W. Van Paepegem. *Drop-weight impact response measurement and prediction for quasi-isotropic carbon-epoxy composite laminates.* In: SAMPE Europe 2016, Liège, Belgium, September 2016.

J. Pelfrene, S. Van Dam, S.W.F. Spronk, W. Van Paepegem. *Experimental Characterization and Finite Element Modelling of Strain-rate Dependent Hyperelastic Properties of PVB Interlayers.* In: Challenging Glass 6 - Conference on Architectural and Structural Applications of Glass, Delft, The Netherlands, May 2018.

S.W.F. Spronk, F.A. Gilabert, R.D.B. Sevenois, D. Garoz, W. Van Paepegem. *Tensile rate-dependency of carbon/epoxy and glass/polyamide-6 composites.* In: ECCM18 - 18th European Conference on Composite Materials, Athens, Greece, June 2018.

R.D.B. Sevenois, S.W.F. Spronk, D. Garoz, F.A. Gilabert, E. Verboven, M. Kersemans, W. Van Paepegem. *Multi-scale approach to predict the orthotropic elasticity tensor of carbon fibres and woven carbon composite by ultrasonic insonification.* In: ECCM18 - 18th European Conference on Composite Materials, Athens, Greece, June 2018.

S.W.F. Spronk, E. Verboven, F.A. Gilabert, R.D.B. Sevenois, D. Garoz, M. Kersemans, W. Van Paepegem. *Dynamic tensile testing of brittle composites using a hydraulic pulse machine: stressstrain synchronization and strain rate limits.* In: ICEM18 - 18th International Conference on Experimental Mechanics, Brussels, Belgium, July 2018.

R.D.B. Sevenois, D. Garoz, S.W.F. Spronk, F.A. Gilabert, C. Hochard, W. Van Paepegem. *Influence of tab debonding on measured stiffness evolution in compression-compression fatigue testing of short gauge length coupons.* In: ICFC7 - 7th International Conference on Fatigue of Composites, Vicenza, Italy, July 2018.

Abstracts in proceedings of international scientific conferences (C3)

S.W.F. Spronk, J. Degrieck, W. Van Paepegem. *Dynamic mode-I delamination of composite laminates using a drop-weight tower and optical data-acquisition.* In: ICEM17: 17th International Conference on Experimental Mechanics, Rhodes, Greece, July 2016.

S.W.F. Spronk, F.A. Gilabert, R.D.B. Sevenois, D. Garoz, W. Van Paepegem. *Investigating tensile rate-dependence in composite laminates using a hydraulic pulse test bench.* In: CompTest 2017 - 8th International Conference on Composites Testing and Model Identification, Leuven, Belgium, April 2017.

R.D.B. Sevenois, S.W.F. Spronk, D. Garoz, F.A. Gilabert, W. Van Paepegem. *Microscale based prediction of matrix crack initiation in UD composite plies subjected to muliaxial fatigue with arbitrary stress ratios.* In: CompTest 2017 - 8th International Conference on Composites Testing and Model Identification, Leuven, Belgium, April 2017.

List of acronyms

AITM	Airbus Industries Test Method
ASTM	American Society for Testing and Materials
AWG	American wire gauge: a measure for the diameter of electrical cables
C/E	Carbon/epoxy
CCD	Charge-coupled device: a type of camera sensor
CLPT	Classical Laminated Plate Theory
CP	Cross-Ply: i.e. a composite with layers only at 0 or 90 degrees
CPU	Central processing unit: the part of computer that performs the logical operations
DC	Direct current: a type of electricity without an oscillating voltage
DCB	Double cantilever beam
DIC	Digital image correlation
ENF	End-notched flexure
ELS	End-loaded split
ETFE	Ethylene tetrafluoroethylene
FE	Finite element
FFT	Fast-Fourier transform
fps	Frames per second
G/PA-6	Glass/polyamide-6
HSC	High-speed camera
ICON	In Dutch: interdisciplinair coöperatief onderzoek (interdisciplinary cooperative research)
ISO	International Organization for Standardization
LVI	Low-velocity impact
M3	Macro Model Mat: the SIM program this research forms part of
MBT	Modified beam theory
Mode-I	A delamination mode in which the two halves separate in normal direction
PA-6	Polyamide-6, or Nylon
PAN	Polyacrylonitrile, a precursor for carbon fibres
PEEK	Polyether ether ketone
PLM	Product lifecycle management

PPS	Polyphenylene sulfide
PTFE	Polytetrafluorethylene (or Teflon)
QI	Quasi-isotropic: i.e. a composite with equal number of layers at 0, 45, -45, and 90 degrees
QS	Quasi-static
QSI	Quasi-static indentation
RUC	Repetitive unit cell
RVE	Representative volume element
SAE	Society of Automotive Engineers
SBO	In Dutch: strategisch basisonderzoek (strategic basic research)
SCF	Stress concentration factor
SG	Strain gauge
SHPB	Split-Hopkinson pressure bar
SIM	Strategic Initiative Materials in Flanders
SISW	Siemens Indurstry Software N.V.
TP	Thermoplastic
TS	Thermoset
UD	Unidirectional

Table of Contents

1 Introduction

Climate change is real and its consequences are not to be taken lightheartedly [1]. Ninety-seven percent of climate scientists agree that climate-warming trends over the past century are due to human activities [2]. Greenhouse gas emissions are the probable cause for this, and thus following the Kyoto Protocol and the subsequent Doha Amendment, 111 parties have committed themselves early 2018 to reduce greenhouse gas emissions by at least $18\,\%$ below the 1990 level in an attempt to bring the climate change to a halt [3, 4]. Looking at the European Union (EU), passenger cars produce around $12\,\%$ of its total CO_2 emission, which is one of the gases targeted by the Protocol. The EU enforces a reduction of the emission in this category with penalty payments for car manufacturers for which the fleet's average CO_2 emission is above the limit [5]. Other countries are following the EU example [6, 7]. Car manufacturers are therefore motivated to meet the demanded emissions reduction. One of the effective methods to do so is to produce lighter cars. As the limit of weight reduction of cars seems to have been reached using conventional materials like metals, alternatives with a higher specific strength and more opportunity to increase part complexity need to be applied to reach the goal. Nowadays, composite materials are used in increasing amounts in the car industry for exactly this purpose [8].

With almost $400\,000$ car passengers dying yearly in automotive accidents [9], passenger safety remains crucial in the development of automotive structures. Using an existing design and simply removing material to reduce its weight is not an option, since the safety and thus strength of vehicles should not be compromised. On the contrary, detailed analysis of the behaviour of automotive struc-

tures under impact is needed to ensure these structures perform as intended during a crash. Such an analysis is usually performed in the form of a finite-element simulation, owing to the typically high complexity of the parts and the relative cost-effectiveness of a numerical verification campaign compared to an extended experimental validation. In fact, many different composite material systems are an option for the car industry [10, 11] and thus having a material model that can accurately predict structural strength is essential to reduce the required number of tests and thereby make composites a viable option for automotive parts. Some experimental input, however, remains necessary, because the simulations rely on experimental data to produce their outcomes. This input, moreover, needs to be generated under the right conditions. The mechanical properties of composites typically change with testing speed [12], and hence testing at impact speed is necessary to generate accurate data for models that intend to predict the impact behaviour of composites.

1.1 The M3Strength project

This thesis is part of a SIM M3 project called M3Strength. The Strategic Initiative Materials 'SIM' is a non-profit virtual research centre, founded in 2009 by the Flemish Materials Industry and the Flemish Universities in order to combine strengthening the local materials research with aiding the local industry dependent on or active in material technology.

The M3 program is one of the currently 8 active programs under the umbrella of SIM, and it is led by Siemens Industry Software N.V. (SISW) located in Leuven, Belgium. M3 is the acronym for Macro Model Mat, and aims to address the gap in efficient macro-level predictive modelling tools for new lightweight material systems of which the use is drastically increasing. The widespread use of lightweight materials in industrial design and development is namely limited by the lack of predictive modelling tools to predict the macro level behaviour of lightweight structures. The currently available tools are either too limited in applicability or computationally too heavy to allow practical use [13]. Siemens, therefore, is the right candidate to lead the M3 program, as they have a direct interest in incorporating the program outcomes into their tools to stay ahead of their competitors, and thus make sure the projects within the program stay on track.

M3Strength is one of the two first projects within M3 which started on the first of March, 2014. It is termed a strategic basic research project (in Dutch: strategisch basisonderzoek (SBO)) with the academic development as its main goal and is led by an academic party. This is in contrast to the other types of projects which have the industrial advancement at their core and are therefore supervised by an industrial partner [14]. M3Strength treats the efficient predictive modelling for composites strength in order to reduce the experimental workload required

during the development of new structures using lightweight materials by allowing actual tests to be replaced by virtual ones. The goal is to work towards models that can predict the strength properties of continuous-fibre composites under many different load cases: quasi-static, fatigue, crash and crush. Crash stands for out-of-plane loading where the bending response is dominant and the material should stay as intact as possible, while crush stands for typically in-plane loading where the material is to be damaged as much as possible to dissipate the largest amount of energy [13].

The research within the M3Strength project is carried out by doctoral students and postdoctoral fellows at three academic partners. These are the three Flemish universities: Ghent University (project leader), the Free University of Brussels and the Catholic University of Leuven. The project is further supported by several industrial partners besides SISW as the M3 program leader: Honda R&D Co. Ltd. and Mitsubishi Chemical Corporation from Japan, and Lazer Sport, Sabca Limburg and 3D Weaving from Flanders, Belgium. Honda R&D, and its supplier Mitsubishi Chemical, support the project furthermore by supplying composite material for the experimental programme. Although not part of the consortium, Ten Cate Advanced Composites has also agreed to supply material for the project. Industrial partners further take part in the regularly planned meetings to understand the progress that is being made and provide advice on what would be the most beneficial routes to follow, given that they are looking into the valorization of the project outcomes both by usage of both the test data and simulation methodologies. It needs to be noted that especially SISW and Honda R&D contributed very actively to this project. Sabca Limburg, Lazer Sport and 3D Weaving had their active role mainly in a parallel SIM ICON project also called M3Strength.

The M3Strength project is divided into three main work packages. The first package deals with the efficient predictive modelling for quasi-static and fatigue strength of composites. The second package deals with the modelling for crash and crush. The third and last package concerns the experimental material characterization, and will serve as key input to the other two packages which are mostly focused on numerical modelling. Clearly, the current research falls under the third work package, although initially it was destined to cover part of the second as well. This part, however, has been taken up by postdoctoral fellows at Ghent University who work on the same project. The third work package is again divided into three different tasks. First, the experimental methodologies for the determination of necessary input data need to be established. Second, the materials under investigation need to be experimentally characterized on multiple attributes to generate this input data. Finally, the package should provide for data that allows global model behaviour to be validated.

1.2 Objectives

The purpose of this research is twofold. First, and most important, the experimental methodologies to obtain reliable data for relevant load cases at material deformation rates common during automotive impacts need to be established. Second, these methodologies need to be applied to automotive composite materials with the goal to generate a large, consistent dataset which allows to (1) thoroughly evaluate the rate-dependency of the materials under investigation, (2) find out which aspects in the material behaviour are of importance to accurately model dynamic composite behaviour, (3) provide input data to such models and (4) allow to validate the predictions of these models.

To answer the main question of how to properly investigate composites dynamically, the rates of interest need to be defined. Research has shown that in a vehicle crash, materials deform at rates between quasi-static and about $200\,\mathrm{s}^{-1}$ for durations above $1\,\mathrm{ms}$ [15–17]. Since strain itself has no unit (or $\mathrm{m\,m}^{-1}$ if you must), the unit of the rate of strain becomes s^{-1}. The current research is thus focused on obtaining data on that entire range, which also means slow and even quasi-static tests are to be carried out. Obtaining material properties at several decades of testing speed will result in data that should give insight into how they vary with rate, or in short: their rate dependency.

There are countless different composite material systems available, and hence a choice needs to be made. It is perhaps superfluous to state that only composite materials which have a promising future in terms of application in automotive structures are considered. It is decided to investigate two very distinct material systems to cover a wide variety in material response and encounter as many of the challenges possible when performing a dynamic material characterization of composites. This way, the developed methods should turn out robust. The first material system is a combination of carbon fibres in an epoxy matrix. This composite is widely applied in the aerospace industry and found its way into automotive through its use in Formula-1, making it a relatively common choice for current high-end automotive applications [18]. The epoxy in this composite is a thermoset. The toxicity of its constituents and the difficulties in recycling are often the fuel for a debate on whether a thermoplastic matrix is not better suited for automotive components [10]. Therefore, the second material under investigation is indeed thermoplastic: glass fibres in a polyamide-6 matrix. This polymer is gaining interest over the last years, supported by the numerous new product introductions based on polyamide-6 by *e.g.* BASF, LANXESS and Ten Cate, with the specific application of automotive structures in mind [19]. The use of glass fibres in the second composite system again increases the variety of material response. Finally, it is worth mentioning that two variants of reinforcement architecture per material system will be investigated: one where the fibres are straight and aligned,

or unidirectional, and one in which they follow a woven architecture.

Two types of material loading are distinguished during automotive impacts: 1: a crushing mode, as part of the crumple zones in a vehicle, and 2: a bending mode, as part of the safety cell. Although both are very relevant for the automotive industry, the current research focuses only on the second type. This covers the behaviour of structural automotive elements like door sills and B-pillars, which will be typically impacted out-of-plane in a crash. Loads that occur locally in a material during an out-of-plane impact can be tensile, compressive and shear, and they can occur in both in-plane and out-of-plane directions. Ideally, every load case is treated here, but time restrictions limit the number of tests to only a subset of those cases.

Tests can be classified in two categories. First, development tests are required to measure the bulk material properties. The goal of this type of tests is to quantify these properties, e.g. in order to serve as input for models during the design stage of structural components. These tests should isolate a certain type of loading and reduce possible influences of other loads or side-effects. These tests are typically basic, in the sense that if the stiffness in a certain direction is needed, a specimen is preferably deformed in only that direction. The second type of tests are validation tests, in which situations are created which more closely resemble load cases which occur in reality. This means both the geometry and the load case can be more advanced: validation tests could comprise multi-axial loading on a curved component. The goal of these tests are to acquire as much data on the behaviour of the material as possible to allow an evaluation of the accuracy of applied models on as many aspects as possible.

Apart from out-of-plane compressive damage in the vicinity of the impact zone, damage in the surrounding zone mostly consists of matrix cracks and delaminations. For thick laminates, it is the shear stress below the impactor which initiates the damage process, while for thin laminates tensile stress on the non-impacted side due to excessive bending causes the first damage to appear. When the cracks grow, they will induce delaminations on the ply interfaces, which subsequently cause matrix cracks to appear in adjacent layers [20].

The delamination, i.e. the separation of the layers of a composite, can occur in three ways: out-of-plane separation of two halves or mode-I, sliding separation of the two halves or mode-II and tearing the two halves apart or mode-III. In agreement with the partners in the project this research is part of (see section 1.1), mode-II, mode-III and dynamic compression loading are not considered due to their difficulty and the fact that the test programme would become too large.

The current work thus focuses on three more fundamental types of loading: tension, mode-I delamination and low-velocity impact, where it needs to be noted that the tensile loading is also used to learn about the shear behaviour of a composite by positioning the reinforcements at an angle $45°$ with the load. The first

two loading types are mostly development tests, and the third serves mostly as a validation test.

1.3 Dissertation outline

This dissertation is organised as follows.

Chapter 2 starts off with an overview of the typical test equipment that is used in literature to investigate material rate dependency in general. Then, each of the three load cases, tension, mode-I delamination and out-of-plane impact, is treated to find out in what way other researchers have performed dynamic tests on composite materials.

In **chapter 3** the basic constituents of a composite material are explained, after which the materials under investigation in the current research are detailed. For both carbon/epoxy and glass/polyamide-6, the specifications from the manufacturer are given and the results of optical microscopic investigation are presented. Additionally, a summary is made of the available data in literature on rate-dependency of any of the material properties treated in this work. This way, expectations of the outcomes of the three test programmes can be formed.

Next, for each of the three load cases, two chapters follow: **chapters 4** and **5** deal with tensile loading, **chapters 6** and **7** treat the mode-I delamination and **chapters 8** and **9** focus on out-of-plane impact. For each load case, the first chapter informs the reader about the experimental methodology, explaining the development of the test set-up, the preparation of the specimens, the correct reduction of the raw data towards useful engineering properties or model input and finally, for the case of out-of-plane impact, the details of the post-mortem inspection. The second chapter presents the results when the methodology of the previous chapter is applied to both material systems, and it discusses the dependency of material properties on test speed and whether it matches with what was found in literature.

Finally, conclusions and proposals for further work are given in **chapter 10**.

References

[1] IPCC. *Climate Change 2014: Synthesis Report. Contribution of Working Groups I, II and III to the Fifth Assessment Report of the Intergovernmental Panel on Climate Change [Core Writing Team, R.K. Pachauri and L.A. Meyer (eds.)]*. Technical report, Intergovernmental Panel on Climate Change (IPCC), Geneva, Switzerland, 2014.

[2] National Aeronautics and Space Administration (NASA). *Climate Change: Vital Signs of the Planet: Evidence*. https://climate.nasa.gov/evidence/, May 2018.

[3] United Nations Framework Convention on Climate Change (UNFCCC). *Kyoto Protocol*. http://unfccc.int/kyoto_protocol/items/2830.php, 2014.

[4] United Nations. *United Nations Treaty Collection, Chapter XXVII Environment, 7. c Doha Amendment to the Kyoto Protocol*. https://treaties.un.org/, March 2018.

[5] European Commission. *Road transport: Reducing CO2 emissions from vehicles*. http://ec.europa.eu/clima/policies/transport/vehicles/index_en.htm, December 2014.

[6] Z. Yang, R. Muncrief, and A. Bandivadekar. *Global baseline assessment of compliance and enforcement programs for vehicle emissions and energy efficiency*. Technical report, The International Council on Clean Transportation (ICCT), 2017.

[7] E. Saikawa, J. Kurokawa, M. Takigawa, J. Borken-Kleefeld, D. L. Mauzerall, L. W. Horowitz, and T. Ohara. *The impact of China's vehicle emissions on regional air quality in 2000 and 2020: a scenario analysis*. Atmospheric Chemistry and Physics, 11(18):9465–9484, September 2011.

[8] C. Aufrere. *Current advances, needs and future challenges in high-volume automotive composite structures*. In ECCM16 - 16th European Conference on Composite Materials, Seville, Spain, June 2014.

[9] World Health Organisation. *Global status report on road safety 2015*. WHO Press, Geneva, Switzerland, 2015. OCLC: 985423312.

[10] J. Osborne. *Automotive composites – in touch with lighter and more flexible solutions*. Reinforced Plastics, 57(2):20–24, March 2013.

[11] A. Patil, A. Patel, and R. Purohit. *An overview of Polymeric Materials for Automotive Applications*. Materials Today: Proceedings, 4(2):3807–3815, 2017.

[12] R. L. Sierakowski. *Strain rate effects in composites*. Applied Mechanics Reviews, 50(12):741–761, 1997.

[13] J. Degrieck. *Proposal for SBO project M3Strength: Efficient predictive modelling for composites strength*. Technical Report 2013-V-2-SBO1, Ghent University, February 2014.

[14] SIM Flanders. *What types of projects exist?* http://www.sim-flanders.be/faq/what-types-projects-exist, 2017.

[15] H. Werner and H. Gese. *Zur Bedeutung dehnratenabhängiger Werkstoffkennwerte in der Crashsimulation*. In Kennwertermittlung für die Praxis, pages 139–146. WILEY-VCH Verlag GmbH & Co. KGaA, May 2007.

[16] X. Xiao. *Dynamic tensile testing of plastic materials*. Polymer Testing, 27(2):164–178, April 2008.

[17] T. Schmack, D. Huelsbusch, R. Righi, J. Rausch, D. Roquette, G. Deinzer, and F. Walther. *Influence of load application and fixture on characteristic values at short-time dynamic compression testing of carbon fiber-epoxy composites*. In ECCM17 - 17th European Conference on Composite Materials, Munich, Germany, June 2016.

[18] A. Schmidt. *New developments for mass production of epoxy automotive composites*. In Composites Europe Forum 2016, Duesseldorf, Germany, December 2016.

[19] J. Blakewell. *Composites are coming*. https://automotivemanufacturingsolutions.com/process-materials/composites-are-coming, March 2015.

[20] S. Abrate. *Damage in laminates from low-velocity impacts*. In Dynamic Deformation, Damage and Fracture in Composite Materials and Structures, pages 35–69. Woodhead Publishing, 2016.

2 Test methods for rate-dependency

2.1 Introduction

To obtain satisfactorily accurate input data for composite numerical models, tests need to be performed to examine composite behaviour both qualitatively and quantitatively. The underlying motivation of the current research is to facilitate the design of parts against car crashes, i.e. dynamic impact events. It thus requires the aforementioned tests to be dynamic as well, because composite material properties have shown to depend on test speed [1]. It must be noted that in light of the application, a dynamic test stands for a single event at speeds above those typically used during quasi-static tests, rather than for a fatigue test, which is another commonly used definition.

As mentioned in chapter 1, three types of loading are treated in this research: tension, mode-I delamination and out-of-plane impact. First, typical test equipment used to carry out dynamic tests is described. Then, for each loading type, the test methods available in literature are explained and the applicability to the current work is discussed.

2.2 Dynamic test equipment

A variety of test methods exists to examine how material properties depend on the strain rate. The applicability of these methods is determined by the rate to be obtained and the mechanical property of interest. This allows for a preliminary selec-

tion from all the available options. Scientific literature provides several overviews where test types are connected to corresponding typical strain rate ranges [1–5], which are summarised in table 2.1. It has to be noted that the achieved strain rate depends on both testing speed and specimen dimensions, and the strain rates in the table are those typically obtained using specimen dimensions common to the methods listed.

The table is ordered on ascending maximum strain rate, which is almost the same as ordering it on descending number of researchers in literature that apply the test method. The major exception is the split-Hopkinson pressure bar (SHPB), which is the typical choice for tests at strain rates around $1000\,\mathrm{s}^{-1}$. The most common test methods that can reach the requested upper strain rate of $200\,\mathrm{s}^{-1}$ are treated below. This concerns the servo-hydraulic, drop-weight (including also pendulum and spring-loaded) and SHPB test methods. As flywheel or pneumatic methods are only very rarely applied, they are not treated here.

Table 2.1. Common mechanical testing methods and typical corresponding strain rate ranges [1–5].

Test method	$\dot{\varepsilon}_{\mathbf{min}}\ \left[\mathbf{s^{-1}}\right]$	$\dot{\varepsilon}_{\mathbf{max}}\ \left[\mathbf{s^{-1}}\right]$
Screw-driven	10^{-5}	10^{-1}
Servo-hydraulic	10^{-4}	10^{2}
Pendulum	10^{1}	10^{2}
Drop-weight	10^{1}	10^{2}
Spring-loaded impact	10^{1}	10^{3}
Flywheel	10^{2}	10^{3}
Pneumatic impact	10^{2}	10^{4}
Split-Hopkinson pressure bar	10^{2}	10^{4}
Blast or pressure loading	10^{3}	10^{4}
Taylor impact	10^{4}	10^{6}
Plate or shock loading	10^{6}	10^{8}

2.2.1 Servo-hydraulic test methods

Hydraulic pressure is used in servo-hydraulic set-ups to move one clamp relative to another. Standard test benches can only operate in a closed-loop control mode, where the position of the piston is directly controlled based on the live displacement- or load measurement. This typically limits the speed to about $10^{-1}\,\mathrm{m\,s}^{-1}$.

Special hydraulic pulse test benches exist for dynamic testing applications, where, next to closed-loop controlling for low-speed tests, the system also allows an 'open-loop' control mode. In that case, an amount of valve opening is selected

beforehand based on the relation between this opening and the resulting actuator speed determined beforehand. After starting the test, the position is no longer actively controlled but the actuator moves in approximately the velocity that was aimed for, powered by the hydraulic fluid that was collected in an expansion tank. The moving clamp is often allowed to move freely for a short distance before the test specimen is strained, to allow it to speed up before the specimen is stretched, see also figure 2.1. The typical upper speed limit of such a device lies at $20\,\mathrm{m\,s^{-1}}$.

The advantage of using a servo-hydraulic machine for dynamic tests is its versatility. The variety and accuracy of possible test speeds, as well as the large range of allowable loads typically result in an operating window that is significantly larger than any other method available: it can test at any speed between practically zero and its upper limit. Drawbacks of this test method are (1) the high complexity of the machine, making it very expensive and (2) the upper limit on maximum achievable strain rate. This limit is formed by the speed at which inertial effects become significant, which can happen already at $10\,\mathrm{s^{-1}}$ [3].

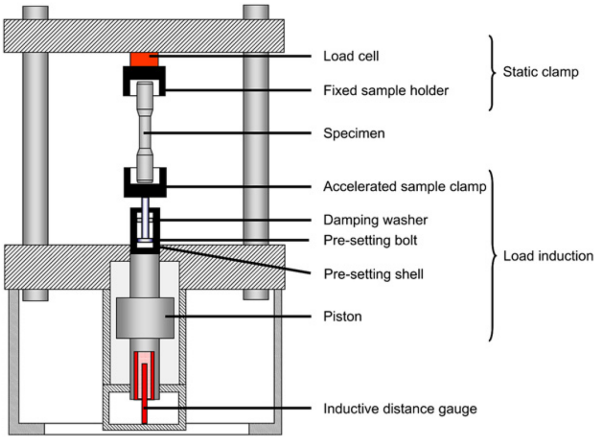

Figure 2.1. Servo-hydraulic testing machine [6]

2.2.2 Drop-weight test methods

Drop-weight impact tests are performed by raising an impactor to a certain height and releasing it to let it fall on a specimen which is fixed at the bottom of the set-up, see also figure 2.2. The weight usually carries an impactor tip with a rounded shape to impact the target and it is usually instrumented with an accelerometer and a force sensor.

An advantage of using a drop-weight impact set-up is that it is a straightforward machine and the costs for acquirement and operation are, therefore, relatively

low. A draw-back is that, instead of the velocity, the mass and drop-height of the impactor are controlled. This makes obtaining a constant velocity for the entire test duration a challenge, because this rate is only constant if the gravitational acceleration is exactly counteracted by the deceleration due to the impact force. One might argue that the same is true for the hydraulic pulse bench in open-loop mode. The inertia of the piston pushed by the hydraulic fluid, however, is much larger than that of the moving impactor. In that case, the test load only causes a small deceleration, in contrast to a typical rebound of the impactor. Also, making the impactor hit the specimen perfectly vertically is a challenge, because this asks for identical friction between the weight and each guiding rail. The impact speed, moreover, is limited in both upper and lower value. The maximum speed attainable depends on the height of the drop and thus the size of the tower, resulting in very large towers if high speeds are demanded. On the other side of the spectrum, below a certain drop height, the energy in the impactor will no longer be enough to fail or even significantly deform a specimen. Quasi-static testing is thus not possible.

A pendulum test set-up is basically a drop-weight tower in which the impactor follows a circular rather than a linear trajectory. The biggest advantage is that the effect of friction can be reduced to a minimum, as the impactor is guided via a rod that connects to a bearing axle, rather than relying on linear bearings to make it follow the right path. The typical way this type of set-up is therefore used is to measure the fracture toughness of a material simply by recording the maximum displacement reached after breaking a sample. Pendulum testers are usually limited to lower speeds than regular impact towers, because the circular trajectory makes that the set-up requires much more space than its linear counterpart.

A way to partially overcome the height needed to reach high impact velocities is to accelerate the impactor faster than by gravitation alone. This is typically done using some form of spring loading [7]. This comes with the cost of added complexity, though the general operating principle of the set-up remains the same.

Because of the similarity of the methods described in this section, in the following, they are not separately considered as different options but rather collected under the denominator of drop-weight impact.

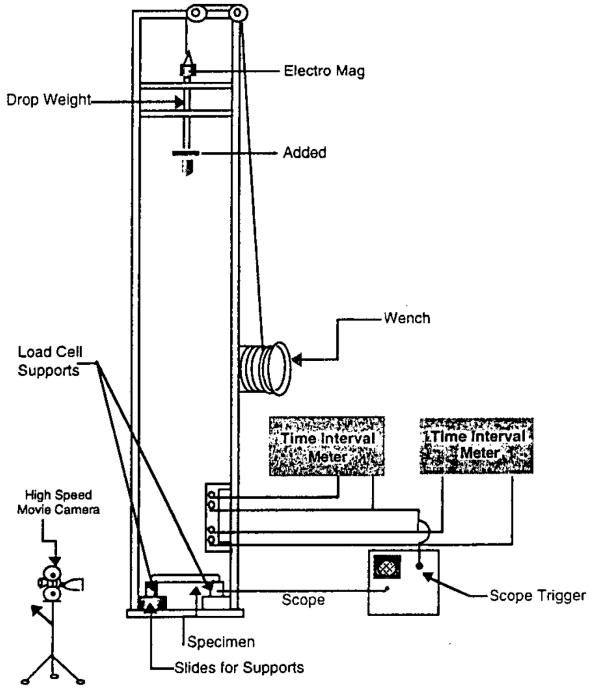

Figure 2.2. Drop weight impactor [3]

2.2.3 Split-Hopkinson pressure bars (SHPBs)

Hopkinson [8] used a metal bar to allow for the measurement of the stress wave caused by impact to this metal bar. The characteristics of the wave give details about the impact. From the seventies, a setup with two Hopkinson bars became a regular choice to obtain strain rate dependent data, and therefore constitutes the final test method which deserves an introduction here. This setup is termed the Split-Hopkinson Pressure Bar (SHPB) technique, and an overview is shown in figure 2.3. It can be used to apply a variety of loads, and is mostly used in the strain rate regime between 1000 and $10\,000\,\mathrm{s}^{-1}$ [2].

The metal bars are supposed to stay in the elastic regime, while the specimen itself can be taken up to large strains. Actuation of the setup is typically performed by striking the end of the input bar using an impactor. The stress wave then passes through the input bar to the specimen. Part of the wave is reflected at the interface of the input bar and the specimen, the remainder passes through the specimen and into the second bar. Strain gauges on the input bar measure the incoming and reflected wave. These two waves should not interfere, which typically results in a rather long input bar, as it should be longer than the pulse duration multiplied

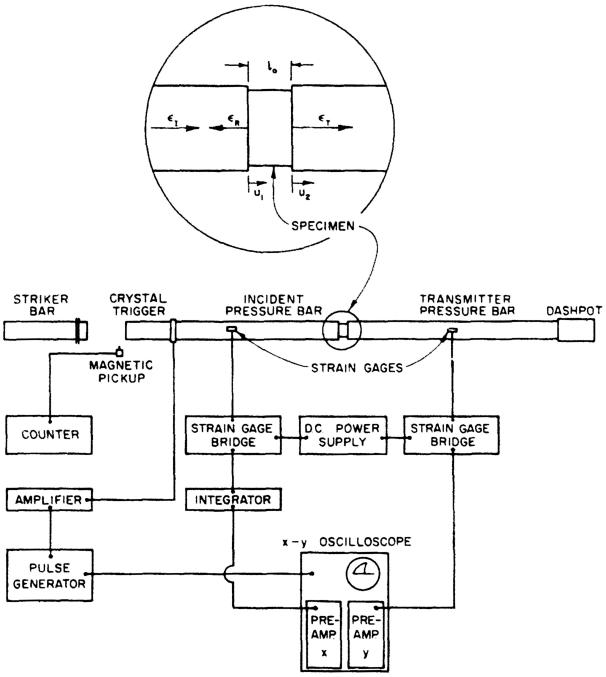

Figure 2.3. Split-Hopkinson pressure bar set-up [9].

by the wave speed in the bar. The specimen should be taken short enough to ensure that multiple end-to-end stress wave reflections can take place before the input pulse ends. This way, the specimen can be assumed to be approximately in equilibrium. Strain gauges on the second bar measure the transmitted pulse. Again, this bar needs to be long enough to prevent the reflection from the free end to interfere with the pulse measurement and the test. The global strain applied to the specimen is computed from the bar end displacements, in turn calculated by integrating the measured bar strains and multiplying the result by the wave speed in the bar material and assuming the entire set-up can be considered as a one-dimensional system. The load is obtained by multiplying the bar strains by their cross-sectional surface area and modulus of elasticity [9].

Since the strain in the specimen is dependent on the integral of the strain in the bar, the strain rate depends directly on the value of the bar strain. For a fixed geometry, the range of attainable strain rates of the SHPB set-up is therefore rather limited. The lower strain rate is bound by (1) the minimum force (and thus the bar strain) and (2) the minimum strain (and thus the integral of the bar strain) needed to break the specimen. The upper strain rate is bound by (1) the maximum velocity of the impactor and (2) the fact that the bar strain should stay below the elastic

limit of the bar material.

For low strain rates, one thus wants a bar with a large radius to produce enough force with the small amount of strain. Using a bar with a very high stiffness would namely imply the need for a very long bar as the speed of sound would also rise. For high strain rates, a thinner bar is preferred because it should be significantly strained.

The SHPB is the most used method to test composite rate-dependency in literature. Looking for sources in which glass or carbon fibre composites are the subject, 55 sources were found using this method, compared to 42 employing any other technique.

2.3 Tensile testing

The first type of test to be carried out in the current research is the tensile test. It is one of the most often performed tests for material characterization in general. The tensile material properties are also important for the design of composite structures against impact. Hence, many researchers have used a dynamic form of the test to investigate the rate dependency of tensile composite material properties. Table 2.2 contains an overview of the articles found in which dynamic tensile test results are given for relevant materials and materials, sorted per test type.

The table shows that most authors use the SHPB to study the tensile rate dependency of composites. In that case, typically, a standard test bench is employed to obtain a quasi-static reference and often also for intermediate-rate values. This means that there is a gap in the obtained data, since the standard bench produces only rates below about $1\,\mathrm{s}^{-1}$ and the SHPB starts at about $500\,\mathrm{s}^{-1}$, see *e.g.* [12].

A special mechanism is needed to actuate the impact bar in tension. Variants are seen where the bar is pretensioned and then released (*e.g.* [51]), the bar is made cylindrical and extended around the transmission bar to allow the use of a normal impact striker (some examples in [3]) or by using a striker which slides around a loading bar until it hits a flange on the end (*e.g.* [17]). Secondly, rather than simply placing a typically cylindrically shaped specimen in between the two bars, the tensile loading requires a carefully designed specimen shape and gripping

Table 2.2. Number of articles containing dynamic composite tensile test results with at least one result in the range of strain rates from 1 *to* $500\,\mathrm{s}^{-1}$.

Test type	Articles	References
SHPB	21	[10–30]
Hydraulic pulse bench	18	[6, 30–46]
Drop-weight impact	6	[1, 37, 47–50].

system (*e.g.* [13]). Specimens embedded in a metal male-threaded part that fits in a corresponding female-threaded hole in the bars seem to lead to the most consistent results (*e.g.* [17]). Specimen dimensions are typically small: gauge lengths of about 10 to $30\,\mathrm{mm}$ and widths of about 3 to $10\,\mathrm{mm}$.

The second most used method to investigate composite tensile rate dependency (table 2.2) is perhaps the most straightforward: pulling specimens apart at a fast pace using a hydraulic pulse test bench. Some device is needed to allow the actuator to move freely before the specimen is gripped, because its acceleration is limited to a finite value, leading to an initial non-constant velocity for the high speeds. Three variants exist [52]. The first variant is by far the most common, where a bottom grip with a piston is attached to the specimen, which is caught by a cylinder attached to the actuated piston of the test bench, see *e.g.* [44]. This is called a slack rod here, which matches the terminology in the manual of equipment available at UGent [53]. Typically a damper is inserted to prevent the excitement of too many high-frequency natural frequencies [54]. The two alternatives are attaching a conical endpiece to the specimen to be caught by a cylinder, or by using a sliding joint which grips the specimen only after a certain delay [39]. The test bench is often used to test at many rates from ranging quasi-static up to about $100\,\mathrm{s}^{-1}$ (*e.g.* [43]). A wide variety of specimen dimensions is used in this set-up, typically with gauge lengths around $50\,\mathrm{mm}$ and widths around $10\,\mathrm{mm}$.

Disregarding the use of a standard test bench to test only up to relatively low rates because the maximum strain rate obtained is typically too low to be of interest for the current research, table 2.2 shows that the drop-weight tower is the third most used set-up for dynamic tensile tests on composites. Something is needed to convert the compressive load from stopping the impactor into a tensile load to break the specimen. All concepts in literature employ a vertical specimen position during the test, with a fixed clamping on its upper end. The tensile load is introduced on its lower end in two manners. Either a guided structure is attached to the bottom grip which extends to above the upper grip, onto which the drop-weight will impact (*e.g.* [49]), or long beams are attached to the impactor to hit on a wider plate mounted on the bottom grip (*e.g.* [50]). Specimen dimensions are widely varying, and no real trend is seen. The typical obtained strain rates lie between 20 and $120\,\mathrm{s}^{-1}$. Lower rates are usually tested using a standard test bench. Another downside, next to the rather limited range of strain rates, are the oscillations which typically appear in the results, leading to the need of filtering in the data reduction procedure [49].

Other, more exotic manners in which composites are characterised in dynamic tension are by the use of an explosive charge [55] or by launching a wedge between the two grips [56]. Although the former can also be applied for a wide range of strain rates with the use of a hydraulic pump, it is not considered further because the requirement of making accurate composite cylinders, which lies beyond the

scope of the current research.

All three of the most often used set-ups are available at UGent. The hydraulic pulse test bench is selected to conduct the tensile test programme, mainly because of the following two reasons. First, it was established in the introduction that data is required for strain rates over the range of quasi-static to $200\,\mathrm{s}^{-1}$. The hydraulic pulse bench can perform tests over this whole range without the need for another set-up. Secondly, also woven composites form part of the materials of interest. The undulated fibre architecture will require that specimen dimensions are large enough to validate the assumption of a uniform stress state, see also chapter 3. Of the candidates for dynamic testing available at UGent, the hydraulic pulse bench can test the largest specimen dimensions without the need for a major change or addition to the existing equipment. The experimental set-up and test results of the dynamic tension test programme are treated in chapters 4 and 5.

2.4 Delamination testing

Several set-ups have been proposed in the literature to perform dynamic mode-I delamination tests on composites. These methods can be classified in three categories according to the three types of equipment of section 2.2.

The first and most common category makes use of a standard universal testing or a hydraulic pulse machine. Most often, a double cantilever beam (DCB) specimen is mounted directly in the clamps and a number of crosshead speeds are applied [57–68]. Typically the ASTM D5528 standard for measuring the mode-I fracture toughness is followed except for the crosshead speed, though sometimes modifications are made to obtain a more beneficial specimen behaviour [69]. Some use the bench only to preload a spring and thus achieve higher test rates using a standard test bench [70]. While following the ASTM standard is the most straightforward to apply, it is not necessarily the best method, since it involves only actuating one end of the specimen, leading to an asymmetric crack opening which is thus no longer pure mode-I [69]. Attempts to overcome this issue involve mounting the specimen vertically and loading both arms simultaneously. This is achieved either by driving a wedge between the specimen arms [71] or loading blocks [72], or the machine is used indirectly to excite a structure that in turn loads the specimen using hinge arms [73].

The second category implements a drop tower, with variants that adapt it to excite a DCB specimen [74, 75] or a simple cantilever beam (SCB) specimen [63], a variant which should produce mode-I loading by out-of-plane impact of a cracked plate [76], or a variant that uses a specially designed specimen to fit in a Charpy impact setup [77].

The third and final category uses a SHPB where a wedge cleaves into the crack of a DCB specimen [78].

Apart from the unsymmetric opening, a second issue hampers the high-rate measurement of the mode-I fracture toughness: load oscillations [74]. Especially when a load cell is measuring on an actuated end of a DCB specimen, oscillations appear in the results. Additionally, the crack does not grow continuously in some cases. This deteriorates the load measurement further with more oscillations, because the specimen needs time to acquire equilibrium again after a sudden crack jump. The wedge-insert method effectively resolves the issue of load oscillations because the load is no longer measured directly on the loading blocks. It also adds a problem though: friction forces now form part of the measured load. This can be a significant part, as the loads to open the arms of a specimen can be as low as $50\,\mathrm{N}$. The friction forces are difficult to measure, so an attempt has been made in literature to minimize them by wedge-loading a bearing shaft [72].

For the current research, it is attempted to alleviate the need for a load cell by performing dynamic delamination using a novel test method in the drop tower where the trajectory of the actuated side of the specimen is tracked. The load is then to be inferred from the acceleration of the loaded block. Additionally, the hydraulic pulse test bench is employed to find out up to which velocity it can be used to correctly retrieve the mode-I fracture toughness. The experimental set-ups and test results are discussed in chapters 6 and 7, respectively.

2.5 Impact testing

The final load case to be treated is out-of-plane impact of composites. Naturally, the instrumented drop-weight tower is the set-up of choice for this type of loading, though also set-ups which drop [79] or launch [80] metal balls at a composite are seen. Still, the instrumented impact is preferred, mainly because of the added information which is gathered during the impact, which can give a clue about what happens inside the specimen.

From a wide selection of articles dealing with composite impact, it is concluded that the specimen is always supported on the outside of its bottom surface by a backing plate with a cut-out in the middle. This cut-out is typically rectangular [81–87], circular [88–93] or square [79, 80, 94, 95] in shape. The specimen is typically held in place by one of two manners. The method most often seen is by clamping it on the backing plate using metal plates or rings [79, 84, 87–89, 91–95] to create a fixed boundary condition along the edge(s) of the specimen. The second method is by barely touching it using four rubber-tipped clamps [81, 83–86] to simulate a simply-supported boundary condition, following the recommendations of several (aerospace) test standards *e.g.* ASTM D7136 [96] or AITM 1.0010 [97]. Typical specimen dimensions range from about 75 to $125\,\mathrm{mm}$, with thickness values between about 1.5 and $6\,\mathrm{mm}$.

Looking at the impactor, typically it is equipped with a hemispherical tip which

is 12.7 [85, 88, 92, 94] or $16\,\mathrm{mm}$ [82–84, 86, 91, 98] in diameter. The impactor mass varies from about 1 to $25\,\mathrm{kg}$ and the impact speed from about 1 to $8\,\mathrm{m\,s^{-1}}$, resulting in impact energies that vary from about 1 to 200 J.

To test material rate-dependency in a drop tower, the only option is to drop the impactor from several heights. For clear damage features which occur before the impactor is stopped, like a significant sudden reduction of load, this method will show the influence of testing speed. The problem with this method is, however, that the amount of impact energy also varies with drop height and thus the amount of damage after testing cannot be compared between several drop heights to assess rate-dependency. This could possibly be overcome by reducing the impactor mass as the drop height increases to match the impact energy, though in that case still the equivalence is questionable because large changes in impactor mass would be required.

A practical alternative could be to use quasi-static indentation to obtain reference results with a complete absence of dynamic effects. The ASTM test standard suggests that it could be used to evaluate the impact resistance of composites [99], though it also clearly states that it does not cover the time-dependent behaviour of the tested materials. When the damage due to indentation matches that due to low-velocity impact, it can be stated that the impact behaviour is rate-independent. When it is not, one could even go as far as to perform indentations at several crosshead speeds, though testing using a drop tower seems to make more sense as it produces velocities which more realistically represent actual impact scenarios.

A downside of the drop tower is its limited maximum velocity. As mentioned above, typically the impact speed does not exceed $8\,\mathrm{m\,s^{-1}}$. Instead of the drop-tower, one could also perform punch tests using the hydraulic pulse test bench described above. This way, a large range of velocities from quasi-static up to $20\,\mathrm{m\,s^{-1}}$ can be covered. The issue with this method is, however, the open-loop control scheme of the bench. At high speeds, it cannot actively control its piston any more in order to test up to a certain force or displacement. Instead, it always tests up to its maximum capability and it does not rebound since the pressure on the piston is not removed during the test. Hence, it would typically penetrate composites with a realistic lay-up, which is not considered a load case equivalent to impact. SHPB testing for out-of-plane impact is not considered because the minimum rate at which it can test is too high.

As the actual structural shapes the materials will be used in are unknown at this stage of the research, a specimen shape can be chosen which is practical to produce and test. In any case, the damage measured in a controlled impact test will not correspond to what occurs when a structure is subjected to impact, a fact for which the ASTM test standard also warns [96]. It can be beneficial to use test conditions which are widely applied to allow assessment of the relative performance of the material. Based upon this argument, and on the fact that material boundary

conditions in a structure never constitute a perfect clamp, it is decided to follow the ASTM D7136 [96] test standard of low-velocity impact on simply-supported rectangular plates. The experimental campaign and corresponding results are detailed in chapters 8 and 9, respectively.

2.6 Conclusion

The available test methods to investigate composite rate-dependency in relation to automotive impact have been explored. Three candidates were found to be most relevant: a hydraulic pulse test bench, a drop-weight impact tower and a split-Hopkinson pressure bar. The latter two require a universal test bench to be employed as well if the entire range from quasi-static to impact rate is to be covered.

The current research deals with three loading types: tension, mode-I delamination and out-of-plane impact. The hydraulic pulse bench and drop tower were found to be most suitable to carry out the tensile and the impact test programmes, respectively. Both of these set-ups are applied to investigate the rate-dependency of mode-I delamination.

References

[1] S. Barré, T. Chotard, and M. L. Benzeggagh. *Comparative study of strain rate effects on mechanical properties of glass fibre-reinforced thermoset matrix composite*. Composites Part A: Applied Science and Manufacturing, 27(12):1169–1181, 1996.

[2] J. E. Field, S. M. Walley, W. G. Proud, H. T. Goldrein, and C. R. Siviour. *Review of experimental techniques for high rate deformation and shock studies*. International Journal of Impact Engineering, 30(7):725–775, August 2004.

[3] R. L. Sierakowski. *Strain rate effects in composites*. Applied Mechanics Reviews, 50(12):741–761, 1997.

[4] I. M. Daniel. *High strain rate properties of unidirectional composites, part 1*. Contractor Report 189083, National Aeronautics and Space Administration (NASA), December 1991.

[5] I. M. Daniel, B. T. Werner, and J. S. Fenner. *Strain-rate-dependent failure criteria for composites*. Composites Science and Technology, 71(3):357–364, February 2011.

[6] M. Schoßig, C. Bierögel, W. Grellmann, and T. Mecklenburg. *Mechanical behavior of glass-fiber reinforced thermoplastic materials under high strain rates*. Polymer Testing, 27(7):893–900, October 2008.

[7] INSTRON. *CEAST 9300 Series | Droptower Impact Systems*, 2009.

[8] B. Hopkinson. *A method of measuring the pressure produced in the detonation of high explosives or by the impact of bullets*. Proceedings of the Royal Society of London. Series A, 89(612):411–413, 1914.

[9] U. S. Lindholm. *Some experiments with the split hopkinson pressure bar*. Journal of the Mechanics and Physics of Solids, 12(5):317–335, 1964.

[10] Y. Zhou, Y. Wang, Y. Xia, and S. Jeelani. *Tensile behavior of carbon fiber bundles at different strain rates*. Materials Letters, 64(3):246–248, February 2010.

[11] A. Gilat. *Study of High Strain Rate Response of Composites*. Technical report, National Aeronautics and Space Administration (NASA), April 2003.

[12] A. Gilat, R. K. Goldberg, and G. D. Roberts. *Experimental study of strain rate sensitivity of carbon fiber/epoxy composite*. Composites Science and Technology, 62:1469–1476, 2002.

[13] R. Gerlach, C. R. Siviour, N. Petrinic, and J. Wiegand. *Experimental characterisation and constitutive modelling of RTM-6 resin under impact loading*. Polymer, 49(11):2728–2737, May 2008.

[14] N. Taniguchi, T. Nishiwaki, and H. Kawada. *Tensile strength of unidirectional CFRP laminate under high strain rate*. Advanced Composite Materials, 16(2):167–180, January 2007.

[15] L. G. Melin and L. E. Asp. *Effects of strain rate on transverse tension properties of a carbon/epoxy composite: studied by moiré photography*. Composites Part A: Applied Science and Manufacturing, 30(3):305–316, March 1999.

[16] B. Bouette, C. Cazeneuve, and C. Oytana. *Effect of strain rate on interlaminar shear properties of carbon/epoxy composites*. Composites Science and Technology, 45(4):313–321, 1992.

[17] P. Kuhn, M. Ploeckl, and H. Koerber. *Experimental investigation of the failure envelope of unidirectional carbon-epoxy composite under high strain rate transverse and off-axis tensile loading*. EPJ Web of Conferences, 94:01040, 2015.

[18] J. Harding and L. Dong. *Effect of strain rate on the interlaminar shear strength of carbon-fiber-reinforced laminates*. Composites Science and Technology, 51(3):347–358, 1994.

[19] X. Chen, Y. Li, Z. Zhi, Y. Guo, and N. Ouyang. *The compressive and tensile behavior of a 0/90 C fiber woven composite at high strain rates*. Carbon, 61:97–104, September 2013.

[20] R. Foroutan, J. Nemes, H. Ghiasi, and P. Hubert. *Experimental investigation of high strain-rate behaviour of fabric composites*. Composite Structures, 106:264–269, December 2013.

[21] R. Gerlach, C. R. Siviour, J. Wiegand, and N. Petrinic. *In-plane and through-thickness properties, failure modes, damage and delamination in 3D woven carbon fibre composites subjected to impact loading*. Composites Science and Technology, 72(3):397–411, February 2012.

[22] J. P. Hou and C. Ruiz. *Measurement of the properties of woven CFRP T300/914 at different strain rates*. Composites Science and Technology, 60(15):2829–2834, November 2000.

[23] L. M. Welsh and J. Harding. *Effect of strain rate on the tensile failure of woven reinforced polyester resin composites*. Le Journal de Physique Colloques, 46(C5):C5–405–C5–414, August 1985.

[24] Z. Wang. *Experimental evaluation of the strength distribution of E-glass fibres at high strain rates*. Applied Composite Materials, 2(4):257–264, 1995.

[25] Z. Wang and Y. Xia. *Experimental evaluation of the strength distribution of fibers under high strain rates by bimodal Weibull distribution*. Composites Science and Technology, 57(12):1599–1607, January 1998.

[26] G. H. Staab and A. Gilat. *High Strain Rate Response of Angle-Ply Glass/Epoxy Laminates*. Journal of Composite Materials, 29(10):1308–1320, July 1995.

[27] X. Yuanming and W. Xing. *Constitutive equation for unidirectional composites under tensile impact*. Composites Science and Technology, 56(2):155–160, 1996.

[28] R. Gerlach, C. R. Siviour, J. Wiegand, and N. Petrinic. *The Strain Rate Dependent Material Behavior of S-GFRP Extracted from GLARE*. Mechanics of Advanced Materials and Structures, 20(7):505–514, August 2013.

[29] N. K. Naik, P. Yernamma, N. M. Thoram, R. Gadipatri, and V. R. Kavala. *High strain rate tensile behavior of woven fabric E-glass/epoxy composite*. Polymer Testing, 29(1):14–22, February 2010.

[30] S. Roberts and J. Harding. *Effect of strain rate on the tensile failure of glass-fibre braided tubes*. Le Journal de Physique IV, 01(C3):C3–353–C3–359, October 1991.

[31] B. L. Peterson, R. N. Pangborn, and C. G. Pantano. *Static and high strain rate response of a glass fiber reinforced thermoplastic*. Journal of composite materials, 25(7):887–906, 1991.

[32] M. Schossig, C. Bieroegel, W. Grellmann, R. Bardenheier, and T. Mecklenburg. *Effect of Strain Rate on Mechanical Properties of Reinforced Polyolefins*. In E. E. Gdoutos, editor, Fracture of Nano and Engineering Materials and Structures, pages 507–508. Springer Netherlands, January 2006.

[33] M. Zrida, H. Laurent, V. Grolleau, G. Rio, M. Khlif, D. Guines, N. Masmoudi, and C. Bradai. *High-speed tensile tests on a polypropylene material*. Polymer Testing, 29(6):685–692, September 2010.

[34] X. Xiao and M. Leach. *Intermediate and high strain rate tensile testing of plastic materials*. General Motors Corporation, Warren, MI, page 48090–9055, 2005.

[35] B. Bonnet. *Comportement au choc de matériaux composites pour applications automobiles*. PhD thesis, École Nationale Supérieure des Mines de Paris, 2005.

[36] S. R. Raisch and B. Möginger. *High rate tensile tests – Measuring equipment and evaluation*. Polymer Testing, 29(2):265–272, April 2010.

[37] H. Al-Zubaidy, X. Zhao, and R. Al-Mahaidi. *Mechanical characterisation of the dynamic tensile properties of CFRP sheet and adhesive at medium strain rates*. Composite Structures, 96:153–164, February 2013.

[38] M. M. Shokrieh, R. Mosalmani, and M. J. Omidi. *Strain-rate dependent micromechanical method to investigate the strength properties of glass/epoxy composites*. Composite Structures, 111:232–239, May 2014.

[39] J. Kwon, J. Choi, H. Huh, and J. Lee. *Evaluation of the effect of the strain rate on the tensile properties of carbon–epoxy composite laminates*. Journal of Composite Materials, page 0021998316683439, December 2016.

[40] J. Lienhard and W. Böhme. *Characterisation of RTM CFRP laminates under high-rate tension-, compression-, and shear-loading*. Engineering Fracture Mechanics, 149:33–350, November 2015.

[41] S. Pardo, D. Baptiste, F. Décobert, J. Fitoussi, and R. Joannic. *Tensile dynamic behaviour of a quasi-unidirectonal E-glass/polyester composite*. Composites Science and Technology, 62(4):579–584, March 2002.

[42] M. Todo, K. Takahashi, P. Béguelin, and H. H. Kausch. *Strain-rate dependence of the tensile fracture behaviour of woven-cloth reinforced polyamide composites*. Composites Science and Technology, 60(5):763–771, April 2000.

[43] Z. Jendli, J. Walrick, M. Bocquet, and J. Fitoussi. *Strain rate effects on the mechanical behavior of carbon-thermplastic matrix woven composites*. In ECCM16 - 16th European Conference on Composite Materials, Seville, Spain, June 2014.

[44] J. Fitoussi, F. Meraghni, Z. Jendli, G. Hug, and D. Baptiste. *Experimental methodology for high strain-rates tensile behaviour analysis of polymer matrix composites*. Composites Science and Technology, 65(14):2174–2188, November 2005.

[45] W. Hufenbach, A. Hornig, B. Zhou, A. Langkamp, and M. Gude. *Determination of strain rate dependent through-thickness tensile properties of textile reinforced thermoplastic composites using L-shaped beam specimens*. Composites Science and Technology, 71(8):1110–1116, May 2011.

[46] D. R. Hufner and S. I. Hill. *High strain rate testing and modeling of a woven E-glass–vinylester composite in dry and saturated conditions*. Journal of Composite Materials, 51(21):3017 – 3039, 2017.

[47] S. V. Hayes and D. F. Adams. *Rate sensitive tensile impact properties of fully and partially loaded unidirectional composites*. Journal of Testing and Evaluation, 10:61–68, 1982.

[48] H. M. Hsiao and I. M. Daniel. *Strain rate behavior of composite materials*. Composites Part B: Engineering, 29(5):521–533, September 1998.

[49] K. A. Brown, R. Brooks, and N. A. Warrior. *The static and high strain rate behaviour of a commingled E-glass/polypropylene woven fabric composite*. Composites Science and Technology, 70(2):272–283, February 2010.

[50] Y. Ou and D. Zhu. *Tensile behavior of glass fiber reinforced composite at different strain rates and temperatures*. Construction and Building Materials, 96:648–656, October 2015.

[51] G. H. Staab and A. Gilat. *A direct-tension split Hopkinson bar for high strain-rate testing*. Experimental Mechanics, 31(3):232–235, September 1991.

[52] International Organization for Standardization. *ISO 26203-2:2011. Metallic materials – Tensile testing at high strain rates – Part 2: servo-hydraulic and other test systems. German version DIN EN ISO 26203-2:2011.* Technical report, International Organization for Standardization, 2011.

[53] W. Dries. *Schenck Hydropuls z25/20 instruction manual*, 1989.

[54] X. Xiao. *Dynamic tensile testing of plastic materials*. Polymer Testing, 27(2):164–178, April 2008.

[55] I. M. Daniel, R. H. LaBedz, and T. Liber. *New method for testing composites at very high strain rates*. Experimental Mechanics, 21(2):71–77, 1981.

[56] G. H. Majzoobi, F. F. Saniee, and M. Bahrami. *A tensile impact apparatus for characterization of fibrous composites at high strain rates*. Journal of Materials Processing Technology, 162–163:76–82, May 2005.

[57] J. W. Gillespie Jr., L. A. Carlsson, and A. J. Smiley. *Rate-dependent mode I interlaminar crack growth mechanisms in graphite/epoxy and graphite/PEEK*. Composites Science and Technology, 28(1):1–15, 1987.

[58] S. Hashemi, A. Kinloch, and J. Williams. *The Effects of Geometry, Rate and Temperature on the Mode I, Mode II and Mixed-Mode I/II Interlaminar Fracture of Carbon-Fibre/Poly(ether-ether ketone) Composites*. Journal of Composite Materials, 24(9):918–956, September 1990.

[59] S. Mall, G. Law, and M. Katouzian. *Loading Rate Effect on Interlaminar Fracture Toughness of a Thermoplastic Composite*. Journal of Composite Materials, 21(6):569–579, January 1987.

[60] A. Smiley and R. Pipes. *Rate Effects on Mode I Interlaminar Fracture Toughness in Composite Materials*. Journal of Composite Materials, 21(7):670–687, January 1987.

[61] H. Zabala, L. Aretxabaleta, G. Castillo, and J. Aurrekoetxea. *Loading rate dependency on mode I interlaminar fracture toughness of unidirectional and woven carbon fibre epoxy composites*. Composite Structures, 121:75–82, March 2015.

[62] H. Liu, W. Yan, X. Yu, and Y. Mai. *Experimental study on effect of loading rate on mode I delamination of z-pin reinforced laminates*. Composites Science and Technology, 67(7–8):1294–1301, June 2007.

[63] S. Benmedakhene, M. Kenane, and M. L. Benzeggagh. *Initiation and growth of delamination in glass/epoxy composites subjected to static and dynamic loading by acoustic emission monitoring*. Composites Science and Technology, 59(2):201–208, February 1999.

[64] X. Wu and Y. A. Dzenis. *Rate effects on mode-I delamination toughness of a graphite/epoxy laminated composite*. International journal of fracture, 112(2):9–12, 2001.

[65] B. R. K. Blackman, J. P. Dear, A. J. Kinloch, H. Macgillivray, Y. Wang, J. G. Williams, and P. Yayla. *The failure of fibre composites and adhesively bonded fibre composites under high rates of test*. Journal of Materials Science, 30(23):5885–5900, 1995.

[66] J. Machado, E. Marques, R. Campilho, and L. F. da Silva. *Mode I fracture toughness of CFRP as a function of temperature and strain rate*. Journal of Composite Materials, page 0021998316682309, December 2016.

[67] H. You and Y. Yum. *Loading Rate Effect on Mode I Interlaminar Fracture of Carbon/Epoxy Composite*. Journal of Reinforced Plastics and Composites, 16(6):537–549, April 1997.

[68] R. Frassine and A. Pavan. *Viscoelastic effects on the interlaminar fracture behaviour of thermoplastic matrix composites: I. Rate and temperature dependence in unidirectional PEI/carbon-fibre laminates*. Composites Science and Technology, 54(2):193–200, January 1995.

[69] M. May. *Measuring the rate-dependent mode I fracture toughness of composites – A review*. Composites Part A: Applied Science and Manufacturing, 81:1–12, February 2016.

[70] H. Kilic, R. Patel, and S. R. Soni. *High Strain Rate Testing of Co-Cured/Z-Pinned Composites in Mode-I*. SAMPE Journal, 41(5):58–66, 2005.

[71] J. Kalthoff, J. Beinert, S. Winkler, and J. Blauel. *On the determination of the crack arrest-toughness*. In Advances in research on the strength and fracture of materials, volume Vol. 3B: Applications and non-metals, pages 751–756. Pergamon Press Inc., 1977.

[72] S. I. Thorsson, A. M. Waas, J. Schaefer, B. Justusson, and S. Liguore. *Effects of elevated loading rates on mode I fracture of composite laminates using a modified wedge-insert fracture method*. Composites Science and Technology, 156:39–47, March 2018.

[73] G. Hug, P. Thévenet, J. Fitoussi, and D. Baptiste. *Effect of the loading rate on mode I interlaminar fracture toughness of laminated composites*. Engineering Fracture Mechanics, 73(16):2456–2462, November 2006.

[74] M. Colin de Verdiere, A. A. Skordos, M. May, and A. C. Walton. *Influence of loading rate on the delamination response of untufted and tufted carbon epoxy non crimp fabric composites: Mode I*. Engineering Fracture Mechanics, 96:11–25, December 2012.

[75] P. Navarro, J. Aubry, F. Pascal, S. Marguet, J. F. Ferrero, and O. Dorival. *Influence of the stacking sequence and crack velocity on fracture toughness of woven composite laminates in mode I*. Engineering Fracture Mechanics, 131:340–348, November 2014.

[76] T. L. Norman and C. T. Sun. *Delamination growth in composite laminates with adhesive strips subjected to static and impact loading*. Composites Science and Technology, 46(3):203–211, 1993.

[77] M. S. Sohn and X. Z. Hu. *Impact and high strain rate delamination characteristics of carbon fibre epoxy composites*. Theoretical and Applied Fracture Mechanics, 25(1):17–29, April 1996.

[78] T. Kusaka, M. Hojo, Y. Mai, T. Kurokawa, T. Nojima, and S. Ochiai. *Rate dependence of mode I fracture behaviour in carbon-fibre/epoxy composite laminates*. Composites Science and Technology, 58(3–4):591–602, March 1998.

[79] C. C. Chamis and L. Minnetyan. *Impact damage and strain rate effects for toughened epoxy composite structures*. Technical Memorandum TM 2006-214253, National Aeronautics and Space Administration (NASA), 2006.

[80] H. T. Wu and G. S. Springer. *Measurements of Matrix Cracking and Delamination Caused by Impact on Composite Plates*. Journal of Composite Materials, 22(6):518–532, January 1988.

[81] E. V. González, P. Maimí, P. P. Camanho, C. S. Lopes, and N. Blanco. *Effects of ply clustering in laminated composite plates under low-velocity impact loading*. Composites Science and Technology, 71(6):805–817, April 2011.

[82] L. Raimondo, L. Iannucci, P. Robinson, and P. T. Curtis. *Modelling of strain rate effects on matrix dominated elastic and failure properties of unidirectional fibre-reinforced polymer–matrix composites*. Composites Science and Technology, 72(7):819–827, April 2012.

[83] D. D. R. Cartié and P. E. Irving. *Effect of resin and fibre properties on impact and compression after impact performance of CFRP*. Composites Part A: Applied Science and Manufacturing, 33(4):483–493, April 2002.

[84] M. de Freitas and L. Reis. *Failure mechanisms on composite specimens subjected to compression after impact*. Composite Structures, 42(4):365–373, August 1998.

[85] P. A. A. E. Mendes and M. V. Donadon. *Numerical prediction of compression after impact behavior of woven composite laminates*. Composite Structures, 113:476–491, July 2014.

[86] H. Yan, C. Oskay, A. Krishnan, and L. R. Xu. *Compression-after-impact response of woven fiber-reinforced composites*. Composites Science and Technology, 70(14):2128–2136, November 2010.

[87] L. S. Sutherland and C. Guedes Soares. *Impact tests on woven-roving E-glass/polyester laminates*. Composites Science and Technology, 59(10):1553–1567, August 1999.

[88] M. Quaresimin, M. Ricotta, L. Martello, and S. Mian. *Energy absorption in composite laminates under impact loading*. Composites Part B: Engineering, 44(1):133–140, January 2013.

[89] L. Iannucci and M. L. Willows. *An energy based damage mechanics approach to modelling impact onto woven composite materials: Part II. Experimental and numerical results*. Composites Part A: Applied Science and Manufacturing, 38(2):540–554, February 2007.

[90] P. O. Sjöblom, J. T. Hartness, and T. M. Cordell. *On Low-Velocity Impact Testing of Composite Materials*. Journal of Composite Materials, 22(1):30–52, January 1988.

[91] V. Tita, J. de Carvalho, and D. Vandepitte. *Failure analysis of low velocity impact on thin composite laminates: Experimental and numerical approaches*. Composite Structures, 83(4):413–428, June 2008.

[92] Y. Hirai, H. Hamada, and J. Kim. *Impact response of woven glass-fabric composites—I.: Effect of fibre surface treatment*. Composites Science and Technology, 58(1):91–104, January 1998.

[93] R. K. Luo, E. R. Green, and C. J. Morrison. *Impact damage analysis of composite plates*. International Journal of Impact Engineering, 22(4):435–447, April 1999.

[94] G. D. Lawcock, L. Ye, Y. W. Mai, and C. T. Sun. *Effects of fibre/matrix adhesion on carbon-fibre-reinforced metal laminates—II. impact behaviour*. Composites Science and Technology, 57(12):1621–1628, January 1998.

[95] D. Liu, B. B. Raju, and X. Dang. *Size effects on impact response of composite laminates*. International Journal of Impact Engineering, 21(10):837–854, November 1998.

[96] ASTM International. *ASTM Standard D7136, 2015, "Measuring the Damage Resistance of a Fiber-Reinforced Polymer Matrix Composite to a Drop-Weight Impact Event"*. Technical report, American Society for Testing and Materials, West Conshohocken, PA, 2015.

[97] Airbus Industrie. *Airbus Industrie Test Method AITM 1.0010, 1994, "Fiber Reinforced Plastics. Determination of compression strength after Impact"*. Technical report, Airbus Industrie, 1994.

[98] S. Rivallant, C. Bouvet, E. Abi Abdallah, B. Broll, and J. Barrau. *Experimental analysis of CFRP laminates subjected to compression after impact: The role of impact-induced cracks in failure*. Composite Structures, 111:147–157, May 2014.

[99] ASTM International. *ASTM Standard D6264, 2012, "Standard Test Method for Measuring the Damage Resistance of a Fiber-Reinforced Polymer-Matrix Composite to a Concentrated Quasi-Static Indentation Force"*. Technical report, American Society for Testing and Materials, West Conshohocken, PA, 2012.

3 Materials under investigation

3.1 Introduction

Chapter 1 mentions that two composite material systems form the subject of the current research: carbon fibres embedded in an epoxy matrix, or carbon/epoxy or C/E, and glass fibres embedded in a polyamide-6 matrix, or glass/polyamide-6 or G/PA-6. This chapter provides more information about these materials.

First, a short general introduction to composites is given. The second section provides details about the micro structure and the expected quasi-static material properties of C/E. In the third section, the expected rate dependency of the material properties of C/E are treated, based on the available literature for each of the loading types of chapter 2. The fourth and fifth sections repeat the structure for G/PA-6.

3.2 Composite materials

A composite material is a combination of two or more distinct phases which has different properties than its individual constituents. The type of composite treated in this work consists of a polymer matrix into which aligned continuous fibrous reinforcements are embedded. Usually the reinforcing phase has a very high strength and stiffness, but it consists of units that are too brittle and small to create useful parts from. The matrix commonly has a good toughness, but it lacks the strength and stiffness to be used for applications with significant loads. Together, however,

they can form a material which is both tough and strong, and which can be made in a large variety of shapes.

3.2.1 Matrix

The matrix is a continuous material which forms the shape of the final part. It surrounds the reinforcements, transfers loads in and out of them, and separates them from each other and the environment. Properties like the environmental resistance, shear strength and transverse tensile strength are mainly defined by the matrix properties.

Although many other matrix materials exist, for instance ceramics or metals, this research only makes use of polymeric matrices, which is the most relevant type for automotive applications. The polymeric matrices can typically be classified into two categories: thermoset and thermoplastic materials.

A thermosetting plastic, in short: thermoset, has undergone an irreversible cure. It consists of long chain molecules which have been chemically crosslinked by the cure, basically forming one large three-dimensional macromolecule which cannot be melted or reformed.

A thermosoftening plastic, or thermoplastic, on the other hand, consists of long chain molecules which are not crosslinked. These materials can be melted to form (viscous) liquids and solidify again upon cooling down.

3.2.2 Reinforcements

Composite reinforcing phases come in a variety of different shapes, see figure 3.1. Only continuous fibres are considered for this research. The main purpose of the fibres in a composite is to carry loads. The stiffness and strength of a composite are dominated by the fibre properties in the fibre direction. Therefore, the choice of reinforcing material is of high importance. The two materials mostly used as fibres in a composite are glass and carbon. Figure 3.1 shows that continuous fibre reinforcements come in various shapes. In this research, only two architectures are treated: unidirectional (UD) fibres and woven fabrics.

In a UD composite layer, all the fibres are straight and aligned with each other. This orientation makes the composite very strong in the direction of the fibres, but susceptible to matrix cracks if it is loaded at an angle to the fibres.

Woven fabrics, or weaves, consist of fibre bundles, also known as tows, which are interlaced at right angles to form a cloth. The bundles are sometimes called yarns, which is technically incorrect. This term namely implies some form of twisting of the bundles, which is usually avoided for the fibres in composites. The bundles in the fabric production direction are named warp tows, the other bundles are weft or fill tows. It is possible to weave tows in a three-dimensional pattern, connecting several layers of warp tows together. In this research, however, only

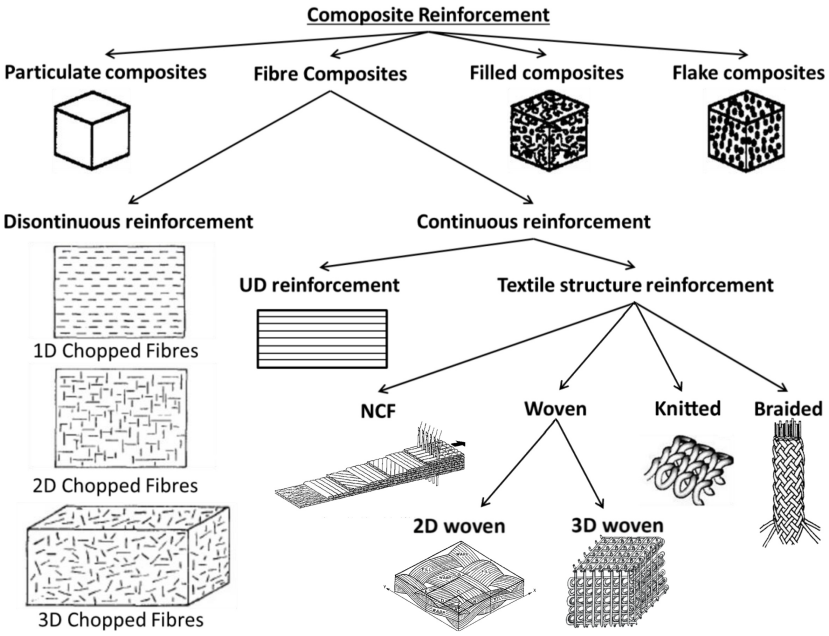

Figure 3.1. Classification of the most used composite reinforcements [1–5]

planar weaves with one layer of warp tows are considered. Several weave patterns exist, see figure 3.2, which have different properties like strength and drapability.

Although a composite with a woven reinforcement is more resistant to in-plane transverse loading than a UD composite, the strength in the longitudinal direction is compromised because the fibres are undulated due to the weaving process. This undulation results from the crossing over of fibre tows at the crimp zones, and introduces what is called crimp into the tow.

3.2.3 The interface

The interface between the reinforcements and the surrounding matrix can be regarded as a third element that determines the composite mechanical properties. The interface is responsible for transferring the loads between the matrix and a reinforcement. The adhesion of the matrix to the reinforcements influences the strength and the fracture toughness of the composite. The characteristics of the interface layer depend on the surface roughness of the reinforcing phase and on the wetting properties. A good wetting means that the matrix spreads easily over the solid surface of the fibres, allowing for a large area to be bonded.

3.2.4 Layup classification

Continuous-fibre reinforced composites typically come in a layered configuration, i.e. a layup. This makes the composites a laminate, and allows for a selection of the direction in which the reinforcing fibres are placed with the aim of providing reinforcement in exactly those directions which experience loads. The layered character causes many different combinations of orientations to be possible, and hence a standard way of defining the layup has been devised to distinguish these layups. Starting from the top, the angle θ in degrees with the longitudinal direction of the reinforcement is indicated for each layer, separating layers from each other using a forward slash and encompassing the whole in square brackets. Rep-

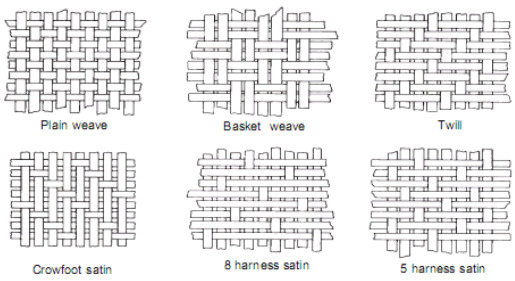

Figure 3.2. Some examples of weave patterns [6]

etitions are indicated with a subscript integer n, using parentheses if these concern only parts of the laminate. Only half of the layup is written for symmetric laminates, and a subscript 's' is added to indicate symmetry, using an overbar on the central layer if it concerns a laminate with an odd number of plies. Woven plies are indicated using a hash (#) after which the principal reinforced directions are indicated between parentheses. If a layer with reinforcement at an angle θ is followed by a layer at an angle $-\theta$, the combination is typically written as $\pm\theta$. An 8-layer composite with intermittently 0- and a 90-degree plies, symmetric around the midplane, is thus written as indicated below.

$$[0/90]_{2s}$$

A 4-layer woven composite where the outside layers contain reinforcements in the +45 and -45, and the inside layers in the 0 and 90 directions, is characterised by the code below.

$$[\#(\pm 45)\#(0/90)]_s$$

3.3 Carbon/epoxy

The carbon/epoxy composite used in this research is supplied by Honda R&D Co., Ltd. and produced by Mitsubishi Chemical Corporation. Two variants are used: a unidirectional composite, PYROFIL TR 360E250S, and a woven composite, PYROFIL TR3110 360GMP. Both composites are a combination of polyacrylonitrile (PAN) based carbon fibres in PYROFIL #360 resin which has a density of $1200\,\mathrm{kg\,m^{-3}}$ and a glass transition temperature of $170\,^{\circ}\mathrm{C}$. This resin is modified to allow curing in under five minutes: it has a gel time of $200\,\mathrm{s}$ at $130\,^{\circ}\mathrm{C}$ [7]. The dry fibre properties given by the manufacturer are summarized in table 3.1. The woven tows come in a plain weave architecture of $0.23\,\mathrm{mm}$ thick with a weight of $0.2\,\mathrm{kg\,m^{-2}}$, which counts almost 5 tow ends per centimetre (12.5 ends per inch) in both warp and weft directions. This means the average tow width equals about $2\,\mathrm{mm}$.

The unidirectional composite laminates are produced using compression molding for 7 minutes at $140\,^{\circ}\mathrm{C}$ and a pressure of $8\,\mathrm{MPa}$. The resulting composite properties supplied by the manufacturer are given in table 3.2. The woven fabric composite laminates are cured for 60 minutes at $130\,^{\circ}\mathrm{C}$ with $0.6\,\mathrm{MPa}$ pressure in an autoclave. The properties can be found in table 3.3.

Figure 3.3 contains images of unidirectional C/E acquired using optical microscopy. The cross-sectional shape of the fibres only deviates slightly from circular. The fibre alignment is good, there are only few small zones of a locally different orientation, an example is indicated with a red arrow in figure 3.3b.

Figure 3.4 shows a stitched microscopic image of the architecture of a woven C/E laminate with all layers oriented in the same direction. It shows that the

Table 3.1. Dry carbon fibre properties for the unidirectional and woven C/E composites.

	Unidirectional [8]	Woven [9]
Designation	TR 50S15L	TR 30S 3L
Number of filaments in tow	15 000	3000
Filament diameter [µm]	6.8	6.9
Tow tensile strength [MPa]	4900	4120
Tow tensile modulus [GPa]	240	234
Elongation at break [%]	2.0	1.8
Density [$\mathrm{kg\,m^{-3}}$]	1820	1790

Table 3.2. Selection of mechanical properties given by the manufacturer for unidirectional composite C/E TR 360E250S [10].

	Strength [MPa]	Modulus [GPa]	Elongation at break [%]	Poisson's ratio [-]	Fibre volume fraction [%]
0° tension	2299	136	1.63	0.31	60*
0° compression	1503	125	0.44	0.33	60*
90° tension	55	9.4	0.62	0.03	65
90° compression	258	10.4	0.42	0.02	65
In-plane shear	54	4.0	-	-	66
Interlaminar shear	71	-	-	-	66

* The given 0° properties are normalized to $v_f = 60\,\%$

Table 3.3. Selection of mechanical properties given by the manufacturer for woven composite C/E TR3110 360GMP [11].

	Strength [MPa]	Modulus [GPa]	Failure strain [%]	Poisson's ratio [-]	Fibre volume fraction [%]
0° tension*	693	60	1.1	-	50
0° compression*	538	54	1.1	-	49
90° tension*	598	59	1.0	-	49
90° compression*	496	52	1.1	-	49
In-plane shear	92	3.4	-	-	51
Interlaminar shear	60	-	-	-	50

* 0° direction is warp direction, 90° direction is weft direction

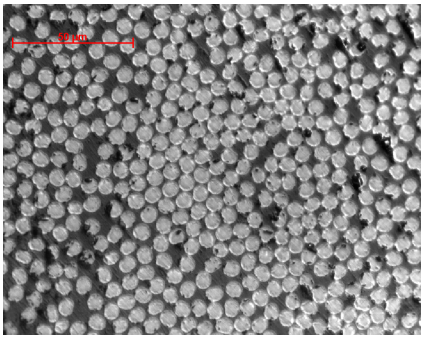

a. Looking in the $0°$ *direction.*

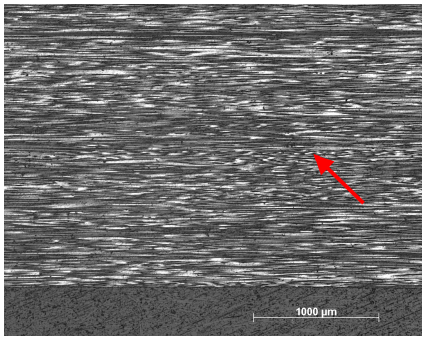

b. Looking in the $90°$ *direction.*

Figure 3.3. Optical micrographs of unidirectional carbon/epoxy polished to a particle size of $2\,\mu\mathrm{m}$*. The red arrow in figure 3.3b points to a small area with fibre misalignment. The horizontal dark line close to the top is a precrack layer inserted to start a delamination.*

composite is well consolidated, and shows some nesting as the surfaces of the individual plies no longer follow a straight line internally. Moreover, matrix pockets are visible at locations where adjacent plies do not fit into each other perfectly. These pockets are the cause for the lower volume fraction compared to unidirectional laminates: compare the volume fractions in table 3.3 to those in table 3.2.

A further zoom-in on the fibre cross-sections reveals that the deviation from round is more pronounced than for the UD laminate, compare figure 3.5 to figure 3.3a.

A small block of approximately 5 by $10\,\mathrm{mm}$ of layup $[\#(0/90)]_8$ was scanned at the custom-designed µCT system HECTOR of the Ghent University Centre for X-ray Tomography (UGCT) [12]. The scan allowed to gain more insight into the shape of the tows across their length and construct a finite-element model that accurately represents the stress state of the tows inside the laminate [13]. The earlier estimated tow width of $2\,\mathrm{mm}$ is rather close to the average tow width that was found in the volume of the scanned block of material, which amounts to $1950\,\mu\mathrm{m}$. This model, and the sub-model used for the tow, can be used to predict elastic mechanical properties of the material which are otherwise very difficult to obtain. The result is given in table 3.4.

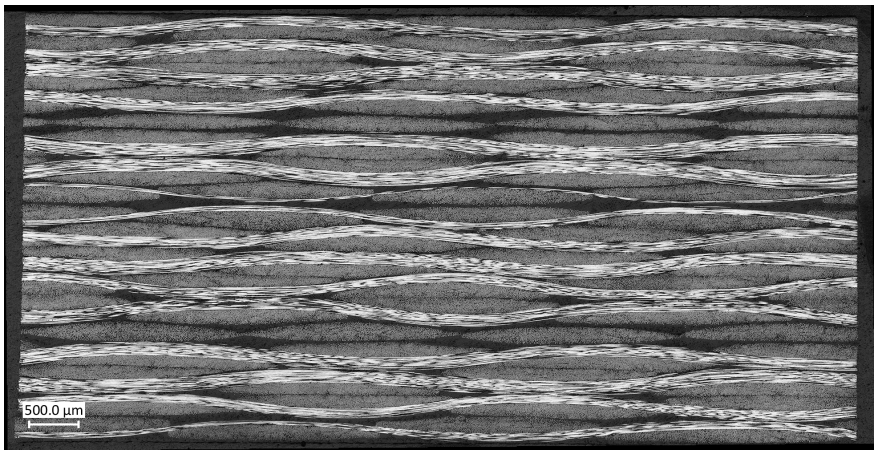

Figure 3.4. Stitched micrograph of a woven C/E laminate with all layers in the same direction. Looking in the weft direction.

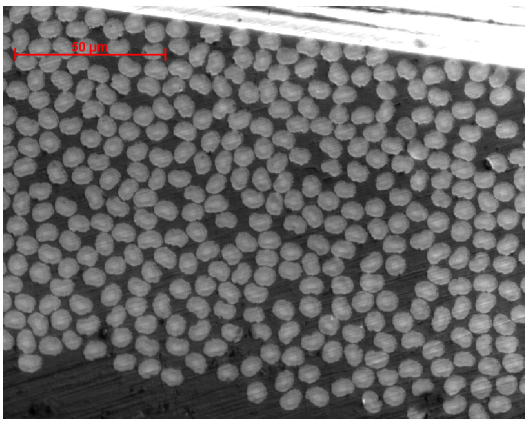

Figure 3.5. Detail of figure 3.4, revealing a deviation from a round shape for the fibre cross-sections.

Table 3.4. Elastic ply properties obtained from finite element predictions [13].

Property	Unit	C/E 0° UD[a]	C/E $[\#(0/90)]^b$
E_1	GPa	152.8	60.52
E_2	GPa	8.0	59.92
E_3	GPa	8.0	7.47
ν_{12}	-	0.31	0.07
ν_{13}	-	0.31	0.46
ν_{23}	-	0.40	0.46
G_{12}	GPa	4.1	3.44
G_{13}	GPa	4.1	2.53
G_{23}	GPa	2.8	2.58

a: 65 % volume fraction tow properties [13]
b: Nested MESI finite element model [13]

3.4 Expected rate-dependency of carbon/epoxy

Before attempting to obtain dynamic material properties, it can be beneficial to find out what can be found in the literature about the rate-dependency of the material under investigation. This section deals with the rate-dependent properties for carbon/epoxy in literature for the three load cases treated in the current research: tension, mode-I delamination and out-of-plane impact.

It needs to be noted that even though a thorough search has been carried out of literature dealing with the rate-dependency of carbon/epoxy in the aforementioned load cases, by no means it is claimed that all relevant available literature has been captured in the following subsections. Also, only literature with at least one test result in the range of $1 \leq \dot{\varepsilon} \leq 500$ has been included.

3.4.1 Tension

An overview of the sources in literature which treat the rate-dependency of a certain tensile mechanical property of any carbon/thermoset composite is given in table 3.5. In the table, x denotes the 0° or fibre direction, y the in-plane transverse direction and xy denotes in-plane shear. E^t stands for the tensile Young's modulus, G for the shear modulus. X^t and Y^t are the ultimate stresses in x- and y-direction and S is the ultimate shear stress. ε^t is the tensile maximum strain and γ the same in shear. Finally, ν stands for the Poisson's ratio. The pure matrix is assumed isotropic, so the values for the x-direction are assumed also to cover for the y-direction.

Shear properties have been included since their rate-dependency is typically tested using a dynamic tensile test on a ± 45-laminate.

Table 3.5. Number of sources that treat the rate-dependency of indicated properties for carbon/thermoset composites in tension.

	Carbon fibres	**TS matrix**	**Carbon/TS matrix**	
			Unidirectional	**Weave**
E_x^t	1 [14]	4 [15–18]	10 [15, 17, 19–26]	5 [27–31]
E_y^t	0		6 [21, 24–26, 32, 33]	3 [28–30]
G_{xy}	0	3 [16, 18, 34]	4 [21, 24, 26, 32]	4 [28–30, 35]
X^t	1 [14]	6 [15–18, 36, 37]	12 [15, 17, 19–26, 38, 39]	5 [27–31]
Y^t	0		8 [21, 24–26, 32, 33, 40, 41]	3 [28–30]
S_{xy}	0	4 [16, 18, 34, 37]	6 [21, 24, 26, 38, 40, 41]	4 [28–30, 35]
ε_x^t	1 [14]	4 [15–18]	9 [15, 17, 19–22, 24, 38, 39]	4 [27, 28, 30, 31]
ε_y^t	0		4 [21, 24, 33, 40]	2 [28, 30]
γ_{xy}	0	3 [16, 18, 34]	4 [21, 24, 38, 40]	3 [28, 30, 35]
ν_{xy}	0	0	1 [24]	1 [30]

The mechanical properties of carbon fibres seem to be independent of strain rate [14].

For thermosetting matrices, mostly epoxy resins, the ultimate stress typically sees an increase while the strain to failure decreases [15, 16, 18, 36, 37, 39]. This is accompanied with an increase in Young's modulus [15–18, 36]. The same conclusion is drawn for the shear properties of several epoxy resins [16, 18].

For unidirectional carbon/thermoset, the results are not as unanimous. For the $0°$-direction most researchers conclude on an absence of (significant) rate-dependency [21, 25, 26, 38], though some see a decreasing modulus [23], others see decreasing ultimate values [24] and some also see an increase in the value of all properties [15, 19].

Researchers typically find an increase in Young's modulus and ultimate stress and strain for pure $90°$ unidirectional carbon/thermoset [26, 32, 38, 40, 41] though sometimes the change is not significant for all three properties [17, 21, 25, 33]. Only in one case were the ultimate values found to decrease with increasing strain rate [24].

Looking at the shear properties, all sources point towards an increasing maximum stress. Most also see an increase in Young's modulus [17, 20, 22, 25, 26] and a maximum strain which is independent of rate [17, 20, 22, 41]. In unique cases the modulus was found not to depend on rate [41], and the ultimate strain to decrease [25] or increase [26].

There is less data on thermosetting polymers with woven carbon-fibre reinforcements. Although the sources agree on an increase in maximum stress with strain rate [27–31], some say the Young's modulus increases [28, 31], while others say it remains relatively constant [27, 30]. Some say the failure strain in-

creases [27], others say it decreases [28] and yet others find the change is not significant with rate [30, 31]. In all cases when the woven laminate was tested also in weft-direction, the same conclusions could be drawn in terms of rate-dependency, though the absolute values of the engineering properties were slightly below those for the warp direction [28–30].

The agreement in literature is much stronger for woven carbon/thermosets loaded in shear: the maximum stress increases and the maximum strain decreases with rate [28–30, 35]. Some show an increasing Young's modulus with rate as well [28, 30], though others see no significant change [35].

The Poisson's ratio was not found to depend significantly on rate for both unidirectional [24] and woven [30] carbon/thermoset.

An overview of the most prevailing trends regarding rate-dependency in literature is given in table 3.6. It can be seen that unidirectional laminates follow the rate-dependency of the fibres in $0°$-direction. Except for the failure strain, the matrix further predicts the trends in rate-dependency of the other laminates.

Table 3.6. Overview of prevailing conclusions regarding rate-dependency of carbon/thermoset material properties tested in tension. $+$ indicates an increase in value with strain rate, $-$ a decrease, and 0 no significant change. A question mark means there is no general consensus and no symbol means no literature was found for that quantity, and a dot that no relevant data was found for that quantity.

	Carbon fibres	**TS matrix**	**Carbon/TS matrix**	
			Unidirectional	**Weave**
E_x^t	0	$+$	0	?
E_y^t	.		$+$	?
G_{xy}	.	$+$	$+$	$+$
X^t	0	$+$	0	$+$
Y^t	.		$+$	$+$
S_{xy}	.	$+$	$+$	$+$
ε_x^t	0	$-$	0	?
ε_y^t	.		$+$	?
γ_{xy}	.	$-$	0	$-$
ν_{xy}	.	.	0	0

3.4.2 Delamination

There is no general consensus in the literature on whether and how the mode-I fracture toughness of carbon/epoxy composites changes with delamination speed [42]. Some find it increases with speed for carbon/epoxy [43–46], others see a decrease [47–50] and yet others see no change [51–55]. Values lie typically in the order of 200 to about $600\,\mathrm{J\,m^{-2}}$, and changes over the rates studied are typically

below $100\,\mathrm{J\,m^{-2}}$. If there is any rate-dependency found in the current study, it is thus expected to be small.

3.4.3 Impact

Although no work was found to treat the rate-dependency of impact, there are several researchers who compare quasi-static indentation (QSI) with low-velocity impact (LVI) for carbon/epoxy laminates. It was concluded in chapter 2 that an equivalence of damage for both test methods indicates rate-independency.

In some cases in literature, indeed the QSI results fall on the average of the scatter band of the LVI results [56, 57]. Some others claim that both result in similar behaviour and/or equivalent damage [58–62], however, the data shows more than 10% difference in the relation between load and damage [58–60], or a more than 12% lower displacement for the same load [62]. Belingardi and Vadori [61] show a more than 16% higher load and displacement at the point of first load reduction for QSI, even though they consider their studied material rate insensitive. Other authors indeed conclude that LVI and QSI are different for C/E [63–69], where it needs to be noted that Bull et al. [69] are investigating a particle-toughened epoxy and the rate-dependence is concluded to be an artefact of the toughening particles only. Kwon and Sankar [64] and Highsmith [65] conclude that QSI leads to a larger damage zone compared to LVI, contradicting with Lagace [63] and the results of Kaczmarek [59]. Nettles and Hodge [66] and Breen et al. [67] show results that indicate QSI leads to a more than 10% higher load compared to LVI, the opposite is seen by Abdallah et al. [68] who observe a 15% reduction in load.

It is concluded from the above that a small change in damage is to be expected between QSI and LVI, and that carbon/epoxy thus behaves slightly rate-dependent. This could also be expected from the tensile results in section 3.4.1. The way the damage depends on speed, though, is unknown as researchers in literature find varying differences.

3.5 Glass/polyamide-6

The second material used in this research is TenCate CETEX glass/nylon-6 from Ten Cate Advanced Composites B.V., again in a unidirectional and a woven variant. The composite is a combination of E-glass fibres in a BASF UltraBatch 2400 polyamide-6 (PA-6) resin. According to the manufacturer, the PA-6 resin is heat stabilised for processing and has a glass transition and melting temperature of $60\,^{\circ}\mathrm{C}$ and $220\,^{\circ}\mathrm{C}$, and a density of $1130\,\mathrm{kg\,m^{-3}}$ respectively [70]. Not much information is given about the fibres, apart from a density of $2540\,\mathrm{kg\,m^{-3}}$, and that the woven tows come in a balanced twill weave architecture with a weight of

$0.6\,\mathrm{kg\,m^{-2}}$. The tows used have a linear mass density of 1200 tex or $1.2\,\mathrm{g\,m^{-1}}$. Observation of the woven material reveals a tow width of approximately $5\,\mathrm{mm}$. Mechanical properties for generic E-glass fibres are given in table 3.7.

Ten Cate applies a proprietary method to produce a semipreg from E-glass fibres and PA-6, from which composite laminates are created during subsequent hot pressing. The exact cycle characteristics of the hot pressing step are again proprietary, though typical processing temperatures lie in the range of $240\,^{\circ}\mathrm{C}$ - $290\,^{\circ}\mathrm{C}$ [70]. The material is still under development, so no validated mechanical properties are available. The unidirectional properties should be close to those of CETEX TC910 though (table 3.8), and the woven properties to CETEX TC912 (table 3.9).

Table 3.7. Dry E-glass fiber properties.

	Generic E-glass [71]
Filament diameter [μm]	17[a]
Number of filaments in tow	2000[b]
Tow tensile strength [MPa]	3620
Tow tensile modulus [GPa]	72.4
Elongation at break [%]	4.8
Density [$\mathrm{kg\,m^{-3}}$]	2540[c]

a: Estimated average based on optical microscopy
b: Estimation by dividing the tow linear density by the fiber density and cross-sectional area
c: Given by manufacturer

Table 3.8. Selection of mechanical properties given by the manufacturer for unidirectional glass/PA-6 CETEX TC910 [72]. Composite density is $1730\,\mathrm{kg\,m^{-3}}$*, which leads to an approximate fibre volume fraction of* $43\,\%$*.*

	Strength [MPa]	Modulus [GPa]	Failure strain [%]	Poisson's ratio [-]
0° tension	900	30	-	-
0° compression	345	-	-	-
90° tension	-	-	-	-
90° compression	-	-	-	-
In-plane shear	-	-	-	-
Interlaminar shear	42	-	-	-

Table 3.9. Selection of mechanical properties given by the manufacturer for woven glass/PA-6 CETEX TC912 [70]. Fibre volume fraction is $46\,\%$*, composite density* $1820\,\mathrm{kg\,m^{-3}}$.

	Strength [MPa]	Modulus [GPa]	Failure strain [%]	Poisson's ratio [-]
0° tension*	470	21	-	-
0° compression*	470	25	-	-
90° tension*	470	21	-	-
90° compression*	470	25	-	-
In-plane shear	90	2.7	-	-
Interlaminar shear	-	-	-	-

* 0° direction is warp direction, 90° direction is weft direction

Figure 3.6 contains microscopic images of a cross-ply glass/PA-6 laminate with unidirectional layers. Although the polishing quality is not optimal - the scratch marks of the polishing particles are still visible in the images - it is good enough to judge on the quality of the laminate. Compared to the carbon/epoxy, the fibre misalignments are now bigger: the sixth layer from the bottom shows fibres that run at an angle with the cutting plane, while it should be parallel, more like the other 90° layers. Figure 3.6b shows a close-up of the cross-section of the glass fibres. Four conclusions can be drawn, comparing the image to the carbon fibres in figures 3.3a and 3.6b. (1) the glass fibres are much larger in diameter; (2) they seem more round in cross-sectional shape; (3) they clearly show a variation in diameter. Finally, the compaction is much less than for the carbon/epoxy: there is more matrix between the fibres than for the carbon/epoxy.

Figure 3.7 shows a stitched microscopic image of a woven G/PA-6 laminate with the same orientation of all layers. The amount of nesting is much larger than for C/E: the individual layers can hardly be discerned from each other because the layers have sunk deeply into each other. As the size of the bundles is much larger than for C/E, also the matrix pockets have become larger. If a single unit cell is taken as the minimum width to resemble bulk material properties, the minimum specimen width to be taken is about $16\,\mathrm{mm}$. Considering the irregularity of the woven structure, however, it is advised to use larger specimen dimensions.

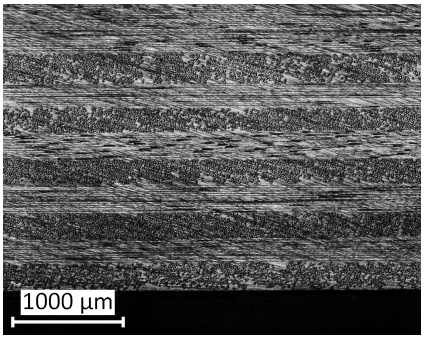

a. The bottom half of the laminate is visible.

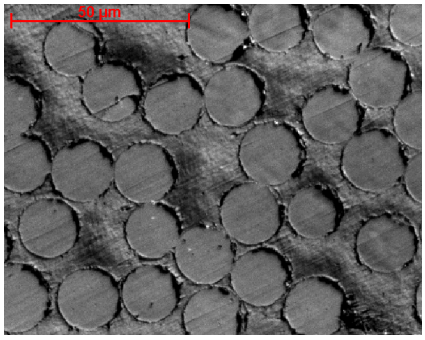

b. Zoom-in on the fibres reveals a variation in diameter.

Figure 3.6. Optical micrographs of glass/polyamide-6 with unidirectional layers polished to a particle size of $10\,\mu\mathrm{m}$*. The thick layer on top in figure 3.6a is at the centre of the laminate.*

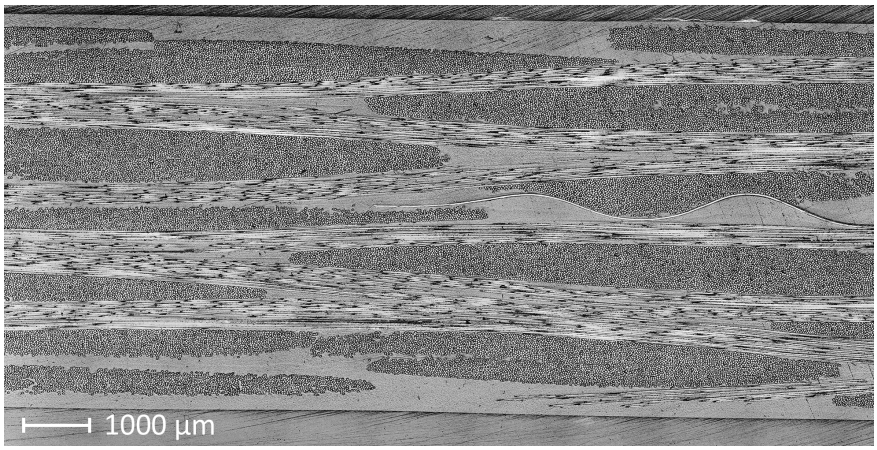

Figure 3.7. Stitched micrograph of a woven G/PA-6 laminate with all layers in the same direction. Looking in the weft direction. A polyimide sheet can be seen in the middle of the right half of the sample, used to create a precrack for delamination testing.

3.6 Expected rate-dependency of glass/polyamide-6

Similarly to section 3.4 for carbon/epoxy, this section deals with the rate-dependent properties for glass/polyamide-6 in literature for the three load cases treated in the current research: tension, mode-I delamination and out-of-plane impact. Again, only literature with at least one test result in the range of $1 \leq \dot{\varepsilon} \leq 500$ has been included.

3.6.1 Tension

An overview of the sources in literature which treat the rate-dependency of a certain tensile mechanical property of any glass/thermoplastic composite is given in table 3.10. The meaning of the symbols is given at the beginning of section 3.4.1.

The two references in literature agree about dry glass fibre behaviour: Young's modulus and failure stress increase with strain rate, and the strain to failure increases only marginally [73, 74].

Although the literature about dynamic tension on thermoplastic matrices treats many different materials, there is overall consensus about an increase in Young's modulus and maximum stress with strain rate [39, 75–82]. The strain to failure is typically found to decrease [39, 75–77, 79], although in some cases the change is not significant [79, 80].

There is no data in literature about the tensile rate-dependency of unidirectional glass-reinforced thermoplastics in the strain rate regime of interest. The only paper found dealt with shear characterization, and found a decrease in Young's modulus, an increase in maximum stress, and the strain to failure did not significantly vary with strain rate [83].

Table 3.10. Number of sources that treat the rate-dependency of indicated properties for glass/thermoplastic composites in tension.

	Glass fibres	**TP matrix**	**Glass/TP matrix**	
			Unidirectional	**Weave**
E_x^t	2 [73, 74]	6 [39, 75, 76, 78–80]	0	2 [84, 85]
E_y^t	0		0	0
G_{xy}	0	0	1 [83]	1 [85]
X^t	1 [73]	6 [39, 75, 76, 80, 81, 86]	0	2 [84, 85]
Y^t	0		0	0
S_{xy}	0	0	1 [83]	1 [85]
ε_x^t	1 [73]	5 [39, 75, 76, 80, 81]	0	2 [84, 85]
ε_y^t	0		0	0
γ_{xy}	0	0	1 [83]	1 [85]
ν_{xy}	0	0	0	0

More dynamic data is available for woven glass-reinforced thermoplastics, though still the number of sources with data is small compared to that for thermosetting composites. The two sources found agree that for loading in the $0°$-direction, the modulus, and maximum stress and strain all increase with strain rate [84, 85]. One of them also treats shear loading, and finds that all three mechanical properties decrease with strain rate [85].

Table 3.11 shows an overview of expected tensile rate-dependency of glass/thermoplastic composites. Although no data was found about how the mechanical properties of a unidirectional glass/thermoplast would vary with rate in the $0°$-direction, it is expected that, like the carbon/thermoset, the dry fibre trends will be followed. It can be seen that this is the case for the woven composites tested in $0°$ as well.

Table 3.11. Overview of prevailing conclusion regarding rate-dependency of glass/thermoplastic material properties tested in tension. $+$ indicates an increase in value with strain rate, $-$ a decrease, 0 no significant change, and a dot that no relevant data was found for that quantity..

	Glass fibres	**TP matrix**	**Glass/TP matrix**	
			Unidirectional	**Weave**
E_x^t	$+$	$+$	·	$+$
E_y^t	·		·	·
G_{xy}	·	·	$-$	$-$
X^t	$+$	$+$	·	$+$
Y^t	·		·	·
S_{xy}	·	·	$+$	$-$
ε_x^t	$+$	$-$	·	$+$
ε_y^t	·		·	·
γ_{xy}	·	·	0	$-$
ν_{xy}	·	·	·	·

3.6.2 Delamination

No literature about the delamination of glass/PA-6 composites is available. A small number of articles was found in which the rate-dependency of mode-I fracture toughness of carbon/PEEK was studied. Although the fibre type is wrong, it is estimated here that it is the matrix which will have the strongest influence on fracture toughness, and considering this concerns a thermoplastic matrix, it is decided that it is worth mentioning. In one of the articles, a strong inverted proportional relationship of the mode-I fracture toughness with testing speed is seen [87]. The other available literature finds an absence of rate dependency [51, 55, 88]. Typical dynamic fracture toughness values lie in the order of $2000\,\mathrm{J\,m^{-2}}$, much higher than

for carbon/epoxy. What would be considered large changes in fracture toughness for carbon/epoxy, would be considered small here. If any, the expected change of the mode-I fracture toughness of glass/PA-6 is a decrease.

3.6.3 Impact

Similar to carbon/epoxy, the current section is based on literature comparing QSI to LVI.

Sources making the comparison of LVI with QSI for composites of any thermoplastic matrix are scarce. Only sources for carbon/PEEK were found, for which conclusions are contradicting. Sjöblom et al. [56] conclude that QSI is equivalent to LVI, while Aymerich et al. [89] see a change in damage mechanism from delamination to fibre failure when switching to QSI.

Judging from the expected rate-dependency in tension, though, a larger difference between QSI and LVI than for carbon/epoxy is expected here, because the fibres are now also known to show rate-dependency.

3.7 Environmental influences

It is important to note that not only the strain rate affects the mechanical response of composite materials. Also the temperature and relative humidity of the environment the materials are loaded in can play a role.

For amorphous thermoplastic polymers, the rate-sensitivity is attributed to the mobility of a portion of the molecules [90]. Fast movement has the same effect as reducing the temperature of the material: the molecules are more restricted to move and the material shows a stronger yet more brittle response. Polyamide-6 is a semi-crystalline polymer [91] and hence this mechanism could explain part of its rate-sensitivity as well.

Although the term 'relative humidity is typically used to express the humidity of an air-water mixture, it is also used as the percentage of water uptake relative to the maximum amount of water that can be absorbed in a material. The relative humidity of a material affects its mechanical response. For PA-6, the strength and modulus go down with increasing moisture uptake [92]. Researchers attribute this effect also to the mobility of the molecules, which increases when water molecules are present between them, because the intermolecular forces decrease with increasing distance [[93].

The above means that strain rate, temperature, and relative humidity all influence the mechanical response of thermoplastics through the mobility of the molecules. The latter two thus need to be accurately controlled if the dependency on strain-rate of such a material is to be obtained. Although automotive structures

experience a large variety of temperatures and humidities, it is decided to focus only on room temperature and a dry material state in the current research.

The environmental effects are less notable on thermoset polymers, because the material kept together by covalent bonds rather than intermolecular forces. As it is, in essence, one large molecule, the intermolecular mobility cannot play a role. Still, the environment influences thermosets as well. For carbon/epoxy composites, a prolonged exposure is needed to show a difference. The mechanical properties are changed due to two effects: (1) a reduction of fibre-matrix interface strength as a result of hydrolysis, and (2) the result of matrix swelling which creates internal stresses [94]. Thermoplastics under prolonged exposure to elevated humidity also suffer from swelling.

3.8 Conclusion

The basic constituents of composite materials were shortly introduced. Two composite material systems will be treated in what follows of this dissertation: (1) carbon fibres in an epoxy matrix and (2) glass fibres in a polyamide-6 matrix. Both material systems were described and manufacturer specifications were detailed.

The current work deals with the assessment of rate-dependency in three different load cases: tension, mode-I delamination and out-of-plane impact. For both material systems, the expected rate-dependency in each of these load cases was determined, based on the available literature. Although there is reasonable consensus in literature about the rate-dependency of the tensile mechanical properties of composites, there are some contradicting results. There is no data on glass/polyamide-6. The conclusions on dependency of mode-I fracture toughness and impact damage, moreover, do not agree.

In the following chapters, the test methods and results for the three load cases are treated. The aim is to develop robust experimental procedures that lead to consistent sets of test data to shed light on the discussion on composite rate-dependency. Chapters 4 and 5 deal with the tensile test method and results, respectively. Chapters 6 and 7 with the delamination method and results. Finally, chapters 8 and 9 treat the impact method and results.

References

[1] A. Long. *Design and Manufacture of Textile Composites*. Cambridge: Woodhead Publishing Limited, 2006.

[2] T. Sugie, A. Nakai, and H. Hamada. *Effect of CF/GF fibre hybrid on impact properties of multi-axial warp knitted fabric composite materials*. Composites Part A: Applied Science and Manufacturing, 40(12):1982–1990, December 2009.

[3] N. Naik, P. Shrirao, and B. Reddy. *Ballistic impact behaviour of woven fabric composites: Formulation*. International Journal of Impact Engineering, 32(9):1521–1552, September 2006.

[4] H. Hamada, K. Kameo, M. Sakaguchi, H. Saito, and M. Iwamoto. *Energy-absorption properties of braided composite rods*. Composites Science and Technology, 60(5):723–729, April 2000.

[5] A. Bilisik. *Three Dimensional Weaving and Braiding*. University of Leeds (Department of Textile Industries), 1991.

[6] M. Singha and K. Singha. *Applications of Textiles in Marine Products*. Marine Science, 2(6):110–119, December 2012.

[7] Pyrofil Department. *Product Data sheet - Quick Cure & High Tg Matrix Resin System PYROFIL #360 / #361*. Technical report, Mitsubishi Rayon Co., Ltd., Carbon Fiber and Composite Materials Division, January 2014.

[8] Pyrofil Department. *PYROFIL TR 30S 3L - Standard Modulus Carbon Fiber - Product Data Sheet*. Technical report, Mitsubishi Rayon Co., Ltd., Carbon Fiber and Composite Materials Division, June 2013.

[9] Pyrofil Department. *PYROFIL TR 50S15L - Standard Modulus Carbon Fiber - Product Data Sheet*. Technical report, Mitsubishi Rayon Co., Ltd., Carbon Fiber and Composite Materials Division, June 2013.

[10] Pyrofil Department. *Mechanical Properties of PYROFIL Unidirectional Composite - TR 360E250S*. Technical report, Mitsubishi Rayon Co., Ltd., Carbon Fiber and Composite Materials Division, December 2013.

[11] Pyrofil Department. *Mechanical Properties of PYROFIL Woven Fabric Composite - TR3110 360GMP*. Technical report, Mitsubishi Rayon Co., Ltd., Carbon Fiber and Composite Materials Division, December 2013.

[12] B. Masschaele, M. Dierick, D. Van Loo, M. N. Boone, L. Brabant, and L. Van Hoorebeke. *HECTOR: A 240kV micro-CT setup optimized for research*. Journal of Physics: Conference Series, 463(1):012012, 2013.

[13] R. D. B. Sevenois, D. Garoz, F. A. Gilabert, S. W. F. Spronk, S. Fonteyn, M. Heyndrickx, L. Pyl, D. Van Hemelrijck, J. Degrieck, and W. Van Paepegem. *Avoiding interpenetrations and the importance of nesting in analytic geometry construction for Representative Unit Cells of woven composite laminates*. Composites Science and Technology, 136:119–132, November 2016.

[14] Y. Zhou, Y. Wang, Y. Xia, and S. Jeelani. *Tensile behavior of carbon fiber bundles at different strain rates*. Materials Letters, 64(3):246–248, February 2010.

[15] H. Al-Zubaidy, X. Zhao, and R. Al-Mahaidi. *Mechanical characterisation of the dynamic tensile properties of CFRP sheet and adhesive at medium strain rates*. Composite Structures, 96:153–164, February 2013.

[16] A. Gilat. *Study of High Strain Rate Response of Composites*. Technical report, National Aeronautics and Space Administration (NASA), April 2003.

[17] A. Gilat, R. K. Goldberg, and G. D. Roberts. *Experimental study of strain rate sensitivity of carbon fiber/epoxy composite*. Composites Science and Technology, 62:1469–1476, 2002.

[18] A. Gilat, R. K. Goldberg, and G. D. Roberts. *Strain Rate Sensitivity of Epoxy Resin in Tensile and Shear Loading*. Technical report, National Aeronautics and Space Administration (NASA), March 2005.

[19] H. AL-Zubaidy, X. Zhao, and R. Al-Mihaidi. *Mechanical Behaviour of Normal Modulus Carbon Fibre Reinforced Polymer (CFRP) and Epoxy under Impact Tensile Loads*. Procedia Engineering, 10:2453–2458, 2011.

[20] I. M. Daniel. *High strain rate properties of off-axis composite laminates, part 2*. Contractor Report 189084, National Aeronautics and Space Administration (NASA), December 1991.

[21] I. M. Daniel and T. Liber. *Strain rate effects on mechanical properties of fiber composites, part 3*. Technical report, National Aeronautics and Space Administration (NASA), June 1976.

[22] I. M. Daniel. *High strain rate properties of angle-ply composite laminates, part 3 (Final Report)*. Contractor Report 189085, National Aeronautics and Space Administration (NASA), 1991.

[23] S. V. Hayes and D. F. Adams. *Rate sensitive tensile impact properties of fully and partially loaded unidirectional composites*. Journal of Testing and Evaluation, 10:61–68, 1982.

[24] G. Yaniv, I. M. Daniel, S. Cokeing, and G. M. Martinez. *Temperature effects on high strain rate properties of graphite/epoxy composites*. Contractor Report 189082, National Aeronautics and Space Administration (NASA), December 1991.

[25] N. Taniguchi, T. Nishiwaki, and H. Kawada. *Tensile strength of unidirectional CFRP laminate under high strain rate*. Advanced Composite Materials, 16(2):167–180, January 2007.

[26] J. Kwon, J. Choi, H. Huh, and J. Lee. *Evaluation of the effect of the strain rate on the tensile properties of carbon–epoxy composite laminates*. Journal of Composite Materials, page 0021998316683439, December 2016.

[27] X. Chen, Y. Li, Z. Zhi, Y. Guo, and N. Ouyang. *The compressive and tensile behavior of a 0/90 C fiber woven composite at high strain rates*. Carbon, 61:97–104, September 2013.

[28] R. Foroutan, J. Nemes, H. Ghiasi, and P. Hubert. *Experimental investigation of high strain-rate behaviour of fabric composites*. Composite Structures, 106:264–269, December 2013.

[29] R. Gerlach, C. R. Siviour, J. Wiegand, and N. Petrinic. *In-plane and through-thickness properties, failure modes, damage and delamination in 3D woven carbon fibre composites subjected to impact loading*. Composites Science and Technology, 72(3):397–411, February 2012.

[30] J. P. Hou and C. Ruiz. *Measurement of the properties of woven CFRP T300/914 at different strain rates*. Composites Science and Technology, 60(15):2829–2834, November 2000.

[31] L. M. Welsh and J. Harding. *Effect of strain rate on the tensile failure of woven reinforced polyester resin composites*. Le Journal de Physique Colloques, 46(C5):C5–405–C5–414, August 1985.

[32] C. C. Chamis and G. T. Smith. *Environmental and High-Strain Rate effects on composites for engine applications*. Technical Memorandum NASA TM 82882, National Aeronautics and Space Administration (NASA), January 1982.

[33] L. G. Melin and L. E. Asp. *Effects of strain rate on transverse tension properties of a carbon/epoxy composite: studied by moiré photography*. Composites Part A: Applied Science and Manufacturing, 30(3):305–316, March 1999.

[34] A. Gilat. *High Strain-Rate and Temperature Effects on the Response of Composites*. Technical report, National Aeronautics and Space Administration (NASA), May 2004.

[35] J. Fitoussi, F. Meraghni, Z. Jendli, G. Hug, and D. Baptiste. *Experimental methodology for high strain-rates tensile behaviour analysis of polymer matrix composites*. Composites Science and Technology, 65(14):2174–2188, November 2005.

[36] R. Gerlach, C. R. Siviour, N. Petrinic, and J. Wiegand. *Experimental characterisation and constitutive modelling of RTM-6 resin under impact loading*. Polymer, 49(11):2728–2737, May 2008.

[37] M. M. Shokrieh, R. Mosalmani, and M. J. Omidi. *Strain-rate dependent micromechanical method to investigate the strength properties of glass/epoxy composites*. Composite Structures, 111:232–239, May 2014.

[38] I. M. Daniel. *High strain rate properties of unidirectional composites, part 1*. Contractor Report 189083, National Aeronautics and Space Administration (NASA), December 1991.

[39] W. Chen, F. Lu, and M. Cheng. *Tension and compression tests of two polymers under quasi-static and dynamic loading*. Polymer Testing, 21(2):113–121, January 2002.

[40] P. Kuhn, M. Ploeckl, and H. Koerber. *Experimental investigation of the failure envelope of unidirectional carbon-epoxy composite under high strain rate transverse and off-axis tensile loading*. EPJ Web of Conferences, 94:01040, 2015.

[41] J. Lienhard and W. Böhme. *Characterisation of RTM CFRP laminates under high-rate tension-, compression-, and shear-loading*. Engineering Fracture Mechanics, 149:33–350, November 2015.

[42] G. C. Jacob, J. M. Starbuck, J. F. Fellers, S. Simunovic, and R. G. Boeman. *The effect of loading rate on the fracture toughness of fiber reinforced polymer composites*. Journal of applied polymer science, 96(3):899–904, 2005.

[43] M. Colin de Verdiere. *Damage and strain rate optical characterisation of standard and tufted non crimp fabric carbon composites for Meso-scale impact models*. PhD thesis, Cranfield University, September 2009.

[44] M. Colin de Verdiere, A. A. Skordos, M. May, and A. C. Walton. *Influence of loading rate on the delamination response of untufted and tufted carbon epoxy non crimp fabric composites: Mode I*. Engineering Fracture Mechanics, 96:11–25, December 2012.

[45] H. Kilic, R. Patel, and S. R. Soni. *High Strain Rate Testing of Co-Cured/Z-Pinned Composites in Mode-I*. SAMPE Journal, 41(5):58–66, 2005.

[46] H. You and Y. Yum. *Loading Rate Effect on Mode I Interlaminar Fracture of Carbon/Epoxy Composite*. Journal of Reinforced Plastics and Composites, 16(6):537–549, April 1997.

[47] M. S. Sohn and X. Z. Hu. *Impact and high strain rate delamination characteristics of carbon fibre epoxy composites*. Theoretical and Applied Fracture Mechanics, 25(1):17–29, April 1996.

[48] S. I. Thorsson, A. M. Waas, J. Schaefer, B. Justusson, and S. Liguore. *Effects of elevated loading rates on mode I fracture of composite laminates using a modified wedge-insert fracture method*. Composites Science and Technology, 156:39–47, March 2018.

[49] X. Wu and Y. A. Dzenis. *Rate effects on mode-I delamination toughness of a graphite/epoxy laminated composite*. International journal of fracture, 112(2):9–12, 2001.

[50] H. Zabala, L. Aretxabaleta, G. Castillo, and J. Aurrekoetxea. *Loading rate dependency on mode I interlaminar fracture toughness of unidirectional and woven carbon fibre epoxy composites*. Composite Structures, 121:75–82, March 2015.

[51] J. W. Gillespie Jr., L. A. Carlsson, and A. J. Smiley. *Rate-dependent mode I interlaminar crack growth mechanisms in graphite/epoxy and graphite/PEEK*. Composites Science and Technology, 28(1):1–15, 1987.

[52] J. Machado, E. Marques, R. Campilho, and L. F. da Silva. *Mode I fracture toughness of CFRP as a function of temperature and strain rate*. Journal of Composite Materials, page 0021998316682309, December 2016.

[53] T. Kusaka, M. Hojo, Y. Mai, T. Kurokawa, T. Nojima, and S. Ochiai. *Rate dependence of mode I fracture behaviour in carbon-fibre/epoxy composite laminates*. Composites Science and Technology, 58(3–4):591–602, March 1998.

[54] G. Hug, P. Thévenet, J. Fitoussi, and D. Baptiste. *Effect of the loading rate on mode I interlaminar fracture toughness of laminated composites*. Engineering Fracture Mechanics, 73(16):2456–2462, November 2006.

[55] A. Smiley and R. Pipes. *Rate Effects on Mode I Interlaminar Fracture Toughness in Composite Materials*. Journal of Composite Materials, 21(7):670–687, January 1987.

[56] P. O. Sjöblom, J. T. Hartness, and T. M. Cordell. *On Low-Velocity Impact Testing of Composite Materials*. Journal of Composite Materials, 22(1):30–52, January 1988.

[57] E. Wu and K. Shyu. *Response of Composite Laminates to Contact Loads and Relationship to Low-Velocity Impact*. Journal of Composite Materials, 27(15):1443–1464, December 1993.

[58] S. M. Lee and P. Zahuta. *Instrumented impact and static indentation of composites*. Journal of Composite Materials, 25(2):204–222, 1991.

[59] H. Kaczmarek and S. Maison. *Comparative ultrasonic analysis of damage in CFRP under static indentation and low-velocity impact*. Composites Science and Technology, 51(1):11–26, January 1994.

[60] D. D. Symons. *Characterisation of indentation damage in 0/90 lay-up T300/914 CFRP*. Composites Science and Technology, 60(3):391–401, February 2000.

[61] G. Belingardi and R. Vadori. *Influence of the laminate thickness in low velocity impact behavior of composite material plate*. Composite Structures, 61(1–2):27–38, July 2003.

[62] Y. Aoki, H. Suemasu, and T. Ishikawa. *Damage propagation in CFRP laminates subjected to low velocity impact and static indentation*. Advanced Composite Materials, 16(1):45–61, January 2007.

[63] P. A. Lagace, J. E. Williamson, P. W. Tsang, E. Wolf, and S. Thomas. *A preliminary proposition for a test method to measure (impact) damage resistance*. Journal of Reinforced Plastics and Composites, 12(5):584–601, 1993.

[64] Y. S. Kwon and B. V. Sankar. *Indentation-flexure and low-velocity impact damage in graphite epoxy laminates*. Journal of Composites Technology & Research, 15(2):101–111, June 1993.

[65] A. L. Highsmith. *A Study of the Use of Contact Loading to Simulate Low Velocity Impact*. Technical report, National Aeronautics and Space Administration (NASA), January 1997.

[66] A. T. Nettles and A. J. Hodge. *The Impact Response of Carbon/Epoxy Laminates (Center Director's Discretionary Fund, Project No. 94-13)*. Technical report, National Aeronautics and Space Administration (NASA), November 1997.

[67] C. Breen, F. Guild, and M. Pavier. *Impact of thick CFRP laminates: the effect of impact velocity*. Composites Part A: Applied Science and Manufacturing, 36(2):205–211, February 2005.

[68] E. A. Abdallah, C. Bouvet, S. Rivallant, B. Broll, and J. Barrau. *Experimental analysis of damage creation and permanent indentation on highly oriented plates*. Composites Science and Technology, 69(7–8):1238–1245, June 2009.

[69] D. J. Bull, S. M. Spearing, and I. Sinclair. *Investigation of the response to low velocity impact and quasi-static indentation loading of particle-toughened carbon-fibre composite materials*. Composites Part A: Applied Science and Manufacturing, 74:38–46, July 2015.

[70] Ten Cate Advanced Composites. *TenCate GA0600/PA6 - Technical data*. Technical report, Koninklijke Ten Cate B.V., March 2015.

[71] MatWeb, LLC. *E-Glass Fiber, Generic*. Technical Report CGF004 / 900, MatWeb, 1998.

[72] Ten Cate Advanced Composites. *TenCate Cetex TC910 Nylon 6 - Technical data*. Technical report, Koninklijke Ten Cate B.V., August 2013.

[73] Z. Wang. *Experimental evaluation of the strength distribution of E-glass fibres at high strain rates*. Applied Composite Materials, 2(4):257–264, 1995.

[74] Z. Wang and Y. Xia. *Experimental evaluation of the strength distribution of fibers under high strain rates by bimodal Weibull distribution*. Composites Science and Technology, 57(12):1599–1607, January 1998.

[75] B. L. Peterson, R. N. Pangborn, and C. G. Pantano. *Static and high strain rate response of a glass fiber reinforced thermoplastic*. Journal of composite materials, 25(7):887–906, 1991.

[76] M. Schossig, C. Bieroegel, W. Grellmann, R. Bardenheier, and T. Mecklenburg. *Effect of Strain Rate on Mechanical Properties of Reinforced Polyolefins*. In E. E. Gdoutos, editor, Fracture of Nano and Engineering Materials and Structures, pages 507–508. Springer Netherlands, January 2006.

[77] M. Schoßig, C. Bierögel, W. Grellmann, and T. Mecklenburg. *Mechanical behavior of glass-fiber reinforced thermoplastic materials under high strain rates*. Polymer Testing, 27(7):893–900, October 2008.

[78] M. Zrida, H. Laurent, V. Grolleau, G. Rio, M. Khlif, D. Guines, N. Masmoudi, and C. Bradai. *High-speed tensile tests on a polypropylene material*. Polymer Testing, 29(6):685–692, September 2010.

[79] X. Xiao and M. Leach. *Intermediate and high strain rate tensile testing of plastic materials*. General Motors Corporation, Warren, MI, page 48090–9055, 2005.

[80] B. Bonnet. *Comportement au choc de matériaux composites pour applications automobiles*. PhD thesis, École Nationale Supérieure des Mines de Paris, 2005.

[81] S. R. Raisch and B. Möginger. *High rate tensile tests – Measuring equipment and evaluation*. Polymer Testing, 29(2):265–272, April 2010.

[82] M. Reiter and Z. Major. *Determination of Tensile Properties of Polymers at High Strain Rates*. EPJ Web of Conferences, 6:39008, 2010.

[83] N. Papadakis, N. Reynolds, M. W. Pharaoh, P. K. C. Wood, and G. F. Smith. *Strain rate effects on the shear mechanical properties of a highly oriented thermoplastic composite material using a contacting displacement measurement methodology–Part A: elasticity and shear strength*. Composites Science and Technology, 64(5):729–738, April 2004.

[84] M. Todo, K. Takahashi, P. Béguelin, and H. H. Kausch. *Strain-rate dependence of the tensile fracture behaviour of woven-cloth reinforced polyamide composites*. Composites Science and Technology, 60(5):763–771, April 2000.

[85] K. A. Brown, R. Brooks, and N. A. Warrior. *The static and high strain rate behaviour of a commingled E-glass/polypropylene woven fabric composite*. Composites Science and Technology, 70(2):272–283, February 2010.

[86] I. Benaceur, R. Othman, P. Guegan, A. Dhieb, and F. Damek. *Sensitivity of the flow stress of nylon 6 and nylon 66 to strain-rate*. International Journal of Modern Physics B, 22(09n11):1249–1254, April 2008.

[87] S. Mall, G. Law, and M. Katouzian. *Loading Rate Effect on Interlaminar Fracture Toughness of a Thermoplastic Composite*. Journal of Composite Materials, 21(6):569–579, January 1987.

[88] S. Hashemi, A. Kinloch, and J. Williams. *The Effects of Geometry, Rate and Temperature on the Mode I, Mode II and Mixed-Mode I/II Interlaminar Fracture of Carbon-Fibre/Poly(ether-ether ketone) Composites*. Journal of Composite Materials, 24(9):918–956, September 1990.

[89] F. Aymerich, P. Priolo, and D. Vacca. *Static loading and low-velocity impact characterization of graphite/PEEK laminates*. In International Conference on Advanced Composites(ICAC 98), Hurghada, Egypt, page 519–528, 1998.

[90] A. D. Mulliken and M. C. Boyce. *Mechanics of the rate-dependent elastic–plastic deformation of glassy polymers from low to high strain rates*. International Journal of Solids and Structures, 43(5):1331–1356, March 2006.

[91] H. Wittich, M. Evstatiev, E. Bozwelieva, K. Friedrich, and S. Fakirov. *Effect of crystallinity on the interlaminar fracture toughness of continuous glass fiber-polyamide composites*. Advanced Composite Materials, 2(2):135–152, January 1992.

[92] K. Hatten, G. Woodham, and D. Pinkston. *Effect of moisture on reinforced nylons*. Plastics Design and Processing, 11(3):28–29, March 1971.

[93] A. Benaarbia, A. Chrysochoos, and G. Robert. *Influence of relative humidity and loading frequency on the PA6.6 cyclic thermomechanical behavior: Part I. mechanical and thermal aspects*. Polymer Testing, 40:290–298, December 2014.

[94] A. Zafar, F. Bertocco, J. Schj?dt-Thomsen, and J. C. Rauhe. *Investigation of the long term effects of moisture on carbon fibre and epoxy matrix composites*. Composites Science and Technology, 72(6):656–666, March 2012.

4 Dynamic Tensile Testing

4.1 Introduction

The first load case under consideration is dynamic tension. In this chapter, the entire experimental set-up is explained: first the data acquisition is treated, followed by the specimen preparation, and then the data reduction is detailed. Finally, the various limits on strain rate discovered in the test development process are discussed and quantified. Chapter 5 contains all the results of the test campaign and a discussion thereof.

4.2 Goal

The goal of the dynamic tension test campaign is to obtain tensile engineering properties versus strain rate. The rates of interest are defined by the application to vehicle impact situations and therefore run from quasi-static up to $200\,\mathrm{s}^{-1}$, as explained in chapter 1. Since it is unknown beforehand which parameters are needed in material models that describe dynamic tensile composite behaviour, the focus lies on obtaining entire stress-strain curves.

4.3 Choice of test method

The only test method available that can cover the entire range of strain rates of interest from quasi-static up to $200\,\mathrm{s}^{-1}$ with specimen sizes significantly larger than

the weave unit cell is testing using a hydraulic pulse test bench, as is concluded in chapter 2. The machine available at UGent is a Schenck Hydropuls z25/20 operated by an Instron 8800 controller (figure 4.1). It can pull up to $25\,\mathrm{kN}$ at a velocity up to $20\,\mathrm{m\,s^{-1}}$. The maximum effective stroke is $200\,\mathrm{mm}$ and the clamp area for the tensile set-up is 20 by $20\,\mathrm{mm}$. Below $1\,\mathrm{m\,s^{-1}}$ it can actively control its position, but above that speed, it operates in an open-loop mode. In this mode, the valve is given a preselected amount of opening after which the actuator starts to move. The absence of direct position control results in a velocity profile that deviates further from a single block wave than is the case at low speeds.

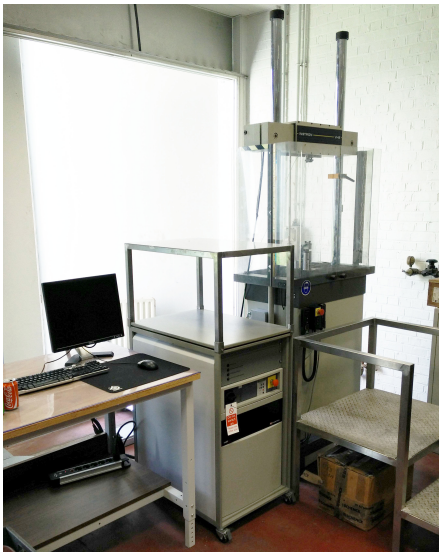

Figure 4.1. Hydraulic pulse test bench at UGent-MMS

4.4 Data acquisition

In order to extract material properties, quantities need to be measured and stored. Ideally, the tests provide entire stress-strain curves, from which values for failure stress and strain, maximum stress, Young's modulus and Poisson's ratio can be extracted. A sufficient number of data points for force and strain is required to provide accurate measurements of the aforementioned quantities. Therefore, not only the test needs to be fast: the data acquisition should be fast enough as well. This section first treats how load is measured, then details the measurement of strain, and finally it is explained how the various data streams are synchronized.

To outline the requirements on the data acquisition, the shortest test duration is taken. The highest required strain rate is $200\,\mathrm{s^{-1}}$, and the layup that is expected

to fail with the smallest strain to failure (90° unidirectional (UD) carbon/epoxy (C/E)) has an ultimate strain of $0.6\,\%$ (see table 3.2 in chapter 3). The combination of these two leads to a value for the duration of the shortest test: $30\,\mu s$.

4.4.1 Load acquisition

Load is typically measured indirectly using some form of strain. The most common type of load cells uses an internal arrangement of strain gauges to allow for the load to be measured from the straining of the internal elements. Such cells have a very high precision but also a relatively small response bandwidth or a low natural frequency, limiting their use to quasi-static applications. Dynamic forces are typically measured using a quartz load cell, which have a much wider response bandwidth and can thus measure faster oscillating forces. The quartz load cell is thus selected for the dynamic tensile tests, see figure 4.2. This type of cells works on the piezoelectric principle of a quartz crystal in compression, which converts applied strain to a measurable charge and is independent of load range. Typically the quartz cell deforms much less to measure the same force as a strain gauge-based load cell. Another advantage is that the load sensitivity is independent of the sensor capacity [1]. The downside of these types of cells is signal drift. Because the measurement is based on charge and no material has infinite insulation resistance, some leakage is always present, decaying the response for any constantly applied load towards zero. This means quasi-static loads are difficult to measure correctly. Another aspect to keep in mind is that the cells only work in compression. Tensile loads are thus measured by unloading of the cell, which is typically kept under compression in a test bench. The type of cell used in this research is a Kistler 9061A 200kN load washer. The charge is subsequently amplified by a Kistler 5011B Charge Amplifier, which has a bandwidth of $200\,\mathrm{kHz}$ [2].

Any used signal conditioning or amplifying device should be capable of handling sufficiently high frequencies. The SAE recommended practise for high strain

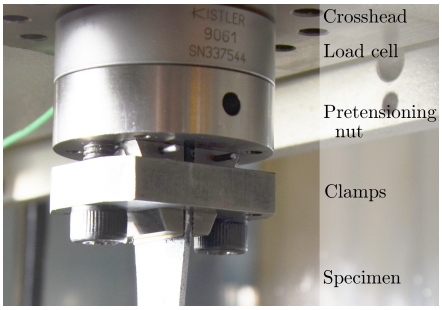

Figure 4.2. Piezoelectric load cell mounted in hydraulic pulse test bench.

rate tensile testing of polymers advises ten times the approximate maximum signal frequency, which is determined by assuming the shortest test resembles a quarter of a sine up to the yield point [3]. Taking the failure point as the yield point, the minimum test duration of $30\,\mu s$ results in a maximum frequency of $8.33\,\mathrm{kHz}$. In that case, the SAE thus advises a minimum frequency response of $83.3\,\mathrm{kHz}$. ISO 26203-2 for testing metallic materials at high strain rates states that the frequency response on force should be at least $1000\dot{\varepsilon}$ [4]. This amounts to $200\,\mathrm{kHz}$ for the current situation. The current equipment covers the most stringent of these two requirements.

The piezoelectric load cell also has another upper limit in terms of testing speed: at high rates, the cell suffers from load oscillations [4]. These stem from an inevitably finite natural vibration frequency of the system, which depends on the stiffness of the load cell and the mass of the structure that keeps it under compression [1]. This is the reason the clamps of the hydraulic pulse machine need to be as light as possible, and therefore they are directly attached to the part that keeps the load washer under compression (figure 4.2).

4.4.2 Strain acquisition

There are several options to measure the strain of a tensile specimen. Using the machine displacement is not considered, because (1) it is inaccurate due to machine compliance and (2) the presence of a slack rod allows free movement of the piston during the initial part of the test and after engaging the bottom clamp, oscillations might be present. A clip-on gauge or extensometer cannot be used since it will be propelled away at failure of the specimen, likely causing it to be broken. Optical fibres are no suitable candidate because the read-out is generally not fast enough. Among the relatively common methods of measuring strain, two candidates remain: strain gauges or optical methods (such as digital image correlation (DIC) or optical extensometry).

The challenges of a fast strain measurement lie fully on the side of data acquisition. Applying the strain gauge or the DIC pattern to the specimen can be done using regular techniques.

To measure strain using strain gauges, general-purpose $350\,\Omega$ CEA-06-250UN-350 gauges by Vishay Precision Group are used. For a meaningful strain gauge readout, wiring needs to be attached first. Here, a three-wire system is used (figure 4.3a) with a shielded and twisted cable for minimization of noise pickup [5], and an AWG-32 (or $0.2\,\mathrm{mm}$ diameter) leadwire as opposed to thicker and thus heavier wires to reduce the chance the solder joints are broken during testing. A powering voltage of $10\,\mathrm{V}$ is chosen to allow for the highest measurement accuracy without heating up the specimen too much [6]. Direct unconditioned measurement of the signal is possible, though the signal-to-noise ratio is low, because a

$1000\ \mu\varepsilon$ extension leads only to about a $5\,\mathrm{mV}$ signal when the bridge is powered at $10\,\mathrm{V}$. Therefore, a Vishay 2100 signal conditioning amplifying system is used in increased bandpass mode. In this setting, at its minimum gain, the system can amplify signals of up to $35\,\mathrm{kHz}$. As mentioned in the previous section, the SAE advises a minimum frequency response of $83.3\,\mathrm{kHz}$. The ISO 26203-2 advise for strain amplification amounts to $20\,\mathrm{kHz}$. The limit of the signal conditioning equipment used for the current research falls in between both limits, and thus it might affect the measured strains. Section 4.8.4 treats the influence of the bandwidth on the strain acquisition, and the resulting consequence for the maximum strain rate that can be correctly measured. The equipment increases the $5\,\mathrm{mV}$ signal at $1000\ \mu\varepsilon$ to about $370\,\mathrm{mV}$. The amplifier is limited to about $10\,\mathrm{V}$ output, hence the bridge voltage needs to be reduced if failure strains of $2.7\,\%$ or higher are expected, considering that the equipment already operates at minimal gain.

A Photron SA-4 high-speed camera (HSC) with DC light sources is used to capture the full strain field of the gauge section of each specimen using 2D digital image correlation (DIC). 3D-DIC is not used since the motion is in-plane so it is not strictly necessary, and it is decided that the potential of added in-plane accuracy does not weigh up to the increased difficulty to bring a large (more than 500 specimens) tensile test programme to a good end. A serious downside of the type of cameras used is the loss of resolution when the frame rate is increased, which is typically not seen in an ultra-high-speed camera. The latter type, though, would be less applicable for the relatively long duration of intermediate strain rate tests due to its usually limited record length [7]. Such a device, moreover, was not available for the current research. As mentioned above, the test duration of the fastest test is about $30\,\mu\mathrm{s}$. The camera should thus record at $500\,000$ frames per second to obtain 15 data points for the stress-strain curve. Recording at this frame rate reduces the maximum image size for the fastest tests to 128 x 16 pixels, see also figure 4.3b. Each pixel then corresponds to a square of about 0.5 by $0.5\,\mathrm{mm}$ size on the specimen. Slower tests are recorded at reduced frame rates and increased image dimensions to reduce the noise on the DIC results.

Only a small portion of the chip is used, which is always set to lie in the optical centre, resulting in an image which is practically undistorted by the lens because most distortion occurs near the edges [8]. Even though the amount of correction provided by the DIC calibration is therefore minor (figure 4.4), it is still performed to remove any influence of lens distortion on the results. The added advantage is that the measured displacements become absolute. The camera, and more importantly the lens, is allowed to warm up before calibration, to take into account a possible heating effect on the lens distortion.

For the high-speed tests, the image resolution is too low to obtain images of sufficient quality of the calibration patterns that fit the field of view. The procedure is therefore carried out at an increased number of pixels. This allows for a bigger

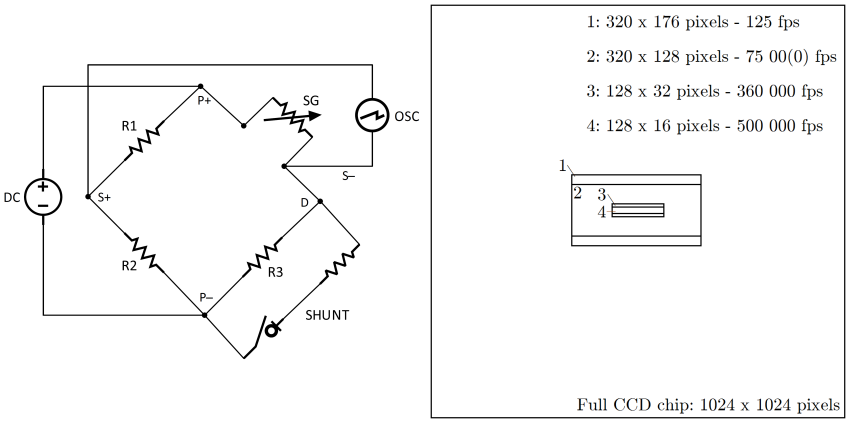

a. Quarter bridge setup used for strain acquisition: SG is the strain gauge, OSC the oscilloscope to measure strain, the SHUNT-part the calibration circuit.

b. Only a portion of the camera's CCD chip is used. The faster the acquisition, the smaller the usable area. Note: area 1 is not limited by the camera's frame rate.

Figure 4.3. Strain acquisition details for (a) gauge strain and (b) DIC.

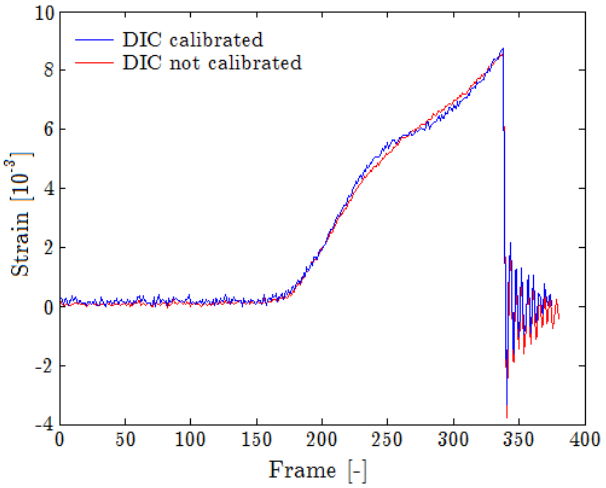

Figure 4.4. DIC result with (blue) and without (red) calibration.

calibration pattern to be recorded, which contains dots of a size large enough for the DIC program to recognise them, see figure 4.5a. Subsequently, the recorded images of the test are resized from their original dimensions to the same ones as for the DIC calibration images, so they look like figure 4.5b. In the process, no figures are scaled but only black is added to the outside. It is ensured, moreover, that both the calibration and the test footage is recorded in the optical centre of the CCD chip. The internal camera architecture prevents from making the smallest resolution an upright rectangle, this is likely due to the way the CCD-chip is read out. It is therefore chosen to rotate the camera 90 degrees to capture a larger portion of the specimen.

The accuracy of the DIC acquisition can be evaluated by recording the movement of a specimen which is only clamped in the lower clamp. This way, no strain should be recorded. The measured displacement, moreover, should match with what is requested from the test bench. The displacement is compared in figure 4.6a. A significant amount of noise is seen on the displacement measured by the bench (marked Bench in the legend), indicating that the internal transducer is better suited for large displacements. The DIC result passes right through the middle of results from the internal displacement transducer, validating the DIC method. The amount of strain of a zero-strain test at the minimum resolution is shown in figure 4.6b. As can be seen, the result is not perfectly zero, but a strain of maximally 2.5×10^{-4} is given by the system. The minimum failure strain to be measured is 6×10^{-3} [9]. The error in this case thus amounts to $4.2\,\%$ of the maximum strain.

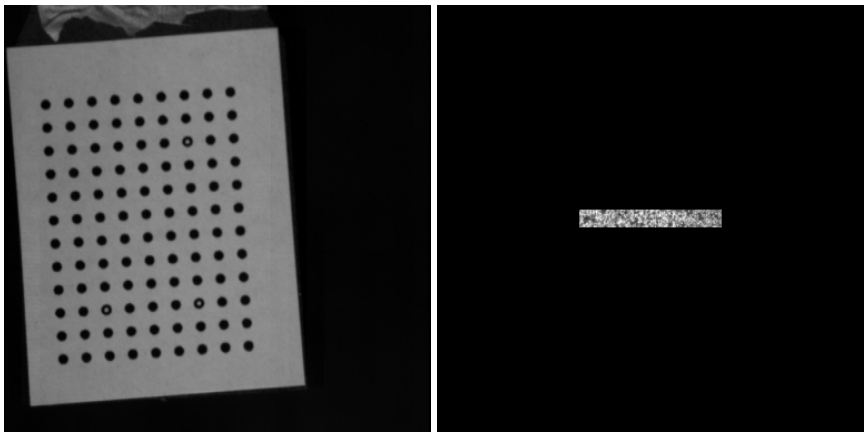

a. DIC calibration at 384x384 pixels, rotated 90 degrees w.r.t. reality (see section 4.4.2).

b. High speed DIC recording resized to 384x384 pixels by adding black, rotated 90 degrees w.r.t. reality.

Figure 4.5. Full-size recording of (a) a calibration grid and (b) a high-rate specimen.

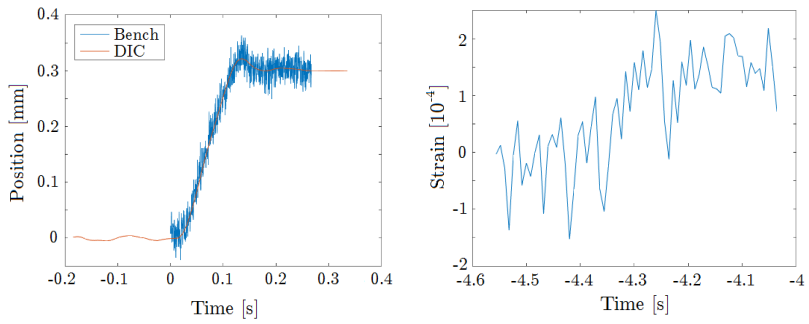

a. Displacement comparison between zero-strain DIC and bench recording.

b. Recorded DIC strain with zero-strain test.

Figure 4.6. DIC performance checks by (a) comparing to bench displacement and (b) calculating zero strain.

4.4.3 Data storage and synchronization

Data storage should take place at sufficient samples per second. A minimum would be the Nyquist frequency, which would be at twice the maximum frequency response of any conditioning equipment (200 kHz). ISO 26203-2 advises four times the limit frequency of the force measurement system, which would lead to 800 kSamples s^{-1}. The output of all the measurement systems is recorded using a GN412 100 Msamples/s data acquisition card in a HBM GEN5i digital oscilloscope, which has a bandwidth of at least 26 MHz [10].

To ensure that both the oscilloscope and the camera capture test data in time, they operate in single-shot mode. In this mode, they continuously acquire and store data while overwriting earlier taken measurements by new ones. As soon as a trigger signal is received, the machines continue until a user-defined fraction of their memory has been written. This way, the remaining portion of the memory contains data from before the trigger signal, and there is no need for a compensation of start-up delay. The trigger signal is produced by the digital oscilloscope when it measures a first load higher than a pre-set threshold value. It then triggers its own measurement cards and it sends a 5 V pulse to the HSC.

Only when the load and strain data are well synchronised, they can be used to build the stress-strain curve and give information about the Young's modulus of the specimen. Perfect synchronisation does not exist, as all electronics produce some form of internal delay. It is attempted here, though, to take these delays into account as much as possible. Figure 4.7 shows the data-acquisition part of the set-up. As the synchronisation is most critical for the fastest test, this is the situation considered here. The resistance of the strain gauge and the charge in the load cell are assumed to change without delay with strain and load, respectively. None of

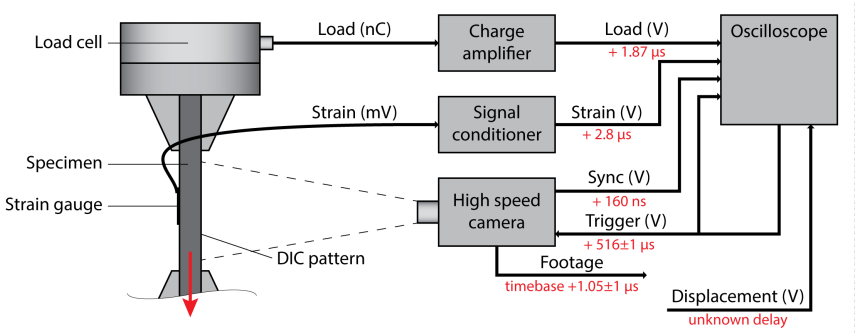

Figure 4.7. The data acquisition in the dynamic tension set-up. The values in red are the non-cumulative delays of the respective signals when recording at the highest rate: for the total delay of e.g. the camera timebase, the indicated values still need to be combined in the correct manner.

the wires used is larger than $5\,\mathrm{m}$ so, assuming all signals travel faster than half the speed of light in vacuum ($3 \times 10^8\,\mathrm{m\,s^{-1}}$), they cause delays of no more than $33\,\mathrm{ns}$ each. This is considered small enough to be negligible for the purpose of this research. The charge amplifier has a delay of $1.87\,\mu\mathrm{s}$ between charge input and voltage output for various input frequencies, which were produced by a function generator and converted to charge via a capacitor. The delay between input and amplified output of the signal conditioner depends slightly on frequency. A comparison of the phase of a curve-fit of the output to that of the input reveals a delay of $1.32\,\mu\mathrm{s}$ at $100\,\mathrm{Hz}$ up to a delay of $2.83\,\mu\mathrm{s}$ at $10\,\mathrm{kHz}$. The latter value is used here, as applying the correct delay is most critical for the fast-changing signals. The trigger delay on the oscilloscope equals $516 \pm 1\,\mu\mathrm{s}$ + maximum 1 sample period [10]. The fastest tests are recorded at $100\,\mathrm{MHz}$, so 1 sample period amounts to $10\,\mathrm{ns}$, and the variable added delay of up to 1 sample period is thus ignored here. It is assumed that the input delay is also limited to 1 sample period, and it is therefore neglected as well. To cover for the $\pm 1\,\mu\mathrm{s}$ uncertainty on the trigger delay, the produced trigger signal is measured again by the oscilloscope, as is indicated in figure 4.7. The HSC manual states that a trigger pulse of $50\,\mathrm{ns}$ or greater is needed to trigger the recording [11], so a delay of that length is assumed for the start of the camera. This delay is added to the moment the trigger pulse reaches a value of $3.3\,\mathrm{V}$, which is the actual voltage at which Photron cameras are triggered [12]. At the highest rate of $500\,000$ fps, the camera acquires a frame every $2\,\mu\mathrm{s}$. As a continuous recording is already started before the trigger signal is received, this causes a maximum added delay of the timebase of the camera of $2\,\mu\mathrm{s}$, because the trigger signal is never received at the exact moment a frame is recorded. To cover for this variable delay, the synchronisation signal of the camera is recorded by the oscilloscope, which is a block signal that indicates the moment of frame recording.

The $160\,\mathrm{ns}$ delay on this signal [11] is taken into account as well. The remaining uncertainty on the synchronization is estimated to lie below $0.1\,\mu\mathrm{s}$. For clarity, the delay values are indicated in red in figure 4.7 and summarized in table 4.1.

Table 4.1. Summary of acquisition equipment, settings and in- and output delays.

Equipment	Purpose	Relevant settings at highest speed	In delay [µs]	Out delay [µs]
Kistler 5011B	Charge amplifier	Short Time Constant, wideband	- [a]	1.87
Vishay 2100	Signal conditioner	Minimal gain, high bandpass mode	- [a]	2.83
HBM GN412	Digital oscilloscope	$100\,\mathrm{MSamples\,s^{-1}}$, wideband	$< 10^{-5}$	516 ± 1 [b]
Photron SA4	High-speed camera	500 000 fps at 128 x 16 pixels	1.05 ± 1	0.16 [c]

[a] Assumed absent
[b] Delay on the trigger output
[c] Delay on the synchronization signal

4.5 Test set-up preparation

For accurate measurements, it should be verified whether the test set-up produces accurate measurements. The displacement transducer is calibrated by comparison with DIC (figure 4.6a) and by using another transducer. The dynamic load cell is calibrated by connecting it in series with a calibrated static cell and matching the outputs. The error is estimated to lie within $\pm 50\,\mathrm{N}$ for a maximum load of $15\,\mathrm{kN}$, or $0.33\,\%$. A velocity calibration is carried out by evaluating the derivative of the measured displacement as a function of the selected valve opening voltage. The velocity obtained during the time the specimens are stretched lies below the requested velocity due to the absence of tensile loads during calibration. The velocities within one test scenario typically do not vary more than $1\,\%$. Finally, the grip alignment is evaluated by means of a gauged straight bar [13]. The alignment is found to be within $0.25°$, which is sufficiently well aligned, see also section 4.7.3.1.

4.6 Specimen preparation

As material is delivered in square plates, some steps need to be carried out before it is ready to be tested.

4.6.1 Overall specimen dimensions

In chapter 1, a strain rate of $200\,\mathrm{s}^{-1}$ was selected as an upper bound. The hydraulic pulse machine can produce a maximum piston velocity of $20\,\mathrm{m\,s}^{-1}$. As will be shown later, the speed is already non-constant at $5\,\mathrm{m\,s}^{-1}$. At $20\,\mathrm{m\,s}^{-1}$, the speed is far from constant, so a small buffer with the limit velocity is taken and $15\,\mathrm{m\,s}^{-1}$ is selected as maximum usable velocity. Assuming the gauge section of the specimens is the only part that deforms, and that this deformation is perfectly elastic, the strain ε can be calculated by dividing the change in length Δl by the gauge section length l_g. The change in length is then equal to the machine displacement d:

$$\varepsilon = \frac{\Delta l}{l_g} = \frac{d}{l_g} \tag{4.1}$$

Using equation (4.1), a theoretical strain rate can be calculated by dividing the rate of displacement, or velocity v, with the gauge length:

$$\dot{\varepsilon} = \frac{v}{l_g} \tag{4.2}$$

Using equation (4.2), a gauge length of $75\,\mathrm{mm}$ is theoretically needed to reach a strain rate of $200\,\mathrm{s}^{-1}$ at $15\,\mathrm{m\,s}^{-1}$. It is however expected that the acquired rate will be lower, due to the fact that (1) the specimen could slip slightly in the grips, (2) parts of the specimen outside of the gauge zone also stretch, and (3) also parts of the test bench will stretch rather than only the specimen. A smaller gauge length of $50\,\mathrm{mm}$ is therefore chosen.

The machine should be able to break the specimens. The width is therefore dependent on the expected maximum stress of the material, which in turn depends on the composite layup. For example, to break a 4-layer unidirectional (UD) C/E composite of $0.9\,\mathrm{mm}$ thick, the width is limited to about $10\,\mathrm{mm}$, considering the maximum strength of $2300\,\mathrm{MPa}$ (table 3.2) and a maximum load of $20\,\mathrm{kN}$ (to allow a buffer to the machine limit of $25\,\mathrm{kN}$). If this calculation results in a width over $20\,\mathrm{mm}$, a width of $20\,\mathrm{mm}$ is selected because it is the maximum width that the grips of the hydraulic pulse machine can clamp.

4.6.2 Lay-ups

As will be explained in section 5.2, for both C/E and glass/polyamide-6 (G/PA-6), a series of different laminates is tested. For model input and development purposes, pure matrix, 0° UD, 90° UD, cross-ply $\pm 45°$ UD as well as $\#(0/90)$ and $\#(\pm 45)$ (i.e. woven) orientations are deemed necessary. Various other lay-ups are tested as well, partially for model validation, see table 4.2. As explained in section 3.2.4, a subscript number indicates the amount of repetitions and a subscript '*s*' stands for symmetry.

Table 4.2. Tested configurations for each material, apart from pure matrix.

UD laminates	Woven laminates
$[0]_4$	$[\#(0/90)]_{4s}$
$[90]_8$	$[\#(90/0)]_{4s}$
$[90/0]_{2s}$	$[\#(\pm 45)]_{4s}$
$[45/0/-45/90]_s$	$[\#(\pm 45)/\#(0/90)]_{2s}$
$[\pm 45]_{2s}$	

4.6.3 Specimen shapes

The clamps introduce stress concentrations in the specimens. It is thus often advised to use a specimen shape that is weaker away from the tabs, but this depends on the layup tested. The test standards for quasi-static tensile testing provide shapes [14, 15], but because of the required strain rate, these shapes are not suitable (i.e. they are too long).

Straight-sided specimens are used for $0°$ UD, $0-90$ UD and ± 45 specimens (both woven and UD), see figure 4.8. Pure $0°$ laminates are not capable of carrying much transverse loads, so in case a dumbbell shape would be used, the wider parts of the specimen would not contribute much to the test. Using a dumbbell-shaped specimen anyway therefore typically results in effectively testing a straight-sided specimen with an overall width equal to the gauge width of the dumbbell, see also section 5.3.2.1. The same typically counts for $0-90$ specimens. The ± 45 material will slightly contract in the centre during testing, providing an automatically occurring slight dumbbell shape, and causing failure away from the clamps.

For pure matrix, $90°$ UD, quasi-isotropic UD and woven specimens other than a ± 45 layup, a dumbbell shape is used. Pure epoxy is tested using the shape that is advised in the ASTM test standard for tensile testing of polymers [15]. A slight adaptation of type IV (to use the full area of the clamps) is used, see figure 4.9a. Pure PA-6 is tested using the advised shape from the ISO standard for tensile testing of polymers [16] (figure 4.9b), mainly because a injection-moulding die was

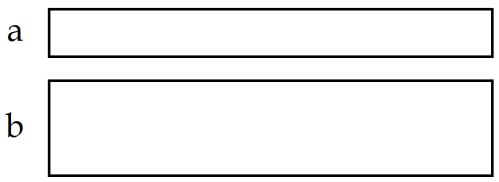

Figure 4.8. Specimen shape type 3 to scale (a) for G/PA-6 $[0]_4$ and $[90/0]_{2s}$, and (b) for $[\pm 45]_{2s}$ and $[\#(\pm 45)]_{ns}$, see also tables 4.3 and 4.4.

available for that shape. Neither of these shapes works for the composite laminates though. In that case, a specimen with cut-outs of only a single curvature is used (figure 4.10), rather than the typical dumbbell shape which has a transition from convex to concave. The shape is based on a research for fatigue of woven composite specimens [17], and scaled to match the aforementioned strain rate requirements and fit the entire clamping area. Hence, these specimens do not have a gauge section with straight edges.

The chosen target dimensions are given in tables 4.3 and 4.4, the relevant variables are indicated for the typical specimen shapes in figure 4.11.

Tabs are needed if the specimen is both sensitive to stress concentrations and needs a high clamping pressure due to a high failure load. Assuming the adhesive layer between specimen and tabs is loaded in pure shear, the average interface shear stress $\bar{\tau}$ for a straight specimen can be estimated based on the material thickness t, the clamp length l_c and the failure stress σ_u of the material:

$$\bar{\tau} = \frac{\sigma_\mathrm{u} t}{2 l_\mathrm{c}} \tag{4.3}$$

This is a crude assumption, as the actual stress state is three-dimensional due to the compression of the clamps. The shear stress occurring in adhesive joints, moreover, shows peaks towards the ends of the joint in the elastic deformation regime rather than being equally spread over the entire length. If it is assumed that the adhesive becomes perfectly plastic at the maximum stress, equation (4.3) should result in a reasonable estimate for the maximum load carrying capacity of the adhesive bond.

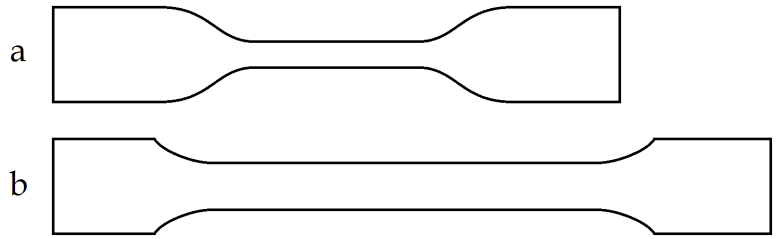

Figure 4.9. Specimen shape type 1 to scale (a) for pure epoxy and (b) for pure PA-6, see also tables 4.3 and 4.4.

Figure 4.10. Specimen shape type 2 to scale for dumbbell-shaped composites, see also tables 4.3 and 4.4.

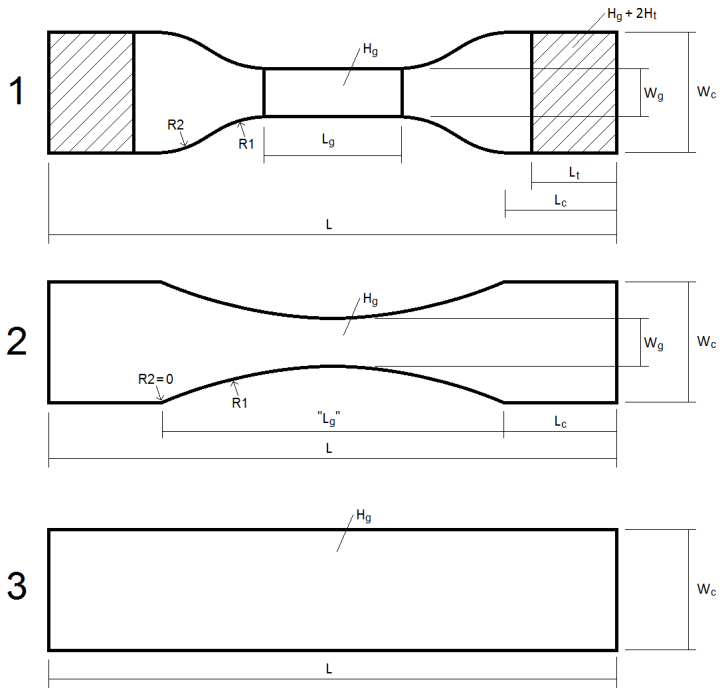

Figure 4.11. Variables to characterise dimensions for dumbbell (types 1 and 2) and straight-sided (type 3) specimens. L, W, H and R indicate length, width, height and radius. Subscripts g, c, and t stand for gauge, at clamp, and tab (when applicable), respectively. The shaded section indicates the presence of tabs.

Table 4.3. Target specimen dimensions for carbon/epoxy in millimetres, see figure 4.11 for variable and type explanation. The shape from [17] for type 2 is scaled to the desired width and length.

	Epoxy	$([0]_4)$ $([90/0]_{2s})$	$[45/0/-45/90]_s$ $[90]_8$ $[\#(0/90)]_{4s}$ $[\#(90/0)]_{4s}$ $[\#(\pm45)/\#(0/90)]_{2s}$	$[\pm45]_{2s}$ $[\#(\pm45)]_{4s}$
Type:	1	3	2	3
$\boldsymbol{L}$	120	94	94	94
$\boldsymbol{L_g}$	33	-	50	-
$\boldsymbol{L_c}$	22	-	22	-
$\boldsymbol{L_t}$	-	22	-	-
$\boldsymbol{W_c}$	20	7.7	20	20
$\boldsymbol{W_g}$	6	-	15.38	-
$\boldsymbol{H_t}$	-	1.2	-	-
$\boldsymbol{R1}$	14	-	136.57	-
$\boldsymbol{R2}$	25	-	0	-
Ref.:	[15]	-	[17]	-

Table 4.4. Target specimen dimensions for glass/polyamide-6 in millimetres, see figure 4.11 for variable and type explanation. The shape from [17] for type 2 is scaled to the desired width and length.

	PA-6	$[0]_4$ $[90/0]_{2s}$ $([45/0/-45/90]_s)$	$[\pm45]_{2s}$ $[\#(\pm45)]_{2s}$	$[90]_8$ $[\#(0/90)]_{2s}$ $[\#(90/0)]_{2s}$ $[\#(\pm45)/\#(0/90)]_s$
Type	1	3	3	2
$\boldsymbol{L}$	152	94	94	94
$\boldsymbol{L_g}$	80	-	-	50
$\boldsymbol{L_c}$	22	-	-	22
$\boldsymbol{L_t}$	-	-	-	-
$\boldsymbol{W_c}$	20	10	20	20
$\boldsymbol{W_g}$	10	-	-	15.38
$\boldsymbol{H_t}$	-	-	-	-
$\boldsymbol{R1}$	20	-	-	136.57
$\boldsymbol{R2}$	0	-	-	0
Ref.	[16]	-	[17]	-

Preliminary tests point out that only $0°$ UD C/E needs tabs, because all other layups can be brought to fail in the gauge section without tabs adhered to the specimens. Aluminium is typically chosen as tab material. The strongest adhesive found to adhere aluminium to composites is Araldite AW4858, which reaches up to $40\,\mathrm{MPa}$ shear strength [18]. Using equation (4.3) to estimate the occurring shear for rectangular 4-layer 0-degree UD Pyrofil TR 360E250S composites ($t = 0.9\,\mathrm{mm}$, $\sigma_\mathrm{u} = 2300\,\mathrm{MPa}$, $l_\mathrm{c} = 20\,\mathrm{mm}$), an estimated required shear strength of $\bar{\tau} = 51.75\,\mathrm{MPa}$ is obtained. It seems rectangular specimens will not work for this material with this clamp length. As mentioned before, dogbones will not work either, since UD composites are too weak in the transverse direction to transfer a sufficient amount of load sideways. Composite tabs, moreover, are prone to fail in interlaminar shear, since the average shear comes very close to their interlaminar shear strength. Still, an attempt is made here, as the compressive stress from the clamps and the possible rate-dependency of the adhesive complicate the situation to such a degree that accurately predicting the result beforehand is impossible.

The choice for a specimen of type 2 (figure 4.11) has consequences for the test results: a stress concentration will occur in the centre section stemming from the curved edges. The dimensions mentioned in the tables result in a ratio of maximum over minimum width of 1.3, and a ratio of cut-out radius over minimum width of 8.88, leading to a stress concentration factor (SCF) of about 1.033 if the specimen were isotropic [19]. This means that the stress at the edges is a factor 1.033 higher than can be expected based on the reduction of area alone.

The tested materials in the current research are not isotropic, and hence the effect is studied using a finite element (FE) analysis. The model dimensions match a 1-mm-thick pure $90°$ UD C/E specimen in tension. Two different material models are used for the specimen, both linear-elastic. The applied material properties for the first model are for the UD C/E. The ply properties from finite element predictions as presented in table 3.4 in section 3.3 are applied, where the 2-direction is aligned with the longitudinal direction of the specimen. The second is an isotropic version of the C/E $[\#(0/90)]_{4s}$ material properties: E was taken $59\,\mathrm{GPa}$ and ν was given the value 0.3. The specimen ends are encastered where they would normally be clamped, though the longitudinal direction of one end is kept free to move. Subsequently, a tensile load of $1\,\mathrm{kN}$ is applied to the free end. $31\,960$ quadratic hexahedral elements of type C3D20 are used to solve the problem using an implicit solver. The maximum dimension of an element is $0.5\,\mathrm{mm}$, the minimum (close to the cut-out edge) $0.1\,\mathrm{mm}$. In the absence of stress concentration, the applied load should lead to a net section stress of $65.02\,\mathrm{MPa}$. A peak stress of $67.02\,\mathrm{MPa}$ is found when using an isotropic material for the specimen. The resulting stress concentration factor equals 1.031, which falls within $0.2\,\%$ of the handbook value. The model is therefore considered validated. The FE model shows a peak stress of $67.77\,\mathrm{MPa}$ for C/E $90°$ UD (figure 4.12), which amounts to

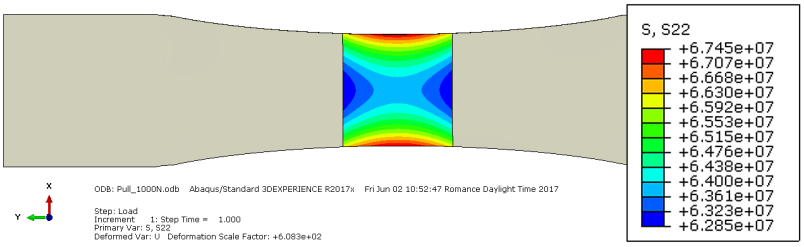

Figure 4.12. Visualization of the stress concentration in a 90-degree UD C/E specimen under tension. The contour plot is limited to a centre section to clarify the different stress levels in that area.

a SCF of 1.042. This layup is the furthest away from isotropic that is tested in this shape, and still the concentration factor falls within $1\,\%$ of the handbook value. It is therefore chosen to apply a SCF of 1.033 (i.e. the handbook value) to all the nominal stress values computed for specimens of shape 2.

Figure 4.12 reveals the occurrence of another effect: not only is the stress at the edges higher than nominal, in the centre of the specimen it is lower than nominal. Assuming that the strain depends linearly on stress, the strain measured with a strain gauge positioned in the centre of a type 2 specimen will not measure even the nominal strain. An additional factor is therefore applied to the strain in order to make it representative for the peak value in the cross section. In case of $90°$ UD C/E, the FE model computes that the net section strain lies a factor of 1.019 above the average strain at the strain gauge area. This can be seen in figure 4.12: the central stress amounts to $63.80\,\mathrm{MPa}$, equal to the net section stress of $65.02\,\mathrm{MPa}$ divided by a factor 1.019. Again, the value for the most non-isotropic material ($90°$ UD C/E) differs less than $1\,\%$ from the value obtained for an isotropic material (1.023). It is therefore decided to continue with the isotropic factors only. To estimate the peak strain for a type 2 specimen based on what has been measured by the strain gauge, the obtained values are multiplied by $1.023 \cdot 1.033 = 1.057$.

It is explained in section 4.7.3 that the DIC resolution is too low to take advantage of the full-field character of the data, and that the available strain values are averaged over a zone approximately the size of a strain gauge in the centre of the specimen. The same combination of factors is, therefore, applied to the strain computed from the DIC results.

4.6.4 Specimen cutting

Specimens are cut using a water-jet cutting machine. This is a fast and versatile method to cut specimens with curved edges. The material is cut using a high pressure and a low progression speed, and each time a wooden support plate is

placed beneath the composite, and both are cut together. This has two advantages. First, the amount of fibre pull out on the lower edges is reduced, and second, the influence of water splashing back up and impinging on the specimen is avoided. The edge quality is far from optimal for the brittle 90° UD C/E composite or pure epoxy. For the latter, clear chips are visible that are removed from the specimen edges during the cutting process (figure 4.13a). For the former, visual inspection shows a 1.5-mm-area at the edges where fibres have been pulled out on the exit side of the jet (figure 4.14).

Milling the specimens to their final shape seems the most promising cutting method. For pure epoxy, this results in a significant improvement of the edge quality compared to waterjet cutting, compare figure 4.13b to 4.13a. A downside of milling composite specimens with carbon or glass fibres, is the large amount of tool wear, making it a costly process. The process is therefore only applied to pure epoxy specimens.

An alternative to waterjet cutting is using a diamond saw. This method, however, is only suitable for straight edges, and is therefore not applied. Due to time restrictions, this method is also not applied for the straight-sided specimens. Laser cutting is not recommended, as it locally burns the matrix, which is expected to negatively influence the test results as well.

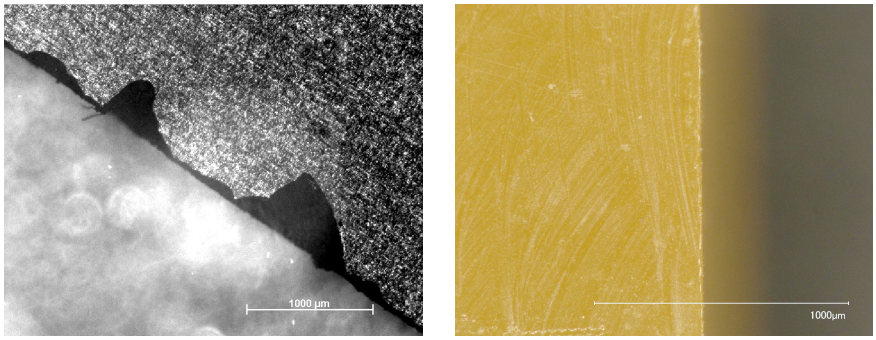

a. Waterjet cut *b. High quality milled*

Figure 4.13. Top view of pure epoxy specimen edges after cutting

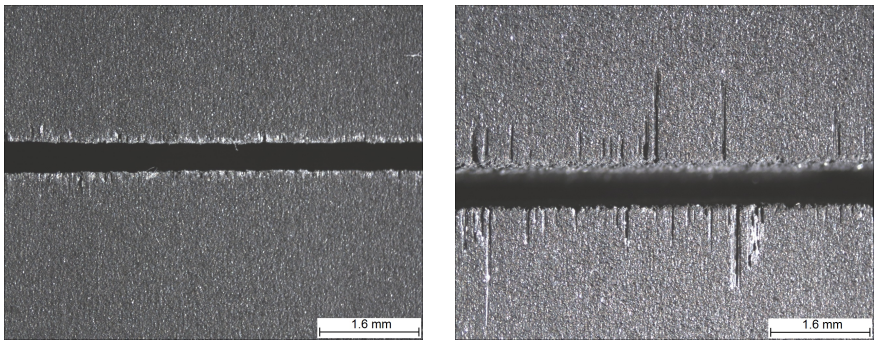

a. Waterjet entry side *b. Waterjet exit side*

Figure 4.14. Top view of pure 90-degree UD C/E plates after water jet cutting - note that the cut flanks are only visible on the exit side, indicating that the edges are not straight .

4.6.5 DIC pattern

DIC patterns are applied after degreasing, slight sanding and subsequent degreasing of the specimen surface. First a matte white automotive spray paint is sprayed as thin as possible but still thick enough to produce a good bright background for the black speckles to follow. After the paint has dried, a speckle pattern is applied by using a matte black spray paint of the same brand and type.

The speckle size for which should be aimed depends on the camera settings. Generally, a darker specimen is better than a lighter one, as the grey value is seldom uniform, allowing the processing software to still discern a pattern. This is not the case for specimens which are too bright. As can be seen in figure 4.3b, several different resolutions are used. Only two levels of zoom are used though, which amount to 128 pixels for a width of $14\,\mathrm{mm}$ or 16 pixels for a width of $7\,\mathrm{mm}$. This means the respective resolutions are 9.1 and 2.28 pixels per mm. Ideally, the speckles and the inter-speckle-spacing both are greater than three pixels in size [20]. This sets the goal for the speckles to be about $0.3\,\mathrm{mm}$ in diameter for the lower-rate specimens and about $1.3\,\mathrm{mm}$ for the higher-rate specimens. This is both possible with a normal spray can.

Pure PA-6 can stretch to over $50\,\%$ at low strain rate [21], which is too much for typical paints to follow. Preliminary testing showed that a white paint that could stretch this much lost brightness due to the black colour of the PA-6 used in this project. Therefore, the choice is made to measure the strain of pure PA-6 using optical extensometry, much like is done by Shirinbayan et al. [22]. A marker is placed near the top and the bottom of the specimen, and the distance between them is recorded using a camera. The increase in distance between the two markers, divided by the original value, is a measure of the macro strain experienced by the specimen.

4.6.6 Strain gauge

As mentioned in section 4.4.2, general-purpose $350\,\Omega$ CEA-06-250UN-350 gauges by Vishay Precision Group are used to measure strain. The strain gauges are adhered to the centre of the specimens with M-bond 200 adhesive by Vishay Precision Group. The application instructions of this adhesive are strictly followed, and can be found on their website [23].

4.6.7 Conditioning

The moisture from the air is absorbed into the material of the composite, even if the matrix is cross-linked [24]. Water molecules place themselves either freely movable between other molecules, or attach to parts of a molecule that have a non-negligible polarity. The bonds that normally exist between molecules are therefore influenced, because they are pushed further apart by the water molecules. In case of a cross-linked molecular structure like that of a thermosetting polymer, the influence is therefore expected to be minor, since the mechanical properties will mostly rely on bonds within the macromolecule. Still, C/E composites show a reduction of glass-transition temperature, and of strength in matrix-dominated load-cases in function of moisture sorption [25–27]. As was noted in section 3.7, water significantly influences the mechanical properties of thermoplastic composites [28, 29].

To reduce variation on the results because of varying levels of moisture sorption, it is made sure that all the specimens are in approximately the same moisture state. Since it is unknown what the nominal state is (it varies for example with weather conditions) it is best to bring them all in a completely saturated or desaturated state.

For this research, the desaturated state is chosen. Thermoplastic composites are dried for 7 consecutive days at $70\,^{\circ}\mathrm{C}$ in a drying cabinet to reach a practically dry state, according to the advice of the manufacturer. This process is adopted as well for the C/E specimens. The effect of drying is measured by adding another piece of the same material in the oven and logging its weight. With regular weighing, the drying process can be monitored. After seven days of drying, the incremental weight loss becomes negligible and the specimen is considered to be dry.

It is important that the specimens are cooled to room temperature before they are tested. A desiccator is used to store the specimens for at least 24 hours in a dry place at room temperature prior to testing. The test environment is not temperature or humidity-controlled. Specimens are therefore tested within one hour after removal from the desiccator to prevent excessive renewed moisture ingression.

4.6.8 Dimensions

The measurement of specimen dimensions is necessary to be able to accurately calculate the material properties from the measured quantities. As both temperature and humidity can influence material dimensions, this task is carried out with conditioned specimens at room temperature. A calliper with $0.01\,\mathrm{mm}$ accuracy is used for in-plane dimensions, and a $0.001\,\mathrm{mm}$-accurate micrometer for the thickness, as prescribed by the standards, e.g. [14]. The target dimensions of the specimen used for each type of layup are summarized in tables 4.3 and 4.4, the actual dimensions of specimens that constituted to a successful test campaign are given in appendix A.

4.7 Data digestion

This section explains how useful results are computed from raw data. First the force is treated, then the velocity measurement, followed by the strain acquisition. Next, it is explained how stress and strain data are aligned. Finally, a method is selected to obtain an average curve for a set of stress-strain curves to allow showing stress-strain behaviour across several rates.

4.7.1 Force versus time

An example of a typical load signal is given in figure 4.15. The load signal is used to define the moment the specimen is actually being pulled. Typically, the test start is chosen a small amount of time before the load clearly rises, say, at $t = -0.15\,\mathrm{ms}$ in figure 4.15. The test end is picked directly after the load drops (around $t = 0.27\,\mathrm{ms}$ in figure 4.15), since any subsequent load signal is only oscillatory and not related to the load in the specimen. The failure stress is computed from the maximum value of the load within the selected start and end, divided by the minimal cross-sectional area, and multiplied by the SCF (section 4.6.3). Several effects in the load signal were seen during the test programme, all of which have their own explanation, as given below.

The load signal sometimes shows some small oscillation before loading, at a frequency of approximately $500\,\mathrm{Hz}$, see also figure 4.16. This frequency is very close to the eigenfrequency of the system of top clamp, specimen, bottom clamp and loading pin combined, which, determined using a small hammer hit, lies around $520\,\mathrm{Hz}$. The slack rod might be slightly sticky to the surrounding sleeve, or the rod might have been dirty, and the (start of the) piston movement causes a short loading of the bottom of the slack rod, which thus starts to vibrate at the aforementioned frequency. It can be seen that the amplitude is only about $10\,\mathrm{N}$, so it is not influencing the test to a significant degree.

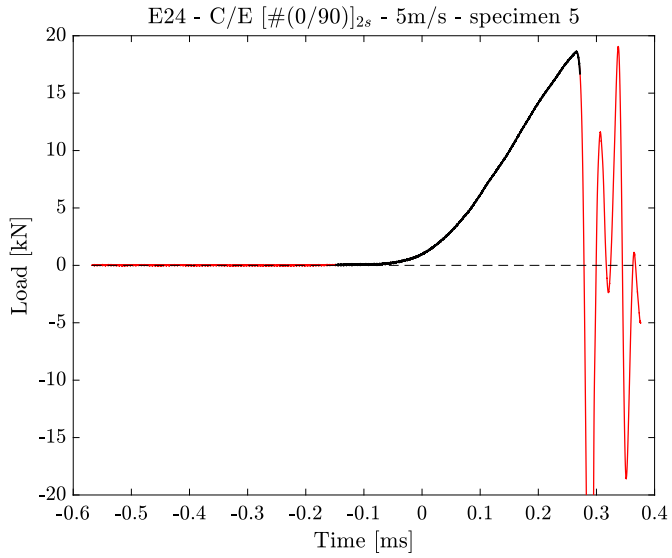

Figure 4.15. Typical results for force versus time of C/E $[\#(0/90)]_{2s}$ *tested at* $5\,\mathrm{m\,s^{-1}}$. *The black parts indicate what has been selected to belong to the actual test.*

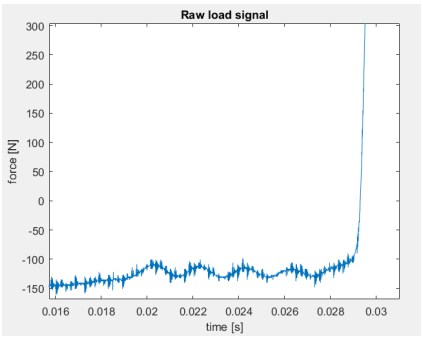

a. Vibrations appear prior to loading.

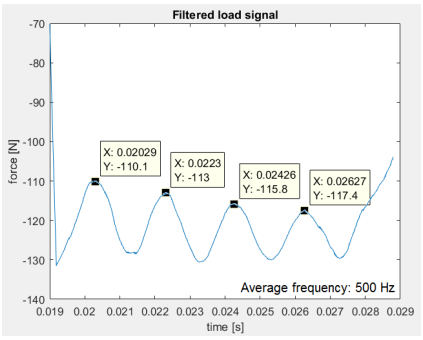

b. Using the approximate period on a smoothed version of figure 4.16a, the frequency of the oscillation can be estimated.

Figure 4.16. Measured oscillations just before specimen loading. The signal is too short for the direct application of fast-Fourier transform to lead to accurate results.

4.7.1.1 Upper speed limit for piezoelectric load cells

After testing, the 'ringing' of the load cell, introduced in section 4.4.1, can be clearly seen (figure 4.17a). The lowest peak frequency lies at about $10.5\,\mathrm{kHz}$, which has a period of $95\,\mu\mathrm{s}$. The post-failure response of a brittle specimen (in the case of the figure, G/PA-6 pure $90°$ UD) is an accepted method to find the natural frequency of the load train [3].

The mean value of the oscillating load after specimen failure is non-zero. This is a result of the deformation of the pretensioning nut that compresses the load cell (figure 4.2). This part namely also holds the grips on its other side, and tightening the grips causes the cell to be slightly unloaded. This small apparent tensile load is removed by balancing the load cell just prior to testing, hence it does not influence the load recording. The subsequent test itself causes a reduction in the grip pressure, likely due to damage of the specimen in the gripping area, which can then show up as a compressive load after testing.

If the test duration approaches the period of the oscillation as the speed is increased, the measured load value no longer solely represents the actual load experienced by the specimen, but added oscillations will appear in the signal. For long enough test durations, their effect is minimum and it is possible to filter the load signal if they would appear. When the time scales of the test and the oscillation coalesce, the load signal is unusable. Section 4.8.2 contains the determination of the strain rate limit for load cell ringing using FE.

If a higher strain rate is desired than the limit, another method of measuring load is needed. The test standard for tensile testing of metallic materials at high strain rates recommends the use of a (second) strain gauge, on the wider part of a dumbbell specimen, where only elastic deformation should occur [4]. Although it is not mentioned in the standard, it is important that the material to which this second strain gauge is adhered does not show rate-dependency, or that at least the extent of dependency is accurately known. The load connected to the strain which is measured with the second gauge is namely calibrated using a static test. The path towards a new method of measuring load is a subject of further research.

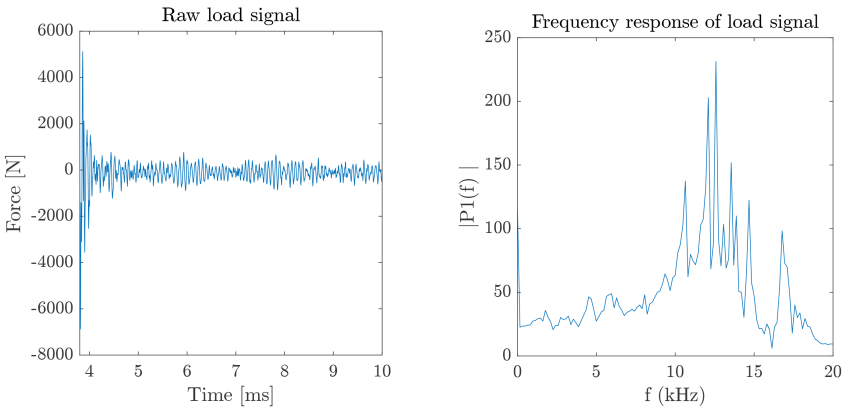

a. Vibrations appear after specimen failure.

b. Using a fast-fourier transform of the signal in figure 4.17a, the frequency of the oscillation can be estimated.

Figure 4.17. Vibrations measured just after specimen failure.

4.7.1.2 Lower speed limit for piezoelectric load cells

As mentioned in section 4.4.1, a piezoelectric load cell is used. Such a cell can show drift towards zero for relatively low-frequency load signals. The charge amplifier used for the current research allows the user to influence the amount of drift by selection of the decay time constant. Falsely selecting a small time constant for a test of relatively long duration causes significant signal drift to appear in the load measurement of long-lasting experiments. A drifted tensile load signal becomes compressive if the tensile load suddenly disappears (e.g. at specimen failure), and hence this is a second source of apparent post-test compression, see figure 4.18a. The figure shows that the compressive signal reduces towards zero again, which is an indicator for the fact that this signal indeed stems from sensor drift. The curve can be corrected by use of a fitted exponential curve $f(t) = a\mathrm{e}^{bt}$ to the (entirety of) the signal after failure. The amount of decay Δf the signal has experienced during a certain time increment Δt is thus assumed to increase exponentially with increasing load. This amount depends on the derivative of the fitted exponential, which is simply the original function multiplied by the exponential factor b, see equation (4.4).

$$f'(t) = ba\mathrm{e}^{bt} = bf(t) \tag{4.4}$$

Hence, the decay can be assumed to depend on the measured load F^d (the superscript d is added to indicate that it concerns the drifted value) according to equation (4.5).

$$\Delta f \approx bF^d \cdot \Delta t \tag{4.5}$$

The corrected load signal values F_i can thus be found by subtracting all the decay increments Δf_i that have preceded, which in turn depend on the drifted signal values F_i^d, as shown in equation (4.6).

$$F_i = F_i^d - \Delta f_i = F_i^d - \sum_0^i bF_i^d \cdot \Delta t = F_i^d - b\Delta t \sum_0^i F_i^d \tag{4.6}$$

The thus obtained load signal is displayed in figure 4.18b. The amount of apparent compression has been almost completely removed, and the load signal is now again usable. The small constant value that still remains is likely due to a change in deformation of the preloading nut, as mentioned in section 4.7.1.1 above.

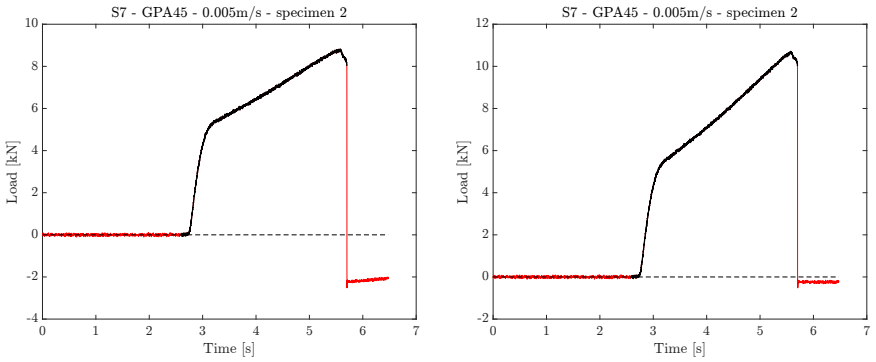

a. Force versus time with significant signal decay as characterised by the large amount of apparent compressive load after failure.

b. The force signal of figure 4.18a, corrected for signal decay

Figure 4.18. Force data with a wrong time decay setting for a $0.005\,\mathrm{m\,s^{-1}}$ *test on G/PA-6* $[\pm 45]_{2s}$*: original (left) and corrected (right).*

4.7.2 Velocity versus time

Velocity versus time is obtained by numerical differentiation of the position signal of the test bench. In this case Forward Euler differentiation is used to obtain the velocity signal, the result is shown in figure 4.19. The noise on the displacement signal (see also figure 4.6a) is smoothened using a moving average filter with a length of 1000 points prior to differentiation.

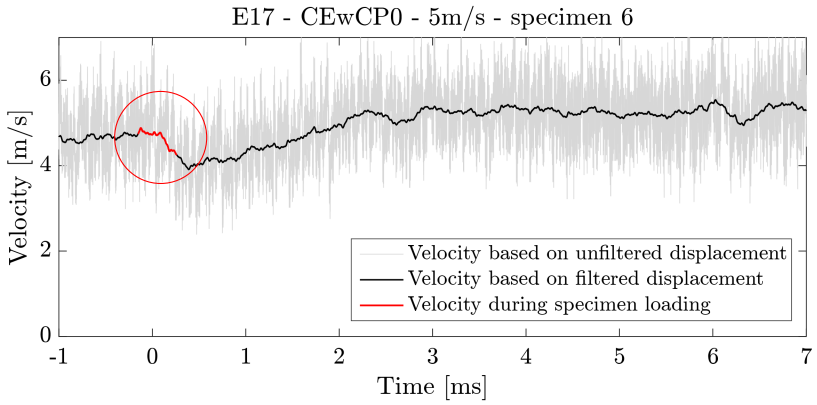

Figure 4.19. Piston speed by smoothing and numerical differentiation of displacement data

4.7.3 Strain versus time

As mentioned before, strain is measured using both DIC and a strain gauge. A typical result is given in figure 4.20.

There are many settings one can apply for DIC digestion, anything not described here is left as set standard in the DIC analysis software. The acquisition resolution is chosen depending on whether lower or higher rate test footage is analysed, as given in table 4.5. As explained in section 4.4.2, this resolution is rather low due to the way the high-speed camera operates. The step size is chosen between a third and a half of the subset size. The subset size is chosen so it encompasses more than the largest speckle on the images. A smaller subset size leads to more resulting data points, but also more difficulties for the software to track the strains because subsets start to look alike. Further settings are the choice of zero-normalised sum of squared differences correlation, which makes the correlation easier when brightness differs between the images, cubic interpolation and affine transformation. Figure 4.21 shows an example of the DIC digestion process of a 128x16 frame.

Table 4.5. DIC resolution settings

	Subset	Stepsize
320x128	13	5
128x16	5	2

The entire field of view is analysed when calculating strains. The relatively low resolution and contrast of the DIC footage results into a large amount of noise.

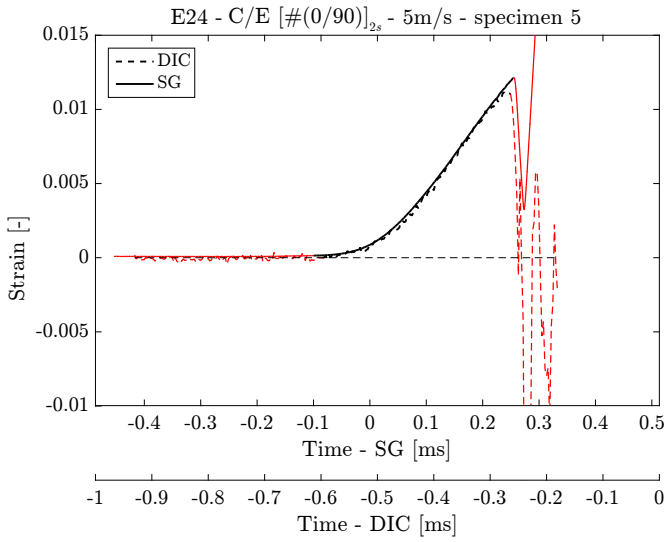

Figure 4.20. Typical results for strain versus time of C/E $[\#(0/90)]_{2s}$ *tested at* $5\,\mathrm{m\,s^{-1}}$. *The black parts indicate what has been selected to belong to the actual test.*

Firstly, a low speckle-background contrast, resulting from the short shutter time of the camera, which in turn is due to the high frame rate, causes a high amount of noise per data point compared to images with a higher contrast [30]. The subsequently low resolution restricts the subset to large dimensions compared to the specimen, leading to only a few data points for each image. It is therefore decided to compute the longitudinal strain by calculating the average strain over a set of data points, thereby losing the full-field aspect of the data. A central rectangle with the size of the sensing area of a strain gauge is chosen to compute the test result. When the rectangle contains the specimen failure location, it is moved until the occurrence of the crack is outside of its borders. The same procedure is applied for specimens for which part of the paint comes off during the test as a result of the failure of underlying fibres at the surface of the specimen. Despite of the noise, a clear trend is seen in the curve, which can thus be used to determine the strain during the test.

A strain gauge is attached to the rear of the specimen. The gauge is connected to a signal conditioner which amplifies at its minimum gain for maximum bandwidth. Before the specimen is clamped on its second end, the signal is balanced to a practically zero-strain output, and the amplified gauge factor is determined using shunt calibration. The typically obtained amplified gauge factor lies at $373\,\mathrm{mV}$ for $1000\ \mu\varepsilon$.

A typical DIC result can be seen in figure 4.20. The average strain from the

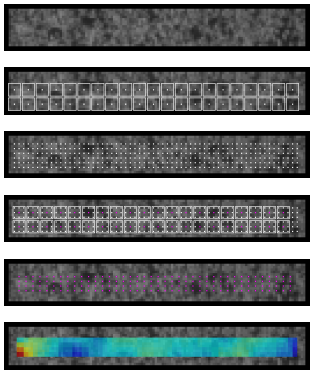

a. A raw frame of 128x16 pixels.

b. Non-overlapping 5x5 subsets are shown.

c. The displacement points, step size: 2.

d. Choice of strain calculation windows.

e. All available strain points.

f. The resulting strain field.

Figure 4.21. Illustration of the DIC digestion of a $15\,\mathrm{m\,s^{-1}}$ *test recorded at 128x16 pixels. A subset size of 5 and a step size of 2 were chosen. The zero-normalized sum of square differences correlation algorithm with subsequent cubic interpolation is used to find the displacements at sub-pixel accuracy. The strain is calculated using 3 x 3 windows in which linear interpolation is applied.*

strain-gauge-sized zone is multiplied by 1.057 if the test was conducted with a type 2 specimen (see section 4.6.3). The same counts for the gauge strain in such a case.

4.7.3.1 Measuring the ultimate strain

The ultimate strain is computed by taking the highest value of the measured strain. The ultimate strain is a very error-prone quantity to measure.

For some layups, many fibres fail at the surface of a specimen before it fails as a whole. In that case, the ultimate strain cannot be accurately recorded using either DIC or a strain gauge, as the paint or the gauge fall off before the specimen fails completely. Probably the only reliable method to measure strain in such a case would be to perform video extensometry with two markers attached close to the clamps, where the least damage due to failure is expected. The question remains whether serious surface damage should already be considered as failure, the answer to which will largely depend on the application. If so, measuring the ultimate strain using surface-based methods poses no problem.

Another source influencing the ultimate strain measurements is the fact that the specimen never fails exactly during the recording of a frame. In that case, the maximum error depends on the strain rate and the frame rate. At a strain rate of $200\,\mathrm{s^{-1}}$ and the highest DIC frame rate of $500\,000$ fps, the maximum error on the ultimate strain measurement amounts to 0.0004. This is only a small error, and it can only have a significant influence on the result if the failure strains are very small as well. For example, in case of pure $90°$ C/E, the expected maximum strain

is only $0.6\,\%$. In this case, the worst-case error would amount to $7\,\%$. Typically the failure strains are significantly larger, though, and the influence of this effect becomes negligible. The only method to mitigate the effect for materials that fail at very small strains is to use cameras with a higher frame rate for the same resolution. The fact that the equipment used for the current research is limited to the aforementioned $500\,000$ fps limits the strain rate to a certain maximum, as outlined in section 4.8.3.

The strain gauge measurements do not have this problem, as the data acquisition occurs at a much higher rate ($100\,\mathrm{Msamples/s}$). As was mentioned in section 4.4.2, though, the bandwidth of the signal conditioning amplifier is limited to $35\,\mathrm{kHz}$. This poses another limit on the maximum test speed at which a test can be carried out, as the strain output of too fast tests will appear smoothed. Section 4.8.4 treats the determination of the maximum strain rate based on the amplifier bandwidth.

At very high speeds, the failure point itself also becomes difficult to measure. At $15\,\mathrm{m\,s^{-1}}$, the recorded footage does not clearly show a failure point, but rather a progressing crack, see figure 4.22.

Stress concentrations resulting from a bad edge condition are also detrimental to the measured ultimate values, even if the data-acquisition would be correctly carried out. Special care is taken to select the optimal pressure and speed for the water jet cutting process, though the edge condition is never free of stress concentrators, see also section 4.6.4.

Another effect that can influence the measured ultimate values is material and specimen misalignment. Material inspection revealed an alignment of fibres to edge better than $0.1°$. The subsequent cutting process was performed computer-controlled, using a careful alignment of the base plates along approved edges, thus assumed not to lead to more than $0.05°$ of misalignment. The specimens were cautiously mounted in the test set-up using their bottom edge, it is assumed this added no more than $0.1°$ of misalignment. Section 4.5 concludes that the clamps are aligned to within $0.25°$. It is therefore estimated that the total alignment of specimen material and loading direction is within $0.5°$, i.e. the sum of the above angles. The effect on the tensile properties should be minimal: using Classical Laminated Plate Theory (CLPT), the Young's Modulus for $0°$-UD C/E or G/PA-6 reduces only by about $0.15\,\%$ for a misalignment of $0.5°$.

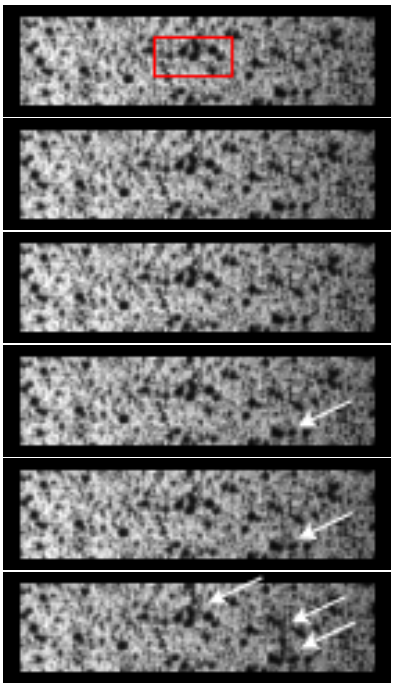

a. First frame and strain calculation zone.

b. The third to last frame.

c. The second to last frame.

d. The last frame: failure occurs.

e. The first frame after failure.

f. The second frame after failure.

Figure 4.22. High speed footage of C/E $[\#(0/90)]_{2s}$ *tested at* $15\,\mathrm{m\,s^{-1}}$*. The red rectangle indicates the zone of strain calculation, the white arrows indicate the position of cracks. The capture is done at* $360\,000$ *frames per second, the resolution is 128x32 pixels.*

4.7.3.2 Computing the actual strain rate

The strain rate is not perfectly constant during the tests, mostly because the piston speed is not constant (figure 4.19). Figure 4.20 also clearly shows that the specimen bottom acceleration is not discrete because the slope increases rather smoothly, which is due to the compression of the damping patch present in the bottom grip assembly. A linear least-squares approximation of the strain versus time data is used to compute the strain rate, also to cope with the noise in the measurements. One could be inclined to calculate the rate between strain values of 0.001 and 0.003, the same interval used to calculate the Young's modulus according to the tensile test standard [14]. The calculation is, however, performed only on data in the strain range of 0.003 and 0.005, because the rate typically shows more or less a plateau only from 0.003 onwards.

The strain rate of a $5\,\mathrm{m\,s^{-1}}$ test on C/E $[\#(0/90)]_{2s}$ was computed this way. A rate of $45.4\,\mathrm{s^{-1}}$ was obtained for the gauge data and $46.6\,\mathrm{s^{-1}}$ for the optical data. Theoretically, the strain rate should be equal to the actuation velocity divided by the gauge length [3, 4], see also equation (4.2). For a $5\,\mathrm{m\,s^{-1}}$ test of a specimen with a gauge length of $50\,\mathrm{mm}$, the theoretical strain rate amounts to $100\,\mathrm{s^{-1}}$.

Both measured strain rate values are lower than the theoretical one, which is also seen in literature [31]. The first cause for this is that the average speed during the test is $4.19\,\mathrm{m\,s^{-1}}$ instead of the requested $5\,\mathrm{m\,s^{-1}}$. The theoretical rate thus drops to $83.8\,\mathrm{s^{-1}}$. This is caused by the open-loop control scheme: the speed is calibrated without a specimen, while during a test the piston is decelerated by the force required to break the specimen. Still, the measured rate is only about $55\,\%$ of the new theoretical value. Bench deformation and possibly some continued grip slippage are the likely causes for the remaining difference. The specimens had a gauge length of $50\,\mathrm{mm}$ and were failing at strains of about 0.01, so only $0.25\,\mathrm{mm}$ of bench deformation or slip is needed to reduce the strain rate to half the theoretical value.

Based on the test data at other speeds, the ratio of actual rate to the theoretical one increases slightly with increasing velocity. The maximum velocity of the test bench equals $20\,\mathrm{m\,s^{-1}}$, resulting in a theoretical rate of $400\,\mathrm{s^{-1}}$ with the current specimen dimensions, based on equation (4.2). The actual rate is thus limited to about $200\,\mathrm{s^{-1}}$.

4.7.4 Stress versus strain

Data from the two different sources (1: load cell, 2: strain gauge or DIC pattern) needs to be plotted against each other to obtain a stress-strain curve. Since both are acquired at different rates, a resampling step is necessary. The data at the highest acquisition rate of the two is downsampled to the lowest rate of the two by linear interpolation at the time points of the lowest sampled rate.

Both the load and the strain acquisition have their own noise, plotting one against the other thus results in noise in two directions. Therefore, orthogonal projection has been applied to compute a linear approximation of the curve in the specific strain regions advised in the test standards to calculate the Young's modulus [14, 32]. The Young's modulus is obtained from the slope of this line.

4.7.4.1 Stress-strain synchronization

A challenge lies in making sure that the time axis of both data is equivalent (i.e. $t = 0$ for the stress data exactly equals $t = 0$ for the strain data). Typically publications about dynamic tensile testing contain no information about data stream synchronisation, nor do the standards. Two minor exceptions are found. The first is the SAE J2749, in which it is stated that the *data streams may need to be reconciled* because of a *measurable time lag* [3] but gives no mention about how this should be done or what is the origin of this lag. The second is a recent publication in which optical strain measurement was applied for dynamic tensile tests on a woven glass/vinylester composite where *load and strain data were manually synchronized* [31]. Although the synchronization is not very critical for the slower tests, errors in the order of a single micro second can have significant effects at high rates. An example is shown in figure 4.23, where the strain rate is close to $45\,\mathrm{s}^{-1}$. In this case, the tests lasts about $300\,\mu\mathrm{s}$, and every $10\,\mu\mathrm{s}$ of synchronization error results in a difference of about $5\,\mathrm{GPa}$ on the resulting modulus.

Looking at the raw data curves of figures 4.15 and 4.20, one might indeed be inclined to manually align the datasets, as was done by Hufner and Hill [31]. Such an approach, however, does not lead to accurate synchronization for the higher rates, because neither the moment of failure, nor the initial loading can be used for this purpose. Aligning the data at failure is not possible because (1) the strain gauge or DIC pattern detach from the specimen before failure (as was mentioned in section 4.7.3 and can be seen in figure 4.20: the maximum strain values are not equal) and (2) the load drop after the specimen breaks is no longer sharp (figure 4.15), because the load cell has finite inertia. Also, the recorded footage does not clearly show a failure point, but rather a progressing crack (figure 4.22). Aligning on the initial part of the test is not accurate due to an initial delay between stress and strain as is explained in the next section. Hence, the only viable option left is to take all the delays (see section 4.4.3) into account and correct for them.

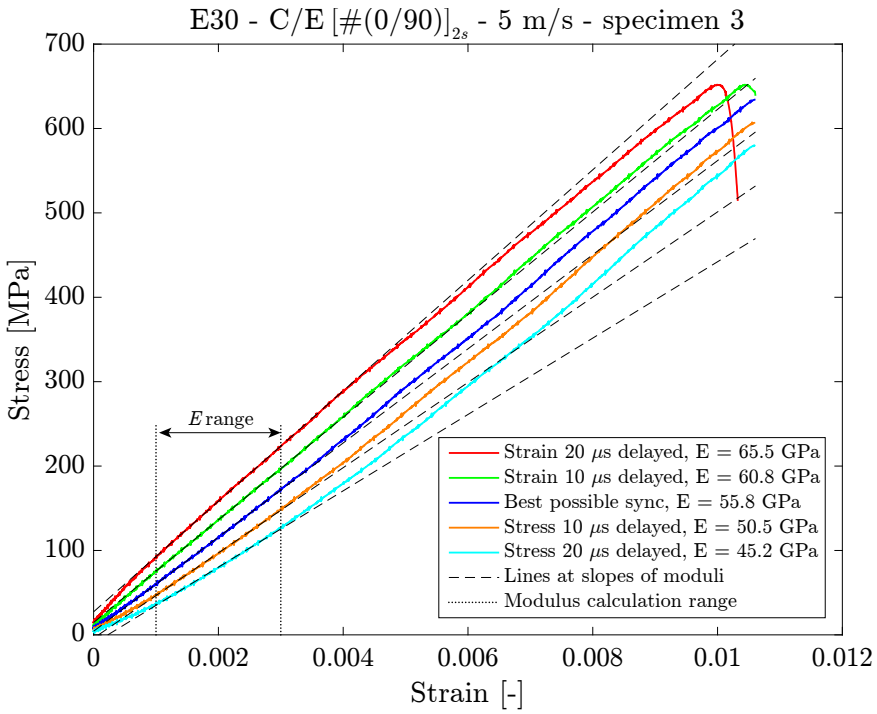

Figure 4.23. The influence of $10\,\mu s$ *steps of synchronisation error between stress and strain on the stress-strain diagram of a* $5\,m\,s^{-1}$ *test. The dashed lines indicate the linear curve fits to calculate the Young's moduli, the plus symbols the range which is used to fit to, as advised by the test standard [14].*

4.7.4.2 Physical delay between stress and strain

Even if the synchronization would be perfect, a physical delay troubles the creation of an accurate stress-strain curve at the highest rates. Strain, and by constitutive laws thus also stress, only propagates inside a material at a finite speed which is assumed to be close to its speed of sound. The strain is typically measured in the centre of the specimen, while the load is measured above the fixed clamp. This requires strain waves at the gauge section to propagate inside the composite to the grips (distance a, see figure 4.24) and subsequently propagate in steel parts to reach the load cell (distance b in figure 4.24). It is hereby assumed that the load path is through the centre of the grips and that load is measured in the centre of the load cell.

The speed of sound in isotropic solids c_{iso} can be calculated based on the Young's modulus E, the Poisson's ratio ν and the density ρ [33]. The metallic parts in the tensile test set-up (grips, blocks, cell) are all assumed to behave like ASTM A284 steel ($E_{\text{steel}} = 206\,\text{GPa}, \nu_{\text{steel}} = 0.29, \rho_{\text{steel}} = 7850\,\text{kg}\,\text{m}^{-3}$ [34]). The speed of sound in the metallic parts thus becomes:

$$c_{\text{iso,steel}} = \sqrt{\frac{E_{\text{steel}}\,(1-\nu_{\text{steel}})}{\rho_{\text{steel}}\,(1+\nu_{\text{steel}})\,(1-2\nu_{\text{steel}})}} = 5828\,\text{m}\,\text{s}^{-1} \tag{4.7}$$

The speeds of sound in the composite laminates have been measured ultrasonically, as is described below in section 4.9. Taking the same case as in figure 4.23: a C/E $[\#(0/90)]_{4s}$ specimen, which has a length of $94\,\text{mm}$, the physical delay between load and strain amounts to about $11.5\,\mu\text{s}$. This has a significant effect on the stress-strain curve at high rates, compare the 'Stress $10\,\mu\text{s}$ delayed' to the 'Best possible sync' in figure 4.23.

The delay is verified by performing a FE-simulation of the dynamic tensile test. The geometry of the model is shown to the right in figure 4.24 and modelled after the load train of the dynamic tension setup: a specimen, four grips, two different grip bases and a load cell. All parts but the specimen are given the linear elastic properties of steel mentioned two paragraphs above. The specimen is given a density and an orthotropic linear elastic material model for C/E $[\#(0/90)]_{4s}$, for which the values are given in table 3.4 in chapter 3. All parts are connected by a tie condition on the mating surfaces. The load cell is split in half perpendicularly to its cylindrical axis as shown by the red line in figure 4.24, and reconnected using a cohesive surface to allow an internal stress measurement exactly at its midplane. The top of the load cell is restricted in vertical motion. A smooth displacement ramp is applied to the bottom surface of the bottom grip support block using a sinusoidal formulation with selected frequencies to match specific test speeds. The model is discretized into $34\,952$ reduced-integration hexahedral elements. This leads to an average global element length of about 0.5 to $1.5\,\text{mm}$

in the specimen, the smaller elements being closer to the clamps. This mesh size is found to be sufficiently fine, because finer meshes produce practically the same strain history in the centre of the specimen. An explicit solver is used to run the model in double-precision, using the default values for bulk damping. Stress and strain are computed from the simulation results in a similar fashion as is done during the experiments. Load is computed by integrating the contact stress on the midplane of the load cell, and converted to nominal true stress by dividing by the instantaneous cross-section. The strain is extracted by computing the average value of the output of a set of integration points. This set forms a surface the size of the grid of a strain gauge, in the middle of the specimen (blue area in figure 4.24 right).

The delay between the initial rise of the strain signal and and that of load amounts to $12.1\,\mu s$, see figure 4.25. This is close to the manually calculated value of $11.5\,\mu s$. It seems like the strain signal can be simply delayed on a case-by-case basis to obtain a more correct stress-strain curve at the higher rates.

The FE results have been presented in the form of two stress-strain curves in figure 4.26: one curve is based on the original timing of the strain results, for the other, the strain has been delayed until it rises together with the load. The figure shows that it is incorrect to align load and strain on the initial rise. The original combination (red curve) retrieves the input Young's modulus (dashed line), while delaying the strain to make it rise when the load does, results in a mismatch (grey curve). Delaying the strain assumes that information only travels from the loaded end towards the load cell, while in reality the stress waves move in both directions to establish an equilibrium within the load train. Therefore, the stress-strain relation only still holds in an average sense: the waves in the results might not represent the constitutive relation, but the curves can still be used to conclude on the overall stress-strain behaviour.

Figure 4.27 shows the stress-strain curves for a $90°$ UD C/E composite tested quasi-statically and at $15\,\mathrm{m\,s^{-1}}$. The influence of synchronizing stress with strain on the initial rise rather than (correctly) taking all the acquisition delays into account becomes clear. The incorrectly synchronized results suggest a strong dependency on rate of the Young's modulus (figure 4.27a), which, in reality, is not the case (as will be shown in section 5.3.2.3). When the data is aligned correctly, the physical delay between stress and strain shows up as a seemingly negative rate-dependency (figure 4.27b). This simply means that the rate at which the faster tests were executed was too high and the specimens could no longer be considered to be in a state of approximate equilibrium. At some velocity the condition of equilibrium is too severely violated to be able to draw conclusions on the constitutive behaviour based on the measurement of load and strain on different locations. Yet another limit on maximum applicable strain rate has thus been identified, which is treated further in section 4.8.5.

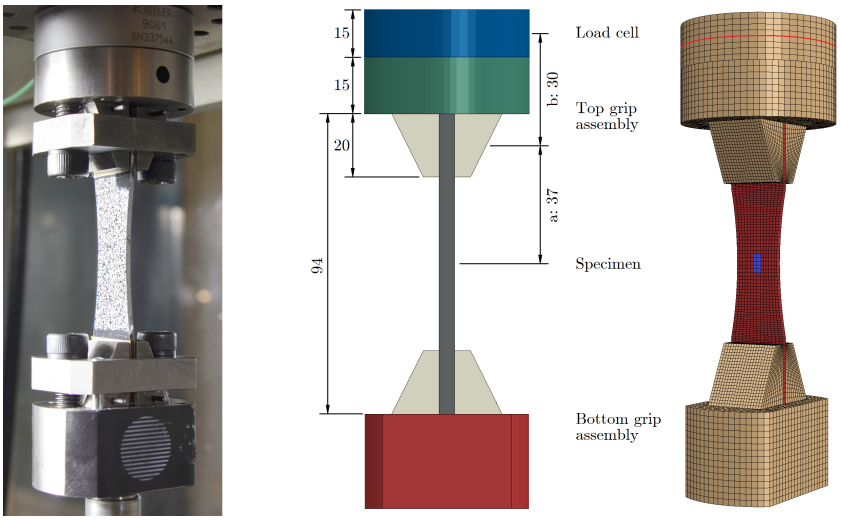

Figure 4.24. A picture of the set-up (left), dimensions of the dynamic tensile test set-up in mm *(middle), and the meshed FE model (right). The red line and blue area in the model show the force- and strain calculation surface areas, respectively.*

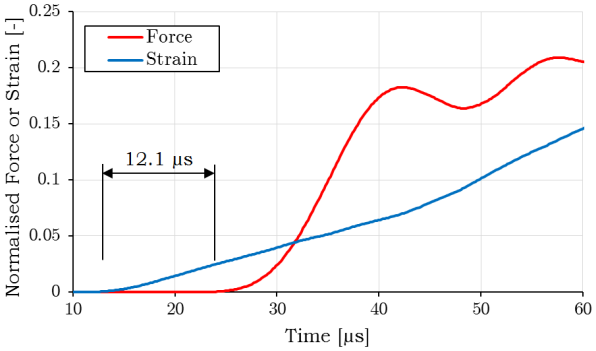

Figure 4.25. Normalised force and strain versus time resulting from FE simulation of a $5\,\mathrm{m\,s^{-1}}$ *tensile test on C/E* $[\#(0/90)]_{4s}$.

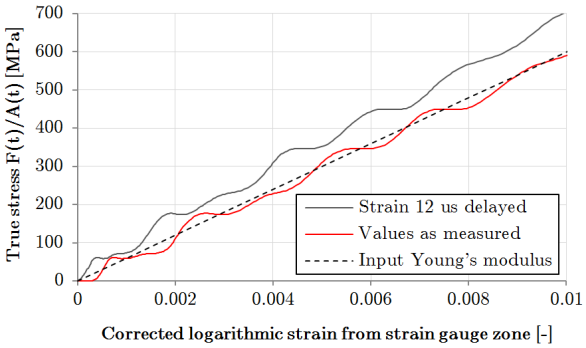

Figure 4.26. Influence of delaying the strain signal to match the moment the load rises on the stress-strain behaviour of a $5\,\mathrm{m\,s^{-1}}$ *test simulated on a C/E* $[\#(0/90)]_{2s}$ *specimen.*

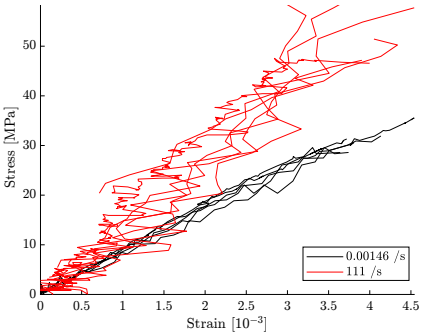

a. Incorrect synchronization, on initial signal rise. A false sense of strong rate-dependency appears in the results.

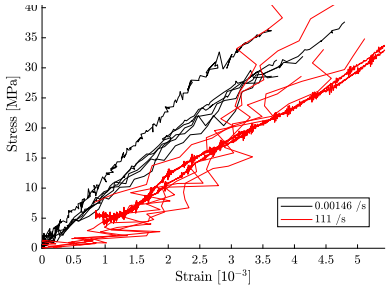

b. Correct synchronization. The delayed stress becomes apparent as the curve for $15\,\mathrm{m\,s^{-1}}$ *now lies below the quasi-static one: it was tested above the maximum allowed strain rate.*

Figure 4.27. Stress-strain curves for C/E $[90]_8$ *tested at* $0.0001\,\mathrm{m\,s^{-1}}$ *and* $15\,\mathrm{m\,s^{-1}}$.

4.7.5 Stress-strain versus strain rate

Having produced a large quantity of test results, the challenge of finding a suitable manner of presenting it remains. It is decided that the most encompassing yet compact way to report on the tests is the stress-strain curve. This form namely contains information on both ultimate values and the Young's modulus, and it also allows interested researchers to fit their own formulae and extract values for dedicated material constants as needed.

Typically, the current test programme leads to 60 stress-strain curves per laminate (6 speeds, 2 manners of measuring strain, 5 repetitions). Displaying them all together in a single figure quickly leads to an overwhelming amount of information which can no longer bring the message across. It is therefore decided to generate curves that show the average behaviour for each test speed, reducing the number of curves per figure to an acceptable 6.

Ideally the average curve for a certain speed is representative for the average ultimate values. Computing the mean stress at a range of strain values (or vice versa) does not lead to accurate curves, however, because jumps will be seen in the curve at the points where individual specimens failed. The number of datasets from which an average is taken namely decreases discretely with increasing strain in such cases. Preventing the occurrence of such jumps by not plotting further than the specimen which fails soonest results in a serious underestimation of the average strain to failure, and is therefore not applied. The choice has been made to lump all available data into a single cloud, and fit a polynomial equation to all data at once using a least-squares algorithm. This method is not perfect either, because the thus computed average curve will lie closest to the data which was acquired at the highest acquisition rate, because those data produce more points in the cloud to which it computes an average. The curves therefore tend more towards the gauge data, as it was not limited by the frame rate of the high-speed camera. Still, the method is applied here, because the produced curves seem to reasonably represent the material behaviour at a certain speed: typically an equal number of raw data lines are above and below the average curves for most parts, and the shape is similar to the raw data curves. The fitting method results in a stress-strain curve of the form:

$$\sigma(\varepsilon) = p_1\varepsilon^n + p_2\varepsilon^{n-1} + \ldots + p_n\varepsilon + p_{n+1} \tag{4.8}$$

for an n-th order fit. The polynomial is fourth order in most cases, and chosen to be able to reproduce most of the general characteristics the individual curves show. They are not meant as material models. Further research is necessary to identify the mechanisms that are acting and constitute equations for the stress-strain with physically accurate parameters for each combination of lay-up and material system.

The curves are all given in chapter 5. In the background, the original, non-

averaged curves are also plotted to give the reader an idea of the amount of spread that is present. The legends contain the average value of the strain rates for each of the background curves belonging to the set, determined as explained in section 4.7.3.2.

4.8 Strain rate limits

Five aspects were identified which limit the maximum strain rate at which a certain lay-up can be successfully tested using the current method. Each of them is explained in this section, as well as the influence on the resulting measurements.

4.8.1 Test bench capability

Perhaps the most obvious limit in strain rate stems from the maximum speed at which the test bench can be operated. It was established in section 4.7.3.2, that the actually obtained strain rate was about $55\,\%$ of what should occur theoretically for the laminate considered. Hence equation (4.2) should be updated with a factor f:

$$\dot{\varepsilon} = f\frac{v}{l_g} \tag{4.9}$$

Although the value likely depends on the properties of the tested laminate, a value of $f = 0.5$ is assumed for the current research. Using the maximum velocity capability of the test bench, $v_{\max} = 20\,\mathrm{m\,s^{-1}}$, the maximum obtainable strain rate can be found directly as a function of the gauge length.

4.8.2 Load cell ringing

When the time from beginning of loading to specimen failure approaches the period of load cell ringing, oscillations will start to appear in the results. These do not represent actual material behaviour and when they become too strong, the results cannot be used any more for the determination of material properties. The test duration depends on both testing speed and strain to failure.

The FE-model described in section 4.7.4.2 is used to investigate the influence of load cell ringing on the results. The ringing frequency in the model amounts to about $57\,\mathrm{kHz}$, higher than is found in the real tests ($10.5\,\mathrm{kHz}$, section 4.7.1.1). This difference stems from the simplified geometry used in the model, especially the absence of the grip clamping structure. However, conclusions can still be drawn from the model results. Figure 4.28 shows simulated force-strain curves obtained at different speeds. At $5\,\mathrm{m\,s^{-1}}$, the oscillation is already clearly visible, although the average behaviour coincides with a linear-elastic response, see also figure 4.26. The force at higher speeds is no longer usable. The simulation at $5\,\mathrm{m\,s^{-1}}$ has a duration of $160\,\mu\mathrm{s}$ until $1\,\%$ strain, while the oscillation period of the load cell

equals about $17.5\,\mu s$. Judging from this result, it is concluded that the test duration to failure t_f should last at leat ten times the period of load cell ringing T_{ringing} for the results to still be useful. This condition can be written as an equation:

$$t_f > 10 \cdot T_{\text{ringing}} \tag{4.10}$$

The period of an oscillation is the reciprocal of the frequency, $f_{\text{ringing}} = 1/T_{\text{ringing}}$. The test duration is directly related to the strain rate and the strain to failure $\varepsilon_{\text{fail}}$:

$$t_f = \frac{\varepsilon_{\text{fail}}}{\dot{\varepsilon}} \tag{4.11}$$

Hence, combining equations (4.10) and (4.11) leads to an expression of an upper bound on the strain rate based on the load cell ringing frequency f_{ringing}:

$$\dot{\varepsilon} < 0.1 \varepsilon_{\text{fail}} f_{\text{ringing}} \tag{4.12}$$

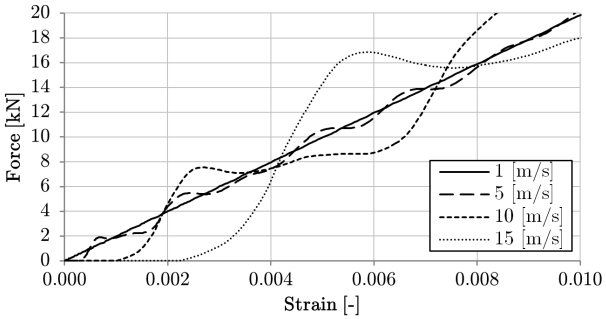

Figure 4.28. Stress-strain behaviour from simulations at up to $15\,\mathrm{m\,s^{-1}}$, strongly influenced by cell ringing at the higher speeds.

Based on the natural frequency of the load train of $10.5\,\mathrm{kHz}$ (section 4.7.1.1), this limits the strain rate to $10.5\,\mathrm{s^{-1}}$ for materials that show a $1\,\%$ strain to failure. Above this limit, the results are not immediately completely invalid, though one should realise that the oscillations in the load data are not related to the stress in the specimen.

There are two opportunities to stretch this limit. The first option is to increase the natural frequency of the load train by using a smaller or stiffer load cell, and/or by reducing the mass of the top clamp arrangement. The amount of increase in natural frequency will be limited since there is not much variation in structural stiffness of the available load cells. The top clamp design, moreover, is already optimised and a switch from high-strength steel to titanium only constitutes a minor improvement in terms of speed of sound. The second option is to switch to a different manner of load measurement. The ISO 26203-2 standard for high rate tensile

tests on metals advises to measure the strain on-specimen, away from the gauge section, using a 'dynamometer section' [4]. The Young's modulus of the specimen material should be rate-insensitive to allow a quasi-static load calibration, which might form a problem here since it is not known a priori how the modulus varies with rate. Yet another way to measure load could possibly be performed by applying the Virtual Fields Method at the higher rates, alleviating the need for a load cell altogether [35]. The resolution which remains at the highest frame rates of the Photron camera is, however, too small to obtain a sufficiently accurate acceleration field. Ultra-high speed cameras are needed to perform these measurements. These typically use an array of photosensitive chips or on-chip data storage to record full-resolution images with only fractions of microseconds in between, albeit that the total number of frames is small. Such a device is not available for the current research. Other challenges connected to the method is that it is limited to relatively high values of strain rate, that the strain rate is far from constant, and that currently, the method is limited to quasi-isotropic laminates as the selection of virtual fields for more complicated material behaviour proves challenging.

Since the load cell ringing becomes problematic at far lower rates than the bandwidth limit of the charge amplifier used to convert the cell charge to a measurable load, the latter is not further considered here.

4.8.3 Maximum frame rate for digital image correlation

It follows from section 4.7.3.1 that both methods of measuring strain result in their own limit on maximum strain rate. For DIC, it is the frame rate of the camera that creates a lower bound for the test duration. If the average error on the strain measurement is to remain at $1\,\%$ of the failure strain, this means that at least 50 frames are needed for the recording of a test. Assuming, namely, a linear increase in strain over the course of the test, about $2\,\%$ of the failure strain is covered between two frames. As the specimen will fail somewhere in between the capturing of two frames, the percentile error on the failure strain will lie between 0 and $2\,\%$, at an average of $1\,\%$. In equation-form, this condition becomes:

$$t_f > \frac{n_{\min}}{f_{\text{cam}}} \tag{4.13}$$

where $n_{\min}$ stands for the minimum requested number of frames (here taken at 50) and f_{cam} for the frame rate of the camera. The maximum frame rate of the high-speed camera used for the current research amounts to $500\,000$ frames per second. Combining equation (4.13) with (4.11), this upper bound on strain rate can be written as:

$$\dot{\varepsilon} < \frac{\varepsilon_{\text{fail}} f_{\text{cam}}}{n_{\min}} \tag{4.14}$$

The only way to improve this is by the using equipment with a higher maximum frame rate.

4.8.4 Bandwidth of the conditioning amplifier

The bandwidth of the signal conditioning amplifier is limited to $35\,\mathrm{kHz}$. This means that the recording of changes in strain which occur too fast will appear smoothed. The FE-model detailed in section 4.7.4.2 was used to evaluate whether the bandwidth of $35\,\mathrm{kHz}$ of the signal conditioner is good enough. Figure 4.29 contains the results of a simulation of a test at a strain rate of about $300\,\mathrm{s}^{-1}$. The figure also shows strain results filtered by a second order Butterworth low-pass filter with several cut-off frequencies to simulate the effect of a limited bandwidth on the obtained strain curve [36]. Only the curve at a $75\,\mathrm{kHz}$ bandwidth can reasonably follow the actual strain variation. The SAE J2749 requirement for an acquisition bandwidth of $83.3\,\mathrm{kHz}$ for a $200\,\mathrm{s}^{-1}$ test [3] seems, therefore, more appropriate than the ISO 26203-2 lower limit of $20\,\mathrm{kHz}$ [37]. The signal conditioner of the current research had a bandwidth of $35\,\mathrm{kHz}$. Applying the SAE requirement detailed in section 4.4.1 in reverse using the conditioner bandwidth results in a minimum test duration of $71.4\,\mu\mathrm{s}$. As increasingly high values of strain rate lead to lower test durations, the strain signal will appear more and more filtered. In equation form, the lower bound on test duration can be written as:

$$t_f > \frac{10}{4f_U} \tag{4.15}$$

where f_U stands for the bandwidth of the signal conditioning amplifier, here $35\,\mathrm{kHz}$. Again, combination with equation (4.11) yields the upper bound on strain rate:

$$\dot{\varepsilon} < 0.4\varepsilon_{\mathrm{fail}} f_U \tag{4.16}$$

Here also an equipment improvement is needed to increase this limit.

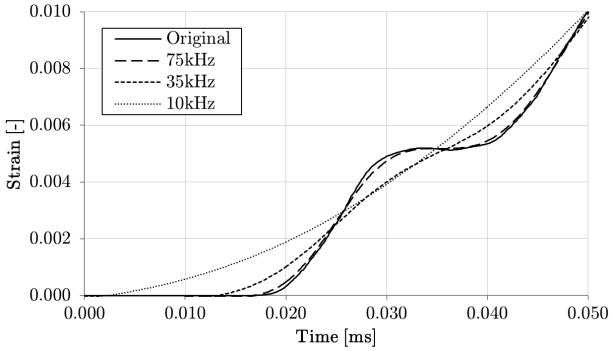

Figure 4.29. Influence of strain acquisition bandwidth on the obtained curve for a simulated $300\,\mathrm{s}^{-1}$ test on C/E $[\#(0/90)]_{2s}$.

4.8.5 Approximate equilibrium in the specimen

As mentioned in section 4.7.4.2, at high speeds, the strain no longer has the time to evenly distribute over the specimen. The effects become noticeable above a velocity of $5\,\mathrm{m\,s^{-1}}$, see figure 4.30 for the strain responses of the FE model to several displacement rates. At that speed, the time needed to reach $0.5\,\mathrm{mm}$ displacement equals $100\,\mu\mathrm{s}$. This is slightly more than the time needed for a stress pulse to travel three times back and forth from end to end in the C/E $[\#(0/90)]_{2s}$ specimen, i.e. six times along the length of the specimen. Apparently, this time is just sufficient for an approximate equilibrium to exist within the specimen. This also matches the condition posed by Xiao based on established research on SHPB testing [38]. This condition leads to the last upper bound in strain rate, which depends on the specimen length L, the failure strain $\varepsilon_{\mathrm{fail}}$ and the speed of sound c in the tested material. The speed of sound in the material required for this computation is determined ultrasonically, see section 4.9. Assuming a linear increase of strain with time, i.e. a constant strain rate, the relationship becomes as follows:

$$\dot{\varepsilon} < \frac{\varepsilon_{\mathrm{fail}} c}{6L} \tag{4.17}$$

To reach higher rates, apart from the other limits mentioned in the preceding sections, specimens should be shorter. However, shorter dumbbell specimens have the drawback that the stress concentration is higher. Moreover, below a certain length, added non-uniformity will appear in the stress distribution due to the proximity of the clamps.

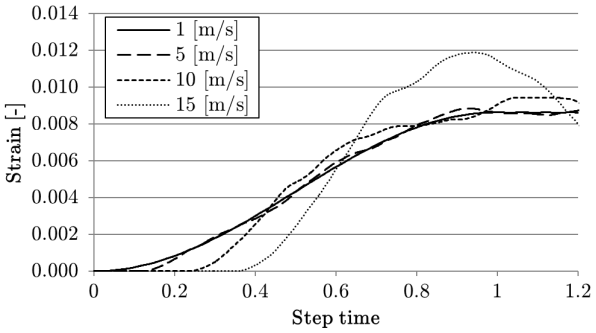

Figure 4.30. Strain versus step time ($t = 1$ at $0.5\,\mathrm{mm}$ displacement, here held constant afterwards) at up to $15\,\mathrm{m\,s^{-1}}$. Above $5\,\mathrm{m\,s^{-1}}$, the strain visibly overshoots the equilibrium value.

4.8.6 Overview of strain rate limits per laminate

Using the measured strains to failure as given in appendix B (table B.2), the measured wave propagation speeds given in section 4.9, the specimen dimensions from tables 4.3 and 4.4, and the various equipment limits mentioned above, the maximum strain rates have been determined for each successfully tested lay-up. The results are given in table 4.6.

Table 4.6. Strain rate limits in $[\mathrm{s}^{-1}]$ *for all tested lay-ups*

	Material	**Test bench** $20\,\mathrm{m\,s^{-1}}$	**Cell ringing** $10.5\,\mathrm{kHz}$	**DIC** $500\,\mathrm{kfps}$	**Conditioner** Bandwidth $35\,\mathrm{kHz}$	**Equilibrium**
C/E	Pure epoxy	250	12.6	120	168	33
	$[90]_8$	185	5.3	50	70	24
	$[\pm 45]_{2s}$	185	23.1	220	308	163
	$[45/0/-45/90]_s$	185	15.8	150	210	124
	$[\#(0/90)]_{4s}$	185	13.7	130	182	139
	$[\#(90/0)]_{4s}$	185	11.6	110	154	117
	$[\#(\pm 45)]_{4s}$	185	73.5	700	980	692
	$[\#(\pm 45)/\#(0/90)]_{2s}$	185	15.8	150	210	148
G/PA-6	Pure PA-6	118	24.2	230	322	67
	$[0]_4$	185	38.9	370	518	296
	$[90]_8$	185	9.5	90	126	44
	$[0/90]_{2s}$	185	47.3	450	630	278
	$[\pm 45]_{2s}$	185	210.0	2000	2800	1002
	$[\#(0/90)]_{2s}$	185	45.2	430	602	305
	$[\#(90/0)]_{2s}$	185	45.2	430	602	305
	$[\#(\pm 45)]_{2s}$	185	189.0	1800	2520	1124
	$[\#(\pm 45)/\#(0/90)]_s$	185	50.4	480	672	495

The table shows that the most stringent problem of the current set-up is the load cell ringing which is often lowest limit for the strain rate. Still, in many cases a slight surpassing of the limit still allows for conclusions to be drawn, as it does not result in an immediate radical change. It rather produces ripples in the result, and the curves are therefore confined to hold only in an average sense. In cases where the strain to failure is small, the equilibrium condition is no longer satisfied. This is a more serious issue, though in this case it can help to reduce the specimen length.

4.9 Ultrasonic material characterization

As preliminary evaluation, small samples of material (figure 4.31) were cut in order to measure the speed of sound in various directions using contact ultrasonics. The speed of sound can be deduced from the time of flight of a sound pulse. A schematic overview of the set-up is shown in figure 4.32.

An emitting (Olympus V110-RM) and a receiving (GE H5K) longitudinal transducer are put on opposite sides of a small piece of composite material with coupling gel, so that the faces of the transducers are between 3 mm and 15 mm apart. For the waveform generation, a NI PXI-5412 card and an AR 150A100B power amplifier are used, while data acquisition is handled by a NI-PXI-5122 card. A $2.5\,\mathrm{MHz}$ single-cycle sine burst with Hamming window is given as an input signal. Multiple echoes in the transmission signal are cross-correlated as well as the first echoes of the transmission and reflection signals respectively to retrieve the bulk wave velocity in the material. The thus obtained speeds of sound in the relevant directions are given in table 4.7, and match well with the expectations [39].

As indicated in the table, only the measurements on pure unidirectional composites resulted in clear signal transmission. For these materials, multiple reflections of the signal could be discerned, constituting to a very accurate measurement of the speed of sound. In other cases the transmitted signal was only weak, or even distorted, likely caused by the inhomogeneous internal fibre architecture.

The accurately measured speeds of sound can be used to determine the components of the stiffness tensor [40], which in turn can be converted to engineering properties. The results for carbon/epoxy are given in table 4.8.

The values determined here are different than the ones found earlier using a finite-element simulation of the block of woven material based on quasi-static constituent properties for which the results were given in section 3.3. The cause for the differences is assumed to be the dynamic nature of the ultrasonic measurements. If the small blocks of material are assumed to displace by about $50\,\mathrm{pm}$,

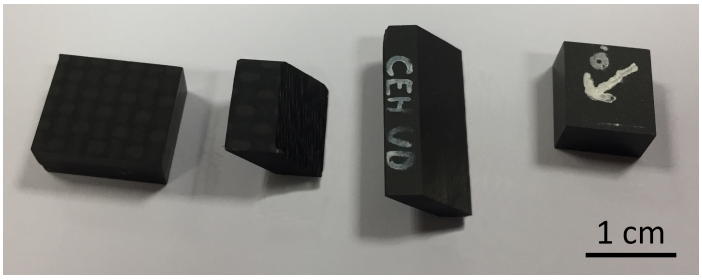

Figure 4.31. Small parts of material are cut for contact ultrasonic measurements, also cuts at $45°$ are made for the shear directions.

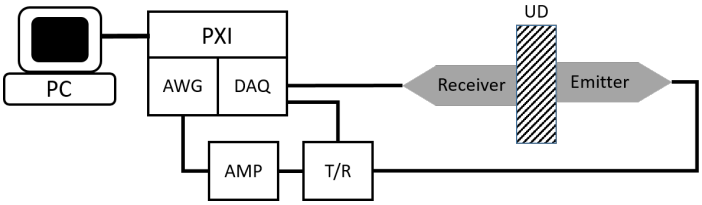

Figure 4.32. A schematic of the contact ultrasonics test set-up to measure the speed of stress waves in composite materials.

Table 4.7. Speeds of sound in the composite lay-ups, measured using contact ultrasonics with longitudinal excitation.

Material	Type	Direction[1]	Speed of sound $[\mathrm{m\,s^{-1}}]$
C/E	$[0]_n$	1	9303
		2	2841
		3	2820
	$[0/90]_{ns}$	1	4248^3
	$[\pm 45]_{ns}$	1	4182^2
	$[45/0/-45/90]_{ns}$	1	4680^3
	$[\#(0/90)]_{ns}$	1	6015^2
		2	5816^2
	$[\#(\pm 45)]_{ns}$	1	5578^2
	$[\#(\pm 45)\#(0-90)]_{ns}$	1	5552^3
G/PA-6	$[0]_n$	1	4513
		2	2821
		3	2755
	$[0/90]_{ns}$	1	3480^2
	$[\pm 45]_{ns}$	1	2827^2
	$[45/0/-45/90]_{ns}$	1	2436^2
	$[\#(0/90)]_{ns}$	1	4869^3
		2	3636^3
	$[\#(\pm 45)]_{ns}$	1	3523^3
	$[\#(\pm 45)\#(0-90)]_{ns}$	1	5818^3

1: 1 is longitudinal or 0° direction;
2 in-plane transverse or 90° direction;
3 out-of-plane transverse or thickness direction.
2: Signals weak.
3: Signals very weak and distorted.

Table 4.8. Ultrasonically measured engineering properties for unidirectional carbon/epoxy [40].

	Value [GPa]	Coefficient of variation[%]
E_1	135.37	0.8
E_2	11.36	2.1
E_3	11.53	2.5
ν_{12}	0.20	28.3
ν_{13}	0.17	35.1
ν_{23}	0.37	5.9
G_{12}	5.40	1.6
G_{13}	5.40	5.2
G_{23}	3.23	6.5

then combined with the excitation frequency of $2.5\,\mathrm{MHz}$ and an assumed stretch length of about $1\,\mathrm{mm}$, this would amount to a strain rate of about $125\,\mathrm{s}^{-1}$. Further measurements are necessary to validate this value.

4.10 Conclusion

In this chapter, the complete set-up for dynamic tensile testing has been explained. A new dumbbell specimen type was designed for the pure $90°$, the quasi-isotropic and the woven cross-ply layups, which resulted in successful failures, consistently away from the clamps. It is possible to investigate composite material properties from quasi-static up to $200\,\mathrm{s}^{-1}$ using this set-up. Digital image correlation using a high-speed camera proved to produce useful results up to the maximum rate for even the brittlest material.

It was shown that the synchronization of the various data streams is of utmost importance at the higher rates. This synchronization was successfully realized by careful analysis of all the measurement chains and taking into account all delays that occur in the various subsystems.

At the upper limit of this range, care should be taken not to mistake dynamic test effects for material behaviour. The causes of all the observed aspects of the test results have been identified, with the help of finite-element analyses. Five limits on the upper strain rate have been encountered and quantified: (1) the test bench capabilities, (2) ringing of the load cell, (3) the frame rate for DIC acquisition, (4) the bandwidth of the strain gauge amplifier and (5) the approximate equilibrium within the sample. Although they do not constitute 'hard' limits, results at higher rates should be interpreted with caution as they will no longer solely represent actual material behaviour.

Ringing of the load cell is currently responsible for the most stringent limits. Two possible solutions to the ringing issue are to measure the load on-specimen using a dynamometer section on the specimen, or the Virtual Fields Method. The absence of equilibrium is the next and perhaps more serious issue, though the use of a shorter specimen could help to push this limit to higher strain rates.

References

[1] Kistler Instrumente AG. *Load Washers*, 2016.

[2] Kistler Instrumente AG. *Kistler 5011B Charge Amplifier*, 2005.

[3] SAE International. *SAE J2749, 2017, "Surface vehicle recommended practise - high strain rate testing of polymers"*. Technical report, Society of Automotive Engineers, 400 Commonwealth Drive, Warrendale, PA 15096, July 2017.

[4] International Organization for Standardization. *ISO 26203-2:2011. Metallic materials – Tensile testing at high strain rates – Part 2: servo-hydraulic and other test systems. German version DIN EN ISO 26203-2:2011.* Technical report, International Organization for Standardization, 2011.

[5] Vishay Precision Group. *Vishay 2100 instruction manual*, 1977.

[6] Vishay Precision Group. *Optimizing Strain Gage Excitation Levels*. Technical Note TN-502, Vishay Precision Group, 2007.

[7] P. L. Reu and M. Nissen. *The evolution of high and ultra-high speed imaging from qualitative to quantitative.* Technical report, Sandia National Laboratories (SNL-NM), Albuquerque, NM (United States), 2014.

[8] A. Charbal, J. Dufour, A. Guery, F. Hild, S. Roux, L. Vincent, and M. Poncelet. *Integrated Digital Image Correlation considering gray level and blur variations: Application to distortion measurements of IR camera*. Optics and Lasers in Engineering, 78:75–85, March 2016.

[9] Pyrofil Department. *Mechanical Properties of PYROFIL Unidirectional Composite - TR 360E250S*. Technical report, Mitsubishi Rayon Co., Ltd., Carbon Fiber and Composite Materials Division, December 2013.

[10] Hottinger Baldwin Messtechnik GmbH. *HBM GEN series GN412*. Data sheet B2627-2.1 en, Hottinger Baldwin Messtechnik GmbH, October 2016.

[11] Photron Limited. *FASTCAM SA4 Hardware Manual - Revision 1.06E*. Technical Report E120120644U, Photron Limited, Tokyo, January 2012.

[12] A. Bridges. *New Uses for Your I/O Signals*, July 2014.

[13] M. Dolphen. *Experimental characterization of the tensile rate dependence of two structural composite material systems for automotive applications*. PhD thesis, Ghent University, 2016.

[14] ASTM International. *ASTM Standard D3039, 2008, "Standard Test Method for Tensile Properties of Polymer Matrix Composites"*. Technical report, American Society for Testing and Materials, West Conshohocken, PA, 2008.

[15] ASTM International. *ASTM Standard D638, 2003, "Standard Test Method for Tensile Properties of Plastics"*. Technical report, American Society for Testing and Materials, West Conshohocken, PA, 2003.

[16] International Organization for Standardization. *ISO 3167. Plastics – Multipurpose test specimens*. Technical report, International Organization for Standardization, 1993.

[17] I. De Baere, W. Van Paepegem, C. Hochard, and J. Degrieck. *On the tension–tension fatigue behaviour of a carbon reinforced thermoplastic part II: Evaluation of a dumbbell-shaped specimen*. Polymer Testing, 30(6):663–672, 2011.

[18] Huntsman Advanced Materials GmbH. *Araldite AW4858 and Hardener HW4858*. Technical report, Huntsman Advanced Materials GmbH, March 2010.

[19] W. D. Pilkey. *Petersons stress concentration factors*. John Wiley and Sons, New York, 2 edition, 1997.

[20] P. Reu. *All about Speckles: Speckle Density*. Experimental Techniques, 39(3):1–2, May 2015.

[21] BASF. *CAMPUS datasheet - Ultramid B3S - PA6*. Technical report, Chemie Wirtshaftsfoerderungsgesellschaft GmbH, Frankfurt, July 2015.

[22] M. Shirinbayan, J. Fitoussi, F. Meraghni, B. Surowiec, M. Bocquet, and A. Tcharkhtchi. *High strain rate visco-damageable behavior of Advanced Sheet Molding Compound (A-SMC) under tension*. Composites Part B: Engineering, 82:30–41, December 2015.

[23] Vishay Precision Group. *Strain Gage Installations with M-Bond 200 Adhesive*. Instruction Bulletin B-127-14, Vishay Precision Group, December 2014.

[24] L. Li, S. Zhang, Y. Chen, M. Liu, Y. Ding, X. Luo, Z. Pu, W. Zhou, and S. Li. *Water Transportation in Epoxy Resin*. Chemistry of Materials, 17(4):839–845, February 2005.

[25] L. E. Asp. *The effects of moisture and temperature on the interlaminar delamination toughness of a carbon/epoxy composite*. Composites Science and Technology, 58(6):967–977, 1998.

[26] D. J. Boll, W. D. Bascom, and B. Motiee. *Moisture absorption by structural epoxy-matrix carbon-fiber composites*. Composites Science and Technology, 24(4):253–273, January 1985.

[27] C. Shen and G. S. Springer. *Effects of moisture and temperature on the tensile strength of composite materials*. Journal of Composite Materials, 11(1):2–16, 1977.

[28] K. Hatten, G. Woodham, and D. Pinkston. *Effect of moisture on reinforced nylons*. Plastics Design and Processing, 11(3):28–29, March 1971.

[29] S. Pillay, U. K. Vaidya, and G. M. Janowski. *Effects of moisture and UV exposure on liquid molded carbon fabric reinforced nylon 6 composite laminates*. Composites Science and Technology, 69(6):839–846, May 2009.

[30] P. Reu. *All about Speckles: Contrast*. Experimental Techniques, 39(1):1–2, 2015.

[31] D. R. Hufner and S. I. Hill. *High strain rate testing and modeling of a woven E-glass–vinylester composite in dry and saturated conditions*. Journal of Composite Materials, 51(21):3017 – 3039, 2017.

[32] ASTM International. *ASTM Standard D3518, 2013, "In-Plane Shear Response of Polymer Matrix Composite Materials by Tensile Test of a +-45 Laminate"*. Technical report, American Society for Testing and Materials, West Conshohocken, PA, 2013.

[33] L. E. Kinsler. *Fundamentals of acoustics*. John Wiley and Sons, New York, USA, 4 edition, 2000.

[34] MatWeb, LLC. *ASTM A284 Steel, grade C*. Technical Report MS284C / 13932, MatWeb, 1999.

[35] F. Pierron and M. Grédiac. *The Virtual Fields Method*. Springer New York, New York, NY, 2012. DOI: 10.1007/978-1-4614-1824-5.

[36] L. D. Paarmann. *Design and analysis of analog filters: a signal processing perspective*. Kluwer Academic Publishers, New York, 2003. OCLC: 71229251.

[37] International Organization for Standardization. *ISO 26203-1:2010. Metallic materials – Tensile testing at high strain rates – Part 1: Elastic-bar-type systems. German version DIN EN ISO 26203-1:2010.* Technical report, International Organization for Standardization, 2010.

[38] X. Xiao. *Dynamic tensile testing of plastic materials*. Polymer Testing, 27(2):164–178, April 2008.

[39] M. Kersemans. *Combined experimental-numerical study to the ultrasonic polar scan for inspection and characterization of (damaged) anisotropic materials*. PhD thesis, Ghent University, Ghent, 2014.

[40] R. D. B. Sevenois, S. W. F. Spronk, D. Garoz, F. A. Gilabert, E. Verboven, M. Kersemans, and W. Van Paepegem. *Multi-scale approach to predict the orthotropic elasticity tensor of carbon fibres and woven carbon composites by ultrasonic insonification*. In ECCM18 - 18th European Conference on Composite Materials, Athens, Greece, June 2018.

5 Tensile rate-dependency

5.1 Introduction

Chapter 4 contains the explanation of the dynamic tension testing and data reduction procedures. That knowledge is applied to a test campaign on the two material systems described in chapter 3. In this chapter, the results of that test programme are presented. First, it is explained what has been tested and why, followed by a section in which the measured strain rates are given and the implications on the validity of the test results is discussed. Finally, the stress-strain data is presented and discussed per layup in the remaining sections.

5.2 Tensile test programme overview

Many different lay-ups can be tested to characterise a composite material in tension. Multiple tests need to be carried out at several speeds to obtain an overview of the dependency of the material behaviour on strain rate, because this is not possible using a single test. Additionally, each test configuration needs to be repeated several times to measure the consistency of the results. This soon leads to a very large test programme, so selection is necessary.

5.2.1 Lay-ups

As mentioned in the introduction of this dissertation, it is decided to set-up a test programme that allows to (1) discover the challenges in dynamic tensile testing of composites and (2) form a collection of data onto which a material model for dynamic composite simulations could be based.

In light of the first goal, very different materials are to be tested to explore the limits of dynamic tensile testing. Both pure matrix materials and fibre-reinforced laminates are to be tested. The fibre architecture can be both unidirectional and woven, and oriented in one or multiple directions. The campaign should cover both laminates with a brittle and those with a ductile response, and both strong and weak lay-ups.

Regarding point (2): the current research forms part of a larger research programme which aims to reach a multi-scale model of composites, possibly woven, under various load cases. The aim is, therefore, to produce data that allows the development of a material model for composite laminates with either unidirectional or woven layers. From a modelling perspective, it is beneficial to have data that can serve as model input, and data that can serve as validation. Tests for input should allow the determination of material properties of the constituents. The basic building blocks of a woven composite are fibre bundles and the surrounding matrix. Assuming that a unidirectional composite behaves in a manner which is representative for a fibre bundle, the former can be tested to investigate the behaviour of the latter. Along that logic, tensile tests on the following laminates are included into the programme:

- Pure matrix
- Pure 0° - or unidirectional (UD)
- Pure 90° - or UD
- $[\pm 45]_{ns}$

where the last item in the list allows to learn about shear behaviour using a tensile test, and where n denotes any integer number larger than zero and s indicates a symmetric layup, as is mentioned in section 3.2.4.

Listing the tests that can generate model inputs shows that the first criterion formed above is almost entirely met as well. This research deals with both a glass/polyamide-6 (G/PA-6) and a carbon/epoxy (C/E) material system, hence the brittle, ductile, strong and weak responses are already covered with the above selection.

To be able to research and/or validate unidirectional composite models, the following laminates are included into the list:

- $[0/90]_{ns}$ - or cross-ply (CP)

- $[45/0/-45/90]_{ns}$ - or quasi-isotropic (QI)

For the development of woven composite material models, the following are added:

- $[\#(0/90)]_{ns}$ - CP
- $[\#(90/0)]_{ns}$
- $[\#(\pm 45)]_{ns}$
- $[\#(\pm 45)\#(0/90)]_{ns}$ - QI

It is chosen to test only balanced and symmetric laminates.

As stated above, tests need to be carried out at several speeds to obtain a global overview of material rate-dependency. A set of stress-strain curves at every decade of strain-rate between quasi-static and $200\,\mathrm{s}^{-1}$ is assumed to be able to make a full rate-dependent parameter identification possible. A test at $0.002\,\mathrm{s}^{-1}$ is taken as representative for the quasi-static situation. The test standard for tensile testing of composites advises to test at another decade smaller strain-rate [1], but the challenge of dynamic testing resides in the upper limit rather than the lower. The chosen bounds mean a stress-strain curve is requested for six decades of strain-rates: 0.002, 0.02, 0.2, 2, 20, and $200\,\mathrm{s}^{-1}$.

The upper speed limit of the hydraulic pulse test bench used here is $20\,\mathrm{m\,s}^{-1}$. At these speeds, the velocity it produces is far from constant, hence it was chosen to operate only up to $15\,\mathrm{m\,s}^{-1}$. A typical gauge length of $50\,\mathrm{mm}$ was chosen for the specimens. To approximately reach the strain rates as mentioned above, the machine was actuated at 0.0001, 0.005, 0.05, 0.5, 5 and $15\,\mathrm{m\,s}^{-1}$.

Table 5.1 summarizes which tensile tests have been conducted, sorted first per material system, then like the bulleted lists above. As can be seen, each scenario was repeated five times to gain insight in the spread of the results. A total number of 475 tensile tests was planned, though eventually over 650 tests were performed, *e.g.* because a number of initial tests was required to define the correct equipment settings, because there were wrong types of failure, or to apply the knowledge gained after the execution of many tests to the earlier test series. For details about the specimen preparation, the experimental set-up and the data reduction, the reader is referred to chapter 4.

Table 5.1. Test programme: the number of tests per layup is indicated per test speed.

	Material	Target test speed $[\mathrm{m\,s^{-1}}]$					
		0.0001	0.005	0.05	0.5	5	15
C/E	Pure epoxy	5	5	5	5	5	5
	$[0]_4$ [1]	-	-	-	-	-	-
	$[90]_8$	5	5	5	5	5	5
	$[0/90]_{2s}$ [1]	-	-	-	-	-	-
	$[\pm 45]_{2s}$	5	5	5	5	5	5
	$[45/0/-45/90]_s$ [2]	5	-	-	-	5	-
	$[\#(0/90)]_{4s}$	5	5	5	5	5	5
	$[\#(90/0)]_{4s}$	5	5	5	5	5	5
	$[\#(\pm 45)]_{4s}$	5	5	5	5	5	5
	$[\#(\pm 45)/\#(0/90)]_{2s}$	5	5	5	5	5	5
G/PA-6	Pure PA-6	5	5	5	5	5	5
	$[0]_4$	5	5	5	5	5	5
	$[90]_8$	5	5	5	5	5	5
	$[0/90]_{2s}$ [2,3]	5	-	-	5	5	-
	$[\pm 45]_{2s}$	5	5	5	5	5	5
	$[45/0/-45/90]_s$ [2]	-	-	-	-	-	-
	$[\#(0/90)]_{2s}$	5	5	5	5	5	5
	$[\#(90/0)]_{2s}$	5	5	5	5	5	5
	$[\#(\pm 45)]_{2s}$	5	5	5	5	5	5
	$[\#(\pm 45)/\#(0/90)]_s$	5	5	5	5	5	5

[1] No suitable specimen shape found, see section 5.3.2.1
[2] Reduced or skipped due to time constraints
[3] Tested in the 90° direction

5.2.2 Strain rates

The strain rates resulting from testing at the speeds from the previous section are given in table 5.2, which shows the average value of the rate for a certain material at a certain speed. The literature contains many wrong examples where data is given as a function of theoretical strain rate (e.g. [2] or [3]), likely because it is what the standards advise [4, 5]. The theoretical value, however, is typically an overestimation of the actual one, especially for brittle materials [6]. Hence, the actually measured strain rates are used in this research. The table shows that the requested six decades of strain rate have been approximately covered.

In contrast to what is typically found in the literature covering the dynamic tensile characterisation of composites (*e.g.* the results at the higher rates in [7] look like a typical case of absence of equilibrium and/or load cell ringing while no mention thereof is made), it is decided here to clearly indicate when the obtained results might be invalid. The various limits on strain rate at which a certain specimen and material can be accurately tested are given in section 4.8. The colours in the table indicate results which should be treated with caution because they were executed at strain rates which surpass one or more upper limits for a data acquisition free of dynamic effects.

Ringing of the load cell affected the results which are indicated in any other colour than black. The effect causes the slope of the stress-strain curve to be no longer constant initially. At $15\,\mathrm{m\,s^{-1}}$, the natural frequency of the load train causes the load to be underestimated exactly in the strain range where the modulus is measured. This makes the obtained value for the Young's modulus too low and not representative for the material behaviour. The curve for C/E QI at $59\,/\mathrm{s}$ in figure 5.14 shows the influence of ringing: initially the curve lies below the quasi-static results, though eventually it overshoots them.

At $5\,\mathrm{m\,s^{-1}}$ and below, the effect of load ringing is typically limited. Only for the cases where the (apparent) plasticity in the dynamic response is significant, the maximum stress can still be significantly affected by the ringing. Figure 5.19 shows the stress-strain response of G/PA-6 $[\pm 45]_{2s}$. The oscillations in the result of the fastest tests cause the maximum stress of the individual tests to be slightly overestimated, as can be seen by the grey background curves at the highest rate. These curves clearly show the cell ringing, though the difference between the test duration and the period of natural frequency is large enough to filter the effect. The values of strain to failure are generally unaffected by the ringing.

The Young's modulus of the tests at which there was no approximate equilibrium (shown in blue or red in the table) is lowered by an added effect. The force signal is namely initially delayed with respect to strain because they are measured in different locations. This leads to an underestimation of the modulus, see also section 4.7.4. These values should therefore not be used to conclude on material rate-dependency. Both load cell ringing and the absence of equilibrium cause an

Table 5.2. Average strain rate $[\mathrm{s}^{-1}]$ of the collection of tests for each lay-up at each test speed.

	Material	**Test speed** $[\mathbf{m\,s^{-1}}]$					
		0.0001	0.005	0.05	0.5	5	15
C/E	Pure epoxy	0.0014	0.067	0.55	6.0	49	113
	$[90]_8$	0.0017	0.086	0.61	5.6	59	112
	$[\pm 45]_{2s}$	0.0011	0.055	0.51	2.8	80	176
	$[45/0/-45/90]_s$	0.0008	-	-	-	57	-
	$[\#(0/90)]_{4s}$	0.0006	0.027	0.22	1.9	48	155
	$[\#(90/0)]_{4s}$	0.0007	0.027	0.22	1.5	46	136
	$[\#(\pm 45)]_{4s}$	0.0012	0.057	0.52	3.4	67	191
	$[\#(\pm 45)/\#(0/90)]_{2s}$	0.0008	0.029	0.26	2.8	47	135
G/PA-6	Pure PA-6	0.0008	0.041	0.37	4.4	43	114
	$[0]_4$	0.0011	0.053	0.47	6.0	60	102
	$[90]_8$	0.0017	0.077	0.62	5.9	72	138
	$[90/0]_{2s}$	0.0010	-	-	5.0	46	-
	$[\pm 45]_{2s}$	0.0013	0.058	0.56	3.1	89	194
	$[\#(0/90)]_{2s}$	0.0009	0.040	0.32	4.1	55	116
	$[\#(90/0)]_{2s}$	0.0009	0.042	0.34	3.9	53	146
	$[\#(\pm 45)]_{2s}$	0.0015	0.068	0.63	4.3	74	205
	$[\#(\pm 45)/\#(0/90)]_s$	0.0010	0.049	0.39	5.4	57	155

Colours indicate surpassing strain rate limits (see section 4.8):

Green:	load cell ringing influences result
Blue:	additionally, no more equilibrium
Red:	additionally, strain acquisition limits superseded

initially underestimated load with respect to strain in the current case, reinforcing each other's effect. Perhaps the choice of a different and possibly larger strain range to compute the Young's modulus can mitigate some of the influence, allowing for a slightly higher strain rate limit.

The results in red are influenced by the finite acquisition speed of the high-speed camera, and/or by the fact that the signal conditioner smooths variations faster than $35\,\mathrm{kHz}$ in the strain coming from the gauges. In both cases, the maximum strain could be underestimated. In the former case, the overall accuracy of the strain data is also compromised.

5.3 Rate-dependency of the tested materials

With all acquisition limits clearly identified in the results, the rate-dependency of the material can be investigated without remaining uncertainty. This section contains the stress-strain curves at several strain rates and a discussion of the rate dependency for each of the successfully tested lay-ups. First the results of the pure matrices are given, followed by the UD-layered composites, and finally the data of the woven-layered composites ends the section.

Two different types of curves are shown in the figures: thick lines and lighter thin ones. The thin lines represent the raw data, the thick lines are polynomial fits, see also section 4.7.5. The polynomials are fourth order in most cases, which captures enough characteristics of the stress-strain behaviour. The exceptions are C/E $[\#(\pm 45)]_{4s}$, which was fitted with a sixth order polynomial, and G/PA-6 $[\pm 45]_{2s}$, G/PA-6 $[\#(\pm 45)]_{2s}$, and the full curves for pure PA-6, which were fitted with a eleventh order polynomial. The higher order fits were needed to capture the large amount of plasticity. The curve fits are generated to show a general trend of rate-dependency of each material.

The number of average curves in each figure often does not add up to the number of speeds that material was tested at. The choice has namely been made to exclude both raw and fitted curves when one of the speed limits for correct data acquisition (section 4.8) has been surpassed. Section 4.7.4.2 shows how the incorrect curves give a false sense of rate-dependency. The curves for the highest rate incorrectly appear below those for the lowest rate because there is no longer an approximate equilibrium within the specimen. If these curves would be added anyway, the visualization of the strain rate dependency of the material at the other rates would be obscured. Hence, the discussion is always based on the results which have not surpassed any of the strain rate limits, i.e. the tests that have a rate indicated in black in table 5.2.

Appendix B contains tabular overviews of the engineering properties and coefficients of variation versus test speed, as well as graphical representations of the variation of these values with strain rate.

5.3.1 Pure matrix

As discussed in chapter 3, rate-dependency is expected in both epoxy [8] and polyamide-6 [9, 10]. How the found change with rate agrees with literature is discussed for either material in this section.

5.3.1.1 Pure epoxy

For epoxy, the literature contains records which show that the tensile strength and Young's modulus both increase with strain rate while the strain to failure decreases [8]. Figure 5.1 shows the stress-strain curves for pure epoxy. The Young's modulus increases from $3.14\,\mathrm{GPa}$ at $0.0014\,\mathrm{s}^{-1}$ to $3.79\,\mathrm{GPa}$ at $6\,\mathrm{s}^{-1}$. The epoxy used here does not show an increase in strength or decrease in strain to failure with strain rate which surpasses the variation in the results. This is probably related to the very brittle failure, which can be seen in figure 5.2. At low rates, the specimens typically break with a clean crack in the gauge section, perpendicular to the loading direction (figure 5.2a). At high rates, the material in the gauge section shatters into many pieces (figure 5.2b). Judging from the fact that the original geometry is retrieved when the pieces are put back together, no significant plasticity has occurred. Due to the brittle response of the tested material, the coefficients of variation for the stress and strain to failure are of relatively high value.

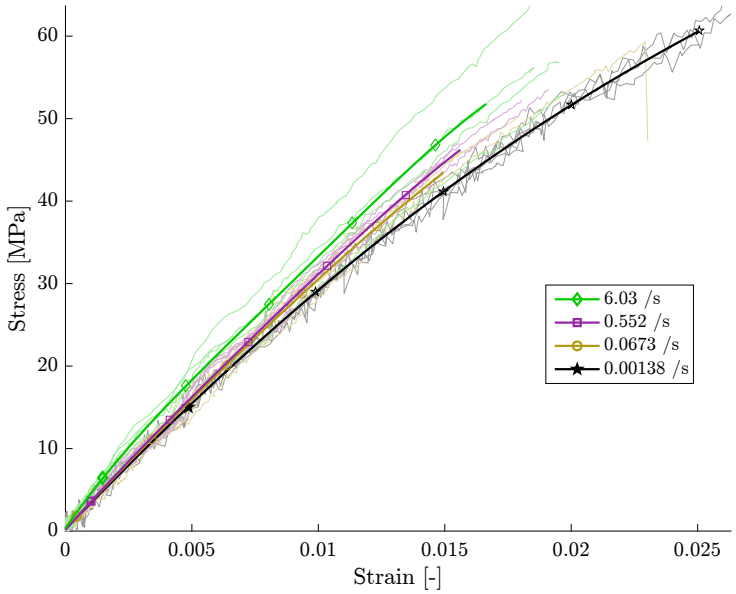

Figure 5.1. Stress-strain curves of pure epoxy at various strain rates.

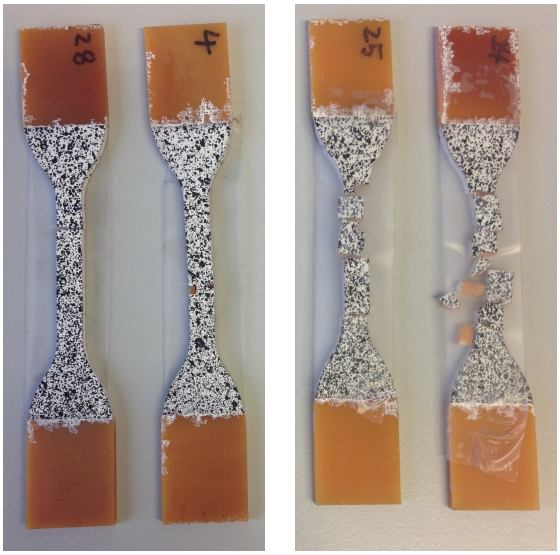

a. $v = 0.0001\,\mathrm{m\,s^{-1}}$; $\dot{\varepsilon} \approx 0.0014\,\mathrm{s^{-1}}$.

b. $v = 15\,\mathrm{m\,s^{-1}}$; $\dot{\varepsilon} \approx 133\,\mathrm{s^{-1}}$.

Figure 5.2. Failed pure epoxy specimens.

The tests at $0.0001\,\mathrm{m\,s^{-1}}$ continue up to strains or stresses which are higher than expected from the other results, based on a linear dependency on strain rate. There is no current explanation for this behaviour. Judging from the comparable amount of variation in the results at all lower rates (see also figures B.1 and B.2 in the appendix), it seems not to be by chance that the specimens tested at the lowest rate are relatively strong.

5.3.1.2 Pure polyamide-6

For PA-6, the full stress-strain curves are given in figure 5.3 and a focus on the initially linear-elastic parts is given in figure 5.4. Figure 5.5 contains pictures of specimens after failure at the lowest and the highest rate.

In literature, polyamide-6 has an increasing yield stress with strain rate, but the Young's modulus is unaffected and the strain to failure, although constant at low rates (<0.05 /s) [9], seems to increase in the high rate regime (>500 /s) [10]. It can be seen in the stress-strain curves that the material shows a significant amount of plasticity at the two lowest rates, while the response remains practically elastic up to failure for the higher speeds. The material shows a large decrease in maximum strain with increasing strain rate, while difference in Young's modulus indeed does not show a significant deviation. The yield stress (or maximum stress in this case) shows a clear increase with strain rate while the speeds are low enough to evoke a

plastic response, here this is the case up to $4.44\,\mathrm{s}^{-1}$. The strain level at which the yield stress occurs lies around 0.05 for all cases. At higher rates, the specimens show a rather brittle failure (as shown in figure 5.5b) which occurs at strains of about half the yield strain, which explains the jump in maximum stress (see figure B.29).

The pure PA-6 shows a very large relative scatter for strain to failure at the three lowest rates, see also figure B.30. Within the slowest test series, some specimens namely failed in a relatively viscoplastic manner while others broke before any significant amount of material flow occurred. Figure 5.5a shows that the specimen length after failure varies largely indeed. This difference could stem from internal defects like microscopic bubbles causing local stress concentrations resulting in early failures. Alternatively, it is possible that not all specimens were in exactly the same conditioning state, as parts of the test series were carried out on different dates, even within the same velocity group. The amount of moisture has a large impact on the material behaviour of PA-6 [11], as was also mentioned in section 3.7.

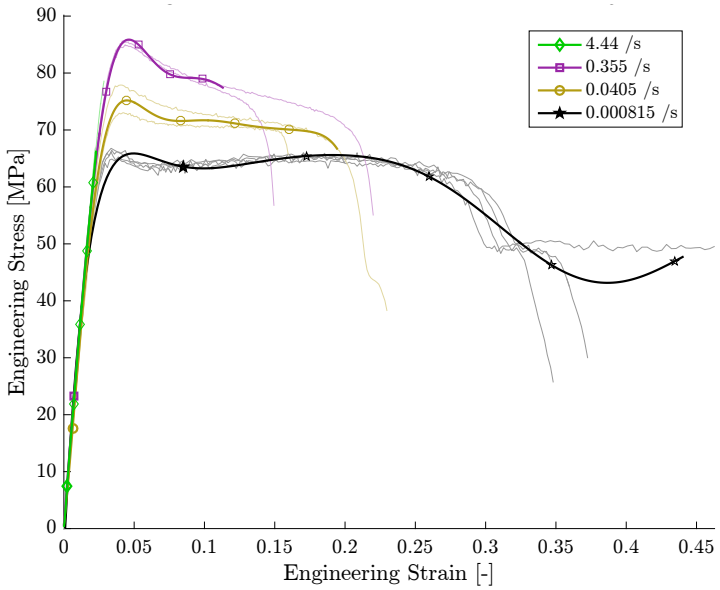

Figure 5.3. Stress-strain curves of polyamide-6 at various strain rates.

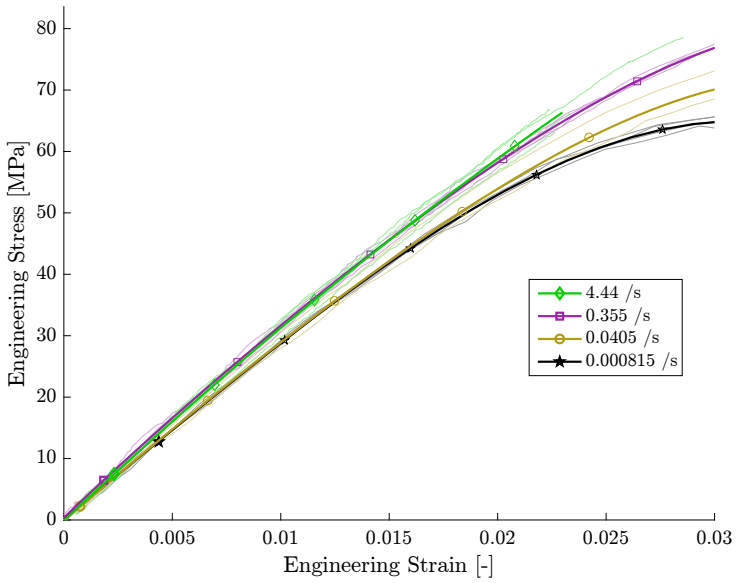

Figure 5.4. Zoomed stress-strain curves of polyamide-6 at various strain rates.

a. $v = 0.0001\,\mathrm{m\,s^{-1}}$; $\dot{\varepsilon} \approx 0.0008\,\mathrm{s^{-1}}$.

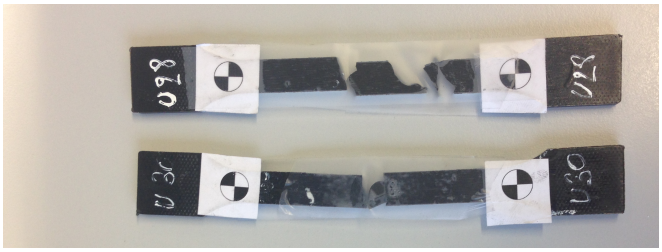

b. $v = 15\,\mathrm{m\,s^{-1}}$; $\dot{\varepsilon} \approx 114\,\mathrm{s^{-1}}$.

Figure 5.5. Failed pure polyamide-6 specimens.

5.3.2 Laminates with unidirectional plies

The tensile rate-dependence of composites with unidirectional layers is treated in this section. This includes the pure 0° and 90° UD lay-ups and further treats the $[0/90]$ and $[\pm 45]$ CP, and the QI laminates.

Looking at the fibre level, the carbon fibres are known not to show any form of rate-dependence [12]. All properties of E-glass fibres, on the contrary, vary with deformation rate [13]: with increasing strain rate, glass fibres show an increase in yield or tensile strength, strain to failure and Young's modulus.

5.3.2.1 Carbon/epoxy 0° UD and 0/90 cross-ply

The behaviour of 0° UD composites is typically fibre dominated. It is therefore expected that the rate-dependency follows that of the fibres. In that case, the properties of 0° UD C/E should be rate-independent. Sources in literature generally support this conclusion [14], though some find a small increase in modulus [15].

As mentioned in section 4.6.3, the specimen dimensions in table 4.3 for C/E 0° UD do not lead to a correct failure. The clamp area is too short to reduce the shear stress below an acceptable level. Several configurations were attempted nonetheless, see table 5.3.

Table 5.3. Attempted configurations for carbon/epoxy 0° UD.

	Configuration	Failure	Reason
1	Rectangular without tabs	At clamp or slip-out	Damage to the fibres due to grip teeth, or not enough clamping pressure
2	Rectangular # C/E tabs	In tab	The shear stress surpassed the woven tab interlaminar shear strength
3	Rectangular aluminium tabs	Adhesive	The shear stress surpassed the shear strength of the tab adhesive
4	Dogbone aluminium tabs	Adhesive	Same as above: longitudinal cracks form a rectangular specimen (figure 5.6)

None of the attempted configurations worked. The shear stress acting in the clamping area is simply too high due to the small grip length. A possible solution of the problem is to use perhaps longer, steel tabs in an attempt to introduce the load over an area which is larger than the grips. Alternatively, bigger grips could be designed, or a thinner specimen (with only three or two laminae) could be used. The challenge with the last option is to produce straight specimens, as the 4-layered plates already showed a small amount of warping. No further effort was

spent on this issue, as the results of other tests and in literature suggest that no rate-dependency is to be expected.

The laminate chosen for the CE CP is twice as thick as the 0° UD specimen, and thus the same number of layers with fibres in longitudinal direction needs to be broken. This means that a comparable shear stress is needed in the clamps to introduce the necessary amount of load into the specimen, making it again a challenge for the adhesive. Dogbone specimens with aluminium tabs are tested at $0.01\,\mathrm{m\,s^{-1}}$ to investigate whether the addition of the 90° layers is sufficient to transfer the load laterally and make the entire clamped area effective. The specimens, however, show a similar failure behaviour as the 0° UD ones, albeit that the 90°-layers delaminate from the parts of the laminate that remain attached to the tabs, see figure 5.7. In this case, a four-layer laminate might have worked, as the 0° UD laminate proves that it can be manufactured, and it would reduce the necessary shear stress in the grips by a factor of 2. No further effort was spent on testing this laminate, though, since the results of other laminates (especially the C/E $[\#(0/90)]_{2s}$) showed that no rate-dependency is to be expected.

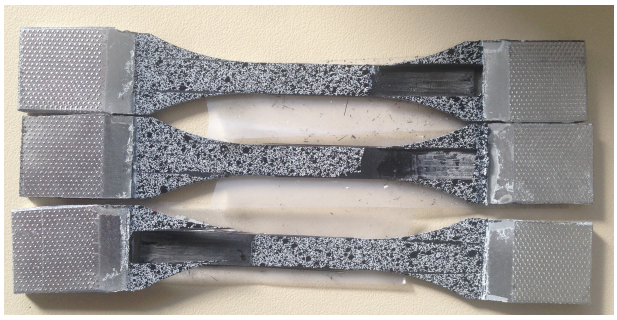

Figure 5.6. Typical failure of dogbone-shaped carbon/epoxy 0° UD specimens.

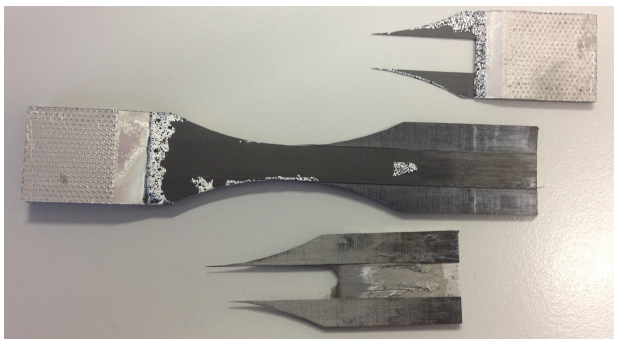

Figure 5.7. Typical failure for a dogbone-shaped C/E $[0/90]_{2s}$ specimen.

5.3.2.2 Glass/polyamide-6 0° UD

Following the line of fibre-dominated behaviour for the 0° direction of UD composites, the properties of 0° UD G/PA-6 should depend on strain rate as described in the beginning of section 5.3.2. Indeed the maximum stress, failure strain and Young's modulus of 0° UD G/PA-6 show an increase in value with strain rate. Over the range of 0.0011 to $6.0\,\mathrm{s}^{-1}$, they increase from 755 to $1390\,\mathrm{MPa}$, from 2.45 to 3.7, and from 36.1 to $44.2\,\mathrm{GPa}$, respectively. Although no literature has been found in which the tensile rate-dependency of UD G/PA-6 is treated, this corresponds with the trend seen for other thermoplastic matrices reinforced with long glass fibres [16, 17]. The fact that the stress-strain curves in figure 5.8 show no plasticity proves that the material behaviour is indeed fibre-dominated. The type of failure hardly changes with rate, see figure 5.9: in both cases the laminate disintegrates upon failure, which is attributed to the large amount of elastic energy which is released from the stretched fibres as they break. It is more violent at high rate, which is reflected by the fact that specimens in figure 5.9b have lost almost all of their paint.

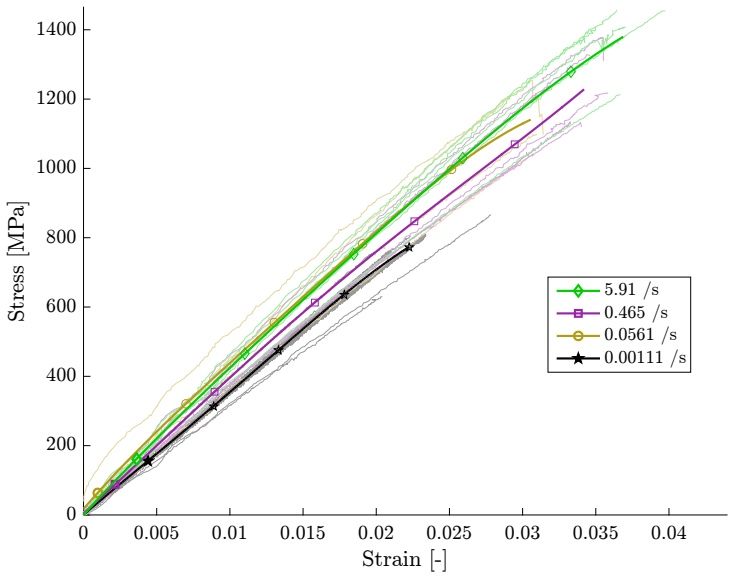

Figure 5.8. Stress-strain curves of G/PA-6 0° UD at various strain rates.

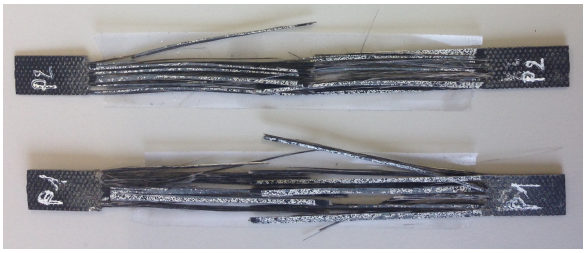

a. $v = 0.0001\,\mathrm{m\,s^{-1}}$; $\dot{\varepsilon} \approx 0.0011\,\mathrm{s^{-1}}$.

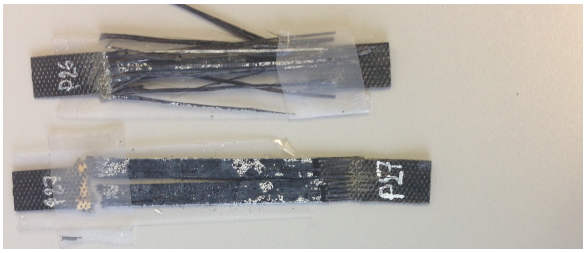

b. $v = 15\,\mathrm{m\,s^{-1}}$; $\dot{\varepsilon} \approx 102\,\mathrm{s^{-1}}$.

Figure 5.9. Failed G/PA $0°$ *UD specimens.*

5.3.2.3 Carbon/Epoxy 90° UD

For 90° UD composites, not only the matrix, but also the fibre-matrix interface plays a large role, because this interface largely determines the strength in this loading direction. The rate-dependency of 90° UD C/E shows, therefore, differences from the pure epoxy: the strain to failure is now also expected to increase with rate [15, 18] rather than decrease. The average stress-strain curves in figure 5.10 show a slight increase of stress, strain and modulus with strain rate, though the changes are not significant: they do not surpass the variation. Figures B.4, B.5 and B.6 in appendix B clearly show the variation is larger than the changes due to rate. This is in part due to the very small amount of strain to failure, which negatively influences the signal to noise ratio. It can be seen in the grey background curves that the noise is indeed relatively large, still the data is useful enough to conclude that there is no significant rate-dependency for this laminate.

Looking at the failure pattern (figure 5.11), in both the quasi-static and the dynamic case the laminate cleanly breaks apart with cracks that lie perpendicular to the loading direction. In the dynamic case, though, multiple cracks appear versus a single crack for the lower speeds. Macroscopically no difference can be observed between the crack flanks of the quasi-statically loaded specimens and those of the dynamically loaded ones.

The values of failure stress and strain are lower than the data sheet values. $32.7\,\mathrm{MPa}$ was measured for the quasi-static maximum stress here, versus $55\,\mathrm{MPa}$

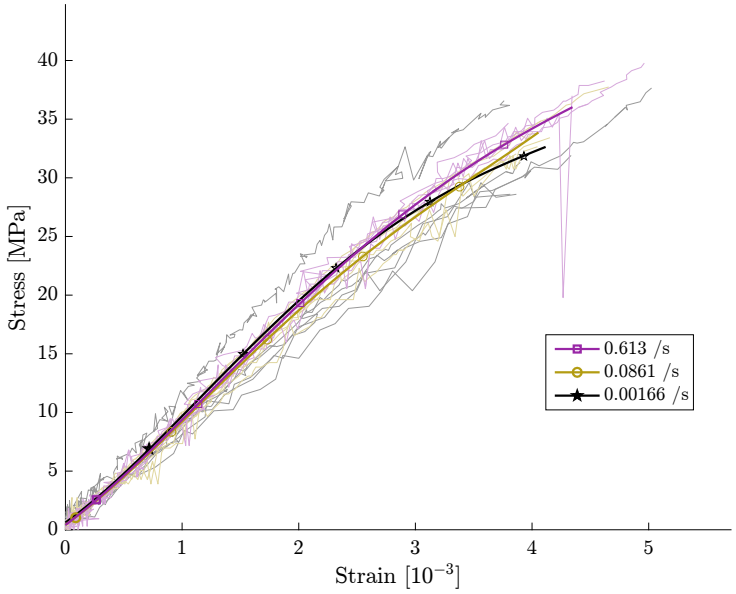

Figure 5.10. Stress-strain curves of C/E 90° UD at various strain rates.

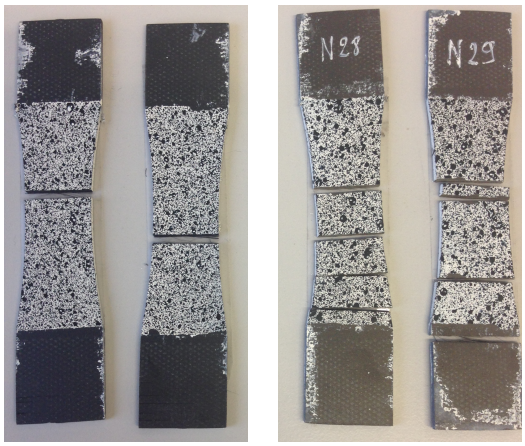

a. $v = 0.0001\,\mathrm{m\,s^{-1}}$; $\dot{\varepsilon} \approx 0.0017\,\mathrm{s^{-1}}$.

b. $v = 15\,\mathrm{m\,s^{-1}}$; $\dot{\varepsilon} \approx 112\,\mathrm{s^{-1}}$.

Figure 5.11. Failed C/E 90° UD specimens.

in the data sheet, and the ultimate strain was $0.42\,\%$ versus $0.6\,\%$ provided by the manufacturer [19]. This discrepancy is caused by the specimen edges, which were not optimal owing to the water jet cutting process (section 4.6.4).

5.3.2.4 Glass/Polyamide-6 90° UD

As for 90° UD C/E, also for 90° UD G/PA-6 differences are expected with respect to the pure PA-6 behaviour. The fibres act as stress concentrators, largely reducing the ductility at low rates, compare figure 5.12 to 5.3. As mentioned before, no sources were found which treat the tensile rate-dependency of UD G/PA-6, though the pronounced decrease of the failure strain and more than doubling of the Young's modulus of the composite with respect to the unreinforced matrix at quasi-static rates is in accordance with the literature [20]. It is interesting to note, though, that the strong reduction of strength due to addition of transverse fibres [20] is not seen in the current research. The rate-dependency of the mechanical properties has practically disappeared: over the range of 0.0017 to $5.9\,\mathrm{s}^{-1}$, no significant change of maximum stress or Young's modulus is seen. The trend of the failure strain is unclear. Perhaps the brittleness of the laminate lies at the basis of this effect: figure 5.13 shows that no macroscopic plasticity occurred as the specimens all failed with clean transverse cracks. The fibres probably limit the matrix plasticity to a microscopic scale, thereby suppressing the effect of its rate-dependency on the overall composite behaviour.

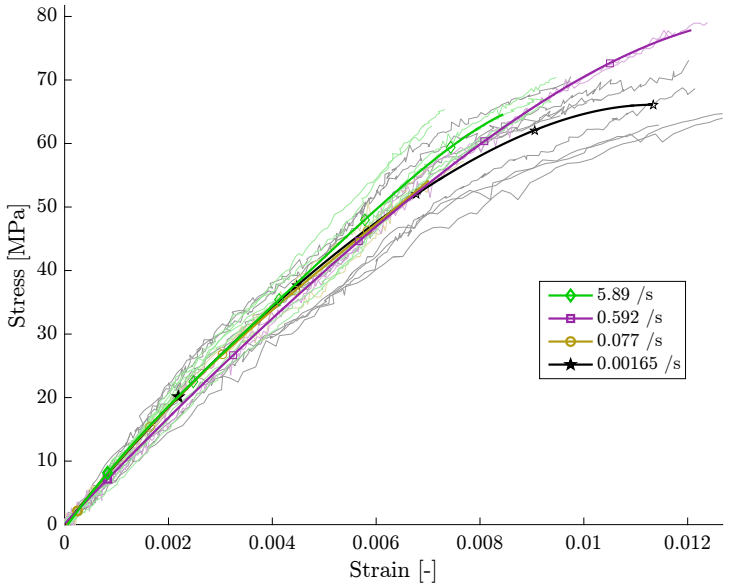

Figure 5.12. Stress-strain curves of G/PA-6 90° UD at various strain rates.

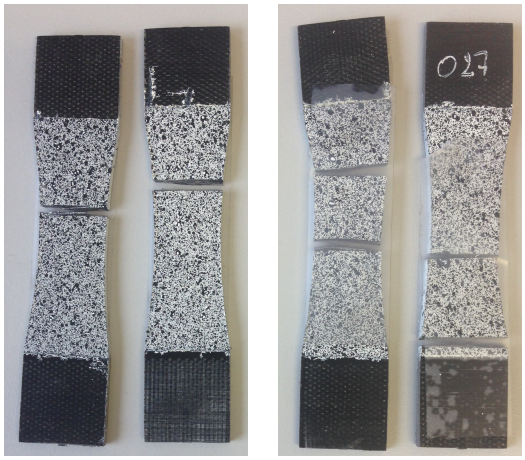

a. $v = 0.0001\,\mathrm{m\,s^{-1}}$; $\dot{\varepsilon} \approx 0.0017\,\mathrm{s^{-1}}$. *b.* $v = 15\,\mathrm{m\,s^{-1}}$; $\dot{\varepsilon} \approx 138\,\mathrm{s^{-1}}$.

Figure 5.13. Failed G/PA-6 $90°$ *UD specimens.*

5.3.2.5 Cross-ply and quasi-isotropic laminates

The addition of fibres in the transverse or $45°$-direction to a $0°$ UD composite generally increases its dependency on strain rate, albeit that the trends seen in the rate-dependency of the fibres are still mostly followed.

The C/E $[45/0/-45/90]_s$ shows no significant change in maximum stress or Young's modulus, though the failure strain shows a small decrease, see also figure 5.14. Note that the curves at the higher rate are included despite having surpassed the limit of load cell ringing, because it is the only non-quasi static result available. Some load cell ringing is thus visible in the results. The failure pattern shows no difference between low or high test speed, and is hence not included.

The stress-strain curves of G/PA-6 $[90/0]_{2s}$ are shown in figure 5.15. The laminate follows the increase in stress and strain to failure also shown by $0°$ UD. In both cases, the strain to failure increases by a factor of 1.7 over the strain rate range from about 0.001 to $60\,\mathrm{s^{-1}}$. The increase in maximum stress is by a smaller percentage for the cross-ply laminate. The increase in Young's modulus of the $0°$ UD laminate is not seen for the cross-ply laminate over the range investigated. The two central longitudinal layers of the quasi-statically tested specimens typically show overall failure like the pure $0°$ UD specimens, though the transverse layers remain largely intact, only breaking near opposite clamps, see figure 5.16a. At high rate, though, the specimen now shows a behaviour which is very different from its unidirectional counterpart (figure 5.16b): the specimens break into multiple pieces.

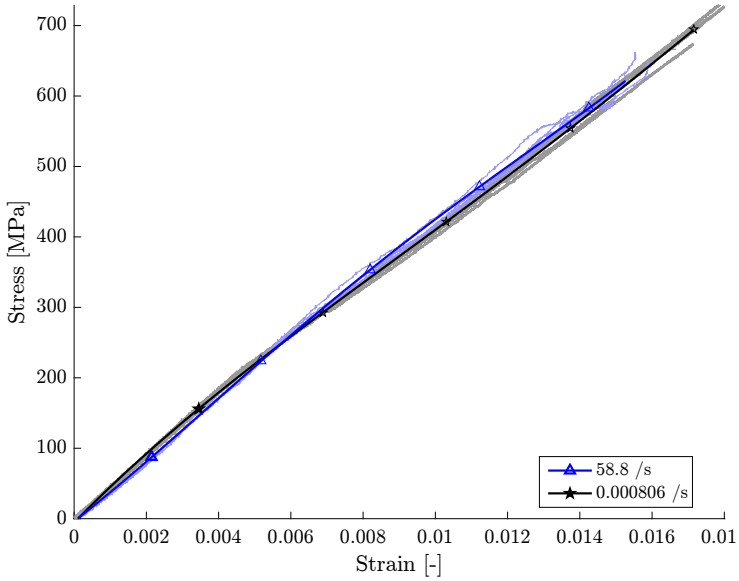

Figure 5.14. Stress-strain curves of C/E $[45/0/-45/90]_s$ *at two strain rates.*

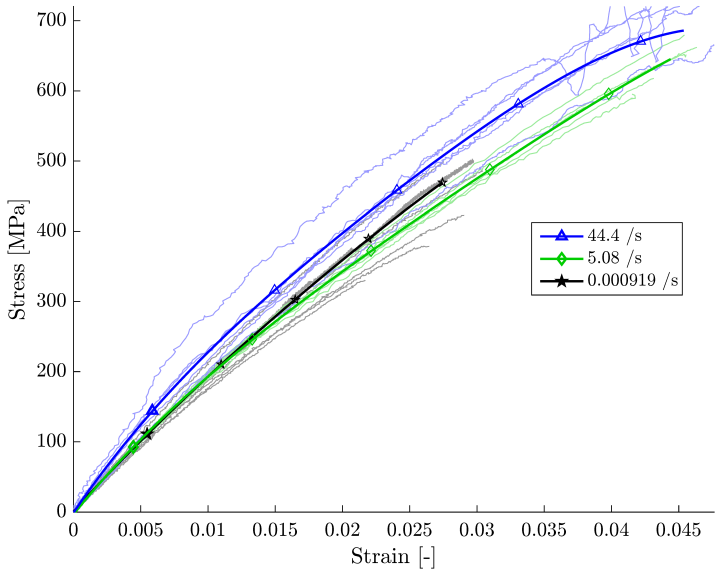

Figure 5.15. Stress-strain curves of G/PA-6 $[90/0]_{2s}$ *at various strain rates.*

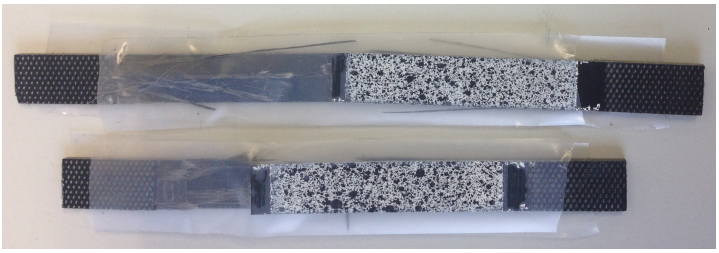

a. $v = 0.0001\,\mathrm{m\,s^{-1}}$; $\dot{\varepsilon} \approx 0.0010\,\mathrm{s^{-1}}$.

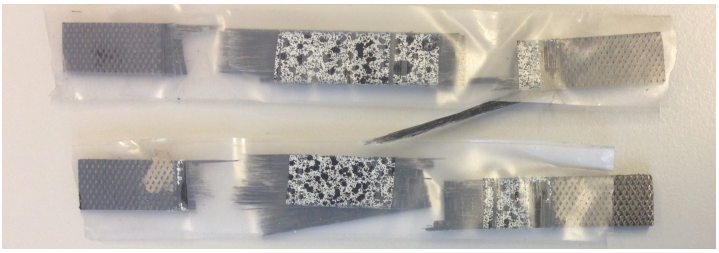

b. $v = 15\,\mathrm{m\,s^{-1}}$; $\dot{\varepsilon} \approx 120\,\mathrm{s^{-1}}$.

Figure 5.16. Failed G/PA-6 $[90/0]_{2s}$ *specimens.*

5.3.2.6 ±45 laminates

The final laminates with unidirectional plies to be treated are the ± 45-laminates.

An increase in modulus and strength is expected for balanced and symmetric angle-ply C/E composites. The strain to failure generally reduces, even though there is no full agreement in literature [21–23]. The current research indeed shows a clear increase of maximum stress and a small increase of the Young's modulus, see also figure 5.17, where the horizontal plateau of each strain rate is distinctly recognizable. The failure strain shows no significant rate-dependency. The increase in testing speed has a large impact on the (surface) damage, compare figure 5.18b to figure 5.18a. While the damage in the quasi-static case is typically confined to a small region around the location of final failure, for the specimens tested at high speed, the specimen shows cracks over its entire surface. As can be seen in the figures, the surface cracks cause the paint to chip off. The same happens to the strain gauge if a crack runs underneath it. Both cases prevent the accurate measurement of the failure strain. This is the cause of the relatively high coefficients of variation in the measured strain to failure of the ±45 materials.

G/PA-6 $[\pm 45]_{2s}$ shows no dependency on rate of its failure strain, and the Young's modulus has no clear trend. The maximum stress increases from just below $200\,\mathrm{MPa}$ at quasi-static test speed until it reaches a plateau at $0.5\,\mathrm{s^{-1}}$ at a value of about $300\,\mathrm{MPa}$ (figure 5.20). Indeed the curves at lower rate can be easily discerned in figure 5.19, while the faster tests produce results that lie closer

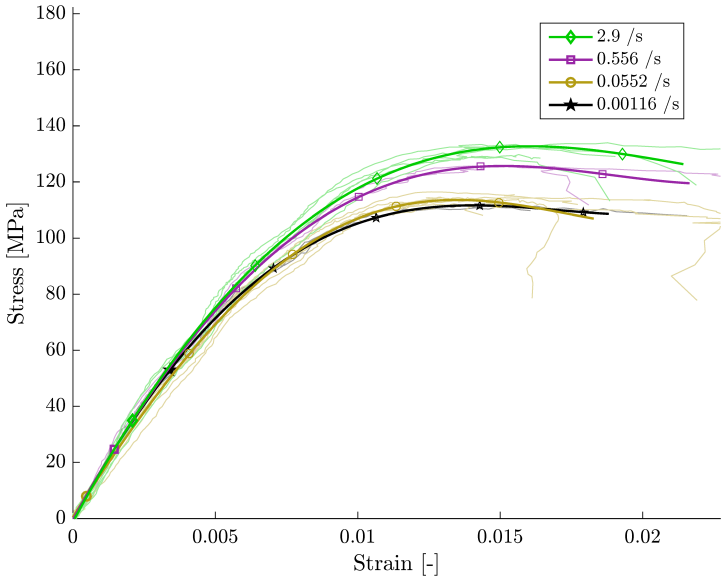

Figure 5.17. Stress-strain curves of C/E $[\pm 45]_{2s}$ *at various strain rates.*

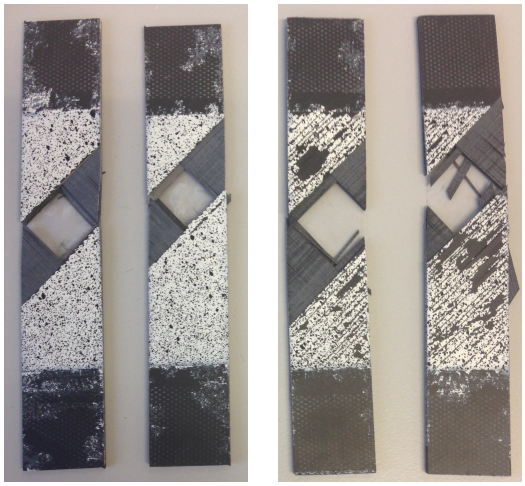

a. $v = 0.0001\,\mathrm{m\,s^{-1}}$; $\dot{\varepsilon} \approx 0.0011\,\mathrm{s^{-1}}$.

b. $v = 15\,\mathrm{m\,s^{-1}}$; $\dot{\varepsilon} \approx 176\,\mathrm{s^{-1}}$.

Figure 5.18. Failed C/E ± 45 *specimens.*

together. The only available literature treating the rate-dependency of a unidirectional angle-ply glass/thermoplastic composite shows a decrease in shear modulus, an increase in maximum shear stress and a rate-independent failure strain [24], so this reasonably matches with the current findings. No significant differences are seen in the failure patterns upon comparison of the quasi-static specimens with the dynamic ones (figure 5.21). What becomes clear from the failed specimens, though, is the serious amount of extension and lateral contraction that still remains after failure. The contraction is also clearly visible on digital image correlation (DIC) footage, compare figure 5.22a to 5.22b, where in the latter a curved edge is visible which was initially straight and just out of vision in the former. This contraction is a scissoring effect: the reorientation of the off-axis fibres towards the loading direction. The damage in the matrix causes the specimens to remain deformed after failure. Plasticity might also play a role, though the tests on pure PA-6 show that not much plasticity is to be expected for the faster tests.

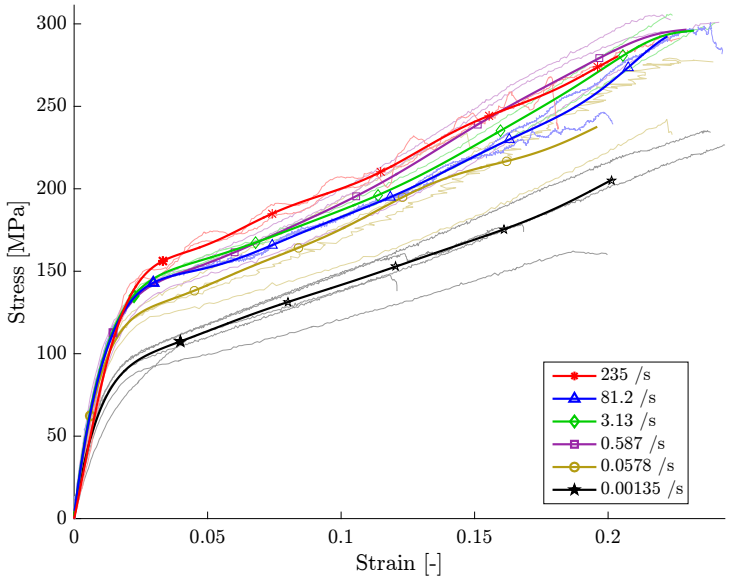

Figure 5.19. Stress-strain curves of G/PA-6 $[\pm 45]_{2s}$ *at various strain rates.*

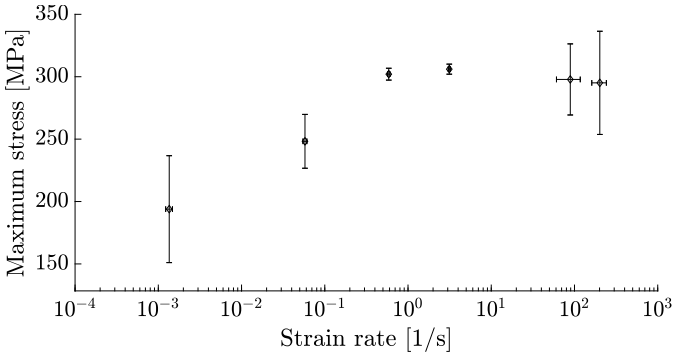

Figure 5.20. Maximum stress versus strain rate for G/PA-6 $[\pm 45]_{2s}$*. A plateau is seen in the stress from about* $0.5\,\mathrm{s}^{-1}$ *onwards.*

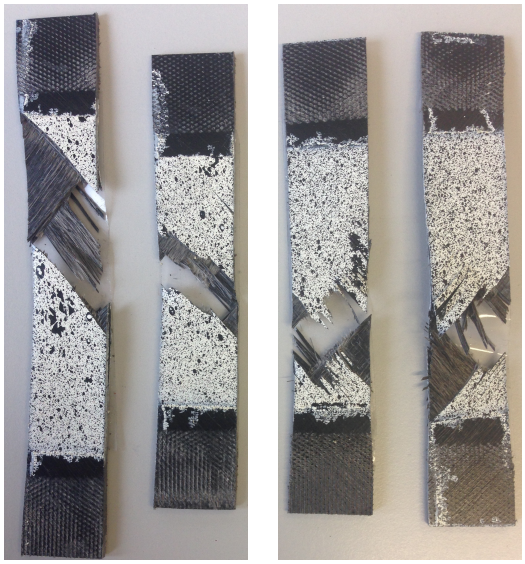

a. $v = 0.0001\,\mathrm{m\,s}^{-1}$*;* $\dot{\varepsilon} \approx 0.0013\,\mathrm{s}^{-1}$.

b. $v = 15\,\mathrm{m\,s}^{-1}$*;* $\dot{\varepsilon} \approx 194\,\mathrm{s}^{-1}$.

Figure 5.21. Failed G/PA-6 ± 45 *specimens.*

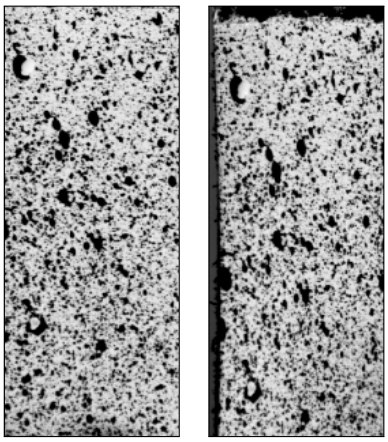

a. The initial frame. *b. A frame close to failure.*

Figure 5.22. Two DIC frames of a $v = 0.0001\,\mathrm{m\,s^{-1}}$ test on G/PA-6 ± 45 ($\dot{\varepsilon} \approx 0.0013\,\mathrm{s^{-1}}$).

5.3.3 Laminates with woven plies

The rate-dependency of woven laminates might be different from that of laminates with unidirectional plies, because of the completely different fibre architecture. The treatment is divided into two parts. First, the laminates with any proportion of fibres in the longitudinal direction are treated. Then, the results of the laminates with fibres solely in the ± 45 direction are discussed.

5.3.3.1 Laminates with fibres in the 0° direction

A small increase in maximum stress is expected for woven CP C/E laminates [25, 26]. There is no consensus in literature about the trend of the failure strain and the Young's modulus. The cause for the lack of consensus is perhaps the independency on rate of the mechanical properties as found in the current research for any of the woven C/E laminates with fibres in the $0°$-direction. Looking at e.g. C/E $[\#(0/90)]_{4s}$ in figure 5.23 it can be seen that the curves lie on top of each other. The same counts for the $90°$ direction of this laminate or the QI variant. Those results are, therefore, only given in the appendix. The stress-strain curves at all speeds show the same increase in Young's modulus with increasing strain, which is attributed to a fibre stiffening effect present in the $0°$ carbon fibres [27]. Images of specimens after failure are given in figure 5.24. The tests at $15\,\mathrm{m\,s^{-1}}$ result in more paint falling off, which suggest that more energy was released upon fracture. Moreover, the fast tests result in the appearance of multiple cracks, a phenomenon

seen in many of the dynamically tested specimens. The rate-dependency of these woven laminates seems to be dominated by the fibre behaviour in longitudinal direction, which is also characterised by an absence of rate dependency.

The stress-strain curves for woven G/PA-6 laminates with fibres in the 0°-direction do not clearly display the trends seen for the mechanical properties. As an example, the stress-strain curves for woven G/PA-6 QI are included in figure 5.25, the others are given only in the appendix. Plots of the properties versus rate for stress, strain and modulus are shown for woven G/PA-6 QI in figures 5.26, 5.27 and 5.28 respectively. The trends in these plots are representative for all three woven G/PA-6 laminates with fibres in the 0°-direction. These plots clearly show that the failure strain and maximum stress follow the trends of the dry fibre: they both increase with rate, although the change is far smaller. The same is seen in literature [28], also for glass/polypropylene [29, 30]. No rate-dependency was measured for the Young's modulus, while the literature suggests a small increase [28]. The found trends are very comparable to those of the UD-layered G/PA-6 CP laminate described in section 5.3.2.

Comparing the warp and weft directions of the woven CP laminates of both material systems, a small (sometimes insignificant) reduction in material properties is seen when the material is tested in the weft rather than the warp direction.

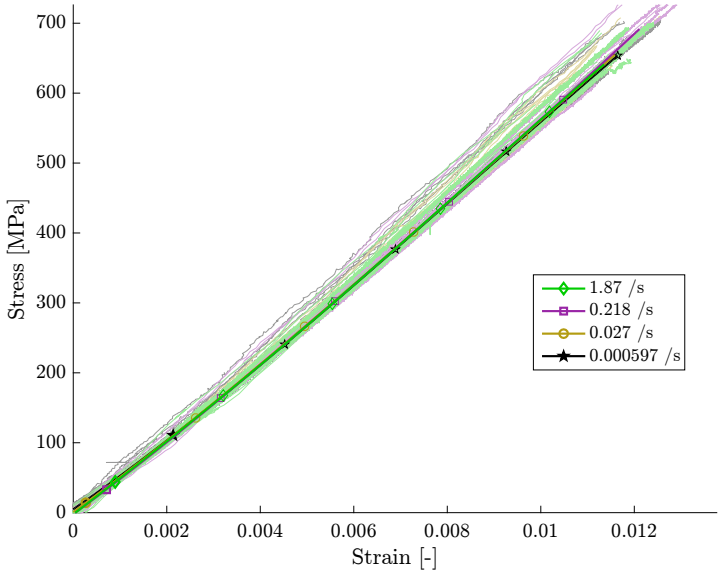

Figure 5.23. Stress-strain curves of C/E $[\#(0/90)]_{4s}$ *at various strain rates.*

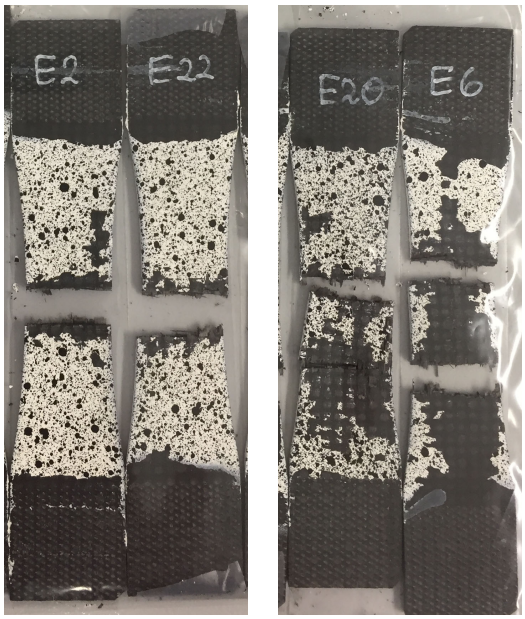

a. $v = 0.0001\,\mathrm{m\,s^{-1}}$; $\dot{\varepsilon} \approx 0.0006\,\mathrm{s^{-1}}$. *b.* $v = 15\,\mathrm{m\,s^{-1}}$; $\dot{\varepsilon} \approx 155\,\mathrm{s^{-1}}$.

Figure 5.24. Failed C/E $[\#(0/90)]_{4s}$ *specimens.*

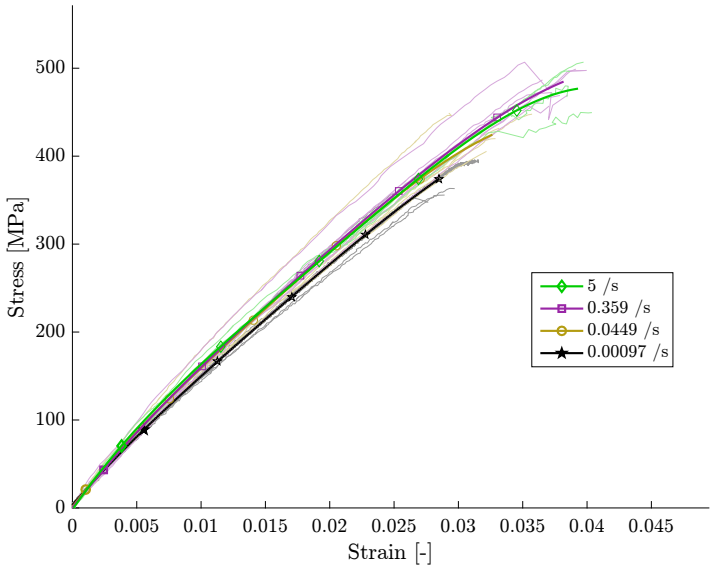

Figure 5.25. Stress-strain curves of G/PA-6 $[\#(\pm 45)/\#(0/90)]_s$ *at various strain rates.*

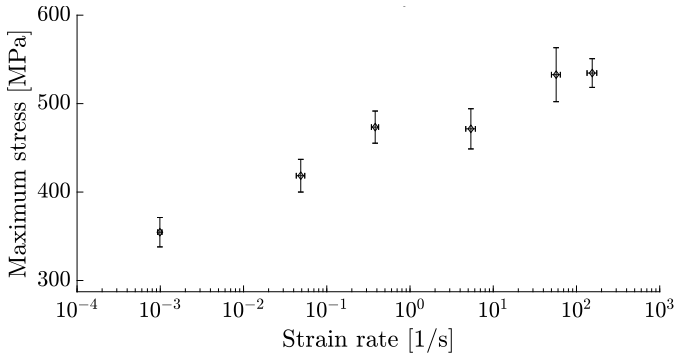

Figure 5.26. Maximum stress versus strain rate for G/PA-6 $[\#(\pm 45)/\#(0/90)]_s$*. The values increase with rate.*

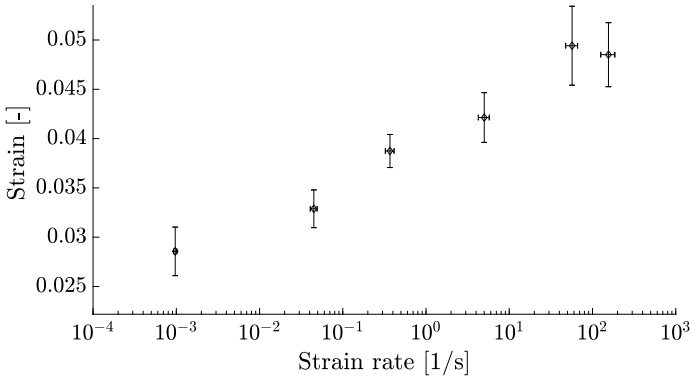

Figure 5.27. Maximum strain versus strain rate for G/PA-6 $[\#(\pm 45)/\#(0/90)]_s$*. The values increase with rate.*

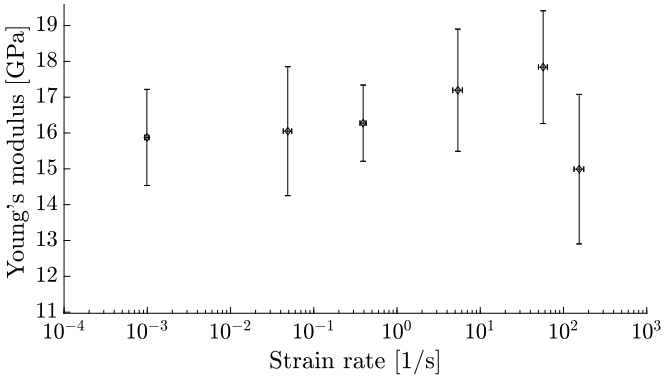

Figure 5.28. Young's modulus versus strain rate for G/PA-6 $[\#(\pm 45)/\#(0/90)]_s$*. No rate-dependency is seen.*

a. $v = 0.0001\,\mathrm{m\,s^{-1}}$; $\dot{\varepsilon} \approx 0.0010\,\mathrm{s^{-1}}$.

b. $v = 15\,\mathrm{m\,s^{-1}}$; $\dot{\varepsilon} \approx 155\,\mathrm{s^{-1}}$.

Figure 5.29. Failed G/PA-6 $[\#(\pm 45)/\#(0/90)]_s$ *specimens.*

5.3.3.2 Laminates with all fibres in the ±45 direction

The $\#(\pm 45)$-laminates show significant rate-dependency again, as their behaviour is largely matrix-dominated.

The maximum stress of C/E $[\#(\pm 45)]_{4s}$ shows an increase with rate, which is seen in the literature as well [26, 31]. It is also suggested that the modulus shows an increase with strain rate [26], but in the current test programme this increase is hardly significant. Not all literature agrees, though the strain to failure is generally seen to reduce with strain rate [26, 31]. In the current research also a decrease is seen, though the error on the measurement is again large due to the formation of surface cracks in a manner similar to the UD-layered ± 45 laminates in section 5.3.2.6, see also figure 5.31. The same difference as mostly seen above exists between the quasi-static and the dynamic tests: the failure of the latter ones was more violent as more paint has fallen off.

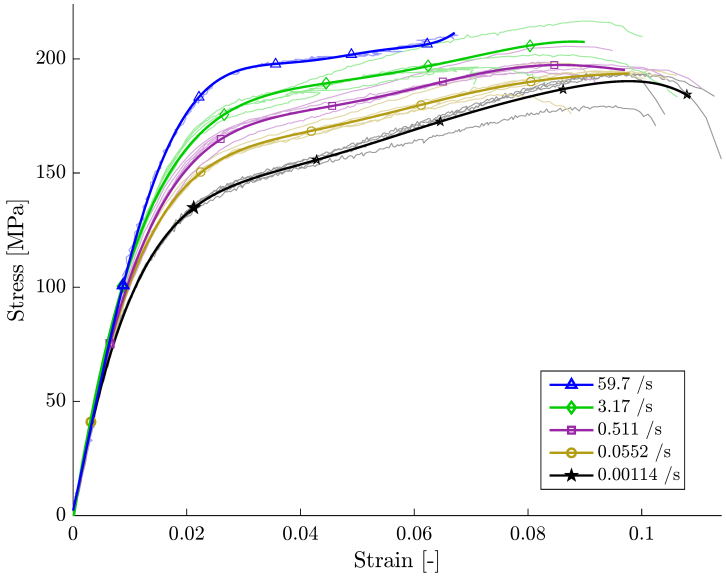

Figure 5.30. Stress-strain curves of C/E $[\#(\pm 45)]_{4s}$ *at various strain rates.*

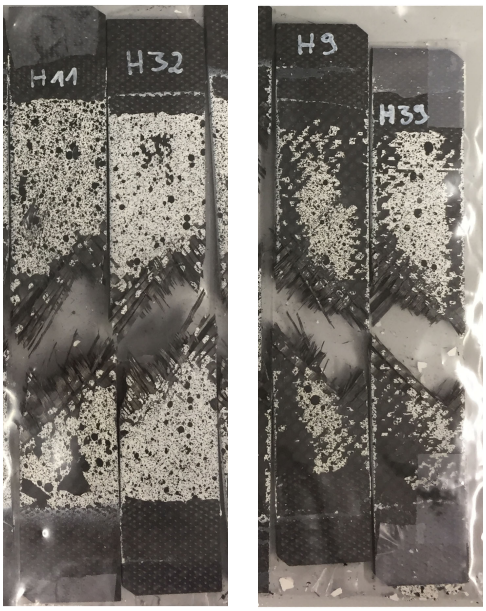

a. $v = 0.0001\,\mathrm{m\,s^{-1}}$; $\dot{\varepsilon} \approx 0.0012\,\mathrm{s^{-1}}$.

b. $v = 15\,\mathrm{m\,s^{-1}}$; $\dot{\varepsilon} \approx 191\,\mathrm{s^{-1}}$.

Figure 5.31. Failed C/E $[\#(\pm 45)]_{4s}$ *specimens.*

For G/PA-6 $[\#(\pm 45)]_{2s}$ (figure 5.32), the maximum stress and Young's modulus increase with increasing strain-rate, while the strain to failure shows no significant trend and the failure pattern, apart from a different amount of paint that remains on the specimens, remains the same (figure 5.33). This contradicts the behaviour of glass/polypropylene where typically a decrease in modulus and strain to failure is seen, and no clear trend for the maximum stress [29, 30]. However, this does not invalidate the current results, because polypropylene and PA-6 could behave significantly different, even though they both belong to the category of thermoplastics. No papers could be found in literature discussing the shear properties of a woven G/PA-6 composite.

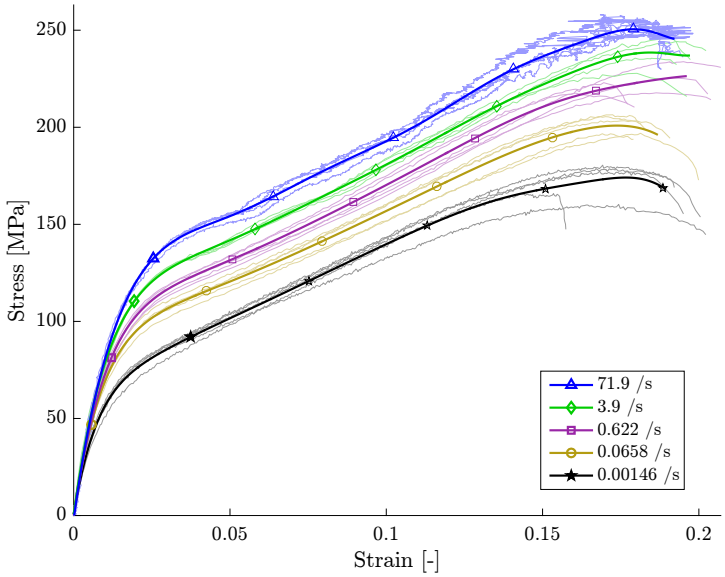

Figure 5.32. Stress-strain curves of G/PA-6 $[\#(\pm 45)]_{2s}$ *at various strain rates.*

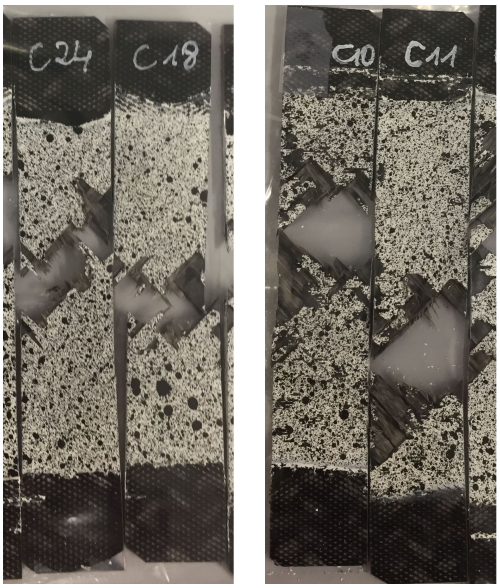

a. $v = 0.0001\,\mathrm{m\,s^{-1}}$; $\dot{\varepsilon} \approx 0.0015\,\mathrm{s^{-1}}$.

b. $v = 15\,\mathrm{m\,s^{-1}}$; $\dot{\varepsilon} \approx 205\,\mathrm{s^{-1}}$.

Figure 5.33. Failed G/PA-6 $[\#(\pm 45)]_{2s}$ *specimens.*

5.4 Conclusion

A large dynamic tensile testing campaign has been performed. 475 tests have been executed to investigate the stress-strain response of a variety of laminates at six speeds for two very distinct material systems. The results are all presented versus the actually measured strain rate. Nowhere in literature is such a large and consistent data set available in literature, especially for glass/polyamide-6 composites, for which there are practically no dynamic data available, even though the material system is gaining more interest for applications in the automotive industry. Great care was taken to include only valid results in the discussion, meaning that no dynamic effects are influencing the results (as discussed in chapter 4), and to inform the reader where the results should be interpreted with caution. This typically resulted in four remaining sets of stress-strain curves per laminate.

The strongest rate-dependency is seen in the pure polymers. No rate-dependency is seen in the literature for carbon fibres, and this makes the overall dependency on test speed of any fibre-dominated laminate of carbon/epoxy practically absent. The $0°$ unidirectional glass/polyamide-6 shows an expected clear rate-dependency which propagates into the other laminates, though the percentile change with rate is reduced. The macroscopic rate-dependency of woven composites with cross-

ply or quasi-isotropic lay-ups mostly follow the behaviour of the $0°$ unidirectional laminates (or fibres) of the same material system, albeit at that the differences become even smaller. For laminates with fibres only oriented in the ± 45 directions, woven or unidirectional, the rate-dependency is strongest on maximum stress and Young's modulus: the stress-strain curves appear to be 'pulled upwards.'

In most cases the fracture surfaces look alike, though the dynamically tested specimens often have multiple cracks and more paint has fallen off, indicating a more violent rupture.

References

[1] ASTM International. *ASTM Standard D3039, 2008, "Standard Test Method for Tensile Properties of Polymer Matrix Composites"*. Technical report, American Society for Testing and Materials, West Conshohocken, PA, 2008.

[2] S. R. Raisch and B. Möginger. *High rate tensile tests – Measuring equipment and evaluation*. Polymer Testing, 29(2):265–272, April 2010.

[3] J. Kwon, J. Choi, H. Huh, and J. Lee. *Evaluation of the effect of the strain rate on the tensile properties of carbon–epoxy composite laminates*. Journal of Composite Materials, page 0021998316683439, December 2016.

[4] International Organization for Standardization. *ISO 26203-1:2010. Metallic materials – Tensile testing at high strain rates – Part 1: Elastic-bar-type systems. German version DIN EN ISO 26203-1:2010.* Technical report, International Organization for Standardization, 2010.

[5] SAE International. *SAE J2749, 2017, "Surface vehicle recommended practise - high strain rate testing of polymers"*. Technical report, Society of Automotive Engineers, 400 Commonwealth Drive, Warrendale, PA 15096, July 2017.

[6] D. R. Hufner and S. I. Hill. *High strain rate testing and modeling of a woven E-glass–vinylester composite in dry and saturated conditions*. Journal of Composite Materials, 51(21):3017 – 3039, 2017.

[7] M. M. Shokrieh and M. J. Omidi. *Tension behavior of unidirectional glass/epoxy composites under different strain rates*. Composite Structures, 88(4):595–601, May 2009.

[8] A. Gilat, R. K. Goldberg, and G. D. Roberts. *Strain Rate Sensitivity of Epoxy Resin in Tensile and Shear Loading*. Technical report, National Aeronautics and Space Administration (NASA), March 2005.

[9] G. Shan, W. Yang, M.-b. Yang, B.-h. Xie, J.-m. Feng, and Q. Fu. *Effect of temperature and strain rate on the tensile deformation of polyamide 6*. Polymer, 48(10):2958–2968, May 2007.

[10] I. Benaceur, R. Othman, P. Guegan, A. Dhieb, and F. Damek. *Sensitivity of the flow stress of nylon 6 and nylon 66 to strain-rate*. International Journal of Modern Physics B, 22(09n11):1249–1254, April 2008.

[11] BASF. *CAMPUS datasheet - Ultramid B3S - PA6*. Technical report, Chemie Wirtshaftsfoerderungsgesellschaft GmbH, Frankfurt, July 2015.

[12] Y. Zhou, Y. Wang, Y. Xia, and S. Jeelani. *Tensile behavior of carbon fiber bundles at different strain rates*. Materials Letters, 64(3):246–248, February 2010.

[13] Z. Wang and Y. Xia. *Experimental evaluation of the strength distribution of fibers under high strain rates by bimodal Weibull distribution*. Composites Science and Technology, 57(12):1599–1607, January 1998.

[14] N. Taniguchi, T. Nishiwaki, and H. Kawada. *Tensile strength of unidirectional CFRP laminate under high strain rate*. Advanced Composite Materials, 16(2):167–180, January 2007.

[15] I. M. Daniel. *High strain rate properties of unidirectional composites, part 1*. Contractor Report 189083, National Aeronautics and Space Administration (NASA), December 1991.

[16] J. Fitoussi, M. Bocquet, and F. Meraghni. *Effect of the matrix behavior on the damage of ethylene–propylene glass fiber reinforced composite subjected to high strain rate tension*. Composites Part B: Engineering, 45(1):1181–1191, February 2013.

[17] S. Duan, X. Yang, and Y. Tao. *Experimental study on strain-rate-dependent behavior and failure modes of long glass fiber-reinforced polypropylene composite*. Journal of Reinforced Plastics and Composites, 34(15):1261–1270, August 2015.

[18] I. M. Daniel and T. Liber. *Strain rate effects on mechanical properties of fiber composites, part 3*. Technical report, National Aeronautics and Space Administration (NASA), June 1976.

[19] Pyrofil Department. *Mechanical Properties of PYROFIL Unidirectional Composite - TR 360E250S*. Technical report, Mitsubishi Rayon Co., Ltd., Carbon Fiber and Composite Materials Division, December 2013.

[20] M. Nikforooz, J. Montesano, M. Golzar, and M. Shokrieh. *Assessment of the thermomechanical performance of continuous glass fiber-reinforced thermoplastic laminates*. Polymer Testing, February 2018.

[21] H. Koerber, J. Xavier, and P. P. Camanho. *High strain rate characterisation of unidirectional carbon-epoxy IM7-8552 in transverse compression and in-plane shear using digital image correlation*. Mechanics of Materials, 42(11):1004–1019, November 2010.

[22] I. M. Daniel. *High strain rate properties of off-axis composite laminates, part 2*. Contractor Report 189084, National Aeronautics and Space Administration (NASA), December 1991.

[23] I. M. Daniel. *High strain rate properties of angle-ply composite laminates, part 3 (Final Report)*. Contractor Report 189085, National Aeronautics and Space Administration (NASA), 1991.

[24] N. Papadakis, N. Reynolds, M. W. Pharaoh, P. K. C. Wood, and G. F. Smith. *Strain rate effects on the shear mechanical properties of a highly oriented thermoplastic composite material using a contacting displacement measurement methodology–Part A: elasticity and shear strength*. Composites Science and Technology, 64(5):729–738, April 2004.

[25] R. Foroutan, J. Nemes, H. Ghiasi, and P. Hubert. *Experimental investigation of high strain-rate behaviour of fabric composites*. Composite Structures, 106:264–269, December 2013.

[26] J. P. Hou and C. Ruiz. *Measurement of the properties of woven CFRP T300/914 at different strain rates*. Composites Science and Technology, 60(15):2829–2834, November 2000.

[27] W. van Dreumel and J. Kamp. *Non hookean behaviour in the fibre direction of carbonfibre composites and the influence of fibre waviness on the tensile properties*. Technical Report LR- 251, Delft University of Technology - Department of Aerospace Engineering, Delft, The Netherlands, July 1977.

[28] M. Todo, K. Takahashi, P. Béguelin, and H. H. Kausch. *Strain-rate dependence of the tensile fracture behaviour of woven-cloth reinforced polyamide composites*. Composites Science and Technology, 60(5):763–771, April 2000.

[29] B. Bonnet. *Comportement au choc de matériaux composites pour applications automobiles*. PhD thesis, École Nationale Supérieure des Mines de Paris, 2005.

[30] K. A. Brown, R. Brooks, and N. A. Warrior. *The static and high strain rate behaviour of a commingled E-glass/polypropylene woven fabric composite*. Composites Science and Technology, 70(2):272–283, February 2010.

[31] J. Fitoussi, F. Meraghni, Z. Jendli, G. Hug, and D. Baptiste. *Experimental methodology for high strain-rates tensile behaviour analysis of polymer matrix composites*. Composites Science and Technology, 65(14):2174–2188, November 2005.

6

Dynamic mode-I delamination testing

6.1 Introduction

To study the effect of loading rate on the delamination properties of composites, a new set-up needs to be designed, because no test standard exists for delamination at non-quasi-static speeds. As mentioned in chapter 2, two set-ups are evaluated. The first is a drop tower method where the load is measured optically to remove the influence of load cell ringing typically seen in experiments at higher speeds (see also chapter 4 or reference [1]). The most important downside of using the drop tower is the limited range of velocities that can be tested, which covers neither the quasi-static regime nor is it fast enough to approach the required upper limit. The second method applied is by use of a hydraulic pulse test bench, which can test the full range of velocities needed, though relying on a load cell to measure the load.

Chapter 1 shortly explains the different delamination modes, and as mentioned there, only mode-I delamination is treated. Details of the experimental equipment and material can be found in chapters 2 and 3, respectively. The two test methods for dynamic delamination are described and analysed in this chapter, along with a treatment of data reduction method. An explanation of the test campaign and a presentation of the results follows in chapter 7.

6.2 Materials

As is the case for the other test programmes, two material systems are investigated in both a unidirectional (UD) and a woven configuration: carbon/epoxy (C/E) and glass/polyamide-6 (G/PA-6).

For C/E, laminates of 330 by $330\,\mathrm{mm}$ are manufactured by the supplier in an autoclave. A $13\,\mu\mathrm{m}$ thick Fluon® ETFE film by Asahi Glass Co., Ltd. is inserted in the midplane during laminate build-up to serve as a precrack. It covers an area of 330 by $100\,\mathrm{mm}$ on one side of the laminate, creating a local stacking sequence of $[0_9/\mathrm{ETFE}/0_9]$ for UD or $[\#(0/90)_9/\mathrm{ETFE}/\#(90/0)_9]$ for the woven variant, both with a thickness of about $4.1\,\mathrm{mm}$, or $2.05\,\mathrm{mm}$ per leg, within the bounds set in the ASTM test standard for mode-I delamination of composite laminates [2]. Typically PTFE would be chosen over ETFE because the latter shows more chemical interaction with resins and a higher friction coefficient. The difference becomes apparent when testing for mode-II delamination [3], where friction plays a large role in the energy dissipation. However, it is assumed that for mode-I delamination, the choice of insert material hardly affects the results as the insert remains completely separated from one of the crack faces after initiation.

The G/PA-6 material is manufactured using the hot pressing technique. Due to the elevated production temperature compared to the C/E, ETFE is no longer suitable. A polyimide film with a thickness of $12.7\,\mu\mathrm{m}$ is therefore used instead. The plates have a dimension of 500 by $500\,\mathrm{mm}$ and a central insert of 200 by $500\,\mathrm{mm}$ is placed at the midplane of the laminate, creating a local layup of $[0_8/\mathrm{polyimide}/0_8]$ for UD or $[\#(0/90)_4/\mathrm{polyimide}/\#(90/0)_4]$ for the woven variant. Both laminates have a total thickness of about $4\,\mathrm{mm}$, or $2\,\mathrm{mm}$ per leg. This is the maximum thickness that could be produced by the supplier. The position of the insert allows the extraction of two rows of specimens with a single-sided delamination from one plate.

The combination of relatively low flexural modulus and high expected fracture toughness of G/PA-6 makes that a thicker laminate would likely be more suitable [2]. Values of about 3000 to $4000\,\mathrm{J\,m^{-2}}$ have been measured for the quasi-static mode-I fracture toughness of a unidirectional G/PA-12 laminate [4]. A fracture toughness of $3000\,\mathrm{J\,m^{-2}}$ is assumed for the woven G/PA-6 of the current research. Using the in-plane stiffness of $21\,\mathrm{GPa}$ from the data sheet and an initial crack length of $50\,\mathrm{mm}$, the advised total laminate thickness can be computed using [2]:

$$h > 8.28\left(\frac{G_{\mathrm{Ic}}a_0^2}{E_{11}}\right)^{1/3} = 8.28\left(\frac{3000\cdot 0.050^2}{21\cdot 10^9}\right)^{1/3} = 5.97\,\mathrm{mm} \tag{6.1}$$

As the used material thickness lies beneath this value, the specimens will likely show too much bending deformation during the tests.

6.3 Quasi-static mode-I delamination

Quasi-static delamination tests are carried out according to the ASTM D5528 test standard [2]. They are done using a screw-driven test bench for the drop tower test series as the drop tower cannot perform tests at quasi-static speeds. When using the hydraulic pulse machine, it is simply actuated at a low velocity to perform the quasi-static tests.

The data acquisition consists of a recording of load, displacement, and footage of the side of the specimen. The specimen is equipped with a scale to allow extraction of the crack length. The determination of the crack length is performed manually by looking at the recorded frames. Typical specimen dimensions are given in figure 6.1.

Data reduction is done as is advised by the test standard. The modified beam theory (MBT) is applied, because it is found to be the most conservative of the three methods suggested in the standard [2]. Using this theory, the mode-I energy release rate can be calculated using:

$$G_{\mathrm{I}} = \frac{3P\delta}{2b\,(a + |\Delta|)} \tag{6.2}$$

where P is the applied load, δ the corresponding displacement, b the width of the specimen and a the delamination length. Δ is determined by plotting the cube root of the compliance δ/P versus the crack length. Its value equals the value of a at which the linear least squares fit crosses the abscissa (i.e. at zero compliance). This added crack length compensates for the fact that the condition at the crack tip is not a perfect clamp.

Preliminary quasi-static delamination tests were performed on woven C/E using a electromechanical test bench to obtain values for the fracture toughness that can be used in a FE-model. The R-curves of these tests are shown in figure 6.2. The average plateau value for the energy release rate amounts to $292\,\mathrm{J\,m^{-2}}$, which lies close to the definitively obtained value given in section 7.3.1. The crack propagation is not perfectly smooth. If only the peak values are used to calculate the fracture toughness G_{Ic}, a value of $314\,\mathrm{J\,m^{-2}}$ is obtained.

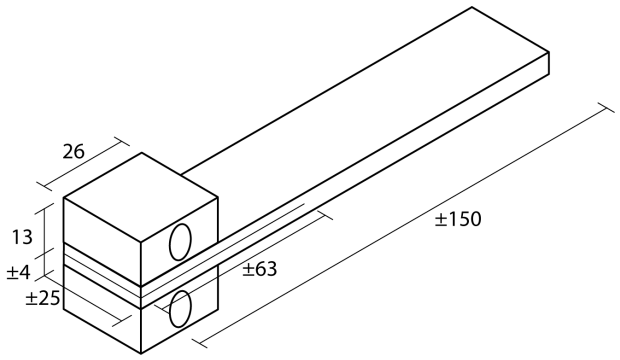

Figure 6.1. Typical specimen dimensions for the (dynamic) delamination test campaigns.

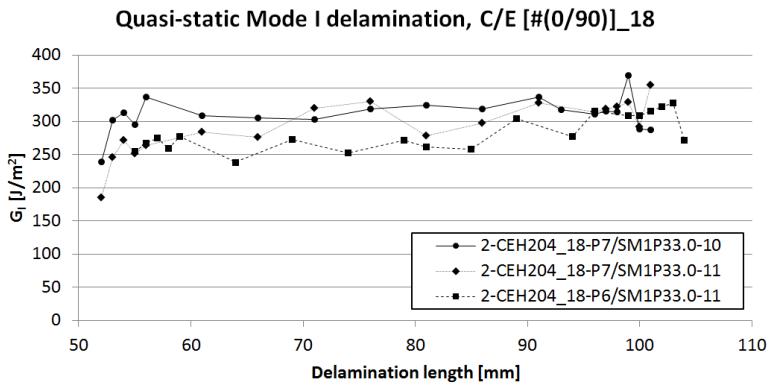

Figure 6.2. R-curves obtained with the modified beam theory from preliminary tests on C/E $[\#(0/90)]_{18}$ *tested at* $0.000033\,\mathrm{m\,s^{-1}}$.

6.4 Mode-I delamination using a drop tower

The use of a drop tower implies that some adaptation is needed to transform the normally compressive load applied by the dead weight to a tensile load that pulls two parts of a composite laminate apart. At higher excitation velocities, a low mass of moving parts is usually recommended, leading to a need for small structures. The compliance in large, light structures would namely lead to oscillations in load introduction [5]. Other researchers who delaminate composites using a drop tower, lead the load around the specimen [1, 6]. To this end, Navarro et al. designed a sliding structure which is attached to both sides of a DCB specimen onto which an impactor falls to induce a tensile failure, see figure 6.3a. The structure is straightforward to use as the impactor simply falls on top of it. The moving part of the structure is to be upheld by the interface alone. This results in a structure which needs to be both light and relatively large to accommodate for the displacement, reducing the frequency of the lowest natural vibrational mode. Colin De Verdiere et al. attached a part to the drop-weight that impacts on both ends of an axis which protrudes the bottom block and the support structure (figure 6.3b). This alleviates the need for a light loading structure, as it forms part of the drop-weight. It comes at the cost, though, of a more stringent alignment because the orientation should align with the impactor as well now, rather than only the position. The risk of an asymmetric loading also increases when the load is introduced in multiple points.

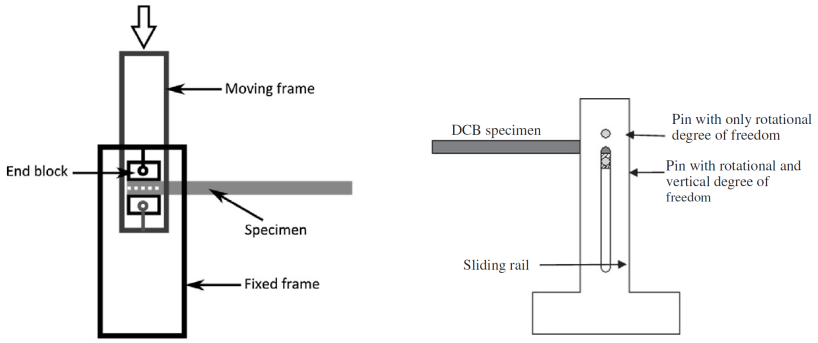

a. A moveable structure is attached to the bottom block. [6]

b. An impactor-mounted part hits the extended axis of the bottom block. [1]

Figure 6.3. Two concepts for dynamic delamination in a drop tower.

6.4.1 Test set-up details

For the current research, a set-up is designed which combines the strong points of both aforementioned concepts. It is chosen to perform the load introduction

through the composite specimen with a slender pin (figure 6.4) rather than around it. This choice comes with the obvious drawback that it is required to make a hole in the specimen and the top block, see also figure 6.6. This layout, however, has the advantages that (1) it is very compact with no stringent requirement on mass except for the load blocks only, (2) the set-up can be rotated horizontally to any position to accommodate the optical acquisition because (3) the load introduction is in one location. The complete set-up is displayed in figure 6.5.

The top block rests in a support structure and can rotate around its axis, the bottom block is left completely free to move to avoid any influence of friction. A small screw touches the front surface of the bottom block in its initial position to ensure that the specimen is horizontal before impact. A small axis is inserted in the bottom block to ensure the loading is vertical despite of inevitable small misalignments at impact. It is held in place by two small screws. The axis is hardened to reduce the wear of multiple impacts of the pin, and it can be replaced if this wear would become too severe. A test is performed by letting the drop-weight fall down to acquire the requested velocity. The slender hardened steel pin will hit the axis of the bottom block, which on its turn will fly downwards after only a short acceleration, delaminating the specimen along the way only by its inertia, as it is no longer in contact with the impactor, see also to the right of figure 6.6. It is decided to omit the vertical guidance as seen in figure 6.3b. Removing this restraint will cause the trajectory of the bottom block to be curved in the direction of the specimen, because the specimen is only on one side of the bottom block, though it has the advantage that there are no (unknown) friction forces between the bottom block and a vertical guidance system. The force between the bottom block and the specimen is to be obtained optically, as explained below. Foam blocks are placed on top of the support structure to decelerate the impactor towards a standstill after the bottom block has been launched away. The design allows the use of specimen outer dimensions which follow the ASTM standard for mode-I delamination testing [2]. The typical specimen dimensions are given in figure 6.1.

Specimens of 150 by $25\,\mathrm{mm}$ are cut from the plates using waterjet cutting with a $0.3\,\mathrm{mm}$ cutting radius, with an overlap of $60\,\mathrm{mm}$ with the insert, see also figure 6.7. A capsule-shaped cutout with a radius of $6.5\,\mathrm{mm}$ and a length of $17\,\mathrm{mm}$ is made using the same method to accommodate for the penetration of the hardened steel impactor pin which has a diameter of $9\,\mathrm{mm}$.

The loading blocks are milled from stainless steel according to the drawings shown in figure 6.8. The blocks are 26 by 25 by $13\,\mathrm{mm}$. They are adhered to the specimens using a Loctite® 480™ rubber-toughened cyanoacrylate adhesive.

The side of the specimens is sprayed white using a general-purpose matte white paint spray to allow for a clear crack tip observation and a millimetre scale is adhered to the same side without covering the midplane.

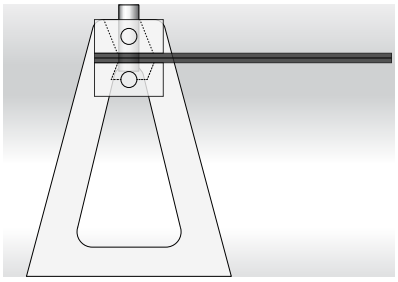

a. A slender pin is attached to the impactor, which can move through the supported top block and the specimen.

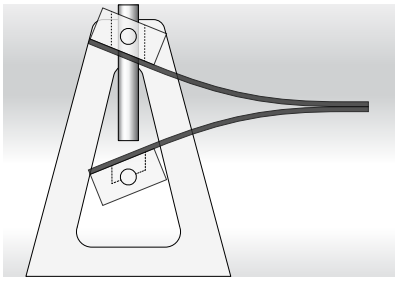

b. The pin hits an axis in the bottom block, taking it down, delaminating the specimen.

Figure 6.4. The current concept for dynamic delamination in a drop tower.

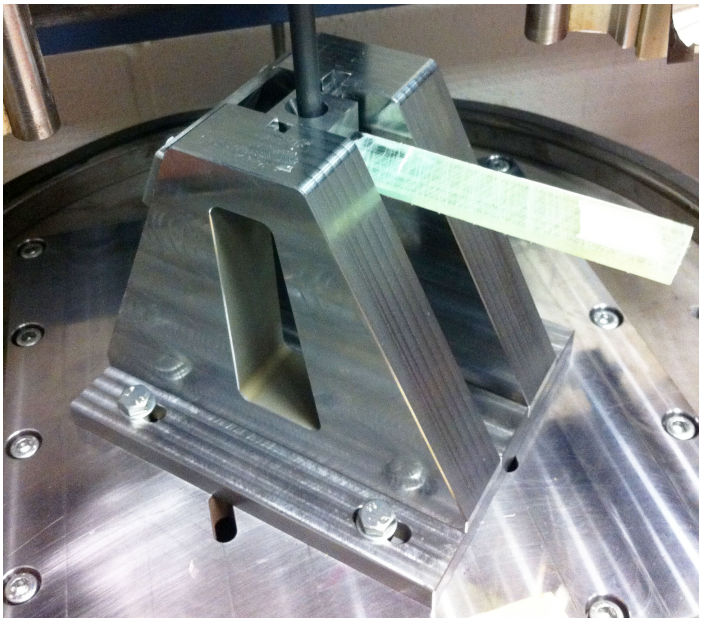

Figure 6.5. The dynamic delamination test set-up with a glass/epoxy test specimen.

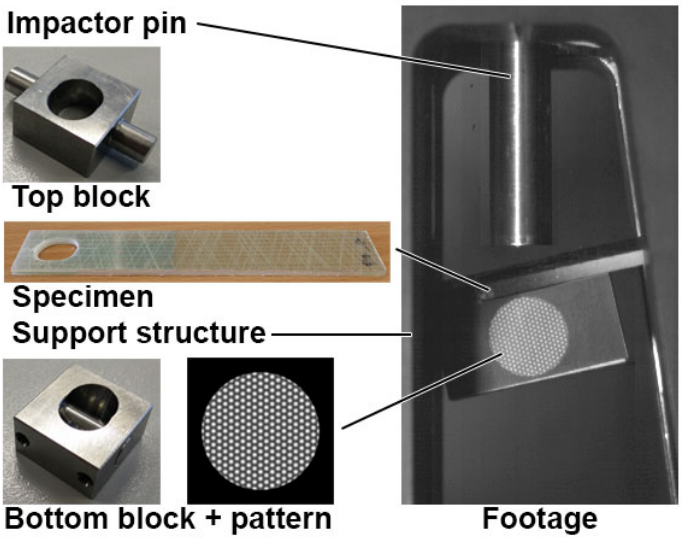

Figure 6.6. Test set-up parts and footage.

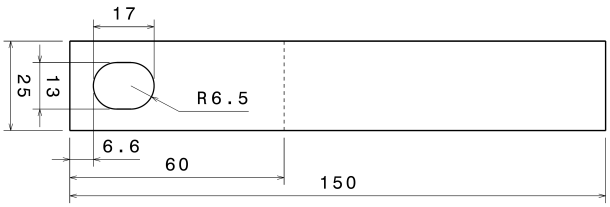

Figure 6.7. Top view of the delamination specimen with dimensions.

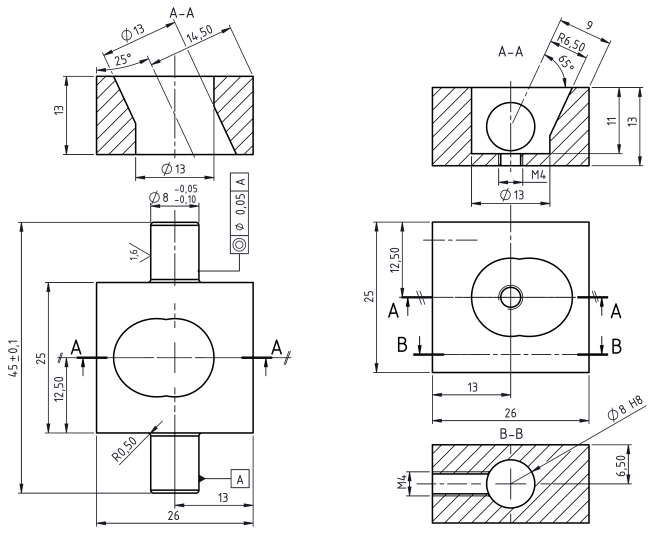

a. The top block. *b. The bottom block.*

Figure 6.8. The loading blocks used in the dynamic delamination concept.

6.4.2 Data acquisition

Data acquisition using the load cell on the falling impactor to which the pin is attached is not expected to produce satisfactory results because of two reasons. First, there is inherent noise when the force is measured this way [1] and second, there is no contact between the impactor pin and the bottom block when the crack propagates. A contactless optical tracking method is therefore applied for the bottom block, which allows the bottom block to be free of restraint. A Photron SA-4 high speed camera records the bottom block, which has been equipped with a pattern of line gratings in a circular shape, see also figure 6.5. The images of the bottom block are processed by an in-house developed software which tracks the circular shape. The images are further processed by a fast-Fourier transform in the spatial domain. The wavelength and orientation of the individual line gratings in the pattern are obtained by finding the corresponding peaks in the transformed image. Subsequently, the change in phase of the gratings between images is used to determine the displacement, making use of the pitch of each grating as measured by the user. The process results in an accurate determination of the in-plane position and rotation from the recorded high-speed footage. The tracking method and data reduction are explained in more detail by Allaeys [7]. Velocities and accelerations can be obtained by differentiation of the results. The load on the bottom leg of the specimen is to be retrieved from the acceleration of the bottom block via a multiplication with its mass. Typical test results are shown in figure 6.9, showing the

displacement and acceleration components for the bottom block during a test.

A second pattern of line gratings is attached to the impactor for an accurate determination of its position and velocity. This, too, is recorded using a Photron SA-4 high speed camera. The load is recorded by a Gen5i digital oscilloscope merely to trigger the cameras to record at the right moment.

The crack length is determined from the footage of the side of the specimen. A challenge lies in the fact that the resolution is rather limited because the required frame rate should be high enough to capture a fast-growing delamination (figure 6.10). Several different techniques have been applied to (automatically) extract the crack length, see figure 6.11. Each of the methods is explained below. Alternatively, crack gauges can be applied to the side of the specimens, which consist of a row of thin wires connected to a common terminal on either side. The crack should pass through these wires, breaking them in the process as they are entirely

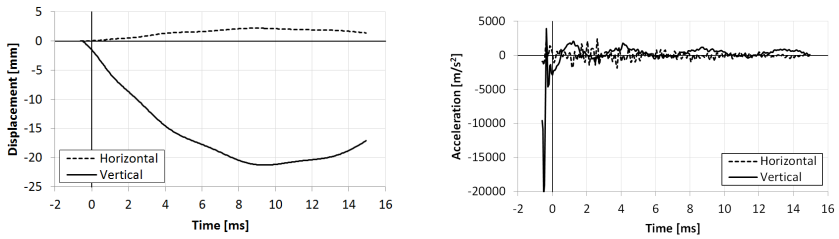

a *b*

Figure 6.9. Typical displacements (a) and accelerations (b) in horizontal and vertical direction.

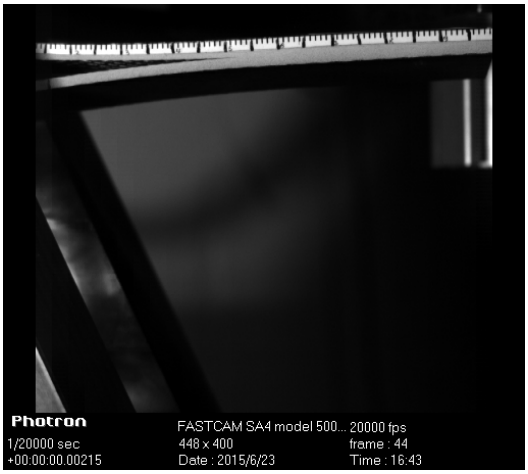

Figure 6.10. Side view of the delamination specimen during drop-weight impact testing.

adhered to the specimen. It remains questionable whether the energy required to break these wires does not already cause a significant change to the measured fracture toughness. The shape of available crack gauges, moreover, is typically narrow with long wires [8], while a delamination specimen would need a wide gauges with short wires. The technique to print wires on specimens, especially both on the side (to measure the crack propagation) and on the top (to attach leadwires), is not yet mature enough to be applied for this work, and is the subject of further research.

Edge detection

As the bottom block does not move down exactly vertically, the crack plane does not remain horizontal. Methods simply relying on one (also horizontal) coordinate to characterise crack length will therefore be inaccurate. Moreover, figure 6.10 shows that the exact crack tip is hard to distinguish because the gray value differs only slightly from its surrounding. It is therefore decided to use the clear gradients created by the crack flanks to find the crack tip. The Prewitt approximation to the derivative of the image is used to return edges where the gradient is maximum. Running the algorithm only in the vertical direction produces figure 6.11a. A script is run to identify the two crack flanks and approximate each by a second-order polynomial. Subsequently, the intersection of the two polynomials is computed to provide a value for the crack tip location.

Regrettably, this method produces no accurate result. The two polynomials are not accurately enough defined by the crack flanks to produce a reliable estimate for the crack tip. In parts of the footage, the two curves do not intersect at all. Increasing the order of the approximating curve does not improve performance.

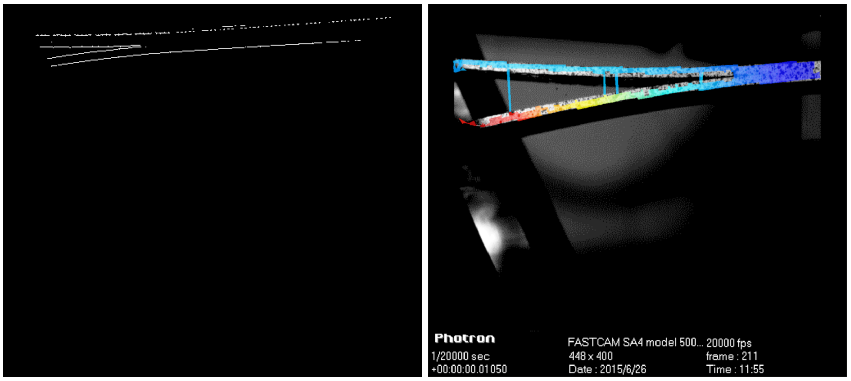

a. Edge detection of figure 6.10 *b. Digital image correlation*

Figure 6.11. Two attempts towards automatic crack detection.

Digital image correlation (DIC)

Another option for automated detection is to make use of digital image correlation [9]. To this end, a specimen is given a black speckle pattern on the white-painted side. Testing and subsequently processing the images in DIC software produces the result shown in 6.11b. The resolution is again too small to allow for a sufficiently small subset, reducing the accuracy of crack tip detection to an unacceptably low value.

Manual extraction

The final option is to compare every image with preceding frames to determine the crack tip location. Although simple to apply, there is a risk of human bias in the extraction. To investigate the variation of detection, the delamination length of a dynamic test is extracted three times by the author, see figure 6.12. The standard deviation of the frame number for a certain delamination length is found to be smaller than 1 frame, which is considered good enough to trust the manual extraction process. It needs to be note that the amount of variation likely increases if different persons were asked to perform the same task. It is, hence, preferred to develop an automated data analysis procedure rather than relying on human observation. The low resolution is again to blame for the slight wavy nature of the delamination length in the figure. When the crack tip is passing from one row of pixels to the next, it is harder to detect.

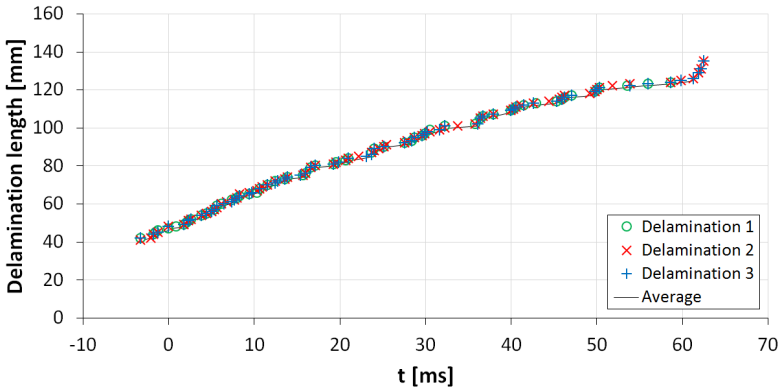

Figure 6.12. Consistency for extracting the delamination length of a $0.5\,\mathrm{m\,s^{-1}}$ *test on woven C/E.*

6.4.3 Preliminary test results

The goal of this thesis is to study the rate-dependency of material properties, or the change of values with speed or rate. Where strain rate is the typical choice for tensile rate-dependency, different rate parameters for dynamic delamination tests can be found in the literature [10] because the strain rate is not well defined in case of a delamination. Here, the time derivative of the delamination length is used, and termed delamination speed. A result for a drop-height of $500\,\mathrm{mm}$ is displayed in figure 6.13a. A smoothing operation with a cut-off frequency of $1\,\mathrm{kHz}$ is applied to account for the discrete nature of the data, which results from the manual detection which is only up to the nearest millimetre. The response shows a clearly non-constant delamination speed. The speed variation depends on the deformation of the specimen which occurs by waves travelling up and down the specimen length. These inertial effects can strongly affect the instantaneous stress distribution at the crack front. Another cause for the variation can be found in the stepwise cracking behaviour that typically occurs when woven composites are delaminated. Figure 6.13b shows that the maximum delamination speed correlates well with the velocity at impact despite the aforementioned variation.

This setup generates a successful delamination process for the carbon/epoxy specimens tested. It allows to vary the delamination velocity by selection of the drop height, in order to assess the rate dependence of the interface properties. Figures 6.9 and 6.13 show, however, that the specimen response to the impact is highly dynamic. The data reduction procedure typically used under quasi-static conditions cannot be applied due to the effects of inertia. The amount of vibration in the loading structure should have been reduced to a minimum by impacting the bottom block with a small pin and letting it move freely. Still, the acceleration of the bottom block shows a large variation in time and it does not provide a useful load history.

An alternative to calculate the crack opening moment without the need for a force measurement is proposed in [1]. The instantaneous crack length and arm displacement of the specimen during the dynamic test are used to calculate the force exerted on the bottom leg. This calculation is based on an experimentally obtained flexural modulus using quasi-static three-point bending tests. The validity of the beam bending formulae used when there is no static equilibrium is questionable. Moreover, the quasi-static bending stiffness might not be equal to the dynamic stiffness of the specimen during a dynamic test, especially when a nylon matrix is used. This method is, therefore, not further investigated.

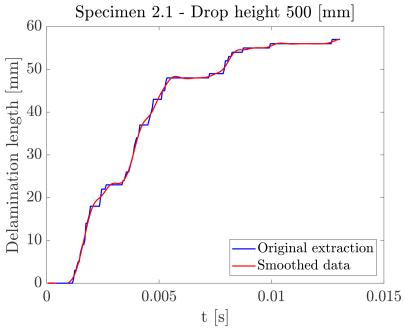

a. Manual delamination extraction result.

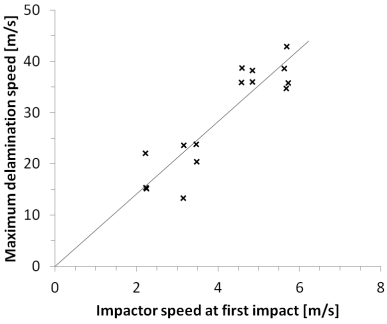

b. Maximum delamination speed versus impact height.

Figure 6.13. Typical delamination result and the relation of maximum delamination speed with impact height.

6.4.4 Using finite-element analysis for data digestion

Based on the above, it is decided to attempt obtaining the dynamic fracture toughness using a combined experimental-numerical method. The aim is to adapt the interface properties until the dynamic behaviour matches what is seen in the test, starting from the quasi-static properties as initial guess. To this end, a 3D finite element (FE) model is developed. The geometry of the model is shown in figure 6.14, and it consists of an impactor pin, two loading blocks, and the two halves of a composite specimen. The model dimensions are made to match the specimens as closely as possible, though only half of each part is modelled to reduce the computational cost. The axes of the coordinate system are indicated in the figure. The origin of the coordinate system is set in the plane of symmetry, which is taken as xy-plane where the x-axis points along the specimen and the y-axis upwards. The z-axis completes the right-hand system by pointing in the width direction of the specimen.

The metal parts are given the (isotropic) properties of ASTM A284 steel [11]. The density of the parts is adapted to match the mass of each part with what is measured on the actual pieces. A small cylindrical part above the impactor pin is given a high density to model the mass of the impactor, which is set to 7 kg for this test series. The resulting properties are given in table 6.1.

The properties for the composite specimen are taken from the finite element analysis of a woven meso-scale unit cell of the same material system as used for the current research [12], which were given in table 3.4 in chapter 3.

The top block and bottom block are attached to the top and bottom leg of the composite, respectively, using a tie constraint. A frictionless hard contact inter-

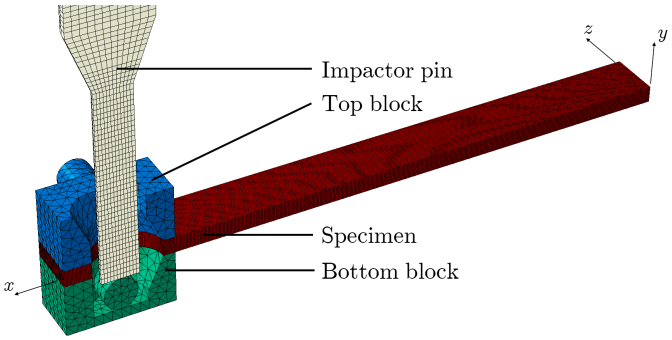

Figure 6.14. The geometry of the dynamic delamination finite-element model. Only half is taken to reduce computational cost.

Table 6.1. Material properties applied to the metal parts.

Property	**Unit**	**Impactor**		**Load blocks**	
		Pin	**Cylinder**	**Top**	**Bottom**
Young's modulus	[GPa]		205.7		
Poisson's ratio	[-]		0.29		
Density	$[\mathrm{kg\,m^{-3}}]$	7274	2.46×10^6	7816	7698

action is defined between the exterior surfaces of all parts. The non-pre-cracked portion of the surface of each composite leg is attached to the other using a cohesive surface interaction. A maximum stress criterion is used to define damage initiation, and the subsequent propagation is computed on the basis of energy release rate. The properties of this interaction are given in table 6.2. For the interface strength in normal direction, it is chosen to use the value from [13] rather than the experimentally obtained values for the quasi-static tensile strength of pure matrix given in appendix B. These results were namely not yet available at the time of development of this model. The default cohesive stiffness is used.

The surfaces of the model in the xy-plane, which form the original midplane of the set-up, are given a symmetric boundary condition: no movement in the z-direction nor rotations around the x- or the y-axis. The whole of the impactor is fixed in x-direction so it can only move vertically. Every node in the axis of the top block, partially visible in figure 6.14, is coupled kinematically to a reference point. This point is in turn allowed only to rotate around the z-axis to simulate the support of the top block.

Table 6.2. Woven C/E composite interface properties, taken from [13] except G_{Ic}, which is determined from preliminary quasi-static experiments, see section 6.3

Interface property	Unit	Value	Description
σ^{u}	[MPa]	71	Strength normal to surface
τ_1^{u}	[MPa]	92	Strength in first shear direction
τ_2^{u}	[MPa]	92	Strength in second shear direction
G_{Ic}	[J m^{-2}]	314	Energy release rate for mode-I
G_{IIc}	[J m^{-2}]	788	Energy release rate for mode-II
η	[-]	1.6	BK mode mixity parameter

Model verification

Several aspects of the model are investigated in a quasi-static analysis before it is applied for the dynamic experiments.

The impactor is removed from the model and a vertical displacement is applied to a reference point to simulate the actuation of a test bench. The point is kinematically constrained to the volume of the axis in the bottom block for all degrees of freedom. The specimen is discretized in first-order full-integration quadrilateral elements (C3D8), the blocks in second-order tetrahedral elements (C3D10M). The system is solved using an implicit solver. The vertical reaction force in the reference point of each block is written to a file, along with the vertical displacement of the reference point of the bottom block.

To verify whether the elastic response approximates the correct value, it is compared to a theoretical force-displacement relation of Hashemi and Williams [14, 15]. They describe the elastic response with a correction for root rotation, using equation (6.3):

$$\delta = P\frac{8\left(a+\chi h\right)^3}{bh^3E_{11}} \tag{6.3}$$

where the term χh accounts for the compliance at the base of the two legs, which are modeled as cantilever beams:

$$\chi = \sqrt{\frac{E_{11}}{11G_{13}}\left(3-2\left(\frac{\Gamma}{1+\Gamma}\right)^2\right)} \tag{6.4}$$

$$\Gamma = 1.18\frac{\sqrt{E_{11}E_{33}}}{G_{13}} \tag{6.5}$$

and where:

a	$[m]$	Crack length;
b	$[m]$	Specimen width;
h	$[m]$	Half the total specimen thickness;
E_{11}	$[Pa]$	Longitudinal Young's modulus;
E_{33}	$[Pa]$	Young's modulus in thickness direction [15];
G_{13}	$[Pa]$	Shear modulus in 13-plane [15].

The used material properties for the woven C/E are given in table 3.4 in chapter 3. Figure 6.15 contains the elastic response of several discretizations of the composite part of the FE-model before any crack propagation. Five increasingly dense meshes are used with cube-shaped elements, from 4 up to 8 elements in the thickness direction of the leg (element size from $0.5\,\mathrm{mm}$ down to $0.25\,\mathrm{mm}$). Additionally, a solid model is discretized at the minimum density using quadratic elements (solid black line in the figure) and a model is made using square shell elements with five integration points through the thickness (green line). Two analytical responses are included: one with, and one without the crack tip rotation correction with a dashed line and a dash-dot-line, respectively. The figure shows that the solid models converge to a response close to the corrected analytical solution, while the shell model is too stiff and closer to the uncorrected analytical solution. This is a known behaviour, because the shells have a rotational constraint at the crack tip, which resembles more the perfect clamp condition. Solids only operate with displacement constraints, thus resulting in added compliance [16], which, in this case, approximates the crack tip compliance seen in reality. The model with 5 elements through the thickness is considered converged, given that the difference with the most finely meshed model is small (within $2\,\%$). This results in elements with a length of $0.4\,\mathrm{mm}$ in each direction, or about $60\,000$ per leg.

The mesh should be fine enough to correctly model the delamination process. It is advised to choose the element size such, that the cohesive zone length spans at least three elements [17]. This length l_{cz} can be estimated using:

$$l_{\mathrm{cz}} = ME\frac{G_{\mathrm{c}}}{\left(\tau_0\right)^2} \tag{6.6}$$

where E is the Young's modulus of the material, G_{c} is the critical energy release rate, τ_0 is the maximum interfacial strength, and M is a parameter that depends on each cohesive zone model, here taken 0.88 [17]. When the longitudinal stiffness E_{11} is used for E, to be conservative, the cohesive zone length amounts to $0.88 \cdot 60.52 \times 10^9 \cdot 314/\left(50 \times 10^6\right)^2 = 0.0067\,\mathrm{m}$. This distance should be discretized in at least three elements for the cohesive zone to be correctly modelled, resulting in the condition that the element length should be below $2.2\,\mathrm{mm}$. This condition is largely satisfied by the chosen discretization.

The crack propagation is verified by a comparison to an analytical solution.

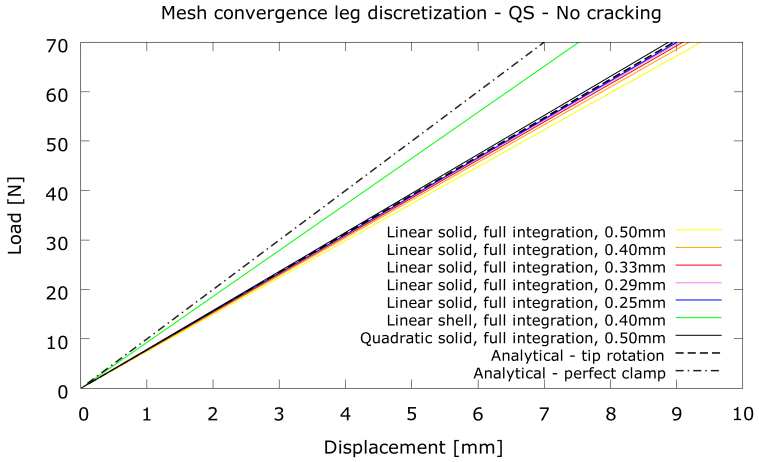

Figure 6.15. Mesh convergence of elastic behaviour of delamination model.

Equations (6.3) to (6.5) can be combined with the corrected force [14, 15]:

$$P = \sqrt{\frac{G_{\mathrm{Ic}} b^2 h^3 E_{11}}{12\,(a+\chi h)^2}} \tag{6.7}$$

where G_{Ic} is the critical strain energy release rate for mode-I cracking. The combination gives an equation for the force dependent on the displacement during crack propagation:

$$P = \frac{\sqrt{8}\,(G_{\mathrm{Ic}}/12)^{\frac{3}{4}}\, b\left(h^3 E_{11}\right)^{\frac{1}{4}}}{\sqrt{d}} \tag{6.8}$$

The analytical solutions for elastic loading and crack propagation are displayed in the following figures using dashed lines.

Using the interface properties given in table 6.2 and various values for the viscous regularization, the green curves in figure 6.16 are produced. The viscous regularization is needed to stabilize the calculation process to allow the solver to converge. Increasing this parameter results in a reduction of calculation cost for a simulation, though a too large value produces wrong results. The minimum needed for the model to run until a fully cracked specimen is 1×10^{-5}. It can be seen, though, that the curves do not agree well with the analytical solution, because they overestimate the load during crack propagation by about $30\,\%$.

The stress should reach a theoretically infinite value at the crack tip. The normal strength of the interface can, therefore, be seen as merely a fitting parameter [16]. It is decided to reduce the value of the strength to $50\,\mathrm{MPa}$ in an attempt to lower the curves. The otherwise unchanged model is run again for various values of the regularization, see the blue curves in figure 6.17. A different value

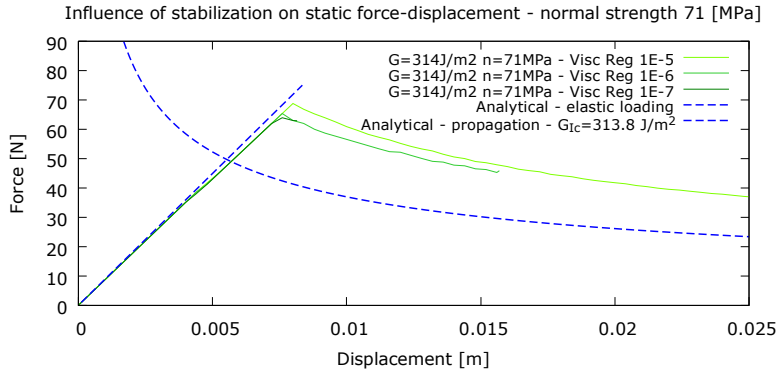

Figure 6.16. The influence of viscous regularization on the force-displacement response of the model with an interface strength of 71 MPa.

for the regularization is now more appropriate, as 1×10^{-5} produces wrong results. A new minimum of 1×10^{-7} is chosen: further reduction results in non-convergence of the implicit analysis. As can be seen, the new choice of interface normal strength results in curves which closely approach the theoretical value.

To verify that a possibly insufficient output frequency is influencing the displayed result, the extracted data points are visualized in figure 6.18. The graph shows that the output frequency is high enough to correctly show the model behaviour. A lower output frequency could have caused the knee point not to be shown accurately, making the maximum load reach appear lower than actually occurring in the simulation [18].

Finally, the model can be validated using the outcome of experiments. The acquisition of quasi-static test data is briefly explained in section 6.3. The preliminary quasi-static test data for the woven C/E results in an energy release rate of $G_{\mathrm{Ic}} = 314\,\mathrm{J\,m^{-2}}$ if only the peak values are used (section 6.3). Figure 6.19 contains the results of the analytical model, the numerical results using the properties selected above, and the results of the three preliminary quasi-static tests. The figure shows that the three agree well with each other, validating the both numerical and the analytical model.

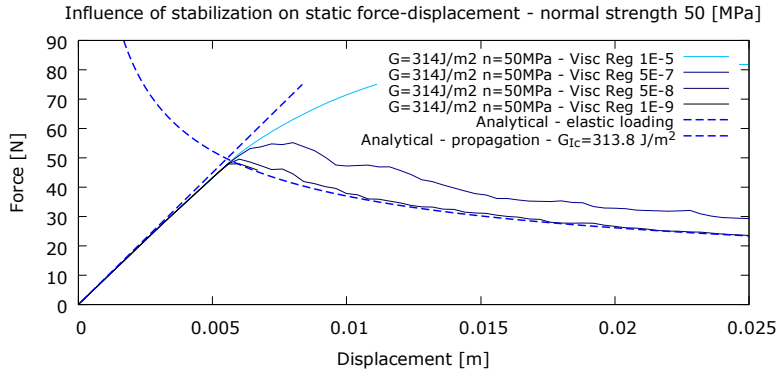

Figure 6.17. The influence of viscous regularization on the force-displacement response of the model with an interface strength of $50\,\mathrm{MPa}$.

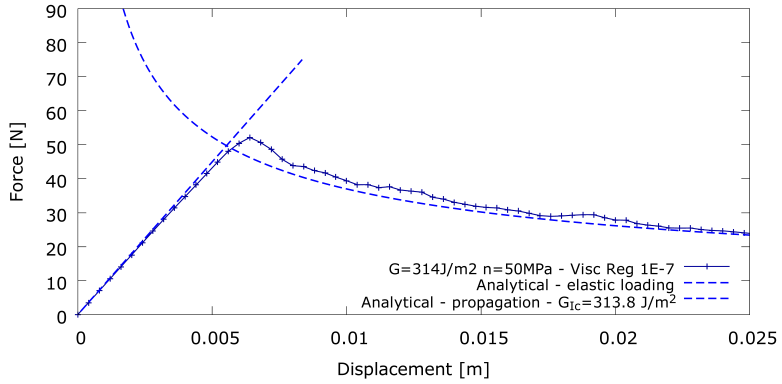

Figure 6.18. A visualization of the output of the quasi-static simulation using the final parameters. Each '+' mark indicates a data point.

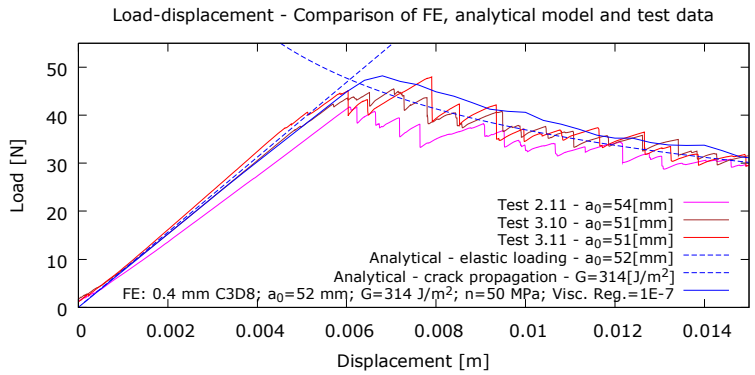

Figure 6.19. Validation of the analytical and numerical mode-I delamination models with test data, which has been shifted to correct for initial compliance.

Dynamic simulations

The dynamic model is constructed using the validated quasi-static model as a start, even though the analysis procedure is fundamentally different and the implicit (or quasi-static) parameter values do not guarantee correct behaviour of the explit (or dynamic) model. The impactor is now used to actuate the bottom block rather than a displacement boundary condition. A gravitational load is set to act on the entire model by a uniform field with an acceleration in the negative y-direction of $9.81\,\mathrm{m\,s^{-2}}$. The impactor is given an initial velocity of $4.8\,\mathrm{m\,s^{-1}}$ to match with one of the dynamic tests. The impactor is discretized using wedge elements (C3D6) because of the cylindrical nature of its shape. The contact between the impactor and the axis of the bottom block is handled by the frictionless hard contact formulation mentioned earlier. An explicit solver is used to compute a solution at double precision.

Output is requested at full precision. The displacement of the centre of the bottom block and the average delamination length are given as output for a selected number of increments. The delamination length is computed by checking the status of each node in the crack plane along a line from the insert to the free edge of the specimen. A node is considered delaminated if the contact surface damage variable (CSDMG) has reached a value of 0.99 to prevent problems with delaminated nodes which have a value not exactly equal to 1. A high damage gradient prevents a measurable sensitivity of the outcome on this value. The number of delaminated nodes (minus 1) is multiplied by the internodal distance and added to the precrack length to retrieve the delamination length.

First, the general behaviour of the model is compared to what is seen in the dynamic tests in figure 6.20: the delamination length is set out versus time using

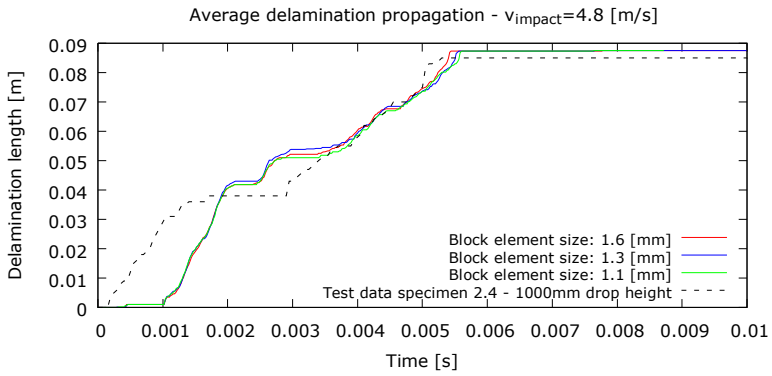

Figure 6.20. Influence of the block discretization on the dynamic crack growth.

colored graphs. The general behaviour matches well with the test result, compare the dashed line with the coloured ones in the figure. Initially the delamination grows at a high rate to about halfway the interface. Then, a plateau is seen without crack propagation, owing to a vibration of the entire specimen. Afterwards, the growth continues at a reduced rate until complete interface failure.

Figure 6.20 also shows the influence of the element size in the loading blocks. Three different discretizations are used: 8, 10 and 12 elements in the blocks' thickness direction, corresponding to an average element length of 1.6, 1.3 and $1.1\,\mathrm{mm}$, respectively. The figure shows that the results hardly differ, hence the coarsest of the three options is used for following analyses.

Figure 6.21 shows the convergence study of the mesh of the composite specimen. Clearly the behaviour changes as a function of discretization. It does not seem to converge, and the use of even finer meshes is inhibited by the computational cost, because the model with the finest mesh already needs multiple days to finish using four CPUs on a dedicated analysis server.

Alternative models are created to find the cause of the non-convergence. Different element types (quadratic versus linear, and full versus reduced integration), impactor formulations (point-mass versus high-density cylinder) or bottom block formulations (solid deformable versus discrete rigid versus point mass with correct inertia) were attempted, but do not solve the problem. Choosing different bottom block formulations results in significant changes in the delamination-time curve, though, indicating that the bottom block might be related to the absence of mesh convergence. A look into the behaviour of the bottom block reveals an average acceleration of about $1.2 \times 10^5\,\mathrm{m\,s^{-2}}$ when the impactor hits its axis. The contact lasts about $80\,\mu\mathrm{s}$, during which approximately $2\,\mathrm{J}$ of energy is transferred from the impactor to the test specimen. This time is considered very short, and is due to the metal-to-metal contact between the impactor pin and the axis in the bottom block,

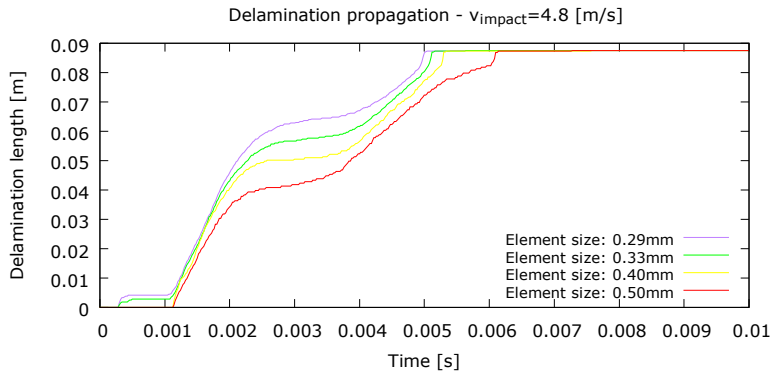

Figure 6.21. Influence of the composite specimen discretization on the dynamic crack growth.

and could be the reason no mesh-convergence is obtained.

To investigate whether the problem could be ill-conditioned due to this short contact during impact, the model is adapted and a smooth step in displacement is applied to the bottom block, to remove the impact entirely. The crack propagation history becomes practically mesh-independent for the studied meshes, see figure 6.22, supporting the conclusion that the short contact during impact is to blame for the mesh-dependency. The mesh with an element size of $0.33\,\mathrm{mm}$ is considered converged, judging from the small difference with the result of the more finely discretized model. It is decided not to continue further along this path for the drop-tower test method, because the position of the bottom block becomes an input to the model this way. The position signal is needed, however, as an output to fit the model to the test results in order to find the right value of fracture toughness. The delamination length or specimen shape as a function of time could be used to

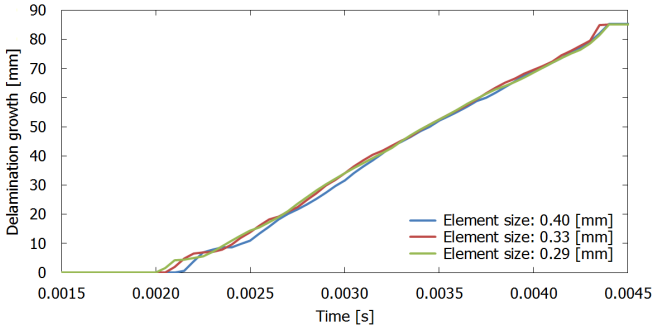

Figure 6.22. Mesh convergence proven for simplified model.

assess the degree of fit instead. The extraction of these properties from the test data is, however, too coarse for this purpose, partially due to the low resolution of the images. To allow the displacement to be a model input parameter, another value should thus be measured. Force is the logical candidate, so another test method is applied where the hydraulic pulse test bench is used to apply the displacement, allowing for a load measurement as well, see also section 6.5.

6.4.5 Application to glass/polyamide-6 composite

Apart from the data reduction, the developed drop-tower method has another drawback. As it relies on the inertia of the accelerated bottom block to pull the specimen apart, the amount of energy available for the fracture process is limited. Where the method can sufficiently delaminate relatively stiff and brittle C/E composites, this is not the case for G/PA-6. This material has a higher compliance and a stronger interface compared to C/E, see also figure 6.23 for an illustration. Specimens of the same dimensions simply open up and close again without any crack propagation. Applying a higher speed to put more energy in the bottom block is also limited to an upper bound: in the current configuration the bottom block touches the set-up below before the delamination grows. The large amount of specimen bending was already expected during material choice, see section 6.2. Considering the data reduction issue explained above, it is decided to make a switch to another test method rather than redesigning the drop tower set-up.

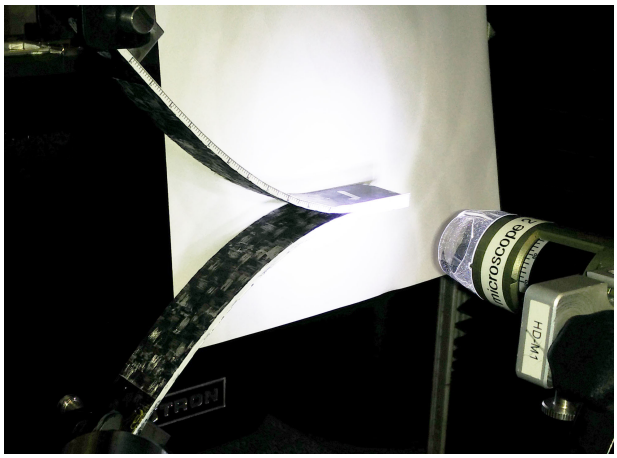

Figure 6.23. Quasi-static delamination test on a G/PA-6 specimen, showing the large amount of leg opening.

6.5 Mode-I delamination on a hydraulic pulse bench

In an attempt to generate a useful load history and allow the G/PA-6 material to be investigated as well, the hydraulic pulse test bench is used for dynamic delamination experiments.

Several authors use regular hydraulic testing equipment at a series of crosshead rates to investigate the rate-dependence of composites in a relatively low-speed regime, i.e. up to about $0.25\,\mathrm{m\,s^{-1}}$. Only one article is found in which a hydraulic pulse machine is used to delaminate composite specimens. Hug et al. use a hydraulic pulse test bench with an additional structure to simultaneously pull both sides of a DCB specimen which is mounted vertically [5]. Although the proposed set-up works well for velocities up to $1.6\,\mathrm{m\,s^{-1}}$, severe vibrations show up at speeds above that value. As the current research focuses on impacts at speeds of about a decade higher, it is decided to perform the test as described by the test standard [2], albeit at an increased velocity.

6.5.1 Test set-up details

The same specimen and block dimensions are used as for the drop-tower set-up (figure 6.1). New fixtures are designed to hold the specimen in place, see figure 6.24a. They are milled from aluminium to achieve a light-weight solution which allows the piston to reach the desired speeds. Reducing the fixture mass to a minimum additionally ensures an eigenfrequency of the load train which is as high as possible. Figure 6.24b shows a specimen mounted in the set-up. The bottom fixture is attached to the slack rod (the slack rod is explained in chapter 2). A small ring of foam was added inside the slack rod to reduce the initial acceleration of the bottom block, which otherwise tends to detach from the specimen for tests at high speed.

A smaller load cell is available for the test bench, because the loads are expected to remain below $1\,\mathrm{kN}$. Still, the large $200\,\mathrm{kN}$ load cell used for the tensile testing campaign is kept because of two reasons. Firstly, the sensitivity of piezoelectric load cells is independent of their capacity [19]. Simply reducing the range of the amplifier will increase the signal-to-noise ratio to acceptable values to measure small loads accurately. Secondly, the rigidity of larger cells is higher than the smaller ones, which is beneficial for the natural frequency of the load measuring assembly.

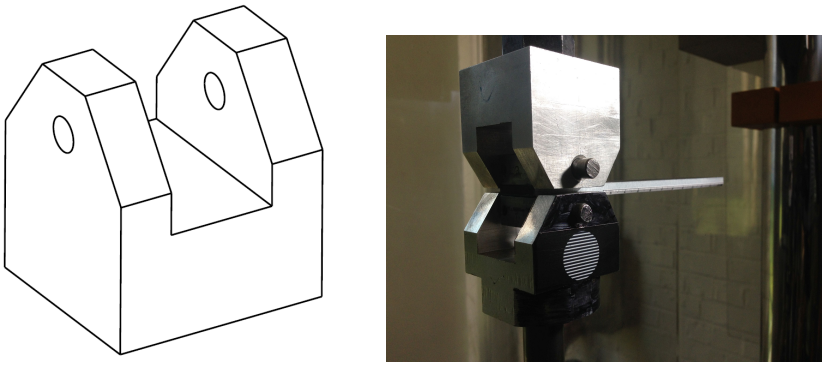

a. New DCB specimen fixture. *b. Specimen mounted in the fixtures.*

Figure 6.24. Mode-I testing on the hydraulic pulse test bench.

6.5.2 Data acquisition

Load is amplified with a sensitivity of $50\,\mathrm{N\,V^{-1}}$, resulting in a maximum measurable load of $500\,\mathrm{N}$. In this case, the total noise on the load acquisition amounts to about $\pm 2\,\mathrm{N}$. The measured signal contains high-frequency oscillations which partially obscure the underlying force data, especially at high speed. A third-order Butterworth filter [20] with a cut-off frequency of $300\,\mathrm{Hz}$ is therefore applied to remove the higher-frequency content.

The position of the bottom fixture is measured using optical pattern tracking, in a similar fashion as is applied to the drop tower tests. This time, however, the pattern consists of only a single grating, in vertical direction. The piston is namely restricted to a purely vertical motion and thus no information extraction about rotation and lateral displacement is required.

The crack length is measured by recording the side of the specimens using a high-speed camera and manually reading out the length, similar to the dynamic delamination tests in the drop tower.

The test durations are relatively long compared to the dynamic tensile tests described in chapters 4. At the highest speed, the tests last $1.5\,\mathrm{ms}$ for delamination instead of down to $30\,\mu\mathrm{s}$ for tension. Therefore, only the trigger delay in the oscilloscope is taken into account to synchronize the images with the load data as a more accurate synchronization is not necessary, see also figure 4.7 in section 4.4.3.

The test standard for mode-I delamination of laminated composites is followed for the data reduction towards an energy release rate [2], see equation (6.2). This is expected to produce accurate results only when the speed is relatively low. For high speeds, dynamic effects invalidate the assumption of equilibrium onto which the equations in the test standard are based. To find out what would be the limiting speed, a FE-model is used, as described in the next section.

6.5.3 Exploring the velocity limits using finite elements

The explicit FE model described in section 6.4.4 is adapted to loading using a smooth step to investigate the maximum speed at which the data reduction from the ASTM D5528 test standard [2] can still be expected to give accurate results. To speed up the analyses, details like the holes in the blocks have been removed and the width has been reduced to $1\,\mathrm{mm}$, and a symmetry boundary condition is applied to both sides of the model. This way, a plane strain condition is mimicked. The step towards a true 2D plane strain model has not been made here, because the cohesive surface behaviour is not available in 2D. A switch to cohesive elements would be necessary, which has not been made, since the properties of the cohesive surface behaviour had already been validated for quasi-static loading. The new model can be seen in figure 6.25. The dimensions equal those of the DCB specimen, and the material and interface properties applied are the same as for the bigger model described in 6.4.4. The fracture toughness value was taken at $G_{Ic} = 292\,\mathrm{J\,m^{-2}}$ this time, i.e. the average value of the energy release rate rather than the peak value of the preliminary quasi-static tests described in section 6.3. The green lines in the figure show tie conditions, the yellow line shows a hard normal and frictionless sliding contact condition, the red line the zone of cohesive behaviour. The nodes in the loading blocks are kinematically constrained to the respective reference points. The model is allowed only to rotate along the two reference points, and, as mentioned before, the two side surfaces are given a symmetry condition. A smooth step in displacement of $100\,\mathrm{mm}$ is applied to RP-1 to simulate a test. The model is discretized into linear, full-integration hexahedral C3D8 elements, and the model is analysed in double precision. The blocks are meshed rather coarsely with an element size of $1.3\,\mathrm{mm}$ because it was shown earlier that their mesh has only little influence on the model outcome (figure 6.20).

First, the delamination history of the quasi plane strain model is compared to the original half-width model, see figure 6.26. The delamination length was extracted the same way as for the original model. In this case, the element size in the composite was taken $0.4\,\mathrm{mm}$. As can be seen in the figure, the results lie very close to each other, while the analysis time was largely reduced. It is therefore

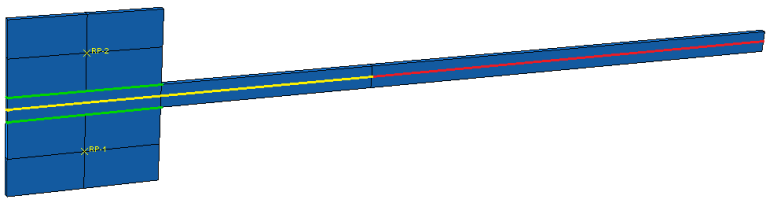

Figure 6.25. The quasi plane strain FE model for dynamic delamination.

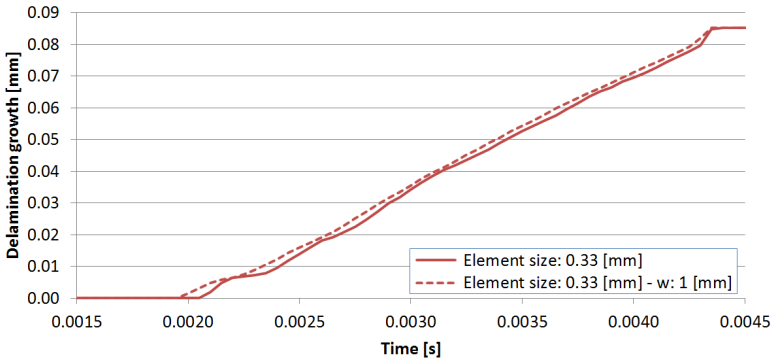

Figure 6.26. The quasi plane strain FE model compared to the half-width model with same leg mesh size.

decided to continue with the quasi plane strain model.

The load was extracted from the model using the reaction force in the pinned reference point constrained to the top block. A total of $10\,000$ values were requested for the force output of the reference point of the top node. The force values have been multiplied by a factor of 25 to make them represent a full-size specimen. Looking at the force history of the model (grey curve in figure 6.27a), a large amount of noise shows up during the crack propagation stage. A moving average filter with a size of 500 samples was applied to the result, producing the red curve. Applying a smaller amount of filtering would result in too much noise still during crack propagation. Although the filtered result matches the initial loading stage very well, the maximum load before propagation is underestimated: the unfiltered grey curve surpasses the filtered red curve at the peak value occurring at about $0.011\,\mathrm{ms}$. It is hard to assess the quality of fit during propagation. The noise is likely related to the stepwise release of energy which occurs on a per-element basis. A more finely meshed model is therefore analysed to investigate the effect of mesh size on the load history. Figure 6.27b contains the load versus time for a mesh size of $0.20\,\mathrm{mm}$. The reduction in noise is striking, compare the grey curves of both graphs. The filter size could be reduced to 100 samples to produce a useful force history which also approximates the peak load better, see the red curve. Interestingly enough, the peak load without crack propagation occurs just before $0.01\,\mathrm{ms}$ now, at a lower load than for the more coarsely meshed model. From figure 6.22 it appeared that the mesh had already converged with an element size of $0.33\,\mathrm{mm}$, because the crack propagation behaviour hardly differed with mesh refinement. This conclusion, however, appears not to be correct after all, because the force behaviour still changes. Another, more suitable criterion should thus be found to assess mesh convergence.

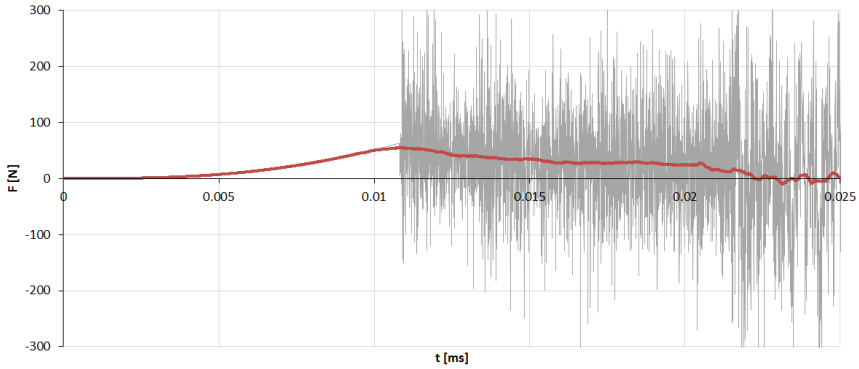

a. Element size $0.33\,\mathrm{mm}$

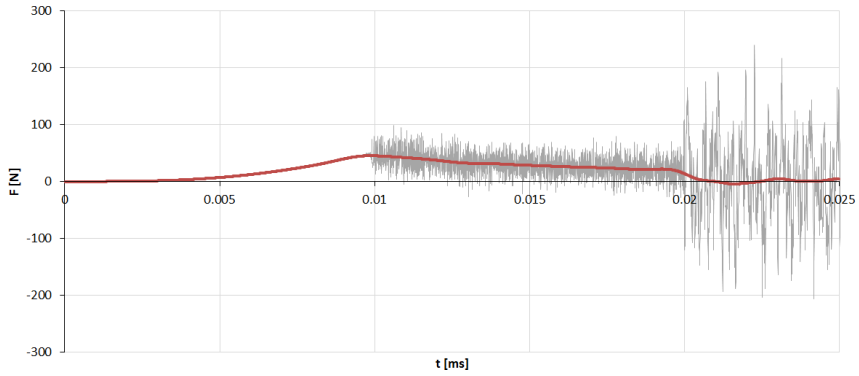

b. Element size $0.20\,\mathrm{mm}$

Figure 6.27. Force history of the quasi plane strain dynamic delamination model, with maximum actuation speed $2.7\,\mathrm{m\,s^{-1}}$ *during the smooth step.*

Figure 6.28 contains the force-displacement responses of the same two models as in figure 6.27, as well as the theoretical curves for elastic loading and crack propagation (equations (6.3) and (6.8), respectively). Also $10\,000$ displacement values were requested from the model, at the reference point constrained to the bottom block. The values required no smoothing operation, as the smooth step in displacement was applied to exactly the point from which output was requested. It can be seen in the figure that the model results for the mesh size of $0.33\,\mathrm{mm}$ overshoot the theoretical curves, while the element size of $0.2\,\mathrm{mm}$ reproduces them accurately. Comparing force-displacement to theory seems a better way to assess mesh convergence, and the latter mesh is thus considered converged. It is important to realise that the output frequency still needs to be very high to obtain an accurate result after smoothing. The original data in figure 6.27b show significant noise still, which will obscure the results if it is not adequately dealt with. The converged result in figure 6.28 shows some deviations with the theoretical curve. First, the sharp corner is rounded-off, which is due to the smoothing operation. Second, at about 11 and $27\,\mathrm{mm}$, the model outcome shows two slight reductions in force, which is deemed a result of the dynamics of the problem, as the applied step was already much faster than quasi-static.

Applying the data reduction method using the modified beam theory from the ASTM test standard to the model responses from figure 6.28, along with the extracted delamination length, the energy release rate versus crack length is obtained, see figure 6.29. The overshoot in force for the coarser model results in an overestimation of the energy release rate: compare the obtained value for fracture toughness with the input value shown by the dashed line in the figure. The model with an element size of $0.2\,\mathrm{mm}$, however, accurately retrieves the fracture toughness that was given as an input, proving that the model operates correctly.

The analysis time of the explicit 1-mm-wide model with an element size of $0.2\,\mathrm{mm}$ is again quite high, especially for small actuation speeds (and thus large test durations) for which the solver needs in the order of several days using four cores on a dedicated server to complete the simulation. Hence, it is decided to analyse the global specimen behaviour using a mesh size of $0.33\,\mathrm{mm}$. The model is actuated using a smooth step of $100\,\mathrm{mm}$ in displacement of several different durations. This leads to a series of maximum actuation speeds, see table 6.3. The delamination propagation, which appears to occur at a rather constant velocity (see figure 6.26) is fitted with a straight line using a linear least-squares algorithm. The slope of this line is taken as the delamination speed, and added to the corresponding rows in table 6.3. As mentioned in the beginning of this chapter, the delamination speed is selected as the parameter which defines the rate of a certain delamination propagation. Figure 6.30 contains the initial part of the force-displacement behaviour of the FE model, the delamination speed is indicated in the legend. A coarser mesh was used to speed up the analyses. Apart from the

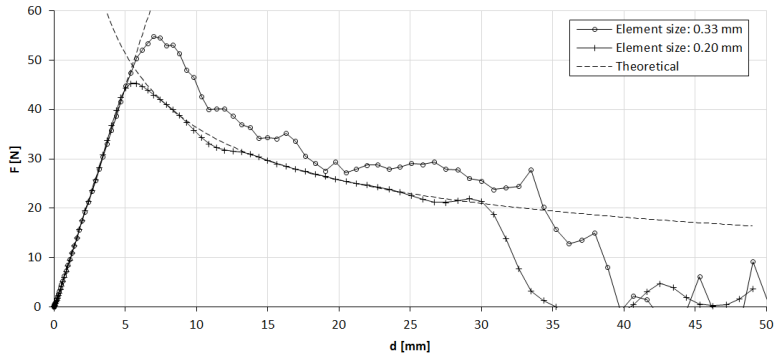

Figure 6.28. Force-displacement curves of two discretizations of the quasi plane strain delamination model, actuated at a maximum speed of $2.7\,\mathrm{m\,s^{-1}}$*, compared to the theoretical behaviour.*

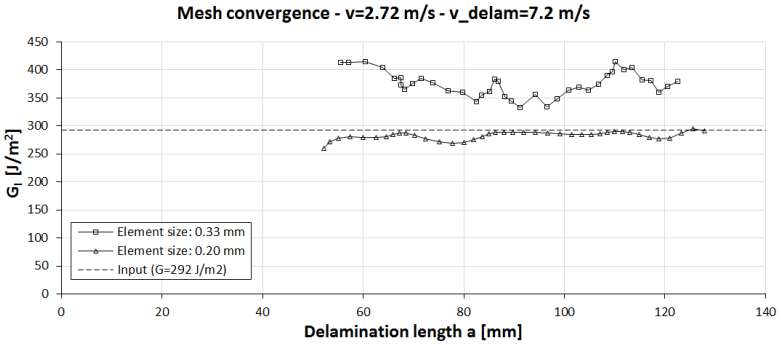

Figure 6.29. Energy release rate versus crack length for the two results from figure 6.28.

Table 6.3. Maximum actuation speeds and average delamination speeds for the different step times to displace the bottom block $100\,\mathrm{mm}$ *in the FE-model.*

Step time $[\mathrm{ms}]$	**Maximum speed** $[\mathrm{m\,s^{-1}}]$	**Delamination speed** $[\mathrm{m\,s^{-1}}]$
200	0.68	1.81
100	1.36	3.61
50	2.72	7.19
20	6.80	17.2
10	13.2	33.9

overshoot during crack propagation which is explained by the coarse mesh, it can be seen in the figure that the two fastest models show non-linearities during elastic loading. These effects are a result of the finite time needed for the load introduced in the bottom block to reach the top block. The specimen is, therefore, no longer in equilibrium at the two fastest actuations. The specimen with a crack propagation speed of $7.19\,\mathrm{m\,s^{-1}}$, actuated at $2.72\,\mathrm{m\,s^{-1}}$, is the fastest test which still shows a straight response during the elastic loading regime. Hence, the actuation speed of $2.72\,\mathrm{m\,s^{-1}}$ is taken as the upper speed limit of delamination testing in the regular manner for woven C/E composites.

The R-curve (G_I versus a) cannot be obtained using the techniques from the ASTM standard for the cases where the specimen is no longer in equilibrium. For example, the modified beam theory relies on the calculation of the compliance and in-plane stiffness of the two legs, based on the instantaneous relation between force, displacement and crack length. An absence of equilibrium causes the computed compliance and in-plane stiffness to become quickly inaccurate, resulting in very unreliable values of the (critical) energy release rate.

Another result of the absence of equilibrium in the dynamic tests is that the two legs are not equally deformed. Both the model and the high-speed footage show that the top leg, at the fixed side of the test bench, deforms more than the bottom leg, which is connected to the actuator, see figures 6.31 and 6.32. This effect is attributed to inertia: the tail of the specimen lags behind and rotates because it only sees load on one side. This effect can probably only be solved by equally accelerating both blocks away from each other, like Thorsson et al. [21], which would come with the added advantage that the time to equilibrium is halved owing to the symmetry, raising the limit velocity by a factor of two. A consequence of the unequal deformation of both halves of the test specimen is that the delamination is not a pure mode-I crack.

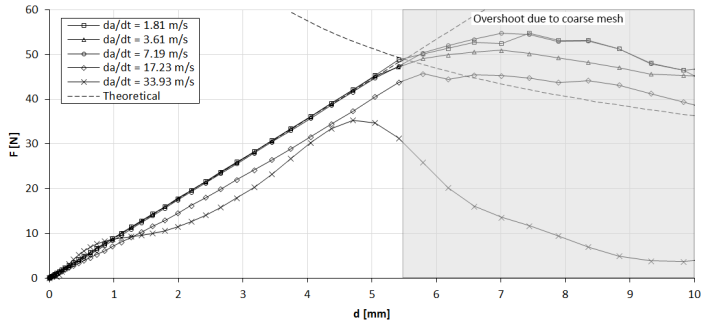

Figure 6.30. Initial force-displacement response at several delamination velocities for the quasi plane strain FE model discretized with elements of $0.33\,\mathrm{mm}$.

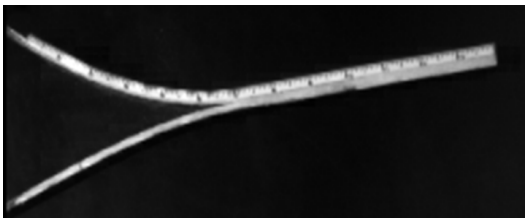

Figure 6.31. Full-specimen recording of a $15\,\mathrm{m\,s^{-1}}$ *delamination test on woven G/PA-6, showing unsymmetric opening of the specimen. The resolution is very low owing to the combination of the high frame rate and large field of view.*

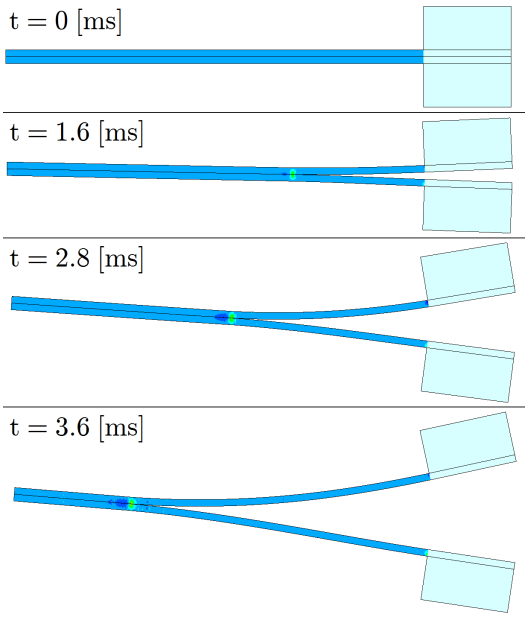

Figure 6.32. Snapshots of the quasi-plane strain FE-model with $13.2\,\mathrm{m\,s^{-1}}$ *maximum speed, showing clear asymmetric opening at* 2.8 *and* $3.6\,\mathrm{ms}$.

6.5.4 Application to glass/polyamide-6 composite

The advantage of using the hydraulic pulse test bench is that the maximum displacement is up to $300\,\mathrm{mm}$, which should be more than sufficient to break even the more compliant G/PA-6 laminates.

A typical load-displacement curve for a mode-I test on woven G/PA-6 is given in figure 6.33. The specimen needs just under $200\,\mathrm{mm}$ of displacement to fail completely. What is perhaps striking from the figure is the very discontinuous character of the curve. Indeed, the crack propagation occurs in distinct steps rather than in a smooth fashion as prescribed by the test standard. In this case, only five steps of propagation show up. Even though this behaviour is not ideal to study the delamination characteristics of the material, still there is a way to extract the energy release rate [18].

A bigger problem is the relatively high propagation speed of the delamination during a step. As mentioned in section 6.4.3, the crack propagation speed is chosen as the rate parameter. This means that it should vary between tests of a different actuation velocity in order to study the rate dependency of the energy release rate. When the propagation occurs in steps like this, it is possible that an increase in actuation velocity simply reduces the time between steps rather than increasing the delamination speed. In that case, the current specimen geometry is not suitable to study the rate-dependency of the mode-I energy release rate of G/PA-6.

The influence of leg separation speed on the crack growth rate is studied by conducting one test at low and one at high velocity. The low-speed test is recorded intermittently at a high frame rate during each crack jump. A continuous recording at a high frame rate would namely require more than the available storage space and using a lower frame rate would result in an inaccurate crack speed determination, especially if the jump in crack length would occur between two frames. The results are shown in figure 6.34. The cracks grow in only a few steps for both

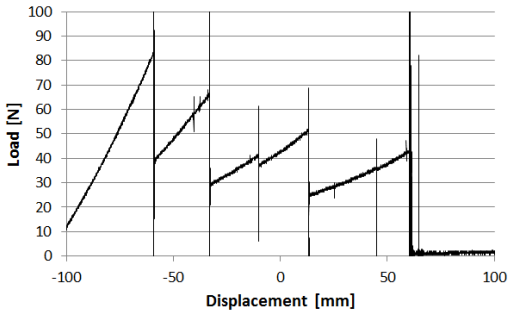

Figure 6.33. Delamination test on a woven G/PA-6 specimen at $0.01\,\mathrm{m\,s^{-1}}$*, showing a very discontinuous crack propagation.*

tests. Moreover, the difference in crack speed seems to depend more on its own length than on actuation velocity. Both tests, namely, show the same trend, and the variation of crack speed between the tests is smaller than that within a test. So indeed the current specimen geometry is not suitable.

In an attempt to obtain a smooth crack propagation, it is decided to stiffen the woven specimen to increase its stiffness to what the test standard prescribes. The stiffness of the legs namely influences the stress distribution after the crack front: at the same leg separation, the stress levels will be higher and spread over a larger area. Stiffening is realized by adhering a strip of material to the outside of each leg of the specimen, along its entire length. An attempt is made using several different materials, an overview is given in table 6.4. The strips are attached using Loctite® 480™ cyanoacrylate adhesive. As can be seen from the table, the addition of a steel plate either results in a plastic deformation of the stiffener if it is too thin, or in a disbond if it is thicker. Even though the thin DC01 steel stiffening produced the best result in terms of crack propagation behaviour, it cannot be used as energy is consumed by the plastic deformation. This makes it impossible to distinguish which amount of energy is taken by the crack propagation. Adding the same glass/PA-6 material on the top and the bottom of the specimen, basically doubling its thickness, also works beneficially: the amount of steps in the cracking process is increased by a factor of 2. Still, no continuous crack propagation is obtained, and hence no rate-dependency is expected as the delamination speed will not vary between slow and fast tests. Despite the intermittent crack propagation, some experiments have been carried out at different speeds to support this conclusion.

The UD G/PA-6 in delamination shows the same stepwise cracking behaviour as the woven laminates. When applying the same reasoning to the UD laminate, stiffening the legs with the same UD material should increase the number of steps. In this case, no metal stiffening is attempted, and again the cyanoacrylate adhesive

Table 6.4. Result of different stiffening measures on the number of steps with which the delamination grows for woven G/PA-6 in mode-I delamination.

Material	Thickness mm	Steps
None	n/a	4-6
DC01 steel	1.5	> 20[1]
S700 steel	2	$-$[2]
S235 steel	4.5	$-$[2]
G/PA-6 $[\#(0/90)]_4$	2	10-12

[1] Plastic deformation of the stiffeners
[2] Debonding of the stiffeners

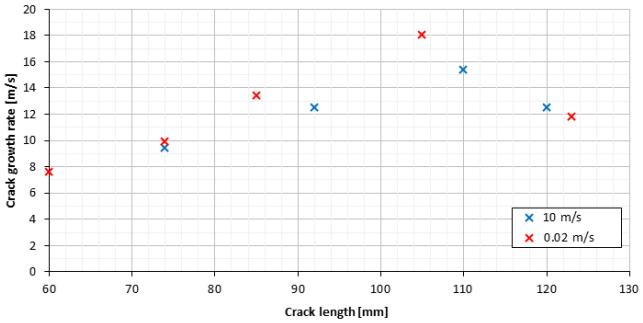

Figure 6.34. Delamination speed versus displacement for a 0.02 *and a* $10\,\mathrm{m\,s^{-1}}$ *test on woven G/PA-6. The cracks propagate in 5 and 4 steps, respectively. The crack speed shows mostly a dependency on its length, not on actuation velocity.*

is applied. The results are shown in table 6.5. Two different thickness values are available for UD G/PA-6. The thick laminate addition results in a disbond. The thin laminate does increase the number of crack steps, though again no continuous crack propagation has been obtained.

It seems that the G/PA-6 laminates cannot be adequately tested for delamination according to the ASTM D5528 test standard, though it is advised to use the recommended minimum thickness, which was not possible here due to manufacturing restrictions. It will follow from the post-mortem inspection of impact test results in chapter 9 that indeed very little delamination shows up in the G/PA-6. One case actually shows an interface crack continuing as a matrix crack, indicating that the interface strength is at least of comparable value as the pure matrix strength. With very little delamination occurring in the material, one can question the need for an investigation of the delamination properties. Further effort towards a successful test method for the delamination of G/PA-6 is therefore considered outside the scope of the current work.

Table 6.5. Result of different stiffening measures on the number of steps with which the delamination propagates for UD G/PA-6 in mode-I delamination.

Material	Thickness mm	Steps
None	n/a	2-4
G/PA-6 $[0]_4$	1.0	6-9
G/PA-6 $[0]_{16}$	3.8	$-$[1]

[1] Debonding of the stiffeners

6.6 Conclusions

Two different test set-ups were evaluated for their applicability to investigate the rate-dependency of the fracture toughness of composite laminates: a drop tower method and the use of a hydraulic pulse machine to apply the standard test at elevated speeds.

The drop tower method is able to delaminate the C/E at different delamination rates, and optical acquisition successfully tracks the position and orientation of the bottom block. The position signal, however, is not smooth enough to extract a useful acceleration history of the bottom block which could be used to compute the force acting on the bottom leg of the DCB specimen. This issue is likely solved when using equipment which can record images of a sufficient resolution at higher frame rates, though such equipment was not available at the time. The data reduction, therefore, relies on a FE-model with an ill-defined condition to introduce the energy into the system, which prevents the model from converging on mesh refinements. The set-up, moreover, is limited to rather stiff composites due to its dimensions, and to interfaces with a rather low fracture toughness due to the limited amount of energy that can be transferred to the bottom block. It is therefore not suitable for G/PA-6.

The hydraulic pulse test bench successfully pulls specimens of both material systems apart, while recording a useful load history. The load signal, however, does require some filtering, especially at higher speeds. Finite element analysis was used to establish a limit on the actuation speed of about $3\,\mathrm{m\,s^{-1}}$, above which the equations used for the quasi-static tests are no longer valid due to the absence of equilibrium. More research is necessary to determine how the fracture toughness could still be extracted from current tests at speeds exceeding the equilibrium condition. The dynamic tests show that the curvature of both legs is also not equal at high speeds, especially in the initial part of the test. This means that the bending moment is not equal in both legs, resulting in a crack propagation which is not pure mode-I. The only way this can be solved is to develop a method in which both legs of a DCB specimen are accelerated with an equal amount in opposite directions.

The hydraulic pulse set-up can successfully test C/E at different speeds. The G/PA-6 material system shows a non-constant crack propagation in only a few steps to failure. This hinders the investigation of rate-dependency because the propagation speed during such a step does not depend on actuation speed. Stiffening the specimens improves the behaviour because an increase in the number of steps is seen, though the problem is not solved because the crack propagation is still far from continuous. It is advised to produce specimens of a greater thickness directly, because the adhesion of stiffening elements to the G/PA-6 specimens is not straightforward. Regrettably, the manufacturer could not supply laminates with a precrack of a greater thickness. Studying delamination of the current G/PA-

6 system is not of the highest interest, however, because it will be shown in chapter 9 that impact loading results in only very limited delamination.

Automated crack front tracking has been attempted using an edge detection algorithm or DIC. Both methods are promising, though fail to produce a reliable result at the low resolutions available. For accurate automatic crack front tracking, again a higher resolution is needed. One could film only a small part of the specimen to partially overcome this issue, though if the crack length is to be automatically tracked from beginning to end, better image acquisition equipment is needed. Manual read-out of the crack length was thus necessary, and although rather time-consuming, it proved to provide reliable results.

Now the test method has been developed and its limits quantified, it can be used to generate data for the two material systems under investigation in the current research. The test campaign and corresponding results for dynamic mode-I delamination are detailed in the next chapter.

References

[1] M. Colin de Verdiere, A. A. Skordos, M. May, and A. C. Walton. *Influence of loading rate on the delamination response of untufted and tufted carbon epoxy non crimp fabric composites: Mode I*. Engineering Fracture Mechanics, 96:11–25, December 2012.

[2] ASTM International. *ASTM Standard D5528, 2007, "Standard Test Method for Mode I Interlaminar Fracture Toughness of Unidirectional Fiber-Reinforced Polymer Matrix Composites"*. Technical report, American Society for Testing and Materials, West Conshohocken, PA, 2007.

[3] Y. M. Le Cahain, J. Noden, and S. R. Hallett. *Effect of insert material on artificial delamination performance in composite laminates*. Journal of Composite Materials, 49(21):2589–2597, September 2015.

[4] J. H. Chen, E. Schulz, J. Bohse, and G. Hinrichsen. *Effect of fibre content on the interlaminar fracture toughness of unidirectional glass-fibre/polyamide composite*. Composites Part A: Applied Science and Manufacturing, 30(6):747–755, June 1999.

[5] G. Hug, P. Thévenet, J. Fitoussi, and D. Baptiste. *Effect of the loading rate on mode I interlaminar fracture toughness of laminated composites*. Engineering Fracture Mechanics, 73(16):2456–2462, November 2006.

[6] P. Navarro, J. Aubry, F. Pascal, S. Marguet, J. F. Ferrero, and O. Dorival. *Influence of the stacking sequence and crack velocity on fracture toughness of woven composite laminates in mode I*. Engineering Fracture Mechanics, 131:340–348, November 2014.

[7] F. Allaeys. *Assessment of the bird strike robustness of turbofan compressor vanes through advanced numerical modelling and extensive calibration testing*. PhD thesis, Ghent University, Ghent, 2016.

[8] Vishay Precision Group. *Special Use Sensors—Crack Propagation Sensors*, July 2014.

[9] S. Fonteyn, L. Pyl, and D. Van Hemelrijck. *Investigation on mode-I fracture toughness of carbon epoxy composites assisted by digital image correlation*. In 17th International Conference on Experimental Mechanics (ICEM17), Rhodes, Greece, 2016.

[10] H. Zabala, L. Aretxabaleta, G. Castillo, and J. Aurrekoetxea. *Loading rate dependency on mode I interlaminar fracture toughness of unidirectional and woven carbon fibre epoxy composites*. Composite Structures, 121:75–82, March 2015.

[11] MatWeb, LLC. *ASTM A284 Steel, grade C*. Technical Report MS284C / 13932, MatWeb, 1999.

[12] R. D. B. Sevenois, D. Garoz, F. A. Gilabert, S. W. F. Spronk, S. Fonteyn, M. Heyndrickx, L. Pyl, D. Van Hemelrijck, J. Degrieck, and W. Van Paepegem. *Avoiding interpenetrations and the importance of nesting in analytic geometry construction for Representative Unit Cells of woven composite laminates*. Composites Science and Technology, 136:119–132, November 2016.

[13] A. Arteiro, G. Catalanotti, A. Melro, P. Linde, and P. Camanho. *Micro-mechanical analysis of the in situ effect in polymer composite laminates*. Composite Structures, 116:827–840, September 2014.

[14] S. Hashemi, A. J. Kinloch, and J. G. Williams. *Corrections needed in double-cantilever beam tests for assessing the interlaminar failure of fibre-composites*. Journal of Materials Science Letters, 8(2):125–129, 1989.

[15] J. G. Williams. *End corrections for orthotropic DCB specimens*. Composites Science and Technology, 35(4):367–376, January 1989.

[16] T. Diehl. *Modeling Surface-bonded Structures with Abaqus Cohesive Elements- Beam-Type Solutions*. In ABAQUS User's Conference, 2004.

[17] A. Turon, C. Dávila, P. Camanho, and J. Costa. *An engineering solution for mesh size effects in the simulation of delamination using cohesive zone models*. Engineering Fracture Mechanics, 74(10):1665–1682, July 2007.

[18] S. Jacques. *Development of a framework for the construction of meso-scale finite element models of textile composites*. PhD thesis, Ghent University, Ghent, 2014.

[19] Kistler Instrumente AG. *Load Washers*, 2016.

[20] L. D. Paarmann. *Design and analysis of analog filters: a signal processing perspective*. Kluwer Academic Publishers, New York, 2003. OCLC: 71229251.

[21] S. I. Thorsson, A. M. Waas, J. Schaefer, B. Justusson, and S. Liguore. *Effects of elevated loading rates on mode I fracture of composite laminates using a modified wedge-insert fracture method*. Composites Science and Technology, 156:39–47, March 2018.

7 Rate-dependency of mode-I delamination properties

7.1 Introduction

In this chapter, the test programme and corresponding results of the dynamic delamination test campaign are presented. Only the hydraulic pulse test method of chapter 6 resulted in values for the fracture toughness, and thus only results of that test method are given in this chapter. As mentioned in the introduction, only mode-I delamination is treated.

First, the test programme is detailed, then the rate dependency of the fracture toughness of each of the tested interfaces is discussed based on the gathered test results.

7.2 Test programme overview

Delamination testing was typically performed at four different speeds for the current research, see table 7.1. Quasi-static testing is done to provide a reference value for the delamination properties. This value allows comparison to the results in literature which are typically quasi-static, and it is needed to discover the magnitude of the possible change in value resulting from executing the tests at a higher speed. As explained in chapter 2, the hydraulic pulse test bench has two modes of operation: a closed-loop-mode for low speeds and an open-loop mode for the

higher speeds. It is decided here to perform tests at the limits of the speed ranges of both control modes. The maximum closed-loop speed amounts to about $0.5\,\mathrm{m\,s^{-1}}$. This velocity is reached almost instantly, and hence the amount of 'slack' between the actuator and rod connected to the bottom leg of a specimen is set to a minimum. In open-loop mode, the bench can actuate its piston between 2 and $20\,\mathrm{m\,s^{-1}}$. As the obtained speed is no longer constant at the upper limit of the test bench, it is decided to operate only up to $15\,\mathrm{m\,s^{-1}}$. In open-loop mode, the piston needs a finite acceleration length to reach the requested velocity.

Per material system, two different interfaces were investigated: a 0-0 and a $\#(0/90)$-$\#(0/90)$ interface. Table 7.1 contains the layups, which contain an insert in the symmetry plane: ETFE for the carbon/epoxy (C/E) and polyimide for the glass/polyamide-6 (G/PA-6) laminates. Different results and a possibly different dependence on test speed are expected, because the unidirectional (UD) interface is rather smooth and constant along its length, while the woven interface will show more variation. This can be attributed to the different fibre orientations and matrix pockets present on the surface, and the nesting of the plies due to the wavy character of the surface.

Laminates typically delaminate at dissimilarly oriented layers, hence the 0-0 interface is not a typically delaminating one in a laminate. Still, it is decided to include this interface rather than, for example, a 0-90 interface, because the crack in the latter is known to deviate from the mid-plane and thus pose additional difficulties for the test campaign. Only the 0-0 interface, moreover, is advised by the test standard.

The typical specimen shape including blocks was given in chapter 6, see figure 6.1. The measured specimen dimensions are summarized in table 7.2.

Table 7.1. Aimed mode-I delamination test programme. A red colour indicates there is no equilibrium in the specimen, a green colour a non-constant crack growth. Blue indicates both effects play a role at the same time.

Layup	**Aimed test speed**			
	0.0001	**0.1**	**1**	**15**
C/E $[0]_{18}$	5	5	5	5
C/E $[\#(0/90)]_{9s}$	5	5	5	5
G/PA-6 $[0]_{16}$	5	5	5	5
G/PA-6 $[\#(0/90)]_{4s}$	5	5	5	5

Table 7.2. Average dimensions and coefficients of variation (in grey) of the dynamic delamination specimens. If one would include the stiffening elements in the layup of the woven G/PA-6, its laminate notation would become: $[\#(0/90)]_{8s}$ *(i.e. a doubling of the number of layers).*

			Average [mm]		
	Layup	**# plies**	L	W	t
C/E	$[0]_{18}$	18	149.84 0.08	24.94 0.06	4.172 0.86
	$[\#(0/90)]_{9s}$	18	149.97 0.05	24.97 0.07	4.013 0.92
G/PA6	$[0]_{16}$	16	149.91 0.03	24.92 0.08	3.92 0.94
	$[\#(0/90)]_{4s}$*	8	149.89 0.15	25.07 0.32	8.346 1.87

* Plus woven G/PA-6 stiffening elements

7.3 Rate-dependency of the tested interfaces

As concluded in chapter 6, the fastest speed is not expected to lead to correct results as the specimen will not be in equilibrium, therefore the corresponding column has been coloured red in table 7.1. The G/PA-6 laminates could not be made to crack in a continuous manner: the delamination in these materials always propagated in a few steps (indicated by a green colour in table 7.1). Specimens for which both effects are present are coloured red in the table. As mentioned in chapter 6, the rate in the term 'rate-dependency' refers to the rate of delamination growth, or delamination speed. The rate-dependency of the G/PA-6 laminates can, therefore, not be investigated with the current test method. It was namely shown that the crack propagation speed depends merely on crack length, and not on actuation speed (section 6.5.4). Still, a limited number of specimens have been tested to estimate the fracture toughness of the material.

The delamination results of the two materials and the two laminate types per material system are discussed in the following subsections. A third-order Butterworth filter was used to smoothen the force data for the non-quasi-static tests, with a cut-off frequency of 300 Hz [1]. The data of each test was recorded with 1×10^6 samples, which were reduced to 1000 after filtering.

7.3.1 Carbon/epoxy

The C/E laminates have a relatively high bending stiffness, owing to the high Young's modulus of the carbon fibres. It is therefore expected that only small dis-

placements suffice to delaminate the specimens. The interface is relatively weak: typically a fracture toughness of about $200\,\mathrm{J\,m^{-2}}$ is found for $0°$ UD C/E [2, 3] and about $450\,\mathrm{J\,m^{-2}}$ for woven C/E, and hence it is expected that the forces occurring will also be small. As shown in chapter 3, there is no consensus in literature about the rate-dependency of the fracture toughness of C/E laminates, and typical changes are small (i.e. [4]). This indicates a possible absence of rate-effects.

UD interface

The four speeds in table 7.1 have been applied in the delamination test campaign for $0°$ UD C/E. The load has been set out against the crack length for the quasi-static tests in figure 7.1. It can be seen that typically, the load required to propagate the crack runs from about $80\,\mathrm{N}$ initially to about $40\,\mathrm{N}$ near complete failure.

Typically, the specimens were precracked to a length of $46\,\mathrm{mm}$. Specimens P2-4 and P2-3, however, were (erroneously) precracked to 37 and $65\,\mathrm{mm}$, respectively. The results for P2-4, with a short precrack distance, initially surpass the values of the other specimens. The results of P2-3, the further precracked specimen, lie beneath those of all other specimens. This difference is attributed to fibres which bridge the crack from flank to flank which are abundantly present for P2-4, while there would be less bridging for P2-3. The precracking is namely followed by an unloading step which brings both crack flanks together again. This causes the bridging fibres to be loaded in compression, and it is assumed that most of them consequently fail during this unloading step. This implies that bridging fibres will only exist from the end of the precrack onwards during the subsequent crack propagation test. Hence, the propagation load for a certain crack length decreases with increasing precrack length. The fact that the results of P2-3 remain below those of the other specimens up to its maximum renewed crack growth of about $55\,\mathrm{mm}$, suggests that some fibres still bridge the crack as far as $55\,\mathrm{mm}$ away from the crack

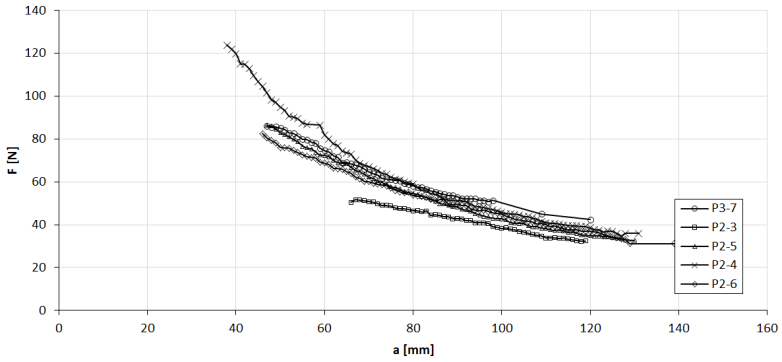

Figure 7.1. Force versus delamination length for C/E $0°$ *UD tested at* $0.0001\,\mathrm{m\,s^{-1}}$.

tip. As is shown later in this section, the amount of bridging is indeed large.

As with the dynamic tensile tests, the current test series was carried out with a slack rod to allow the piston to speed up before actuating the specimen. Although the slack rod was only needed to provide a short acceleration distance for the faster tests, it was installed during the entire test programme. The tight tolerances on the new grips (figure 6.24), however, caused the friction of the slack rod to be higher than usual. The small forces required to pull the specimens apart resulted in a relatively large influence of these friction loads on the slack rod on the result - either during actuation or during load balancing. Regrettably, a large portion of the test programme had been carried out before this issue had been resolved by relaxing the tolerances on the grips. Only the quasi-static tests, two tests at $0.1\,\mathrm{m\,s^{-1}}$, and the tests at the highest velocity were carried out with reduced rod friction. The force measurement at $15\,\mathrm{m\,s^{-1}}$, however, cannot be used due to the absence of equilibrium in the sample (see for illustration the result for the fastest simulation in figure 6.30).

The resulting test programme is left with seven data sets. The R-curves belonging to these sets are displayed in figure 7.2. Specimens P1-8 and P1-4 were precracked to 34 and $41\,\mathrm{mm}$, respectively. The quasi-static data underlines the importance of precracking when crack bridging is relevant, as the precrack length has a large influence on the resulting energy release rate: the curve for P2-3 lies about $100\,\mathrm{J\,m^{-2}}$ below the average of the other four curves at the same speed. Table 7.3 contains the average results for this test series. The delamination speed is computed by taking the slope of the linear least-squares fit to the delamination versus time, see figure 7.3. It thus constitutes an average crack speed. Note that the actual crack speed is not constant. The table shows that the average delamination speed equals about five times the actuation velocity.

FE-analysis suggests that the effect of kinetic energy plays an insignificant role on the data reduction at test speeds below $2\,\mathrm{m\,s^{-1}}$ (section 6.5.3). Hence, the results in table 7.3 suggest a decrease of fracture toughness by $14\,\%$ with respect to the quasi-static value when the delamination speed increases to $0.7\,\mathrm{m\,s^{-1}}$. Indeed, the two curves for an actuation velocity of $0.1\,\mathrm{m\,s^{-1}}$ in figure 7.2 lie at a rather low energy release rate. Without rate-dependency, they would be expected to lie at the level of specimen P2-4, considering their precrack length. To definitively

Table 7.3. Fracture toughness values determined from average plateau energy release rate for C/E 0° UD.

$v\,[\mathrm{m\,s^{-1}}]$	$\frac{da}{dt}\,[\mathrm{m\,s^{-1}}]$	$G_{Ic}\,[\mathrm{J\,m^{-2}}]$
0.0001	0.0005	246
0.1	0.7	211

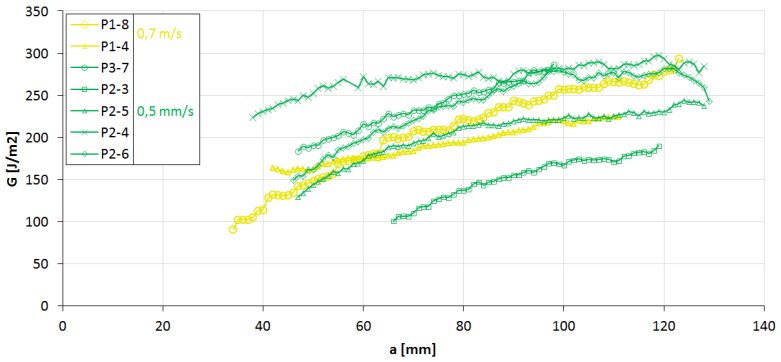

Figure 7.2. Energy release rate for C/E $0°$ *UD tested at* 0.0001 *(green) and* $0.1\,\mathrm{m\,s^{-1}}$ *(yellow). The legend indicates the average delamination rate.*

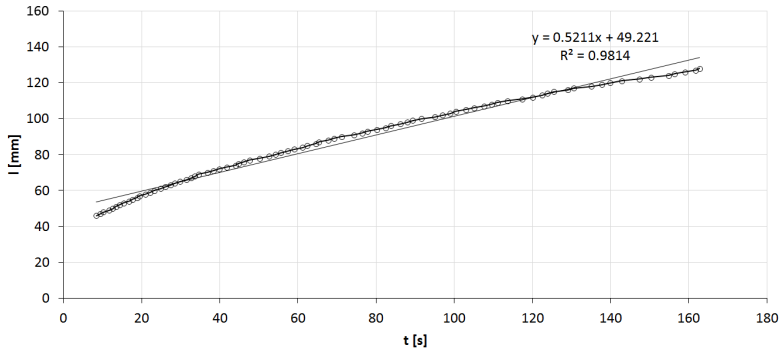

Figure 7.3. Crack length versus time and linear approximation for a C/E $0°$ *UD specimen tested at* 0.0001 *(P2-5).*

conclude on the rate-dependency of the fracture toughness, a new test series should be carried out to retrieve five correct results per test speed, carefully precracked to the same delamination length.

Finally, the amount of bridging is visualised by taking an image of a specimen during quasi-static delamination, see figure 7.4a. There is a clear amount of bridging, which spans about $80\,\mathrm{mm}$, supporting the earlier claim that fibre bridging is significantly affecting the test results. Whether the amount of bridging changes with rate cannot be determined from the high-speed footage, because the resolution and the brightness are too low to see whether bridging fibres are present or not at high speed. The crack surface shows hardly any variation in the lengthwise direction, which indicates that the crack progression occurred rather smoothly.

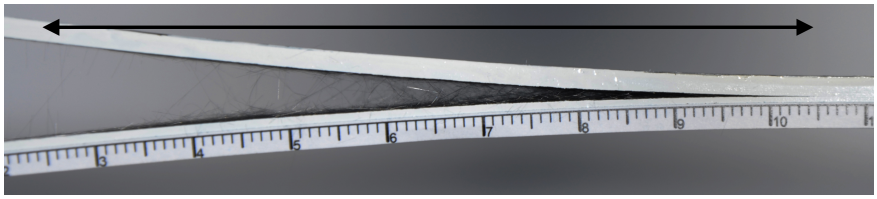

a. About $80\,\mathrm{mm}$ *of distance is measured between the crack tip and the furthers bridging fiber (see arrow).*

b. The crack surface is smooth, indicating a very continuous crack propagation.

Figure 7.4. Mode-I delamination of C/E UD.

Woven interface

The woven C/E was chosen as initial material for the drop tower test campaign. As explained in section 6.4, this method did not result in accurate force measurements. Some remaining specimens were tested in the hydraulic pulse test bench with relaxed grip tolerances to reduce friction, as explained above. Two test speeds were applied: 0.0001 and $0.5\,\mathrm{m\,s^{-1}}$. It was decided to test at the latter speed as it constitutes the fastest test in the low-rate setting of the test bench, providing a rather constant speed and a relatively low amount of noise on the force signal, compared to higher speeds.

The typical force-displacement behaviour of a quasi-static test on the woven C/E is shown in figure 7.5. The figure shows that the crack propagation is not

continuous, though it progresses in many steps and some continuous propagation is seen between the steps, so it is decided to continue. The force history of a test at $0.5\,\mathrm{m\,s^{-1}}$ is given in figure 7.6. The amount of noise has strongly increased and filtering is necessary to obtain a useful result. The different steps in crack propagation can no longer be discerned from either the filtered or the unfiltered data, though the footage suggests the growth is still not entirely smooth.

Figure 7.7 shows the R-curves and table 7.4 contains the average plateau values of energy release rate for the woven C/E tested at two speeds. The quasi-static value lies close to the preliminary test result given in section 6.3. A clear difference is seen between the groups of results: the fracture toughness has decreased by $32\,\%$ at $0.5\,\mathrm{m\,s^{-1}}$ with respect to the quasi-static case. The filtering of force might be contributing to this reduction: the FE results of the more finely meshed model in figure 6.29 show that the obtained R-curve lies partly slightly below the theoretical one. This difference, though, amounts to about $10\,\mathrm{J\,m^{-2}}$, so the measured reduction of $88\,\mathrm{J\,m^{-2}}$ in the test results is considered significant.

A specimen during and after failure is shown in figure 7.8. Figure 7.8a shows that some fibre bridging does occur, though it is very small: the furthest bridging fibres can be found only up to $7\,\mathrm{mm}$ from the crack tip. The crack surface in figure 7.8b reveals the cause of the discontinuous delamination growth: the delamination surface is not smooth but has an imprint of the weave architecture in it. This shows that the delamination follows the fibre-matrix interface rather than a straight path between the layers. As it is very unlikely that the stress situation at the delamination front is constant as it moves along this wavy path, this is seen as the cause of the intermittent crack propagation.

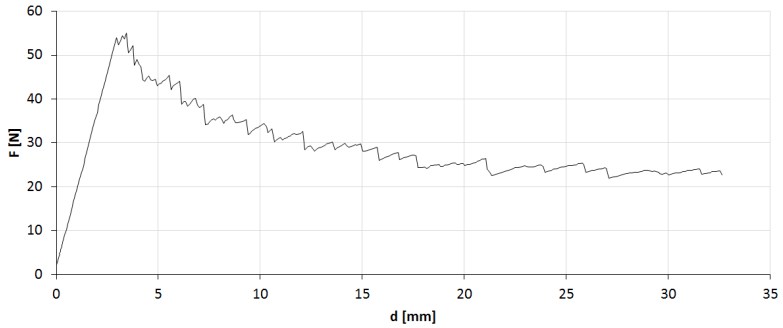

Figure 7.5. Force versus displacement for C/E $\#(0/90)$ (specimen C1-2) tested at $0.0001\,\mathrm{m\,s^{-1}}$.

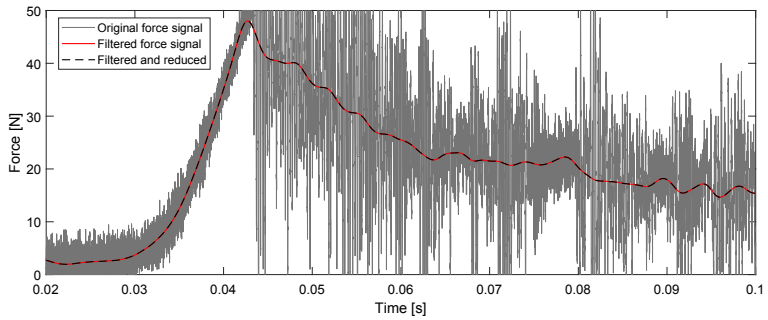

Figure 7.6. Force versus time for C/E $\#(0/90)$ *(specimen U9) tested at* $0.5\,\mathrm{m\,s^{-1}}$.

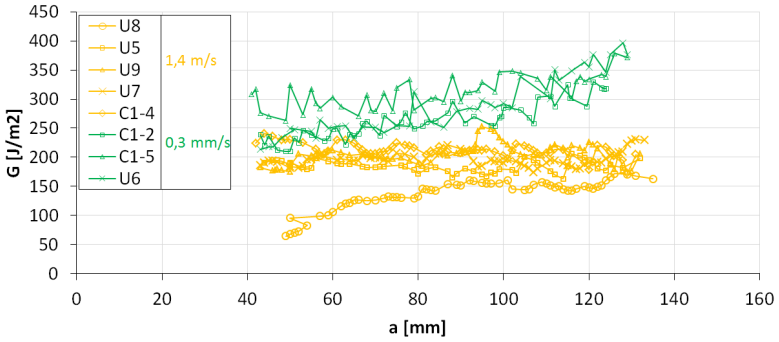

Figure 7.7. FEnergy release rate for C/E $\#(0/90)$ *tested at* 0.0001 *(green) and* $0.5\,\mathrm{m\,s^{-1}}$ *(yellow). The legend indicates the average delamination rate.*

Table 7.4. Fracture toughness values determined from average plateau energy release rate for C/E $\#(0/90)$.

$v[\mathrm{m\,s^{-1}}]$	$\frac{da}{dt}[\mathrm{m\,s^{-1}}]$	$G_{Ic}[\mathrm{J\,m^{-2}}]$
0.0001	0.0003	278
0.5	1.4	190

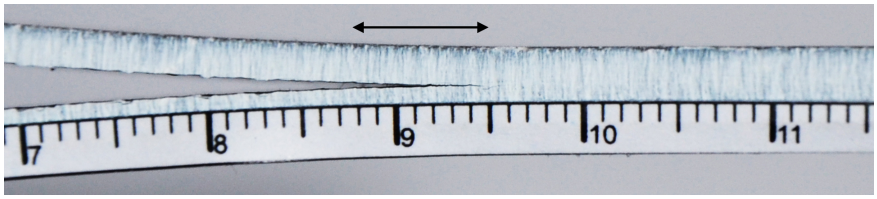

a. Woven C/E shows very little crack bridging.

b. The weave pattern is embossed on the crack surface, and is the cause of discontinuous crack propagation.

Figure 7.8. Mode-I delamination of woven C/E.

7.3.2 Glass/polyamide-6

As mentioned before, the G/PA-6 materials only crack in a stepwise manner, and this behaviour was slightly improved by stiffening the samples, though no continuous cracking was obtained. This section compares the results of unstiffened DCB specimens with those from stiffened specimens where the stiffening layers did not debond (see also tables 6.4 and 6.5). The modified beam theory from the ASTM D5528 test standard is applied [5] since the stiffening layers were made of the same laminates as the specimens itself. The results are characterised by the average crack propagation speed, even though this is not an accurate measure for the delamination rate, because of the stepwise growth. The peak values during unstable propagation are, however, approximately equal for different actuator speeds, see figure 6.34. The crack propagation speed would hence not be suitable to distinguish different tests for the G/PA-6 material.

No records could be found in the literature describing the rate-dependency of the delamination behaviour of G/PA-6. The quasi-static fracture toughness is expected to lie around $2.6 \times 10^3\,\mathrm{J\,m^{-2}}$ [6]. The available literature that describes the rate-dependency of composites with a thermoplastic matrix typically concerns UD carbon/PEEK, which has a comparable fracture toughness to G/PA-6. The conclusions differ though: some suggest a reduction of the fracture toughness with rate [3, 7], while others conclude on rate-independency [2, 8].

UD interface

Several preliminary tests were executed on $0°$ UD G/PA-6, of which three resulted in a successful crack propagation without debonding of the stiffening layers. One (specimen 2) was tested without stiffening layers, and the two others (specimens 31 and 33) with four $0°$ UD G/PA-6 stiffening layers on each leg. The R-curves are given in figure 7.9, the corresponding plateau energy release rate values in table 7.5. The curves show very few data points, only taken at the peak load values just before unstable crack propagation. The obtained fracture toughness approaches the expected value from literature, though it is on the low side for the unstiffened specimen, possibly due to the excessive specimen bending (see also figure 6.23). The results for the stiffened specimens namely lie above those for the regular specimen.

Figure 7.10a shows that the G/PA-6 UD experiences fibre bridging along about $35\,\mathrm{mm}$ of specimen length. Since it concerns a UD material, significant fibre bridging was expected. The figure also shows that the two halves of the specimen bend rather far apart (compare to the pictures for C/E in the previous section). Figure 7.10b shows how the delaminated surface looks after testing. There are some clear lines across the width of the specimen, which correspond to the areas where the delamination tip arrested.

As mentioned before, no more investigation was done on the rate-dependency of the fracture toughness of UD G/PA-6, since the delamination propagation speed was found to be independent of the actuation velocity due to the discontinuous crack growth. Using more stiffening layers resulted in a further improvement of cracking behaviour, though the thickness was tripled this time since the only other available UD material was the undelaminated portion of the same plate. This caused such a strong stiffness increase that the stiffening layers debonded during the process. It is advised to find a way to produce thicker samples to investigate the rate-dependency of this material and prevent the need for a strong adhesive bond between the specimen and stiffening layers.

Table 7.5. Fracture toughness values determined from average plateau energy release rate for G/PA-6 $0°$ UD.

Specimen type	$G_{Ic}[\mathrm{J\,m^{-2}}]$
Unstiffened	1.5×10^3
Stiffened	2.0×10^3

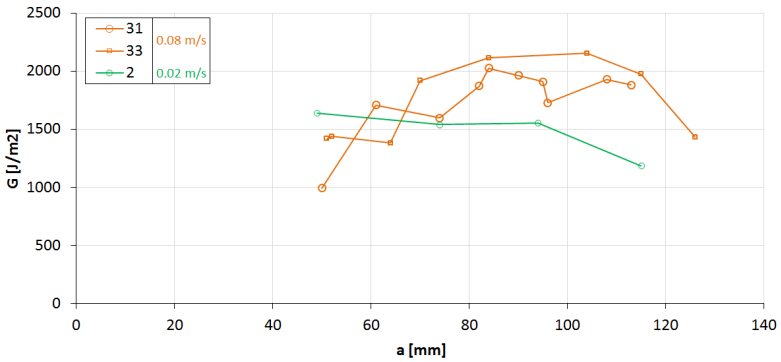

Figure 7.9. Energy release rate for G/PA-6 $0°$ UD tested quasi-statically with no stiffening (green) or with 4 $0°$ UD G/PA-6 stiffening layers (orange). The legend indicates the average delamination rate.

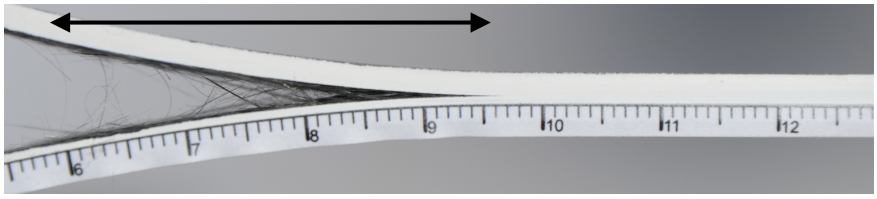

a. About $35\,\mathrm{mm}$ of crack bridging is seen for G/PA-6 UD.

b. The crack surface shows clear transverse lines where the crack has arrested during testing. This specimen cracked in four steps.

Figure 7.10. Mode-I delamination of G/PA-6 UD.

Woven interface

As the tests on woven G/PA-6 resulted in slightly more crack steps than for the UD variant, it was decided to test the stiffened version at all speeds mentioned in table 7.1 to see if there would be any rate-dependency regardless of the fact that the crack propagation speed does not seem to depend on actuation velocity. All specimens were stiffened by adhering a laminate of four-layers G/PA-6 $\#(0/90)$ to either side. As the peaks and valleys were no longer distinguishable in the load signal at the higher speeds, it was decided to base the fracture toughness value on

all data.

Figure 7.11 contains the R-curves of the test series, and table 7.6 the average plateau energy release rate for each test speed. As mentioned before, testing at the highest rate (actuation at $15\,\mathrm{m\,s^{-1}}$) did not produce useful test results. These are therefore not included here. The graphs show a considerable amount of noise, owing to the combination of peak and valley data in a single overview. Still, a trend can be discerned, which also appears in table 7.6: a reduction of $24\,\%$ of the fracture toughness is seen when comparing the result at $1\,\mathrm{m\,s^{-1}}$ with the quasi-static one. Since the delamination velocities hardly change between tests of different actuation speeds, it becomes clear that the delamination velocity is not an accurate quantity to describe the rate-dependency of mode-I delamination. Something independent of crack propagation speed must be the cause for the rate-dependency. Perhaps the stiffness of the material (locally) varies due to its dependency on strain rate, causing this change to appear. The tensile Young's modulus was found, however, not to depend strongly on strain rate (see also table B.3 in the appendix).

Figure 7.12a visualizes the crack bridging occurring for a woven G/PA-6 specimen. Clearly some crack bridging still occurs: fibres that span both halves of the specimen are seen up to about $26\,\mathrm{mm}$ from the delamination tip. The dense zone close to the tip is an entire tow, which is still partially attached to either flank of the delamination. The delamination passed underneath this tow on the side from which the photo was taken, but above the tow on the other side of the specimen. This could cause a significant rise in the energy required to delaminate the specimen. A reduction in the amount of bridging is also sometimes given as a possible cause of rate-dependency of delamination properties [4], which could thus be the case here as well. The fracture surface is depicted in figure 7.12b. It shows a very irregular pattern, indicating that (1) the production quality is not as high as was seen for the C/E materials, and (2) there are many zones where a delamination could arrest due to a locally high bond strength.

Table 7.6. Fracture toughness values determined from average plateau energy release rate for G/PA-6 $\#(0/90)$.

$v[\mathrm{m\,s^{-1}}]$	$\frac{da}{dt}[\mathrm{m\,s^{-1}}]$*	$G_{Ic}[\mathrm{J\,m^{-2}}]$
0.0001	0.0001	3.4×10^3
0.1	0.02	2.8×10^3
1	0.8	2.6×10^3

* Average value during entire test duration

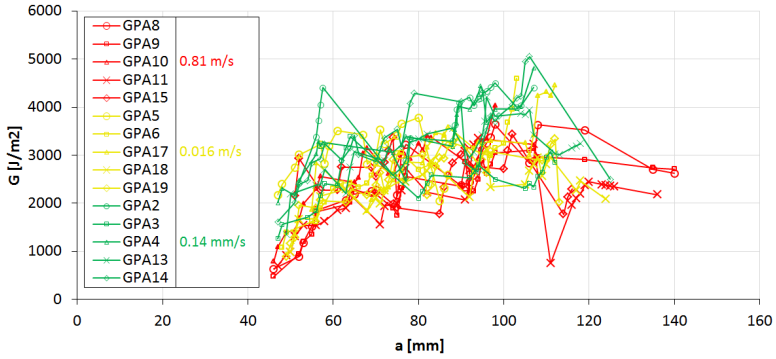

Figure 7.11. Energy release rate for G/PA-6 $\#(0/90)$ tested at 0.0001 (green), 0.1 (yellow) and $1\,\mathrm{m\,s^{-1}}$ (red) with a 4 G/PA-6 $\#(0/90)$ stiffening layers. The legend indicates the average delamination rate.

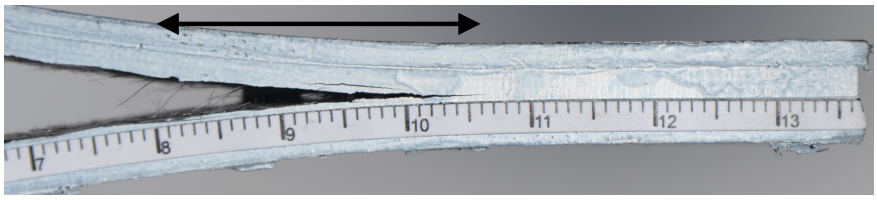

a. About $26\,\mathrm{mm}$ of crack bridging is seen for woven G/PA-6. The stiffening layers can also be seen in the picture. Notice a dense zone of bridging close to the tip.

b. The weave pattern clearly appears on the delamination surface. It is not nearly as regular as the for woven C/E in figure 7.8b.

Figure 7.12. Mode-I delamination of woven G/PA-6.

7.4 Conclusion

The hydraulic pulse test bench was employed to investigate the influence of actuation speed on the fracture toughness of a $0°$ unidirectional and a $\#(0/90)$ woven interface of carbon/epoxy and glass/polyamide-6 laminates.

Although the loading at high speed was no longer pure mode-I and the crack propagation for the glass/polyamide-6 laminates was not continuous, still the conclusion can be drawn that for the materials investigated, the fracture toughness decreases with rate in the range of actuation speeds from quasi-static to $1\,\mathrm{m\,s^{-1}}$. For carbon/epoxy, a decrease of $14\,\%$ was seen for the unidirectional, and $32\,\%$ for the woven interface. For woven glass/polyamide-6, a decrease was seen of $24\,\%$. This rate-dependency might be caused by a change in the amount of bridging with testing speed, though more research is necessary to prove this claim, because the resolution and the brightness of the high-speed footage are too low to see whether bridging fibres are present or not at high speed.

The average delamination speed was selected as the governing parameter for the rate-dependency of fracture toughness. The glass/polyamide-6 showed a reduction in the results despite of the absence in variation of delamination speed between different actuation speeds. The crack propagation speed is therefore likely not the best value to assess rate-dependency with.

References

[1] L. D. Paarmann. *Design and analysis of analog filters: a signal processing perspective*. Kluwer Academic Publishers, New York, 2003. OCLC: 71229251.

[2] J. W. Gillespie Jr., L. A. Carlsson, and A. J. Smiley. *Rate-dependent mode I interlaminar crack growth mechanisms in graphite/epoxy and graphite/PEEK*. Composites Science and Technology, 28(1):1–15, 1987.

[3] S. Mall, G. Law, and M. Katouzian. *Loading Rate Effect on Interlaminar Fracture Toughness of a Thermoplastic Composite*. Journal of Composite Materials, 21(6):569–579, January 1987.

[4] S. I. Thorsson, A. M. Waas, J. Schaefer, B. Justusson, and S. Liguore. *Effects of elevated loading rates on mode I fracture of composite laminates using a modified wedge-insert fracture method.* Composites Science and Technology, 156:39–47, March 2018.

[5] ASTM International. *ASTM Standard D5528, 2007, "Standard Test Method for Mode I Interlaminar Fracture Toughness of Unidirectional Fiber-Reinforced Polymer Matrix Composites"*. Technical report, American Society for Testing and Materials, West Conshohocken, PA, 2007.

[6] H. Wittich, M. Evstatiev, E. Bozwelieva, K. Friedrich, and S. Fakirov. *Effect of crystallinity on the interlaminar fracture toughness of continuous glass fiber-polyamide composites*. Advanced Composite Materials, 2(2):135–152, January 1992.

[7] R. Frassine, M. Rink, and A. Pavan. *Viscoelastic effects on the interlaminar fracture behaviour of thermoplastic matrix composites: II. Rate and temperature dependence in unidirectional PEEK/carbon-fibre laminates*. Composites Science and Technology, 56(11):1253–1260, January 1996.

[8] S. Hashemi, A. Kinloch, and J. Williams. *The Effects of Geometry, Rate and Temperature on the Mode I, Mode II and Mixed-Mode I/II Interlaminar Fracture of Carbon-Fibre/Poly(ether-ether ketone) Composites*. Journal of Composite Materials, 24(9):918–956, September 1990.

8 Low-velocity impact

8.1 Introduction

The final load case of the current research concerns out-of-plane low-velocity impact. This chapter contains the explanation of the test method, data acquisition, data reduction and post-mortem inspection for this type of test. As the available drop-weight impact tower needed a revision, the discussion is preceded by a section which describes the development of a new drop tower. Chapter 9 contains the results and discussion of the test campaign and the post-mortem inspection.

8.2 Goal

The goal of the impact campaign is twofold. On one hand, the damage due to impact should be characterised to know how the composites from the previous chapters behave during impact. This allows the validation of predictive finite-element (FE) models for composite (automotive) structures undergoing impact situations. On the other hand, in line with the other two test methods in this dissertation, it should be found out if the damage behaviour of the composite depends on impact speed.

8.3 Method

As mentioned in chapter 1, this chapter focuses on transverse out-of-plane impact. The ASTM D7136 test standard [1] seems most applicable to study this material behaviour, even though the boundary conditions prescribed by the standard (simple support) aim to simulate part of a stiffened panel typically seen in aircraft structures rather than automotive parts. The usual way to carry out tests according to the standard is using a pure gravity-operated drop tower.

Figure 8.1 shows how the test standard prescribes the specimen support. A rectangular cut-out of 125 by $75\,\mathrm{mm}$ is made in a steel support plate, onto which the specimen can be placed. The specimen dimensions are 150 by $100\,\mathrm{mm}$, and it thus covers the entire cut-out with a $12.5\,\mathrm{mm}$ overlap along its perimeter. Four rubber-tipped clamps are positioned with their tips touching the specimen above this overlap at two locations on either long edge of the specimen. They are configured such that they exert minimal force on the specimen in closed configuration so that they only prevent it from moving up or sideways. Some amount of rotation is thus possible, and as such they create a representation of a simple support boundary condition along the edges of the specimen.

The influence of testing speed on the composite behaviour will be investigated in two ways. First, the impactor will be dropped from several heights to make it hit the specimen at different speeds. The downside of this method is that the range of speeds is rather limited: the highest speed depends on the size of the tower, and the lower bound of the speed is formed by the fact that a too small drop height no longer damages the specimen. Therefore, it is decided to add another method to test the behaviour at very low speeds: quasi-static indentation. The ASTM D6264 test standard [2] is followed for this test. The boundary conditions (both the specimen support and the indentor) are taken the same as for the impact.

The composite behaviour will be characterised by the force-displacement results generated by the tests. Impact experiments will be accompanied by a visual

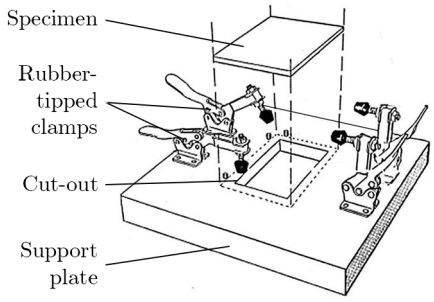

Figure 8.1. Specimen support according to ASTM D7136 [1].

recording of the specimen surface during the test to capture any damage visibly occurring at its surfaces. Curling-up of the corners will also be captured optically. The damage will be characterised by post-mortem inspection using both destructive and non-destructive techniques.

8.4 Development of a drop tower

An in-house developed drop tower was available at UGent, which could drop a $7.72\,\mathrm{kg}$ instrumented impactor onto a support structure (figure 8.2). The drop-weight could be moved to the desired height using a manual winch, and released by powering a permanent electromagnet which causes it to temporarily lose its magnetic attraction. It could prevent a second impact after rebound by the extension of two clips, onto which the drop-weight would impact after they have extended some time after impacting the specimen. An anti-rebound system is necessary to make the impactor hit the specimen only once and facilitate the analysis and subsequent modelling. The problem with this method of catching the impactor, though, is that it exerts high forces on the support structure. In case of the original drop tower, the support structure consisted of two separate frames suspended from a wall, with each frame supporting a rail to guide the impactor. The large forces coming from the anti-rebound system catching the impactor were assumed to be the cause of the fast misalignment of the two guiding rails, resulting in a large spread of the impact velocity when testing from a certain drop height. The bearings, moreover, which sled over the rails, were not designed to handle the speeds that were seen during an impact test, and would show significant wear over time.

The support structure can be seen in the bottom of figure 8.2. A barrel sits on the ground and is closed off on the top with a round plate. This round plate contains a square cut-out into which a specimen support plate is positioned. Although in the picture the dynamic delamination set-up is mounted (see chapter 6), for the current research, the specimen support plate is made to comply to the ASTM D7136 test standard and thus contains a rectangular cut-out and rubber-tipped clamps as depicted in figure 8.1. Figure 8.2 shows that the barrel has a cut-out on its side, and there is another on the other side. These cut-outs allow obtaining a visual of the bottom of the impacted specimen by use of a mirror at 45 degrees.

The beginning of this section makes it clear that a new drop tower was needed for the execution of an impact test programme with consistent results. The goal of the new design is to create a set-up that can facilitate dropping an impactor of about $10\,\mathrm{kg}$ from at least $2\,\mathrm{m}$ onto the existing specimen support structure while remaining aligned and sustain possible wear for a prolonged period of time. This amounts to impacts up to about $200\,\mathrm{J}$. Other requirements are:

- the set-up should be safe to operate;

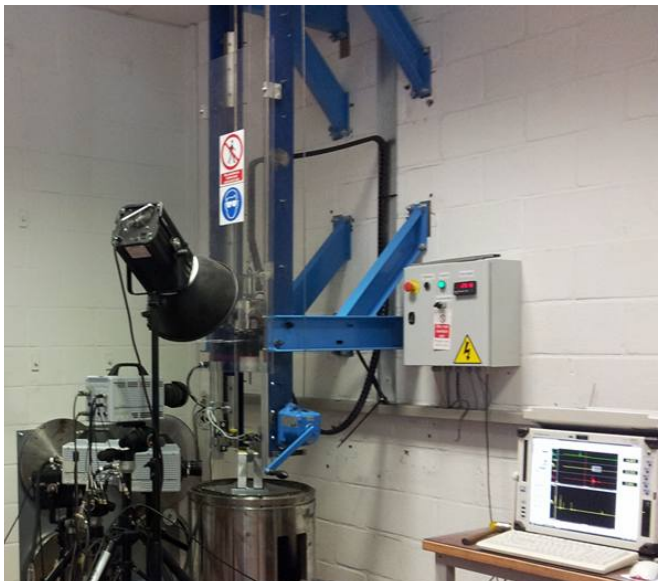

Figure 8.2. Original drop-weight set-up at UGent-MMS

- load, acceleration and displacement should be measured by a renewed use of all the sensors from the original drop tower;
- the impactor eigenfrequency should be as high as possible;
- the frame should fit between floor and ceiling of the laboratory;
- a second rebound should be prevented;

8.4.1 Support frame

The support frame should provide a stable base for the guiding system of the impactor. The guidance, in turn, should block any other movement other than a vertical displacement of the impactor. Typical commercially available drop towers (Instron, Zwick, Imatek, ...) use two columns to guide the drop-weight on either side, and these columns are supported on their top and bottom by a single support structure which surrounds the columns and rests on the floor. Although some guidance systems allow to support the impactor only on one side, it is decided to guide it also on two sides for the current set-up. A single-sided suspension namely has the drawback that the guidance sees a moment load for every impact because the centre of mass is away from the support point, which would not aid the durability of the set-up.

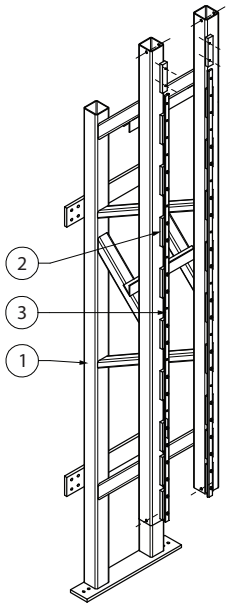

Figure 8.3. Frame design of the new drop tower. 1 is the welded frame, 2 are the guidance rail support blocks, and 3 are the guidance rails.

In contrast to the original drop tower, the new support frame consists of a single structure of beams welded together to ensure continued alignment (figure 8.3). It will be supported on the ground and attached to the wall, so the area on the operator-side of the specimen is kept entirely free to allow the greatest versatility of specimens and support structures to perform impact experiments on. The alignment of the longitudinal beams of the frame is not ensured due to deformation resulting from the welding process. Small blocks are therefore welded to them, of which the inner and front surfaces are aligned by a final milling procedure.

It was decided that a vertical guidance with (1) a minimal number of parts and (2) a support along its entire length is optimal. Support along the rails is necessary in the current case, as there is no big rigid structure at the bottom end of the rails. The system that complies to these requirements is a set of rails with a v-shape (item 3 in figure 8.3) onto which wheels with a w-shape (item 2 in figure 8.4) can roll. This provides all the required boundary conditions with minimal parts for a rail that is supported along its length: four wheels and two rails. The wheels namely prevent the impactor from moving to the front or back because the groove fits around the v-shape of the rails. Two wheels are taken with an eccentric centre bolt to allow fine-tuning of the clearance between wheels and rails.

8.4.2 Impactor

To obtain a natural frequency which is as high as possible, it was decided to produce most of the impactor from a single solid piece of steel. A drawing of the impactor is given in figure 8.4. A T-shaped cross-section is chosen for the body of the impactor. Most of the production steps can hence be carried out from one side to facilitate the fabrication of the part. The shape is designed such, that the wheels align with the impactor's centre of mass.

Figure 8.5 contains an impression of the impactor body. The flanges have two horizontal threaded holes each to hold the wheels. Four large vertical holes are made in the centre part of the impactor to facilitate the placement of sensors. The two outer holes are through from top to bottom so that wires can run from the load cell at the bottom to the wire attachment point envisioned at the top back of the part. The load cell (number 12 in figure 8.4) is attached with a screw thread to a conical part (number 9 in figure 8.4). This part is in turn screwed into the third hole in the impactor, positioned on the bottom between the two first holes and threaded to accept the male thread on the conical piece. A fourth hole is made on the top of the body between the two first holes, and visible in figure 8.5. This is a large hole with a small threaded hole at its bottom to attach an accelerometer in approximately the centre of mass of the assembled impactor, see also region A in figure 8.4. The holes to the right in figure 8.5 accept the attachment of a displacement sensor, indicated in figure 8.4 with number 1 on the left side. The idea behind this placement is that the corresponding strip it senses to determine its position can be attached to the rear of the guiding rail for accurate positioning.

The geometry of the assembled impactor was imported as a single part into a finite-element analysis software to determine the lowest natural frequency associated with a vertical impact load on the bottom of the pin. The entire part was given the material properties of isotropic steel ($E = 205\,\mathrm{GPa}$, $\nu = 0.286$, $\rho = 7.85 \times 10^3\,\mathrm{kg\,m^{-3}}$). The part was left completely free to move by an absence of boundary conditions. A discretization into full-integration tetraeder elements (C3D10) with an approximate edge length of $4\,\mathrm{mm}$ was considered converged, as an analysis with a $6\,\mathrm{mm}$ mesh yielded comparable results. The Lanczos algorithm was used in a first step to extract the 50 first natural mode shapes and corresponding frequencies, which were fed into a subsequent modal dynamic analysis step to investigate the frequency response to an impact. The second step used a vertical impulse load of $1\,\mathrm{N}$ on the bottom of the impactor tip to excite the natural modes. A time frame of $0.01\,\mathrm{s}$ was simulated, which is longer than the typical impact duration. All the modes were damped with a small factor of 0.01. The acceleration at the tip of the impactor pin was used to characterise the vibration of the model. The lowest natural frequency appearing in the signal (excluding the peak at zero frequency) was found to lie at about $2.9 \times 10^3\,\mathrm{Hz}$ (figure 8.7), well above the natural frequency of the original impactor, see section 8.4.4.

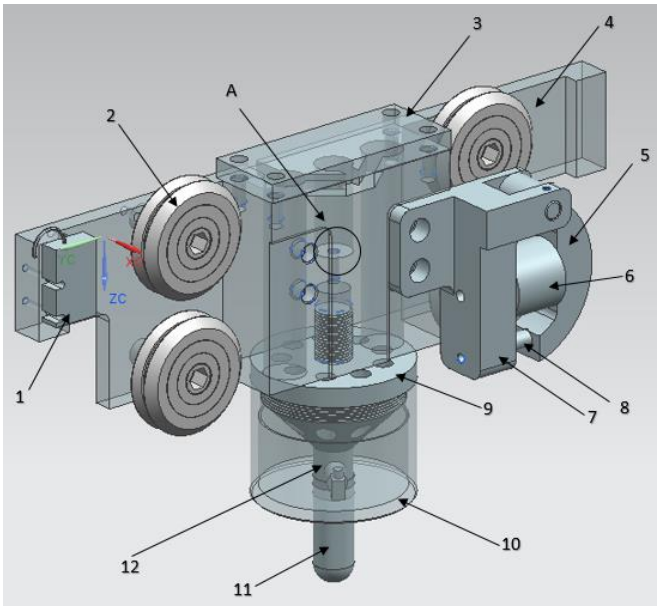

Figure 8.4. Rear view of the impactor design of the new drop tower, without the left part of the anti-rebound assembly and with translucent parts. 4 is the impactor body from a single piece (see figure 8.5), 2 are the w-groove guidance wheels, 1 is the displacement sensor, 5-8 form the anti-rebound assembly (see also section 8.4.3), and 9-12 the load sensing assembly.

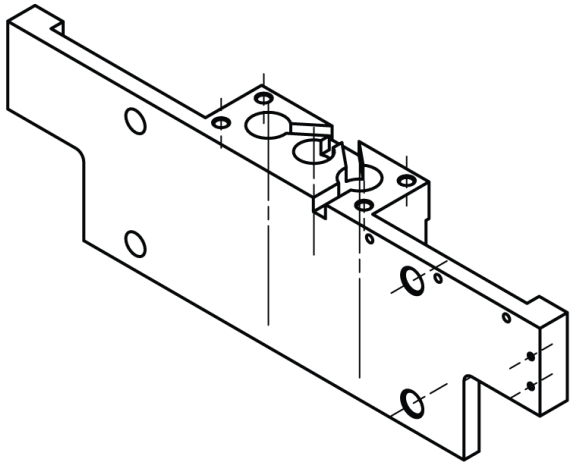

Figure 8.5. Front view of the impactor body.

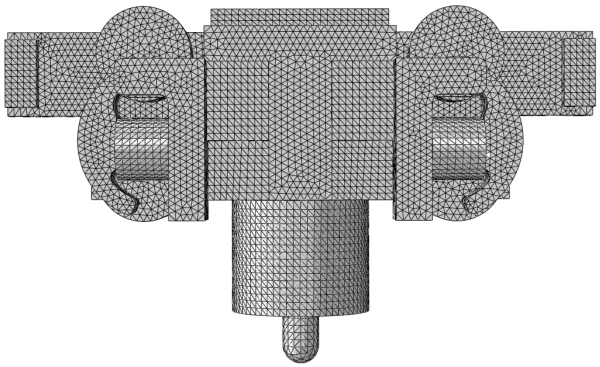

Figure 8.6. Rear view of the finite element model of the impactor including wheels, load measuring parts and anti-rebound assembly.

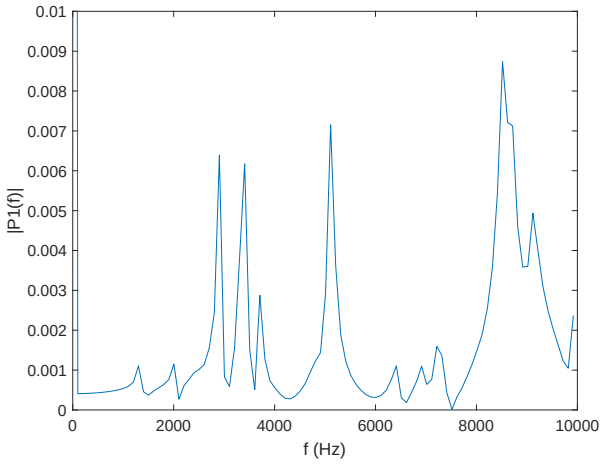

Figure 8.7. Frequency response spectrum of the simulated force history after a vertical impulse load on the model shown in figure 8.6.

8.4.3 Anti-rebound

The goal of the impact test campaign is to determine the damage resulting from an impact event. For side-impact on flat laminated composites, the impact energy is typically partially stored as elastic energy in the specimen, which is returned to the impactor after it has come to a standstill at maximum displacement. This return means the impactor bounces back up and, if nothing is done to stop it in its way, come back down to hit the specimen another time, only definitively stopping when all the initial energy has been dissipated by the creation of damage or due to friction. As a single impact is much easier to characterise and model, an anti-rebound device is needed to stop the impactor in some way after it has lost contact with the specimen for the first impact.

The original anti-rebound system is visible in figure 8.8. It consisted of an inductive sensor, an on-delay timer and two clips with foam which are held in place by permanent electromagnets while a spring exerts a force to pull them towards each other. The sensor feels the presence of the impactor, and the timer sends a pulse to the magnets after some time. This pulse causes the magnets to release the clips, which are pulled towards each other and thereby obstruct the path of the impactor. Instead of impacting a second time on the specimen, the drop-weight impacts on the clips.

While the design was very effective, it had two main drawbacks. First, all the energy that remained in the impactor after rebound was dissipated over a very small distance, causing high loads on the anti-rebound assembly and the support frame of the tower, which in turn resulted in fast part wearing and misalignment of the tower. Second, the only way to remedy the first drawback was to move the anti-rebound system to another position for each test scenario in order to minimize the distance between the height of the rebound and the clips. In practise, the system was typically mounted as low as possible to accommodate the largest variety of rebound scenarios without the need of a user intervention, thus typically causing high loads on the equipment.

With the above in mind, the anti-rebound system of the new tower should comply to the following criteria:

- the impactor should be stopped with minimal force on the support frame;
- minimal set-up change should be required for different impact scenarios;
- the system should be fail-safe: no falling impactor upon power loss;
- the impactor should remain compact to maximise its natural frequency;
- the number of parts should be minimized to reduce the risk of failure.

Many different designs are possible, some of the more promising concepts are described below.

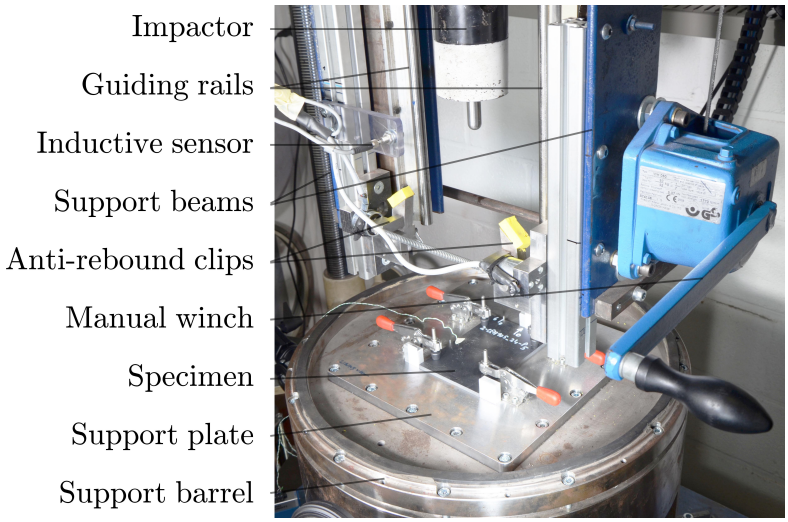

Figure 8.8. Detail of the original drop tower facility at UGent-MMS with a specimen mounted in the ASTM D7136 support plate. The two support beams are suspended from the wall for a wide selection of structures to impact on, in this case the support barrel is placed. The anti-rebound system is visible in the centre.

Catching clips

The first option is to use an improved version of the original concept, as anti-rebound systems on commercially available drop towers typically rely on the same concept as well. The large difference of the current situation with those towers is, however, that the current frame is partially suspended, while the others completely rest on the ground, and thus easily direct the load out of the structure. As mentioned in section 8.4.1, the frame is open on the front, and the part which guides the impactor is not directly in contact with the ground. This is the reason for the first criterion mentioned above: the anti-rebound loads should remain small not to deform the tower too much. The only way to reduce the load without requiring the user to change the set-up between different test scenarios is to use multiple clips and thus reduce the drop height on the clips, see also figure 8.9. To prevent possibly high moments, the system needs to be installed on either side of the impactor, as was the case of the original concept. Hence, the number of parts needed to realise this system is rather high.

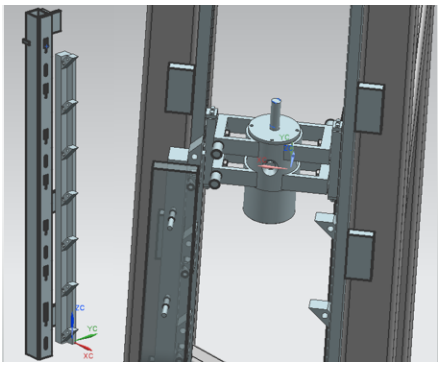

Figure 8.9. Impactor anti-rebound concept 1: multiple clips on the frames to catch the impactor, in extended position on the right column, retracted on the left.

Brakes

The second option is to add a system to the impactor or tower that increases the friction forces after impact. This way, if timed correctly and applied close to the maximum height of rebound, there would be both little force on the frame and little wear of the system because the impactor is almost at a standstill. It seems best to add a braking system to the impactor (a concept is shown in figure 8.10). Adding a brake to the tower would require it to span the entire length if it is to comply with the second criterion of the list. Many different actuation options exist: the brakes can be extended magnetically, pneumatically or using springs, for instance. The challenges of this concept are to produce enough brake force and to make it fail-safe.

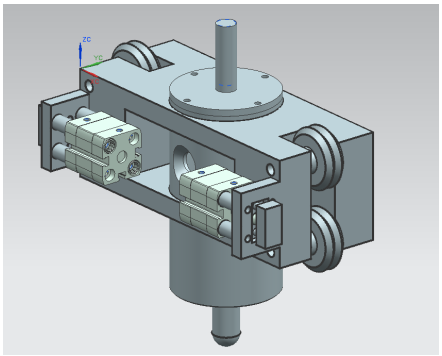

Figure 8.10. Impactor anti-rebound concept 2: brakes on the impactor - in this case pneumatic.

Controllable feathered end stops

Instead of minimising the drop height on the clips of the first concept, an alternative is to increase the braking distance using, for instance, pneumatic pistons, see figure 8.11. This way the need for multiple subsystems over the length of the frame to comply to the first two criteria is alleviated. The challenges lie in the absence of interference during the impact test and in the compactness of the system. If the system is namely not to interfere with the test, it should be controllable and extended only after impact. This extension, moreover, should be carried out fast enough to be ready to stop the impactor as soon as it comes down for the second time, though not too fast as in that case it could launch the impactor away. The system should also be compact: it cannot protrude below the bottom of the tower because it would increase the necessary length of the impactor, decreasing its natural frequency. This compactness makes the deceleration length rather short again, and such a short brake distance leads to high required forces, making the pistons rather bulky, as can be seen from the image. This results in rather large parts needed on the impactor to reach to the pistons.

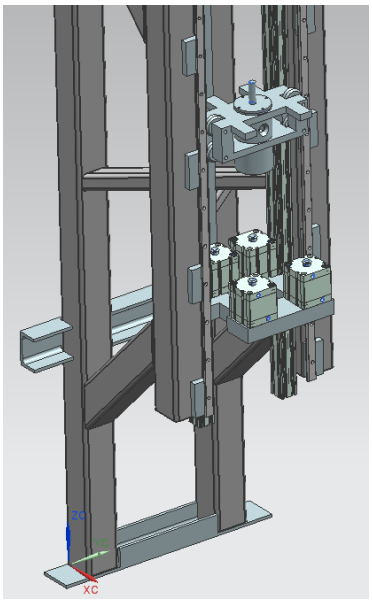

Figure 8.11. Impactor anti-rebound concept 3: feathered end stops on the frame - in this case pneumatic.

Trade-off

Although there are many more concepts conceivable, the current discussion is limited to the three above as they were the most promising in terms of the criteria mentioned above and seem feasible to develop within the time frame and budget available. It is chosen here to continue with the brake concept, as it constitutes both the most compact design and it should produce the smallest loads on the frame.

Detailed design

To produce enough brake force while still being fail-safe, the brakes are designed such, that the brake force increases with an increase of the downward load, i.e. a self-braking system. This is achieved by levering the brake from the top, see figure 8.12. With this design, a small force F_s coming from *e.g.* a spring is enough to generate a large brake force F_b. The moment of this brake force around the hinge on the top namely pushes it further open. This leads to a (much) larger surface normal force F_n than the spring could produce on its own. For this system to work, the friction coefficient between the brake pad and the frame (shaded region in figure 8.12) should be high enough to make the brake force grow beyond the weight of the impactor pushing down on the brake pad (F_i) through its housing. To achieve this, the brake pads are covered with rubber. An added advantage of the design is that braking at the exact right moment to reduce wear is no longer essential. The brakes are applied when the impactor moves up. During the upwards movement the brake force is reversed, counteracting the spring load, thus reducing the normal force and thereby lowering the brake force again. This way, the system automatically only really engages when the impactor starts to move down.

A picture of the brake system is shown in figure 8.13, which shows both the open and closed states. Actuation of the brakes is initiated with the use of the inductive sensor and delay timer, recovered from the original drop tower. The timer sends a pulse to a permanent electromagnet (item 6 in figure 8.4) fitted in the space between the pad (5) and the housing (7). This pulse deactivates the magnet, making a spring fitted at the bottom (8 in figure 8.4) push the pad against the drop tower frame. The gap between brake and tower, the strength of the magnet and the size and constant of the spring are all taken to achieve the correct behaviour. In the closed situation, the magnet's strength far surpasses the force produced by the spring, preventing premature brake activation. In the opened situation, the air gap is large enough to make the attraction force of the magnet drop below the pushing force of the spring, which prevents the brakes from deactivating when the power would be removed from the system, thus creating a fail-safe design. Yet the air gap is small enough to allow the magnet force to overcome the spring load when it is powered in reverse polarity to increase its attraction force rather than removing it. This enables the user to retract the brakes with the simple switch of a button.

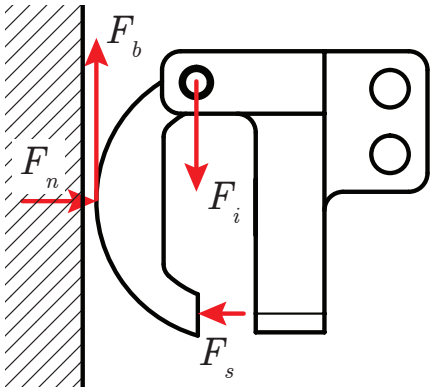

Figure 8.12. Detailed design of anti-rebound concept 2: self-braking levered pads.

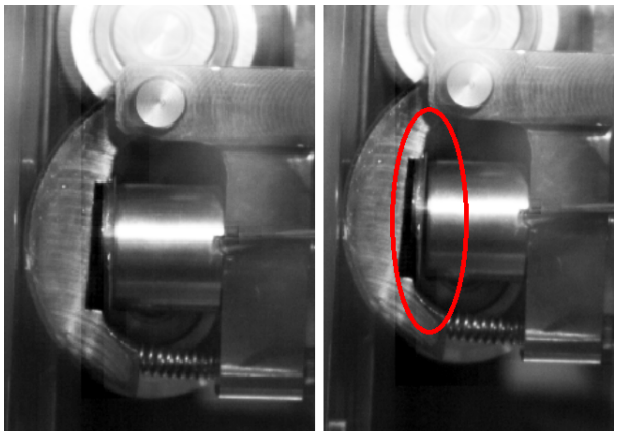

Figure 8.13. High-speed footage of the brake in action while the impactor is moving up after hitting a specimen. The left frame shows the brake inactive. In the right frame it has been activated, as can be seen by the small air gap between the magnet and the metal disc within the red ellipse.

8.4.4 Design evaluation

The finished drop-weight impact test set-up is displayed in figure 8.14. As can be seen in the bottom of the figure, the support barrel with ASTM D7136 support plate is recovered from the original set-up, and placed underneath the tower to hold the specimens during impact. The complete impactor assembly, including all sensors and cables, has a mass of $9.84\,\mathrm{kg}$. It can be seen that the manual winch mechanism has been taken over from the original tower, which is also the case for the permanent electromagnet to release the impactor. The tower can only be operated from behind a safety curtain (the rail can be seen in the image) to prevent contact between operators or bystanders and possible debris flying away due to the impact. With this addition, the tower also complies to the third requirement in the beginning of section 8.4 that it should be safe to operate.

The natural frequency of the impactor has been measured by hanging it at a convenient height and hitting the impactor tip with a hammer. An oscillatory signal is captured by the load cell. The lowest frequency (excluding zero) which occurs in the signal is found to lie at about $1000\,\mathrm{Hz}$, see also figure 8.15. Using the same method, the original impactor was also evaluated. Its lowest natural frequency was found to lie at about $500\,\mathrm{Hz}$. The new impactor design thus doubles the lowest natural frequency. The FE-model resulted in a natural frequency of $2.9 \times 10^3\,\mathrm{Hz}$, almost three times the value found after production. The exact reason for this difference is unknown. The material used for the impactor will have slightly different properties, and the shape will not be exactly the same, though these effects are not expected to make such a large difference. Likely the fact that the actual impactor has several parts connected together instead of being one single solid block of metal has a big influence on the results.

Using a laser doppler vibrometer, the vibrations of the specimen support structure have been measured during a series of impact tests. The worst-case result is plotted in figure 8.16, where the maximum displacement of the support plate equals $5.9\,\%$ of the maximum displacement measured for the impactor.

It was investigated using a finite element model whether this behaviour could be easily improved, while still allowing the bottom of the specimen to be recorded during a test as was done with the original set-up. A quarter of the round plate with a square cut-out covering the barrel and a quarter of the square ASTM D7136 support plate with rectangular cut-out were modelled using the dimensions measured on the test set-up. The parts were given the linear elastic isotropic properties of steel ($E = 205\,\mathrm{GPa}$, $\nu = 0.286$). It was assumed that the support deforms symmetrically, and hence the cut planes were given symmetric boundary conditions. The mating surfaces of the two plates were tied together. The outer part of the bottom surface of the round plate was restricted to move in any of the three nodal degrees of freedom. The edge of the cut-out was kinematically constrained to a reference point, which was loaded by a vertical load during an implicit anal-

Figure 8.14. The new drop-weight impact test set-up.

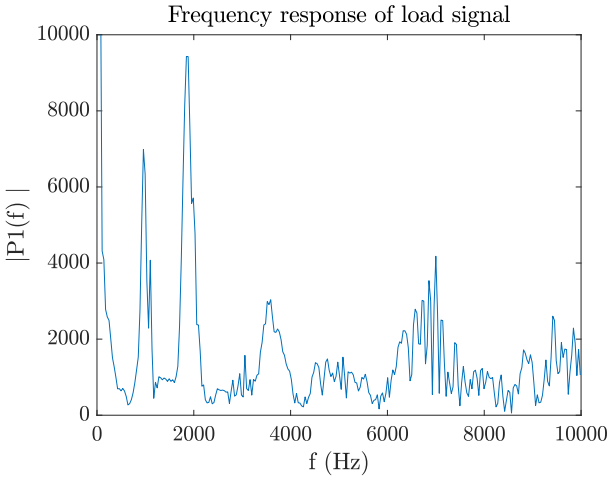

Figure 8.15. Frequency response of load signal after a vertical hammer hit on the impactor tip, measured using the new impactor.

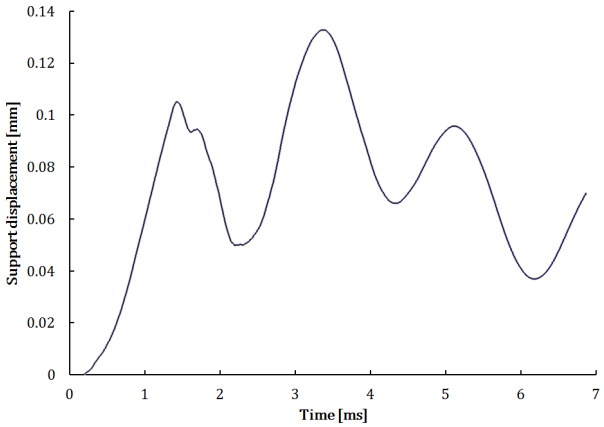

Figure 8.16. Displacement of the support plate at a corner of the cut-out (see also figure 8.1) during a impact test from $0.1\,\mathrm{m}$ *on cross-ply carbon/epoxy.*

ysis step. The model was discretized into about $10\,000$ full-integration hexahedral C3D8 elements. The magnitude of the vertical load was $20\,\mathrm{kN}$, which is the maximum expected load that the support structure will likely see, given the capacity of the load cell.

Three configurations were examined. First, the original design of the support plate was analysed. The results are shown on top in figure 8.17. The maximum vertical displacement given by the finite-element model amounts to $1.08\,\mathrm{mm}$. Two alternatives were simulated: one with stiffening ribs on the outer plate and another with stiffening ribs on the inner plate. The results for these alternatives are shown in the middle and the bottom of figure 8.17, respectively. The figure shows that the newly obtained maximum displacements are 1.05 and $0.80\,\mathrm{mm}$, respectively. This improvement is considered too small for the added effort needed to produce new plates, and hence it is decided to leave the support structure as-is.

Tables 8.1 and 8.2 contain the impact velocity characteristics of the original and new drop towers, respectively. The coefficient of variation is significantly reduced for most of the drop heights with the new drop tower, indicating a more consistent behaviour. The exact reason for the low coefficient of variation for a $1.2\,\mathrm{m}$ drop height with the old tower is unknown. It could be related to the fact that fewer specimens were tested at this height: a similar reduction is seen for the new drop tower at the largest drop height. The tables also show that the new tower needs a larger drop height to reach approximately the same velocity. Where the original tower converts, on average, $79\,\%$ of the potential energy to kinetic energy upon impact, the new tower converts only $71\,\%$. This is likely a result of the tight tolerances that were set between the impactor wheels and the guiding rails. Practically no sideways movement was possible at the time of the test campaign. Possibly some improvement in terms of impact speed could be obtained by allowing a very small gap between the wheels and the rails. The increase in consistency far outweighs the drawback of a reduced impact velocity, though.

Figure 8.18 shows test results of 10 tests of the same scenario. Especially

Table 8.1. Average value and coefficient of variation of impact speed using the original drop tower.

Original tower		
Drop height $[\mathrm{m}]$	**Impact velocity**	
	Average $[\mathrm{m\,s^{-1}}]$	**C.V.** $[\%]$
0.10	1.28	2.7
0.30	2.19	2.9
0.80	3.39	3.0
1.20	4.29	0.7

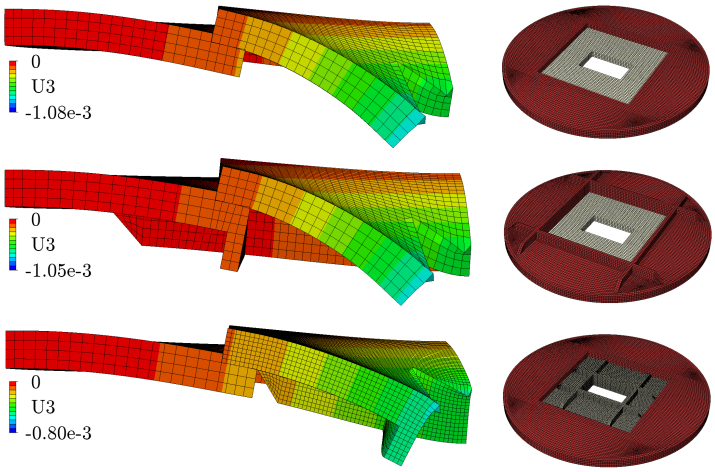

Figure 8.17. Exaggerated displacement profile (left) and bottom view of duplicated model (right) of the support plate of the impact tower. Vertical displacements in mm *indicated on the far left.*

Table 8.2. Average value and coefficient of variation of impact speed using the newly developed drop tower.

New tower		
Drop height [m]	**Impact velocity**	
	Average [$\mathrm{m\,s^{-1}}$]	**C.V.** [%]
0.10	1.20	0.28
0.25	1.86	0.80
0.40	2.34	0.89
0.90	3.57	0.20

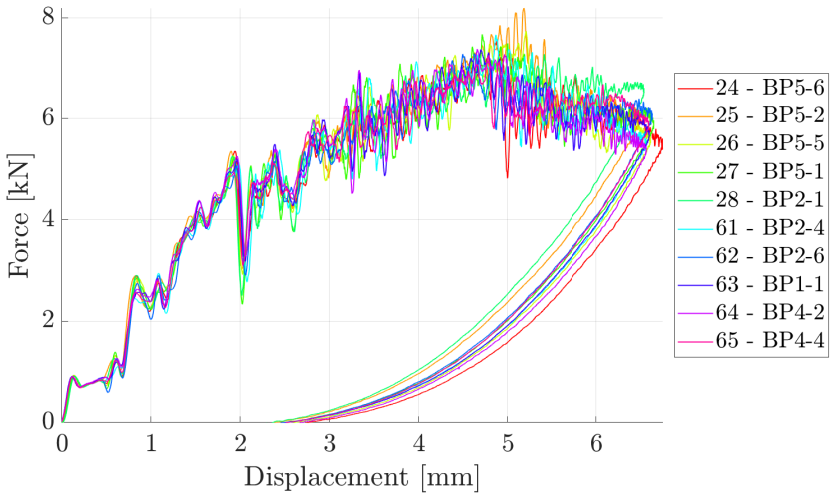

Figure 8.18. Overlay plot of the force-displacement response of 10 *impact experiments on quasi-isotropic carbon/epoxy specimens from a height of* 0.4 m *using the new drop tower.*

during loading, the curves follow each other closely, proving that indeed the drop tower operates very consistently. Only when significant damage is starting to develop, say from about 5 mm displacement, the results start to vary.

Finally, the acceleration signal of the original impactor would show oscillations which were likely a consequence of the fact that it was mounted on a flange. Positioning the accelerometer near the centre of mass of the new impactor has resolved this issue, as will be shown in section 8.7.1.

8.5 Test execution and data acquisition

This section provides the details of how the tests are carried out and how data is obtained during these experiments. As mentioned in section 8.3, the rate-dependency of impact damage is not only investigated by dropping an impactor from various heights, but also by using indentation damage as a quasi-static reference. Hence, in the following sections, two experimental procedures are described: first low-velocity impact (LVI) is treated, followed by quasi-static indentation (QSI).

8.5.1 Low-velocity impact

A LVI test is carried out by first mounting a specimen and adjusting the rubber-tipped clips on the support plate so that they exert only a minimal force on the specimen. Next, the impactor is lowered until it just touches the specimen, and

the displacement readout is set to zero for this height. Subsequently, the impactor is lifted to the required drop height. After activation of the data recording, the impactor is released by powering the permanent electromagnet which is holding it in place. The impactor falls and hits the specimen, and it is stopped during rebound.

The data acquisition is the same for the original and the new drop tower set-up. The impactor is equipped with an Endevco Isotron 23-1 load cell that holds a 16-mm-diameter hemispherical hardened solid steel impact tip. The maximum force it can measure is $22\,\mathrm{kN}$ in compression. Other sensors on the impactor are a Kistler K-Shear 8704B500 accelerometer and a Kübler 8.LI50.1111.2250 displacement transducer. The displacement signal from the transducer cannot be used for accurate position and velocity measurements during a test, as the sensor head suffers from vibrations and even in the absence of these vibrations, the signal contains too much noise (figure 8.28). A line pattern is therefore attached to the impactor to allow optical tracking of the vertical position using a Photron Fastcam SA-4 high-speed camera, as was done during the dynamic delamination experiments, see section 6.4.2.

Two other high speed cameras are employed to record the test. One looks at the bottom of the specimen using a mirror at $45°$ to see the possible development of damage on that surface (figure 8.19). To enhance the visibility of damage, the surface has been painted using an airbrush to deposit a thin layer of white paint. The other camera takes an overview shot and thereby also captures the curling-up of two of the corners of the specimen (figure 8.20). The cameras typically operate at about $20\,000$ frames per second.

Data storage is performed using a HBM Gen5i digital oscilloscope, which is set to record samples at a rate of $1\,\mathrm{MHz}$. Based on the force signal, the oscilloscope sends a trigger signal to the cameras upon which they start recording their frames.

Temperature is also recorded, using either a thermocouple or a laser thermometer. The necessary lighting for the high-speed cameras namely causes the specimens to warm up to above room temperature.

Finally, for a selection of samples with unidirectional (UD) layers, the surface strain is recorded in four locations. Two $350\,\Omega$ CEA-06-250UN-350 gauges from Vishay Micro Measurements are adhered to each face of the specimen according to the manufacturer's procedure [3], and on the locations indicated in figure 8.21. The strain gauges are each connected to a NI-9945 $350\,\Omega$ bridge completion module, in turn connected to a NI-9237 C-series bridge input module mounted in a CompactDAQ-9174 multi-slot chassis. Sampling is performed at the card's maximum rate of $50\,\mathrm{kHz}$. Synchronization can be done using the load and the trigger signals, which are both also recorded using a NI-9215 voltage measurement card in the same chassis.

Figure 8.19. High-speed recording of the bottom of a specimen during a drop-weight impact test.

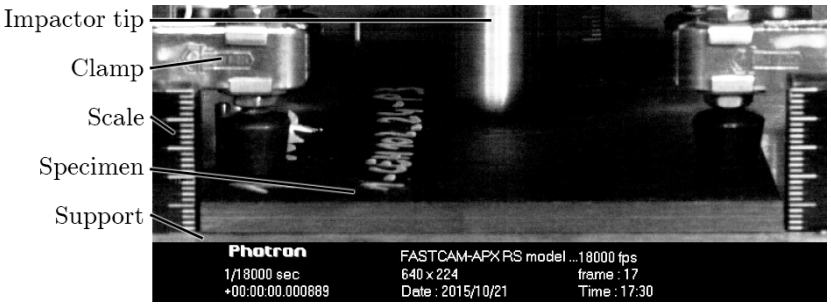

Figure 8.20. High-speed overview recording of a drop-weight impact test.

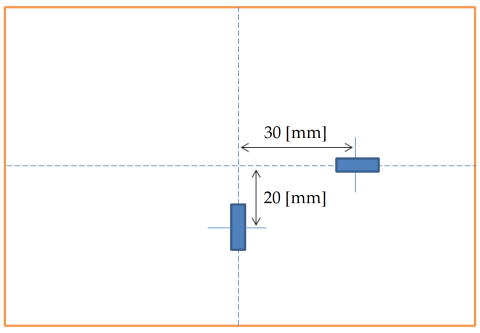

Figure 8.21. Strain gauge locations (in blue) on the top and bottom of the impact specimen (orange rectangle).

8.5.2 Quasi-static indentation

The QSI tests are performed on an Instron 5800R electromechanical universal test bench. The support plate and hemispherical impactor tip are taken from the drop-weight tower, and mounted on the crosshead and loadcell, respectively, of the quasi-static test bench (figure 8.22). This mimics exactly the same boundary conditions as on the impact tower, though the specimen support is stiffer as the plate is supported over its entire surface. A loadcell with a capacity of $10\,\mathrm{kN}$ is employed to perform the indentation scenarios for which the corresponding impact test remained below that value. Otherwise, a $100\,\mathrm{kN}$ cell is used.

It can be seen in the figure that linear variable differential transducers (LVDTs) are used to measure the displacement close to the long edge on either side of the specimen. The internal displacement transducer of the test bench is not accurate due to the inevitable deformation of parts of the bench. The average value of the two LVDTs is therefore used for the displacement.

The cross-head is moved at $2\,\mathrm{mm\,min^{-1}}$ to execute a test. Force, displacement from the LVDTs and surface temperature are recorded at a rate of $50\,\mathrm{Hz}$ on a NI-9215 voltage measurement card in a CompactDAQ-9174 multi-slot chassis. The digital microscope on the right of figure 8.22 records the curling-up of one corner of the specimen during the test. Again, for a selection of UD-layered specimens the surface strain is recorded in the same manner as for the LVI campaign.

The QSI tests are planned to be equivalent to a LVI scenario. Hence, some quantity needs to be selected to define this equivalence. Drop height or impact energy are not applicable to QSI tests. If material rate-dependency plays a role, it affects the maximum force, so it cannot be used. The displacement, measured using the LVDTs, is therefore chosen to define the test end condition, as is done in

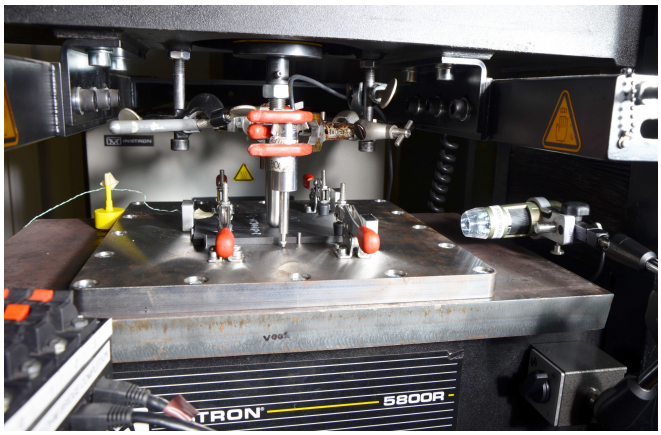

Figure 8.22. Close-up of the quasi-static indentation set-up.

e.g. [4]. This signal should also behave smoothly, facilitating its use as a controlling parameter for the test bench. For each scenario tested for LVI, a representative maximum displacement is obtained which is used for QSI. Only two or three repetitions per scenario are carried out because of the small difference between test repetitions.

8.6 Specimen preparation

As the results for the QSI tests are to be compared to those from LVI, the same specimen dimensions are taken for both tests. In light of a possible future execution of compression after impact tests on the specimens, it is decided to follow the ASTM D7136 test standard for LVI [1]. The test standard prescribes specimen dimensions of 150 by $100\,\mathrm{mm}$. The waterjet cutting process is employed again to cut the specimens from the square plates that were obtained from the manufacturer. In hindsight, this was not the best choice, since the resulting specimens did not meet the requirements for surface roughness and edge perpendicularity (see also figure 4.14) which would be needed for subsequent compression-after-impact testing [5].

Table 8.3. Average dimensions and coefficients of variation (in grey) of the specimens for LVI or QSI per layup.

	Layup	# plies	Average [mm] L	Average [mm] W	Average [mm] t
C/E	CP: $[0/90]_{6s}$	24	149.94 0.06	100.00 0.02	5.537 0.79
	QI: $[45/0/-45/90]_{3s}$	24	149.96 0.03	100.01 0.02	5.537 0.74
	CP: $[\#(0/90)]_{12s}$	24	149.97 0.05	99.96 0.04	5.299 1.26
	QI: $[\#(\pm45)\#(0/90)]_{5s}$	20	149.92 0.04	99.95 0.02	4.237 1.66
G/PA6	CP: $[0/90]_{5s}$	20	150.01 0.03	100.07 0.08	4.748 0.60
	QI: $[45/0/-45/90]_{3s}$	24	150.06 0.02	100.11 0.12	5.882 0.72
	CP: $[\#(0/90)]_{5s}$	10	149.99 0.04	100.03 0.03	5.999 1.18
	QI: $[\#(\pm45)\#(0/90)]_{3s}$	12	149.98 0.04	100.02 0.03	4.985 1.68

As will be explained in section 9.2, four laminates are tested for both carbon/epoxy (C/E) and glass/polyamide-6 (G/PA-6): a cross-ply (CP) and a quasi-isotropic (QI) variant, each in a UD- and a woven-layered configuration. Based on the ply thickness given by the manufacturer, the number of plies was taken to reach a thickness closest to 5.0 mm with a balanced symmetric layup, as prescribed by the test standard [1]. The resulting laminates are given in table 8.3, which also contains the measured dimensions after conditioning for 7 days at 70 °C and subsequent cooling in a desiccator (see also section 4.6.7).

8.7 Data digestion

It is explained in this section how to get to useful data from the raw test results. First, it is explained how the force history can be obtained, second, the displacement is treated, after which one is set-out against the other. Finally, various ways of obtaining the absorbed energy versus time are discussed.

This section typically focuses on the data digestion for the LVI tests. Compared to LVI, the data digestion for QSI is namely quite straightforward, because the difficulties encountered during LVI do not show up during QSI due to the low rate of displacement.

8.7.1 Force versus time

Figure 8.23 contains a typical force history from a LVI test. The load rises with some oscillations up to a certain maximum, after which it reduces back to zero. These oscillations are typically attributed to a combination of major damage creation events and impactor and specimen ringing. A second effect that can be seen is that the curve is not symmetric around its maximum. This also points to damage, as it indicates some energy dissipation mechanism is active.

It is not directly straightforward to select the beginning and the end of a test from a force signal. The signal namely suffers from noise. It is therefore opted to manually select the start, as no robust algorithm could be devised to produce an accurate start point of each test. The curve in figure 8.23 shows a non-zero slope when it comes back to zero force during the unloading. This suggests that the compressive load actually becomes tensile after testing. The point of test end is taken at zero load.

The change of sign of the load is physically impossible since there is nothing attached to the impactor tip to pull it down. Typically, a slowly decaying tensile load with a maximum of about 100 N is seen. The cause for this is sensor drift. Apparently the compressive load on the load cell already acts long enough to drift the output slightly towards zero, showing up as a tensile load after unloading. This effect is also seen for the dynamic tensile tests, see figure 4.18a. There, it could

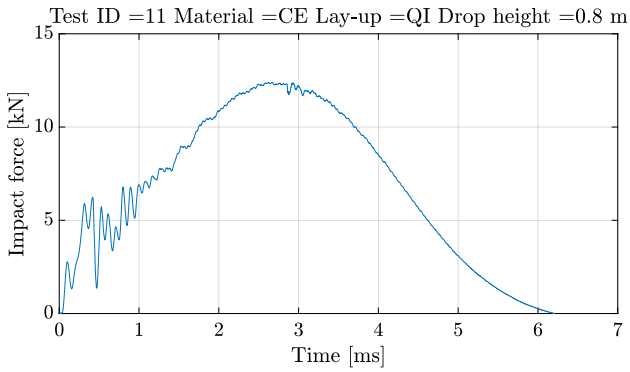

Figure 8.23. Force-time history of a drop-weight impact test from $0.8\,\mathrm{m}$ *on C/E* $[45/0/-45/90]_{3s}$.

be solved by selecting a more appropriate time constant of the charge amplifying unit. In the current case, the load cell has an internal charge amplifier with a fixed time constant which operates using a small excitation current provided by the digital oscilloscope. The time constant is likely chosen on the small side by the manufacturer to achieve a broad frequency response. Nevertheless, the drop tower load cell is not exchanged by one of the same type as on the hydraulic pulse test bench, because the voltage signal from the former is not as easily disturbed by external influences as the charge signal from the latter. A small amount of drift on the load signal must therefore be accepted.

Another option would be to use the accelerometer to measure the load on the impactor, by multiplying its signal with the mass. Its high frequency response of up

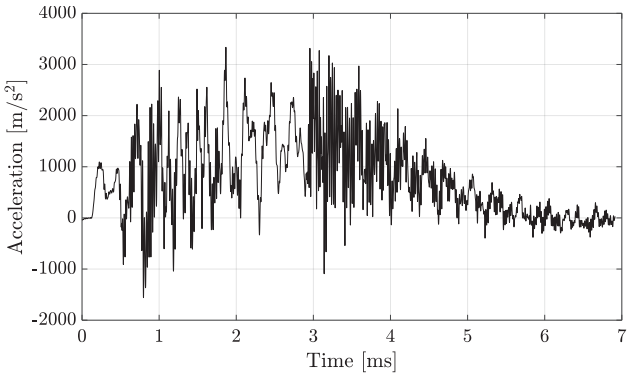

Figure 8.24. Acceleration-time history of a drop-weight impact test from $0.8\,\mathrm{m}$ *on C/E* $[45/0/-45/90]_{3s}$*, using the accelerometer mounted on a flange on the original impactor.*

to $10\,\mathrm{kHz}$ [6], however, causes high-frequency content to obscure the results, see figure 8.24. Moreover, an oscillatory response is seen, which is due to the fact that the accelerometer is mounted on a flange of the original impactor. The signal can therefore not be used to compute the load. The placement of the accelerometer at the centre of mass for the new impactor greatly improves its reading, though the high-frequency content remains, see figure 8.25. If the oscillations with a frequency of above $2\,\mathrm{kHz}$ are removed using a moving average filter, the blue curve in the figure is obtained. The maximum acceleration then lies at $1074\,\mathrm{m\,s^{-2}}$. With an impactor mass of $9.84\,\mathrm{kg}$, this would amount to a maximum load of $10.6\,\mathrm{kN}$, while the maximum load of that test measured using the load cell was $12.4\,\mathrm{kN}$.

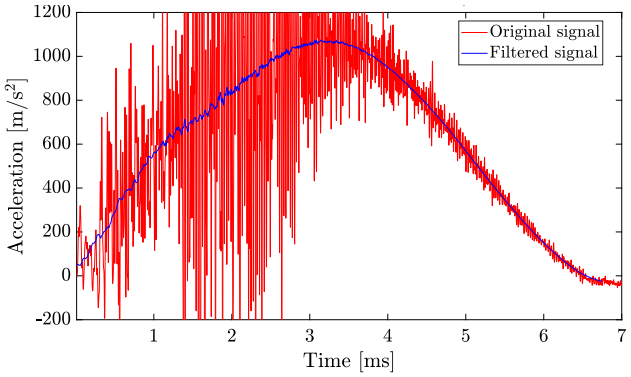

Figure 8.25. Acceleration-time history of a drop-weight impact test from $0.4\,\mathrm{m}$ *on G/PA-6* $[\#(\pm 45)\#(0/90)]_{3s}$*, using the accelerometer mounted near the centre of mass of the new impactor.*

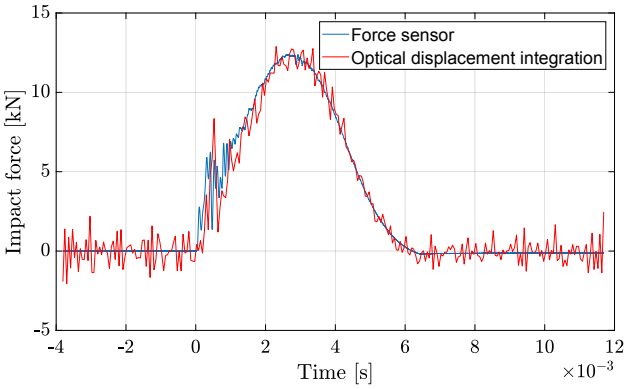

Figure 8.26. Force-time history of a drop-weight impact test from $0.8\,\mathrm{m}$ *on C/E* $[45/0/-45/90]_{3s}$*, using a double differentiation of the optically obtained displacement (figure 8.27). The loadcell-measured force is also indicated.*

As mentioned in the next section, the displacement is accurately measured using the optical pattern tracking method. The load history could also be obtained by differentiating this displacement signal twice and multiplying the result by the impactor mass. There are, however, two issues with this approach. First, the two differentiation steps strongly amplify the inevitable noise present in the displacement signal, making that smoothing of the data is necessary. Second, the data acquisition rate for the images is on the low side. This, together with the smoothing, limits the bandwidth of the signal to a low value, and makes that the curves do not contain the level of detail as the data obtained directly from the force sensor. When a filter with a cut-off frequency of $2\,\mathrm{kHz}$ is applied in both differentiation steps, the red curve in figure 8.26 is produced. Despite the two aforementioned issues, the two curves lie on top of each other, proving the accuracy of the optical tracking method. The reduced amount of detail of the optically determined load becomes clear when comparing the two curves.

8.7.2 Displacement versus time

The displacement versus time is obtained from recording the optical pattern using a high-speed camera. Figure 8.27 contains a typical result for a LVI test. It can be seen that a very smooth signal is obtained, even though no smoothing was applied in the process of displacement extraction from the footage. The maximum displacement measured equals $6.24\,\mathrm{mm}$.

A displacement sensor is present on the impactor to set it to the correct height before dropping on the specimen. The sensor can also be read out during the test, in which case the results shown in figure 8.28 are obtained. The first difference is the much larger amount of noise compared to the optical data. This is simply the inherent noise on the system. Secondly, the data does not start at zero, which indicates that either the sensor has slightly drifted, and/or the value was not set to zero with the impactor just touching the specimen. Looking closely to the curves, moreover, an oscillation can be seen which is not present in the optical data. It stems from the fact that for the original impactor, the sensor was mounted on a thin bracket, which oscillated during impact, effectively moving the sensor up and down. The new impactor has the displacement sensor mounted directly to its body, and the increased rigidity compared to the old impactor results in an absence of these vibrations in the measured displacement. The noise, however, remains in the signal, thus still limiting its use to merely setting the correct impact height. If the measurements are filtered, the sensor shows a maximum displacement of about $7\,\mathrm{mm}$ if the value just before impact is taken as a reference. The overshoot likely stems from the deformation of the bracket at maximum indentation.

Finally, the displacement can also be obtained by double integration of the acceleration. The procedure to obtain the displacement from the force history is

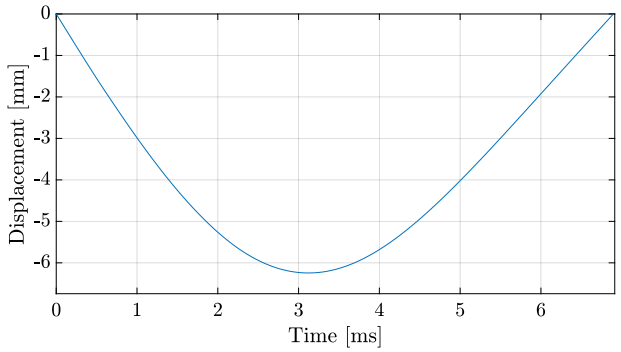

Figure 8.27. Displacement-time history of a drop-weight impact test from $0.8\,\mathrm{m}$ *on C/E* $[45/0/-45/90]_{3s}$*, using optical tracking.*

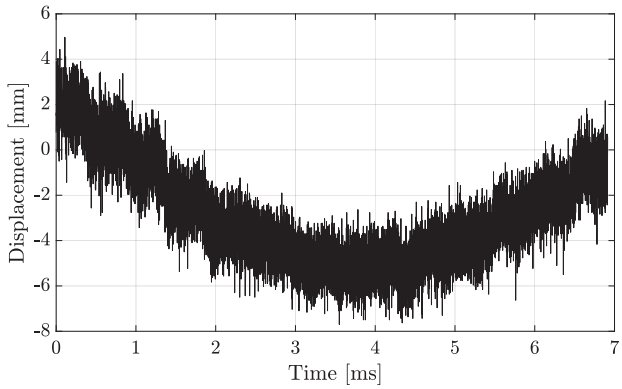

Figure 8.28. Displacement-time history of a drop-weight impact test from $0.8\,\mathrm{m}$ *on C/E* $[45/0/-45/90]_{3s}$*, using the displacement sensor.*

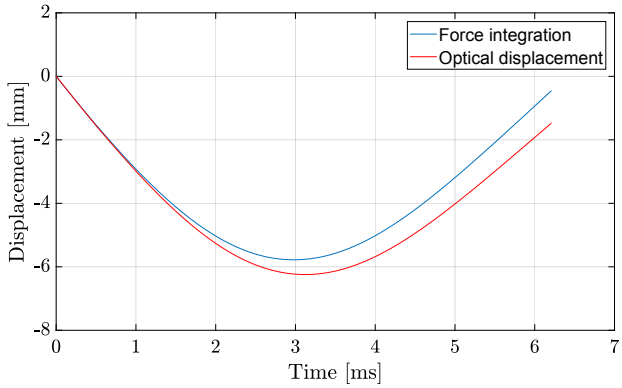

Figure 8.29. Displacement-time history of a drop-weight impact test from $0.8\,\mathrm{m}$ *on C/E* $[45/0/-45/90]_{3s}$*, using the double integrated output of the load cell.*

also explained in the ASTM D7136 test standard [1]. The velocity is obtained by integrating the values of force divided by the mass using the trapezoidal rule, taking into account the constant gravitational acceleration and setting the velocity to zero at maximum displacement. The displacement is obtained by using the trapezoidal rule again to integrate the velocity, setting the displacement zero at the point of initial contact. The result can be seen by the blue curve in figure 8.29. For reference, the optically measured displacement has been indicated by a red curve in the figure. The two curves show an increasing difference with time. The cause of the difference seems to stem from the initial part of the loading, where the physically measured force is visibly higher than the optically obtained value. The exact cause of the difference is unknown.

The curves in figure 8.29 stop when the load becomes zero. The displacement is not back to zero yet when that happens. This has two causes. First, some permanent indentation damage occurs on the surface, causing the impactor to lose contact at a negative displacement. Second, as mentioned before, the load signal drifts towards zero, causing the measured load to be zero before the actual load is.

8.7.3 Force versus displacement

For QSI, the force measured by the load cell is simply set-out against the average displacement of the two LVDTs, which were zeroed when the impactor tip just touches the specimen. The data is recorded on the same time stamps, so no intermediate steps are required.

For LVI, the situation is not as easy. Either the displacement can be obtained using the force as explained in the previous section and suggested by the ASTM standard, in which case all the data is acquired on the same time. For the current research, however, an accurate optical measurement of displacement is available. This optically measured displacement is more accurate than integrating the load twice, and is therefore used for the force-displacement curve. The lower acquisition rate of the camera requires the displacement signal to be upsampled to be able to plot the data. The samples are taken by interpolation of the displacement values at the synchronized timestamps of the force values. The relatively smooth character of the displacement signal results in a negligible upsampling error. A resulting force-displacement curve is given in figure 8.30.

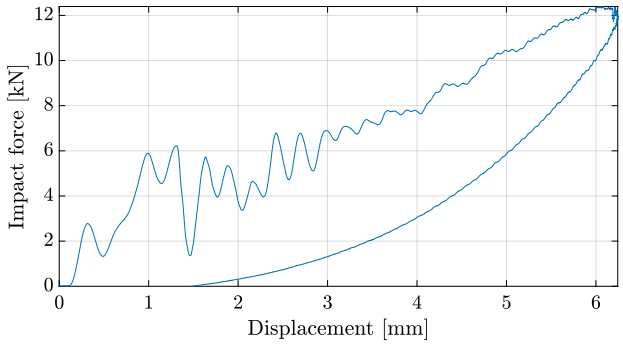

Figure 8.30. Force-displacement history of a drop-weight impact test from $0.8\,\mathrm{m}$ *on C/E* $[45/0/-45/90]_{3s}$*, using load from the load cell and optical displacement.*

8.7.4 Energy versus time

The ASTM D7136 test standard describes how the velocity $v(t)$ and displacement $\delta(t)$ obtained from the force signal can be used to obtain the evolution of the absorbed energy versus time $E_a(t)$ [1]:

$$E_a(t) = \frac{m\left(v_i^2 - v(t)^2\right)}{2} + m\,g\,\delta(t) \tag{8.1}$$

where m is the impactor mass, v_i is the impact velocity and $g = 9.81\,\mathrm{m\,s^{-2}}$. In the current case, the velocity and the displacement are accurately measured using the optical pattern tracking method, and hence these quantities are used instead. Figure 8.31 contains a typical energy evolution of an impact test. The absorbed energy is calculated using equation (8.1). The kinetic energy is computed using $E_k(t) = 0.5\,m\,v(t)^2$ and the potential energy using $E_p(t) = m\,g\,(\delta(t) - \delta_{\min})$. The sum of these three energies is a constant value, equal to the impact energy. The remaining absorbed energy after the contact is lost is assumed to be dissipated only in the form of damage. The final value of this curve is thus used as a measure of damage created during a test.

The absorbed energy can also be obtained by integrating the force - displacement graph. The result is the same as the red curve in figure 8.31 if the optical pattern is used to compute the load as well. When the load and/or the displacement are based upon the measurements from the loadcell, the difference which appeared in section 8.7.2 causes the energy values to differ as well.

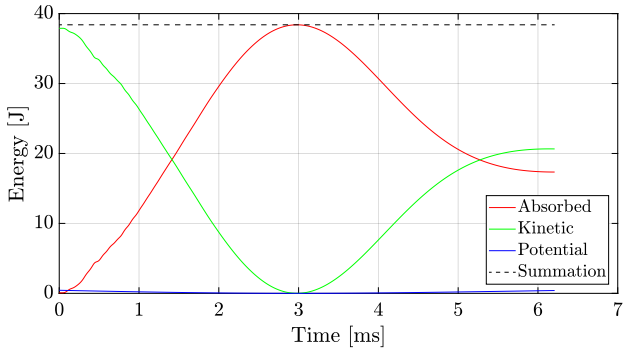

Figure 8.31. Energy evolution during a drop-weight impact test from $0.8\,\mathrm{m}$ *on C/E* $[45/0/-45/90]_{3s}$.

8.8 Post-mortem inspection

Specimens are inspected after testing to assess the extent of damage that was created due to the impact or indentation. Apart from a basic visual inspection to see the damage features on the surface, ultrasound and optical microscopy have been used to obtain data on what happened inside the specimens. Each of them is detailed below.

8.8.1 Ultrasound inspection

The damaged zone of a specimen is assessed using water-coupled ultrasonic C-scans in reflection and transmission (figure 8.32). A GE H5K transducer with diameter $13\,\mathrm{mm}$ and a GE USIP40 pulser/receiver are used to perform the scans,

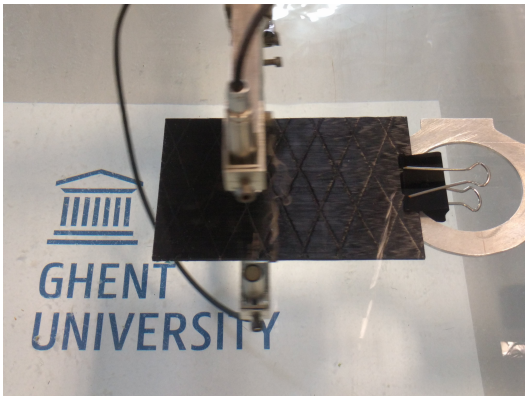

Figure 8.32. The C-scanning set-up at UGent in action.

using ultrasonic pulses with a central frequency $f_c = 5\,\mathrm{MHz}$. The pulser/receiver samples at $400\,\mathrm{MHz}$, evaluating the maximum amplitude in the selected time gate. The distance between transducer(s) and inspected sample is approximately $70\,\mathrm{mm}$. The grid step is $1\,\mathrm{mm}$ in the transverse and $0.1\,\mathrm{mm}$ in the longitudinal direction. The scanning speed is $50\,\mathrm{mm\,s^{-1}}$. The water temperature is $19\,^{\circ}\mathrm{C}\ \pm 1\,^{\circ}\mathrm{C}$.

Three different techniques have been applied to characterise the damage, each explained below.

A. Transmission

An example of a transmission C-scan can be seen in figure 8.33. Internal cavities attenuate a significant portion of the sound that is irradiated on the specimen, and as such a reduction in transmission can be considered indicative of damage. Sound is reflected most easily on surfaces perpendicular to the travel direction. The technique is therefore most suited to detect delaminations. Note that the transmission strength drops to zero outside the specimen, which is the result of applying scanning settings with which a completely unobstructed signal falls outside the measurement range.

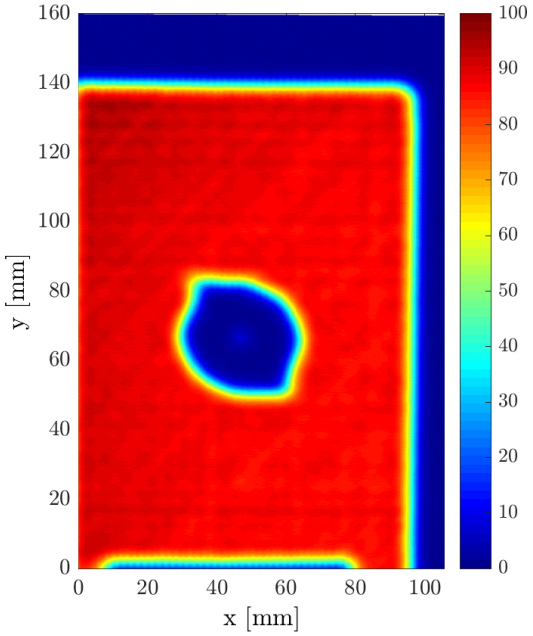

Figure 8.33. Transmission ultrasound scan of a UD-layered QI C/E sample impacted from $0.1\,\mathrm{m}$ *using the original drop tower. The colours show the transmissive signal strength normalised to the reference strength outside the damaged zone.*

The transmission scans can be used to estimate the integrated damaged area of each specimen. An area is assigned to each 'pixel', the value of this area is determined by the scan specifications mentioned above. The maximum transmission power in the undamaged zone is selected as a reference. A transmission amplitude reduction of $62\,\%$ of the reference value is selected to consider the specimen damaged at a certain scanning point, close to the generally accepted value of $50\,\%$ [7]. The choice of this specific value is motivated by the fact that the scanned size of the clamp, as seen in the bottom of the scans in figure 9.6, is closest to its actual length of $71.3\,\mathrm{mm}$. As is shown in section 9.4.4, this choice also leads to a reasonably good prediction of damage length compared to optical microscopy.

B. Surface reflection

The pulse echo of the front surface is employed to assess the geometry of the dent due to the impactor. By dividing the time of flight of the surface echo by twice the speed of sound in the scanning medium (distilled water, $c = 1480\,\mathrm{m\,s^{-1}}$), one obtains the distance of the source/receiver to the specimen. Note that this approach is only valid for deformations with limited slopes. This technique is used to determine the indentation profile after the test, figure 8.34 contains an example. The vertical axis is scaled to emphasize the differences in distance. Only part of the specimen is scanned. Notice that the edges of the scan are not horizontal. First of all, the specimen is never perfectly aligned with the scanning apparatus and secondly, the specimen is slightly curved which could be a result from internal

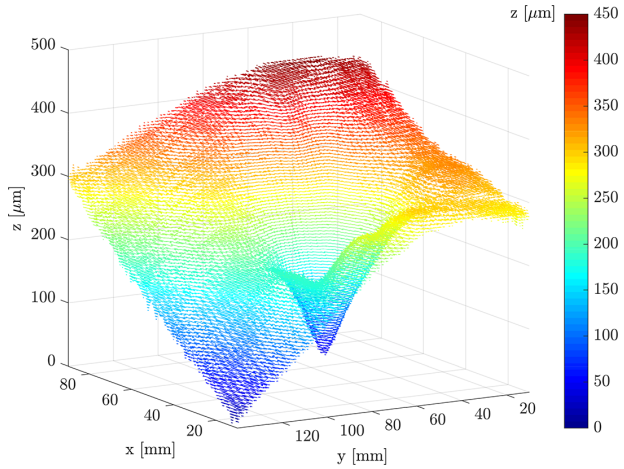

Figure 8.34. Surface reflection scan of UD-layered QI C/E after LVI from $0.8\,\mathrm{meter}$ *on the original drop tower. Notice the different scale on the z-axis compared to the in-plane axes. The colour indicates the elevation in* $\mu\mathrm{m}$.

stresses created during curing.

The ASTM D7136 test standard defines the dent depth as *the maximum distance in a direction normal to the face of the specimen from the lowest point in the dent to the plane of the impacted surface that is undisturbed by the dent* [1]. For none of the scanned specimens, though, do the edges lie on a shared plane and in most cases they are not even straight. It is impossible to find an appropriate undisturbed plane in this case. The 'undisturbed surface' is therefore redefined as the curved surface resulting from the two-dimensional linear interpolation of the elevation of the edges of the scan. The largest difference in elevation between this surface and the measurements is taken as the dent depth. The error due to non-horizontality is negligible (below $0.01\,\%$) because the alignment is within $0.66°$.

C. Internal reflection

The pulse echo of the front surface is further employed to dynamically adapt the time gate for the C-scans in reflection. This dynamic time-gating compensates non-horizontality of the samples, resulting in a constant imaging depth. Evaluation of the time-of-flight of the signal echo then yields information on the depth distribution of the delaminated area. This way, the internal damage can be visualised in three dimensions using the approximate depth from which the ultrasound was reflected. A reflection scan of the same impacted specimen as shown in figure 8.33

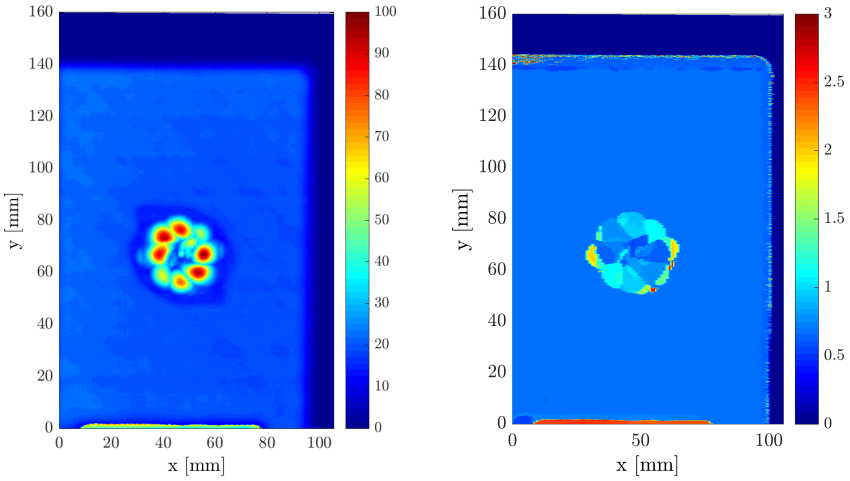

a. Reflection strength in percentage of the maximum.

b. Time-of-flight in [µs].

Figure 8.35. Reflection ultrasound scan of the same UD-layered QI C/E sample impacted from $0.1\,\mathrm{m}$ *as in figure 8.33 with two different colour schemes. A larger value of the time of flight in (b) corresponds to a deeper delamination.*

is displayed in figure 8.35. The colours either indicate the reflection strength or the depth of reflection calculated through time-of-flight. The scale is adapted to the strongest reflection or to the deepest significant reflection, and undamaged parts are set at the depth of the surface facing the transducer.

8.8.2 Optical microscopy

Specimens are cut through their lateral and longitudinal centrelines to be able to perform optical microscopy on those planes. The cutting process is performed by a Struers Secotom-15 precision cutting machine using a 0.5-mm-thick alumina cut-off wheel rotating at 3000 revolutions per minute and advancing at $0.5\,\mathrm{mm\,s^{-1}}$. Two inner surfaces per specimen are sanded and subsequently polished down to a particle size of $1\,\mu\mathrm{m}$. This way, 2 clear views of the cross-section of the damaged zone for the specimens under consideration are obtained. A Keyence VHX-900F digital microscope is used to create stitched images of the entire damage fields at a magnification of 200x.

A micrograph of the transverse cross section of a CP C/E specimen after QSI is given in figure 8.36. As the contrast between the damage features and the constituents of the composites is rather small (see also the inserts in the figure), automatic identification of the damage was not possible. The damage therefore had to be manually identified in the images.

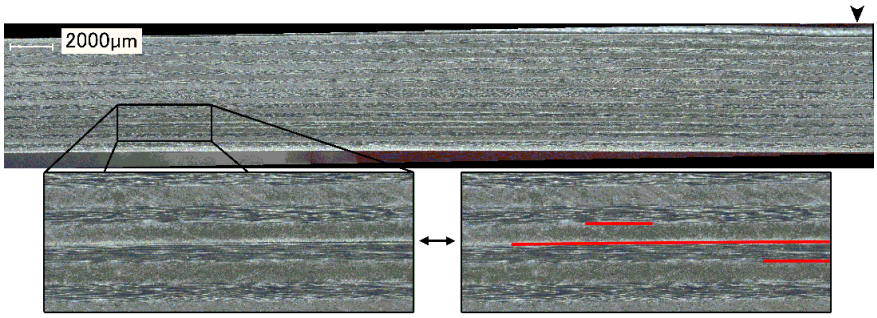

Figure 8.36. Stitched micrograph of a CP C/E specimen after QSI. The indentor pushed down close to the right side of the figure, indicated with an arrowhead. Zoomed section shows the tip of the delamination, delaminations indicated in the picture on the right.

8.9 Conclusion

In this chapter, the complete procedures for low-velocity impact and quasi-static indentation testing, and successive post-mortem inspection, have been treated.

A new drop-weight impact testing set-up has been developed, based on the original design, which resulted in an increase in natural frequency, a significant improvement of the acceleration measurement, and a reduction in the standard deviation of impact velocity. The set-up is capable of preventing a second impact of the impactor after rebound by employing a brake system which exerts only little force on the frame due to a self-braking design. The new set-up was used to perform the impact tests, a standard electromechanical test bench was applied for the indentation.

A contactless optical tracking method was applied to measure the displacement during the impact tests. It proved to be accurate enough to reproduce the load using a double differentiation of the measured displacement. This agreement validates the measurement method. The amount of detail in the optically measured load is limited, though, due to the limited frame rate of the optical acquisition with respect to the direct measurement of the load using a load cell. Integrating the load twice to obtain the displacement resulted in a difference with the optically measured value.

The dent depth and the damage area are measured ultrasonically in the post-mortem study. Additionally, several specimens are analysed using optical microscopy. It is expected that enough data is gathered this way to (1) asses the rate-dependency of the damage behaviour and (2) allow for the validation of finite-element models which aim to predict composite impact damage.

References

[1] ASTM International. *ASTM Standard D7136, 2015, "Measuring the Damage Resistance of a Fiber-Reinforced Polymer Matrix Composite to a Drop-Weight Impact Event"*. Technical report, American Society for Testing and Materials, West Conshohocken, PA, 2015.

[2] ASTM International. *ASTM Standard D6264, 2012, "Standard Test Method for Measuring the Damage Resistance of a Fiber-Reinforced Polymer-Matrix Composite to a Concentrated Quasi-Static Indentation Force"*. Technical report, American Society for Testing and Materials, West Conshohocken, PA, 2012.

[3] Vishay Precision Group. *Strain Gage Installations with M-Bond 200 Adhesive*. Instruction Bulletin B-127-14, Vishay Precision Group, December 2014.

[4] E. A. Abdallah, C. Bouvet, S. Rivallant, B. Broll, and J. Barrau. *Experimental analysis of damage creation and permanent indentation on highly oriented plates*. Composites Science and Technology, 69(7–8):1238–1245, June 2009.

[5] ASTM International. *ASTM Standard D7137, 2012, "Compressive Residual Strength Properties of Damaged Polymer Matrix Composite Plates"*. Technical report, American Society for Testing and Materials, West Conshohocken, PA, 2012.

[6] Kistler Instrumente AG. *K-Shear Accelerometers - General Purpose, Voltage Mode Accelerometers, Type 8702B500..., 8704B500...*, 2008.

[7] R. A. Smith, A. B. Marriott, and L. D. Jones. *Delamination sizing in fibre-reinforced plastics using pulse-echo amplitude*. Insight, 39(5):330–336, 1997.

9 Side-impact rate-dependency

9.1 Introduction

The test and the data analysis procedures are explained in chapter 8. They were applied to test the material systems detailed in chapter 3. The current chapter contains the results of those tests, as well as the findings from a post-mortem inspection campaign. First, an overview of the impact test campaign is given. Second, the digested test results are presented, along with a discussion on the implication of material rate-dependency. Finally, the results of the post-mortem inspection programme are given and discussed.

9.2 Side-impact test programme overview

Low-velocity impact (LVI) tests are carried out by letting the impactor drop on the specimen from a specific height. Three drop heights per laminate are selected. The lowest drop height causes a minimal amount of damage, while the highest results in widespread damage across the specimen without complete penetration. Half of the impact programme was carried out on the original drop tower before it was decided to design a new tower. The impactor mass is not the same for both set-ups, and the relation between drop height and impact velocity has also changed, as did the amount of variation on this velocity. It is therefore decided to present result overviews separately per tower. Tables 9.1 and 9.2 contain an overview of all tested scenarios on the old and the new tower, respectively. As can be seen, all specimens

with unidirectional (UD) layers, so both the cross-ply (CP) and the quasi-isotropic (QI) layup, were tested on the original tower. All the woven-layered composites were tested on the new one. Each scenario is repeated at least five times, resulting in about 120 tests in total. The corresponding average impact energy and speed are also indicated. All scenarios fall in the category of a large-mass impact, in which the test durations are much larger than the time needed for stress waves to reach the boundaries [1]. The tests are therefore appropriately termed 'low-velocity' and the plate deformation should be similar to quasi-static indentation (QSI).

Table 9.1. Overview of tested scenarios in terms of material (UD-layered), layup and drop-height for the original drop tower.

		Drop height $[\mathrm{m}]$			
Material	**Layup**	0.1	0.3	0.8	1.2
C/E	CP: $[0/90]_{6s}$	x	x	x	
C/E	QI: $[45/0/-45/90]_{3s}$	x	x	x	
G/PA6	CP: $[0/90]_{5s}$		x	x	x
G/PA6	QI: $[45/0/-45/90]_{3s}$		x	x	x
Average impact speed $[\mathrm{m\,s^{-1}}]$:		1.28	2.19	3.39	4.29
Coefficient of variation $[\%]$:		2.7	2.9	3.0	0.7
Average impact energy [J]:		6.3	18.5	44.5	71.1
Coefficient of variation $[\%]$:		5.4	5.6	5.9	1.5

Table 9.2. Overview of tested scenarios in terms of material (woven-layered), layup and drop-height for the new drop tower.

		Drop height $[\mathrm{m}]$			
Material	**Layup**	0.1	0.25	0.4	0.9
C/E	CP: $[\#(0/90)]_{12s}$	x	x	x	
C/E	QI: $[\#(\pm 45)\#(0/90)]_{5s}$	x	x	x	
G/PA6	CP: $[\#(0/90)]_{5s}$		x	x	x
G/PA6	QI: $[\#(\pm 45)\#(0/90)]_{3s}$		x	x	x
Average impact speed $[\mathrm{m\,s^{-1}}]$:		1.20	1.86	2.34	3.57
Coefficient of variation $[\%]$:		0.28	0.80	0.89	0.20
Average impact energy [J]:		7.1	17.0	27.1	62.7
Coefficient of variation $[\%]$:		0.56	1.61	1.78	0.40

9.3 Test results

This section contains the results of the test campaign. On the basis of these results, the rate-dependency of the material to out-of-plane impact is evaluated. Some force-displacement plots are discussed first to evaluate the global behaviour. Next, characteristics of all F-d plots are combined in overviews to see their rate-dependency. Finally, the dissipated energy is treated.

In section 8.5.2 it was already stated that the indentation tests are carried out up to the same maximum displacement as the representative LVI tests they are corresponding to. Rate-dependency is namely expected to influence the force if it is present. All curves are therefore plotted against maximum measured displacement, dynamic or quasi-static, to allow a comparison of results between test types. Note that a difference can be seen for maximum displacement between the two test methods, which is attributed to the finite stiffness of the static test bench.

The same symbols are used for each composite type in overview plots, see also table 9.3. LVI results are always plotted with filled symbols and solid lines, QSI results with empty symbols and dotted lines.

Table 9.3. Symbols used consistently for the indicated laminates and test types throughout chapter 9

			LVI	QSI
C/E	CP	UD	◆	◇
		#	★	☆
	QI	UD	■	□
		#	✶	✲
G/PA-6	CP	UD	▲	△
		#	▼	▽
	QI	UD	●	○
		#	⬟	⬠

9.3.1 General force-displacement behaviour

For each of the combinations of material, lay-up and drop-height, one of the five impact results is selected as representative for that specific situation. Figure 9.1 contains the unfiltered results of the representative LVI tests for a drop height of $0.8\,\mathrm{m}$ on the original tower, together with the corresponding QSI results. This concerns tests on laminates with UD layers. Figure 9.2 contains the same thing for the woven composites on the new drop tower.

Figures 9.1a and 9.1b show that both UD C/E layups behave similarly for QSI and LVI, disregarding the oscillations in the dynamic results. The load increases until a sudden reduction, after which it climbs again at a reduced stiffness. The maximum load and displacement only slightly differ between LVI and QSI. The same can be concluded for the woven C/E layups, compare the curves in figures 9.2a and 9.2b. Although epoxy shows rate-dependency of the Young's modulus in tension [2], the initial loading stiffness seems hardly influenced by the test speed. This stiffness is, however, hard to determine from the dynamic result, especially for the tests on the original tower, due to the oscillations present in the signal. Perhaps a small rate-dependency is obscured by these oscillations.

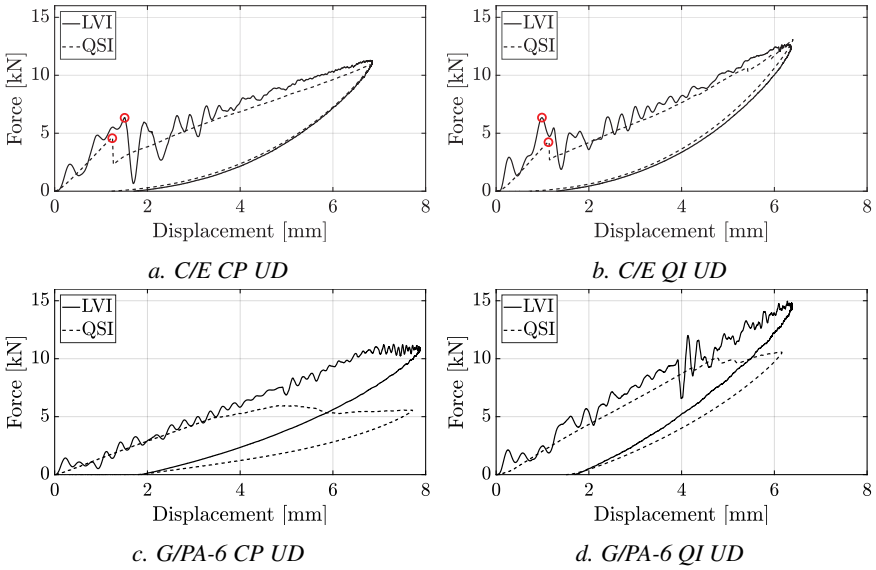

a. C/E CP UD *b. C/E QI UD*

c. G/PA-6 CP UD *d. G/PA-6 QI UD*

Figure 9.1. Representative force-displacement diagrams for LVI (solid) from $0.8\,\mathrm{m}$ *on the original drop tower and their representative QSI (dashed) counterparts on unidirectional C/E and G/PA-6 laminates. The circles in plots 9.1a and 9.1b for C/E indicate the selected moments of initial load drop.*

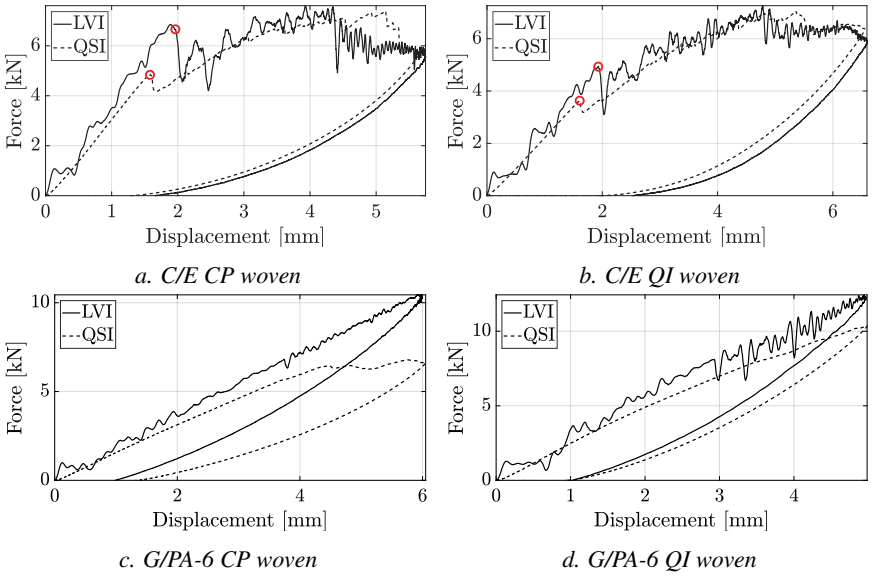

a. C/E CP woven *b. C/E QI woven*

c. G/PA-6 CP woven *d. G/PA-6 QI woven*

Figure 9.2. Representative force-displacement diagrams for LVI (solid) from $0.4\,\mathrm{m}$ *on the new drop tower and their representative QSI (dashed) counterparts on woven C/E and G/PA-6 laminates. The circles in plots 9.2a and 9.2b for C/E indicate the selected moments of initial load drop.*

G/PA-6 shows a similar behaviour for LVI and QSI until a maximum load is reached for QSI (figures 9.1c and 9.1d for UD, and 9.2c and 9.2d for woven). QSI then shows a practically horizontal plateau until unloading, while the load of LVI climbs higher before it deviates from the initially linear behaviour. Figure 9.2d hardly shows a plateau for the QSI result, because the plateau starts at a load of about $10\,\mathrm{kN}$, which has only just been reached for that QSI test.

The plateau indicates that the impactor is penetrating into the material rather than continuing to deform the entire specimen. The result is a decrease in strength for G/PA-6 upon switching to QSI tests. This relates directly to the rate-dependency of 1: the strength of glass fibres [3] and 2: the flow stress and strain to failure of the PA-6 matrix [4, 5]. There is thus a clear rate-dependency in the behaviour of G/PA-6, in contrast to C/E, for which the difference is not as pronounced. For the CP layup, the plateau is reached at a lower load, and also the LVI result shows a plateau.

Further research into the strain rates during impact is needed to conclude on the expected influence of constituent rate-dependence on the impact response.

9.3.2 Force and displacement at force drop

The C/E laminates show a drop in force during the loading stage for both LVI and QSI testing (circles in the results for C/E in figures 9.1 and 9.2), attributed to a sudden major damage increase. Note that some damage is likely created before this drop which does not significantly change the bending stiffness.

The G/PA-6 does not show this behaviour. Although the LVI result for the QI laminate in figure 9.1d does show a sudden oscillation at $10\,\mathrm{kN}$ where the QSI result shows a plateau. This behaviour is typical for many of the impact test results for G/PA-6, both woven and UD. The stiffness, however, remains practically unchanged after this oscillation. It is therefore uncertain whether it is related to the occurrence of damage and hence this subsection focuses solely on C/E.

The force and displacement just before the load drop are plotted against maximum displacement in figure 9.3 for all C/E laminates. Each plot shows three groups of results, corresponding to the three scenarios per laminate as outlined in tables 9.1 and 9.2. Logically, a larger maximum displacement relates to a higher drop height. The proximity of all the data points within each scenario demonstrates that the reproducibility is good. Load and displacement are almost consistently higher for LVI compared to QSI. On average, the force is $1.8\,\mathrm{kN}$ higher and the displacement $0.19\,\mathrm{mm}$ more for LVI.

Note from the solid lines in figure 9.3 that the force measured just before the sudden decrease shows an increasing trend for LVI. The displacement at this drop decreases slightly, though only for the UD specimens. The impact behaviour of C/E seems to be influenced by rate, and this could indicate an increasing brittleness with testing speed. This conclusion can, however, not be drawn with full certainty, owing to the oscillations in the dynamic force results. The laminate, moreover, is also loaded strongly in out-of-plane shear, and tests with that load scenario are needed to form definitive conclusion on the mechanism behind the observed rate-dependency here. The values remain constant for QSI, again demonstrating the good reproducibility.

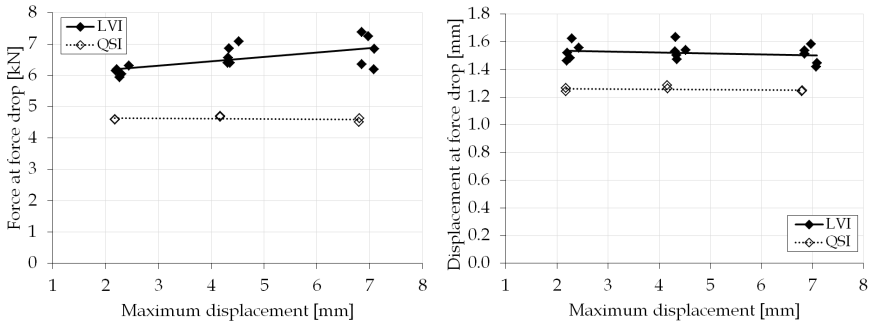

a. C/E CP UD: force at force drop

b. C/E CP UD: displ. at force drop

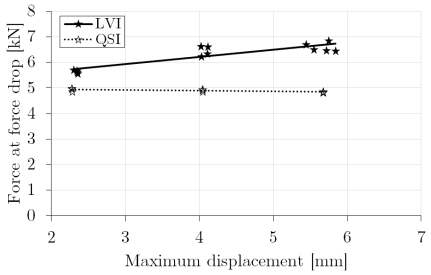

c. C/E CP woven: force at force drop

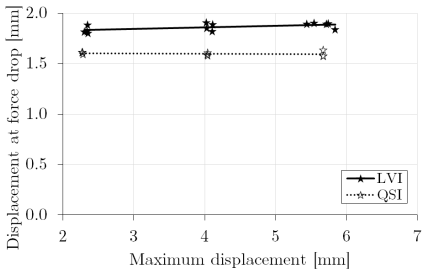

d. C/E CP woven: displ. at force drop

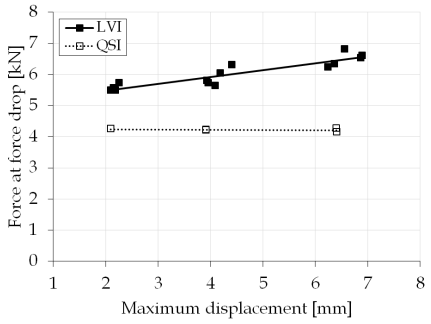

e. C/E QI UD: force at force drop

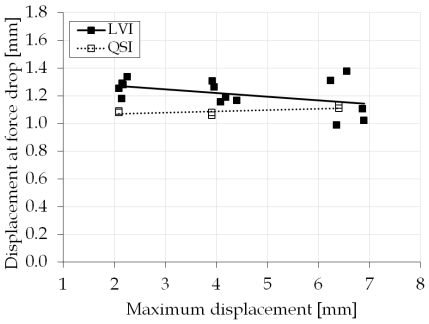

f. C/E QI UD: displ. at force drop

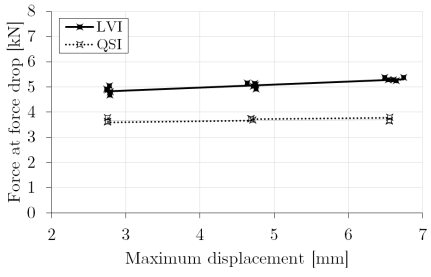

g. C/E QI woven: force at force drop

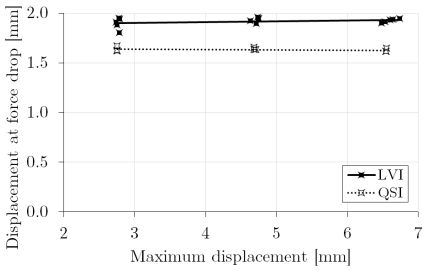

h. C/E QI woven: displ. at force drop

Figure 9.3. Force (left) and displacement (right) for C/E layups just before the force drop, versus maximum displacement. See also the circles in figures 9.1a and 9.1b.

9.3.3 Maximum force and displacement

The maximum force for each of the eight laminates is plotted against the maximum displacement in figure 9.4. The average QSI result is below that for LVI for each scenario.

One could argue that the absolute difference in maximum force between QSI and LVI decreases slightly with increasing drop height for C/E (the top four graphs in figure 9.4). The difference is small, though, and the QSI results fall inside the scatter band of the LVI results for many of the groups of results. These curves thus seem to suggest an absence of rate-dependency for C/E.

On the contrary, G/PA-6 shows a clear difference between LVI and QSI (the bottom four graphs in figure 9.4), which increases with drop height. This trend is a result of the force plateaus during QSI. Where the LVI tests keep showing an increase in force, the QSI tests all show approximately the same maximum load. Here it can also be seen that for woven QI G/PA-6, the maximum force for QSI indeed lies at about $10\,\mathrm{kN}$, as was mentioned in section 9.3.1.

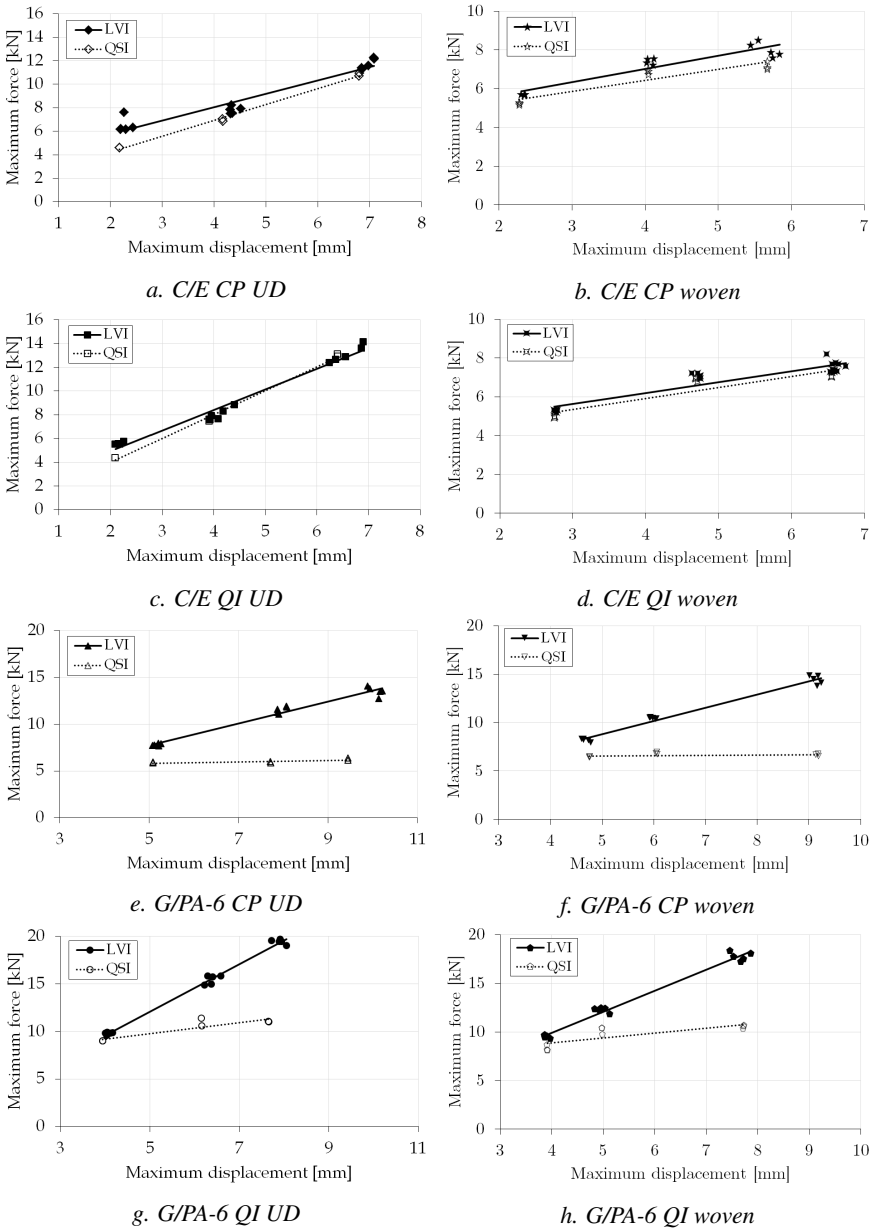

a. C/E CP UD *b. C/E CP woven*

c. C/E QI UD *d. C/E QI woven*

e. G/PA-6 CP UD *f. G/PA-6 CP woven*

g. G/PA-6 QI UD *h. G/PA-6 QI woven*

Figure 9.4. Maximum force results versus maximum displacement.

9.3.4 Dissipated energy

The ASTM standard prescribes that the dissipated energy during impact should be calculated by means of the loss of kinetic and potential energy with respect to the start of the impact [6]. The displacement signal suffices to calculate this loss, as the velocity for the kinetic energy is obtained by differentiation. For the current research, however, the final value of the evolution of absorbed energy is taken, as explained in section 8.7.4. It was verified that both methods of computing the dissipated energy result in practically overlapping values for all tests. The dissipated energy at the end of the impact is a measure of the amount of damage created in the material. For all eight layups, the dissipated energy is plotted versus maximum displacement in figure 9.5.

For C/E, all QSI values fall within the scatter band of the LVI results (top four graphs in figure 9.5). For G/PA-6, some difference can be discerned (bottom four graphs). For the CP layups, the QSI results drop further underneath those for LVI with increasing maximum displacement, while for the QI layups the opposite is true. The small differences for G/PA-6 are deceiving: the force-displacement curves showed a large difference between QSI and LVI, and it will follow from the microscopic inspection that dissimilar damage patterns are created by both tests. It is thus concluded that energy dissipation is not suitable to characterise the rate dependency of laminates under out-of-plane loading.

Comparing the different material systems with each other, it can be seen that C/E dissipates more energy than G/PA-6 for the same maximum displacement. One could, however, question the validity of this comparison. The laminate thickness values are namely not equal and even if they were, the bending stiffness would not be the same between different laminates, resulting in different values of absorbed energy for a certain displacement. No further effort is spent to find a suitable unit for an honest comparison.

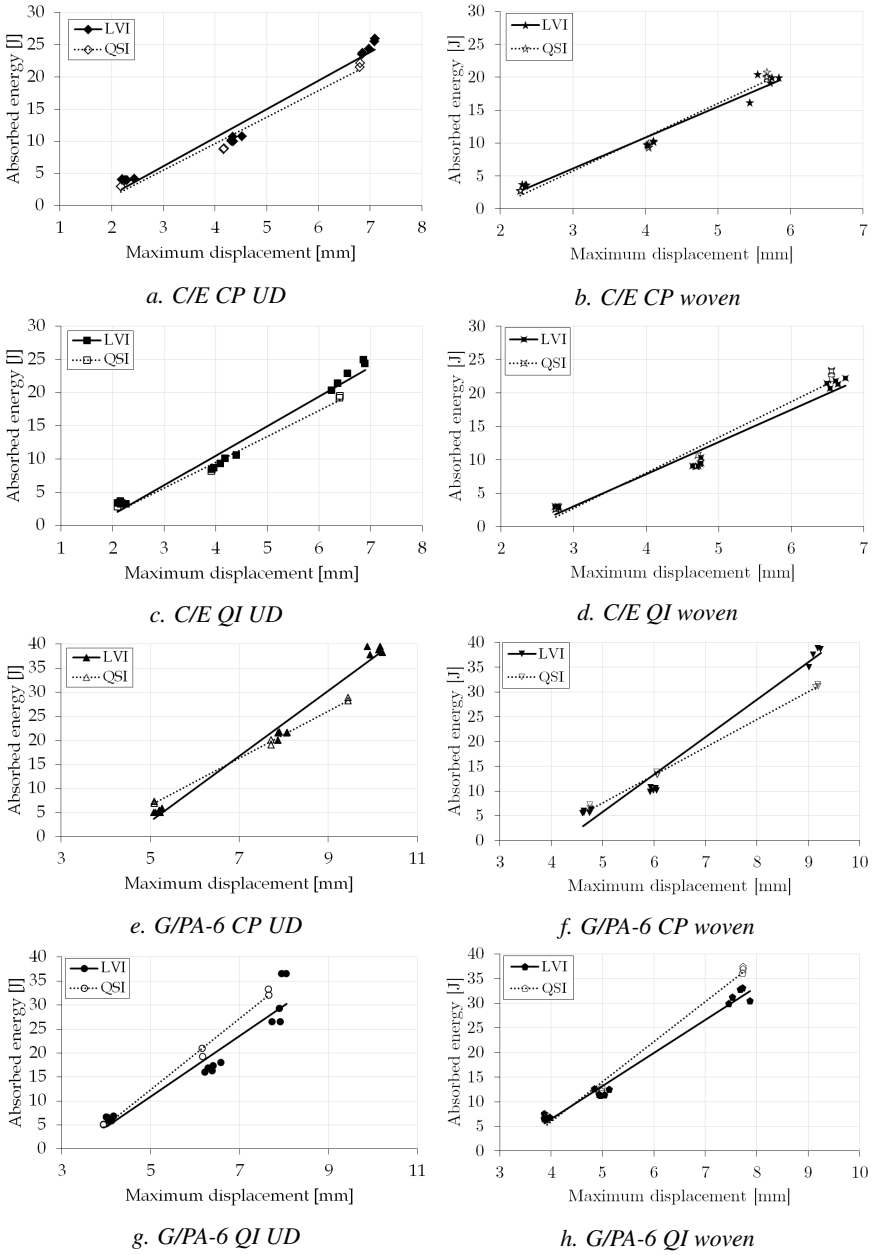

a. C/E CP UD *b. C/E CP woven*

c. C/E QI UD *d. C/E QI woven*

e. G/PA-6 CP UD *f. G/PA-6 CP woven*

g. G/PA-6 QI UD *h. G/PA-6 QI woven*

Figure 9.5. Dissipated energy versus maximum displacement.

9.4 Post-mortem inspection results

One specimen is selected for each test condition, for which the results seem most representative for the combined data of all repetitions, and subjected to ultrasound post-mortem analysis. A total of 48 specimens (24 impacted, 24 indented) is thus analysed this way. Subsequently, eight C-scanned UD-layered specimens are inspected using optical microscopy. The damage features have been identified on four of the resulting micrographs.

First the results of the ultrasound inspection programme are given: each of the three techniques explained in section 8.8.1 is treated. Subsequently, the results of the microscopic investigation are presented.

9.4.1 Transmission ultrasound for damage area

Figures 9.6 and 9.7 contain several examples of a transmission C-scan. As can be seen in the figures, the UD C/E shows the largest damaged zones for all the specimens, even though the impact height was the smallest. The lateral distance of the damage in the carbon/epoxy to the point of impact equals just over $36\,\mathrm{mm}$ in one direction. This means that the damaged area partially surpasses the unsupported area, because the specimen support starts at $35\,\mathrm{mm}$ from the centre in lateral direction. The damage has likely been influenced by the boundary conditions in this case, and it might be that the delaminations would have been larger if the boundary conditions were further away.

The damage shapes are not as regular for the woven specimens. This is attributed to the more irregular nature of the interface of a woven ply, which causes plies to be nested into each other. The woven structure is not visible in the woven C/E (figures 9.7a and 9.7b), likely because the tow width of $2\,\mathrm{mm}$ is much smaller than the diameter of the ultrasonic transducers used for the analysis. The woven G/PA-6 laminates clearly show their woven structure on the C-scans, see figures 9.7c and 9.7d. The tow width of the G/PA-6 weaves is about $5\,\mathrm{mm}$, still smaller than the transducer size, but now multiple scanning points fall within one tow. The blue areas away from the central damage in the images could point to matrix pockets or other variations in the weave pattern, because the size of the tows is relatively large ($5\,\mathrm{mm}$) compared to the scan steps (maximum $1\,\mathrm{mm}$). They are likely not badly consolidated areas, considering the absence of air pockets in the micrograph of the woven G/PA-6 material in figure 3.7.

It was explained in section 8.8.1 how the area of the damaged zone was obtained from the scans. The calculated damage areas are set out against the maximum displacement in figure 9.8. For C/E, QSI consistently results in a larger damaged area compared to LVI (figures 9.8a and 9.8b). Section 9.3.4 concludes that the energy dissipation is equal, indicating a stronger presence of another dissipating mechanism, *e.g.* fibre or matrix cracking. The damage area is negligibly

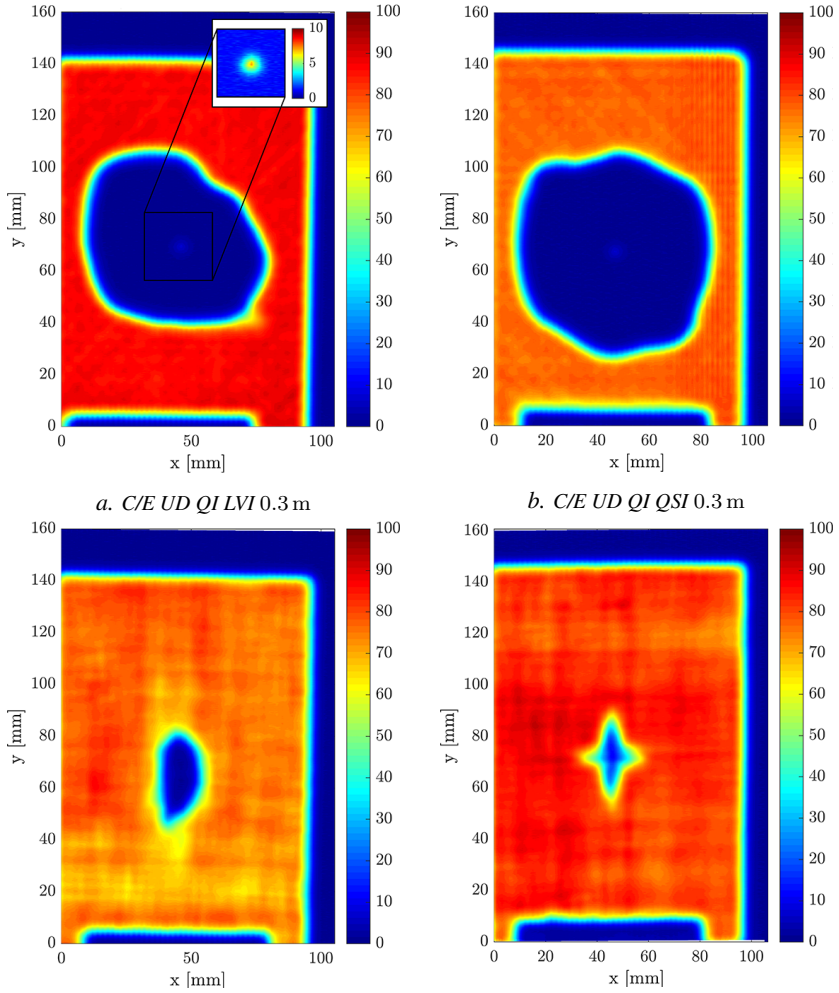

a. C/E UD QI LVI 0.3 m

b. C/E UD QI QSI 0.3 m

c. G/PA-6 UD CP LVI 1.2 m

d. G/PA-6 UD CP QSI 1.2 m

Figure 9.6. Transmission ultrasound scans. The colours show the transmissive signal strength normalised to the reference strength outside the damaged zone. The height next to QSI specimens is the drop height of the corresponding LVI specimens. The insert of figure 9.6a shows the centre section at a different colour scale.

different for woven quasi-isotropic C/E laminates.

G/PA-6 shows a different behaviour (figure 9.8c): the damaged area after QSI is consistently *below* that after LVI. For the woven laminates the difference is small at low maximum displacements though. It is even negligible for all tested heights for woven CP. The QSI tests result in a more localized damage, matching the conclusion drawn in the final part of section 9.3.1 based on the plateaus in the

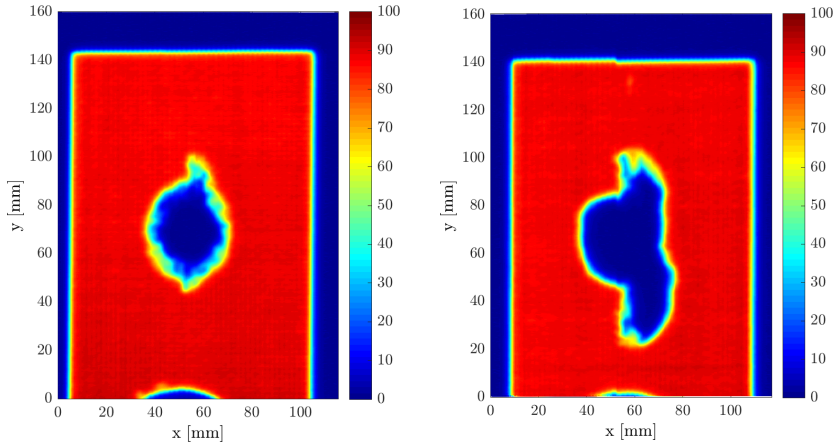

a. C/E woven CP LVI 0.4 m

b. C/E woven CP QSI 0.4 m

c. G/PA-6 woven QI LVI 0.9 m

d. G/PA-6 woven QI QSI 0.9 m

Figure 9.7. Transmission ultrasound scans. The colours show the transmissive signal strength normalised to the reference strength outside the damaged zone. The height next to QSI specimens is the drop height of the corresponding LVI specimens.

force response. The higher speed of the impact tests invokes a more bending-type of response, causing a larger part of the laminates to play a role in resisting the out-of-plane load, thus resulting in the larger damage area.

Upon comparing the two materials with each other, the difference in area between the UD-variant of the two material systems is striking: figures 9.8a and 9.8c differ by an order of magnitude. This is the reason that the scans in figure 9.6 for UD G/PA-6 are for a drop height of 1.2 m while those for C/E are for 0.3 m. Still the UD C/E shows a larger damage size, it is much more prone to delamination

than the UD G/PA-6. Both the woven laminates, however, have comparable damage areas. Where the woven structure brings a significant improvement for C/E compared to the UD material, for G/PA-6 it practically doubles the damage area. The cause of this is currently unknown. There might be local consolidation issues in the woven G/PA-6 laminates which were not captured with optical microscopy, because the shape of the damaged area for these specimens shows irregular and asymmetric shapes. This effect which is not seen in the UD G/PA-6 (compare figures 9.6c and 9.6d to figures 9.7c and 9.7d).

Finally, the damage area for CP is consistently smaller than that for QI. Likely the impactor pushes more easily through the CP laminates than QI ones. The latter are namely expected to be better at spreading the load.

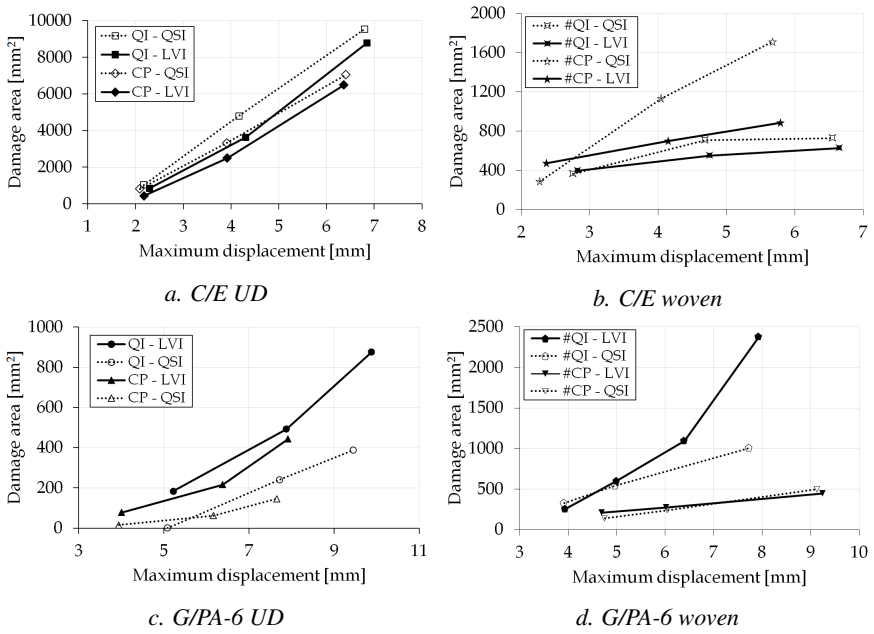

a. C/E UD *b. C/E woven*

c. G/PA-6 UD *d. G/PA-6 woven*

Figure 9.8. Damaged area versus maximum displacement.

9.4.2 Surface reflection ultrasound for dent depth

Using the surface reflection of the ultrasonic signal, the height profile of the specimens is obtained, from which the dent depth can be calculated (section 8.8.1). The thus obtained dent depths are plotted against the maximum displacement in figure 9.9. All dent depths increase with increasing maximum displacement. QSI consistently shows a higher dent depth than LVI, though the difference is small for UD C/E (figure 9.9a) and practically absent for woven C/E (figure 9.9b).

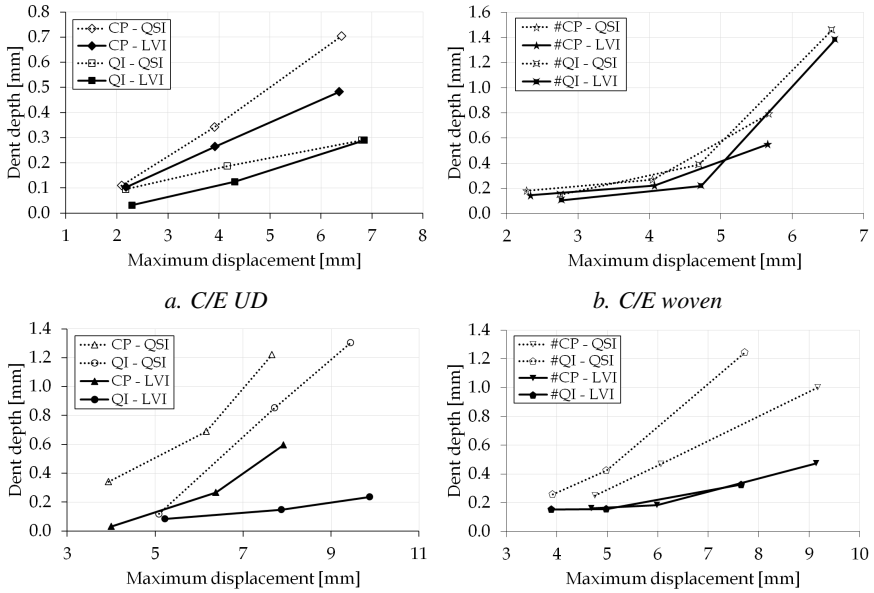

a. C/E UD *b. C/E woven*

c. G/PA-6 UD *d. G/PA-6 woven*

Figure 9.9. Dent depth versus maximum displacement.

For G/PA-6, the differences are much larger (figures 9.9c and 9.9d). For QSI, the indenter simply pushes through the material at some point, going deeper for higher maximum displacements. For LVI, however, a larger part of the plate responds, as said, in a more bending-type of way. This prevents the impactor from penetrating as much as the quasi-static indenter does and thus explains the increasing difference with increasing maximum displacement.

Overall, the depths are larger for the CP than for the QI laminates, the same counts for the difference between QSI and LVI. It was verified that, when the specimens are kept dry, no relaxation occurs: the dent depth of a G/PA-6 specimen was found not to reduce with time.

Comparing the G/PA-6 dent depth trends with those for the damage size in figures 9.8c and 9.8d, once again the change in damage mechanism between QSI and LVI becomes clear. While the damage size for QSI is smaller than for LVI, the dent depth is larger, proving that something different is happening there.

9.4.3 Reflection ultrasound for damage shape

Looking at the QI C/E specimen in figure 9.10a, delaminations in different planes follow a staircase-like pattern around the impact zone in a point-symmetrical fashion. The deeper delaminations seem not to run further inward than the outer edge of a more shallow delamination. This is a shadowing effect, caused by the nearly full reflection of ultrasound at a delamination. Scanning from both sides can partially resolve this issue, see figure 9.11. The deeper delaminations indeed reach further inward than the outer edge of others closer to the top surface, although again they are obscured at the centre. It appears the largest delaminations are not closest to the bottom: they do not follow a conical shape through the thickness.

Comparing the result of QI C/E after QSI (figure 9.11a) with that after LVI (figure 9.10a), one can see that the shape of the damaged regions look alike, indicating that the damage mechanisms are similar as well. The same can be concluded for CP laminates.

As mentioned before, only delaminations reflect a significant amount of ultrasound back to the emitting transducer. These thus abundantly exist in the UD C/E specimens. The situation is different for UD G/PA-6 (figure 9.10b). Typically the scans show no clear reflection for any depth, suggesting that only a very small amount of delamination is present. The same can be said for the woven G/PA-6 specimens. Micrographic analysis shows more fibre waviness and layer thickness variations for G/PA-6 than for C/E (chapter 3), compare also the differences in reflection for the undamaged material in figure 9.10b to 9.10a. Moreover, PA-6 is expected to show a stronger ultrasound damping compared to epoxy. Both effects hinder the reflection of ultrasound.

The reflection scans of the woven C/E laminates provide hardly any extra information compared to the transmission scans. There seems to be no significant change in area with depth, and thus no further analysis is performed on these images.

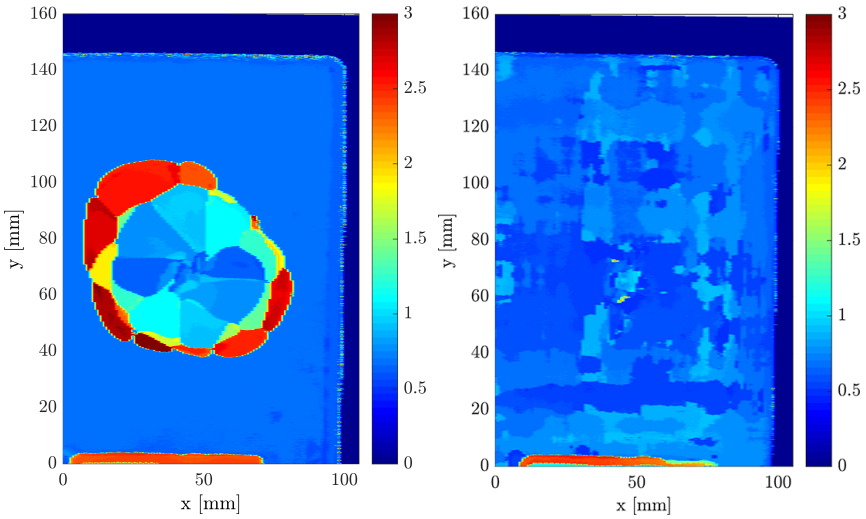

a. C/E QI LVI 0.3 m *(see also fig. 9.6a)* *b. G/PA-6 CP LVI* 1.2 m *(see fig. 9.6c)*

Figure 9.10. Reflection C-scans of the same LVI specimens as in figures 9.6a and 9.6c. The colours indicate the time-of-flight in µs*, a larger value thus corresponds to a deeper delamination.*

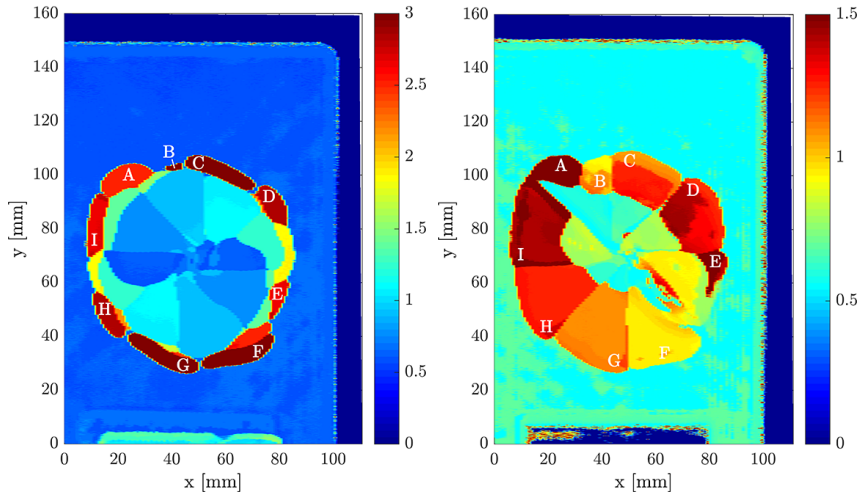

a. C/E QI QSI 0.3 m *top* *b. C/E QI QSI* 0.3 m *bottom*

Figure 9.11. Reflection C-scans of QSI UD QI C/E (figure 9.6b) from both sides of the specimen. The colours indicate the time-of-flight in µs*. Specimen orientations are equal, so the delaminations are located in the same positions in each figure. For clarity, delaminations visible in both scans have been indicated with a letter. The mentioned height is the drop height of the LVI equivalent.*

9.4.4 Optical microscopy

Eight C-scanned UD-layered specimens are inspected using optical microscopy. Damage identification on the micrographs is done for only four of the available images, because of a restriction in time, see figures 9.12 and 9.13. The geometry is indicated in black, damage in various colours. The arrowhead indicates the point of impact/indentation.

The end of the delaminations away from the impact zone show a large similarity for both test methods. In both cases, it can be verified that the delamination lengths increase from the top interface towards three-fourths of the depth, after which some smaller delaminations follow. These conclusions are supported by the pulse echo C-scanning in section 9.4.3.

The damage patterns also show differences which are larger than can be simply attributed to scatter in local properties. The delaminations continue underneath the impact zone for the impacted specimen, while this is practically not the case for the indented specimen. The C-scans indicate that this difference only exists for the CP specimens. The insert in figure 9.6a clearly shows the area underneath the impacted UD QI C/P is also less damaged than its surroundings. Another remarkable difference is a severe concentration of matrix cracks just aside of the impact for LVI, against a more even distribution of fewer matrix cracks for QSI. Energy dissipation for LVI is more matrix-cracking-dominated, which also agrees with the earlier conclusion (section 9.4.1). The differences are not as striking as for the G/PA-6. Still, it is concluded here that the differences are of such an order that the behaviour of the C/E laminate can be marked as rate-dependent. Special care should thus be taken if one intents to validate high-fidelity finite-element models using out-of-plane testing.

The differences in overall behaviour (force-displacement, energy dissipation) between LVI and QSI, both woven and UD, are deemed small enough, though, that for design purposes one could interchange LVI with the much easier to perform QSI. This is especially true considering that the LVI properties are slightly underestimated by QSI, leading to a conservative design.

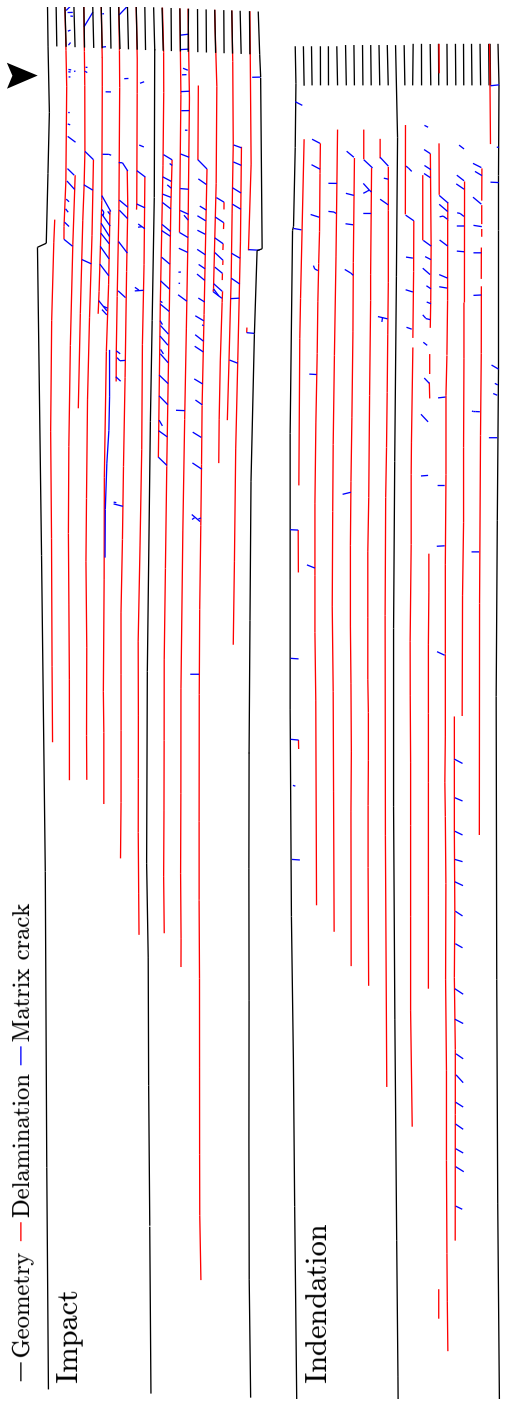

Figure 9.12. Damage characterized from stitched micrographs of CP C/E after LVI from 0.3 m *(top) and its corresponding QSI specimen (bottom, see also figure 8.36). Both images are set to the same scale and aligned at impact, indicated with an arrowhead.*

The damage features of UD QI G/PA-6 after LVI from $1.2\,\mathrm{m}$ and its QSI counterpart are shown in figure 9.13. There is a large difference in the damage. The impacted specimen shows widespread matrix cracking in its bottom half. Some delaminations are present, mostly in the top half and close to the impact zone. The indented specimen shows few matrix cracks and delaminations, implying that PA-6 has a higher ductility at low deformation rates. Instead of the matrix cracks and delaminations, there is severe damage underneath the indenter tip. It becomes clear that this material shows strong rate-dependency.

The different damage mechanisms for QSI and LVI on QI G/PA-6 demonstrate the misleading character of the energy absorption plot in figure 9.5g. The plot shows an almost equal energy absorption for both methods, which could lead to false conclusions when basing on dissipated energy alone.

An interesting feature of the G-PA-6 LVI specimen is the large horizontal crack just above the middle, which is indicated with an arrow. It consists of a delamination which for a large part travels within a layer rather than at its interface. This proves that the fibre-matrix adhesion is as strong as the matrix itself, explaining the small amount of delamination in the G/PA-6 specimens.

Material properties for G/PA-6 obtained using QSI severely underestimate its performance under LVI, except for the energy dissipation. It seems by chance, however, that the resulting values lie so close to each other. It is hence not recommended to base the impact resistance of structural designs on QSI-properties for G/PA-6, as they will likely become overly conservative.

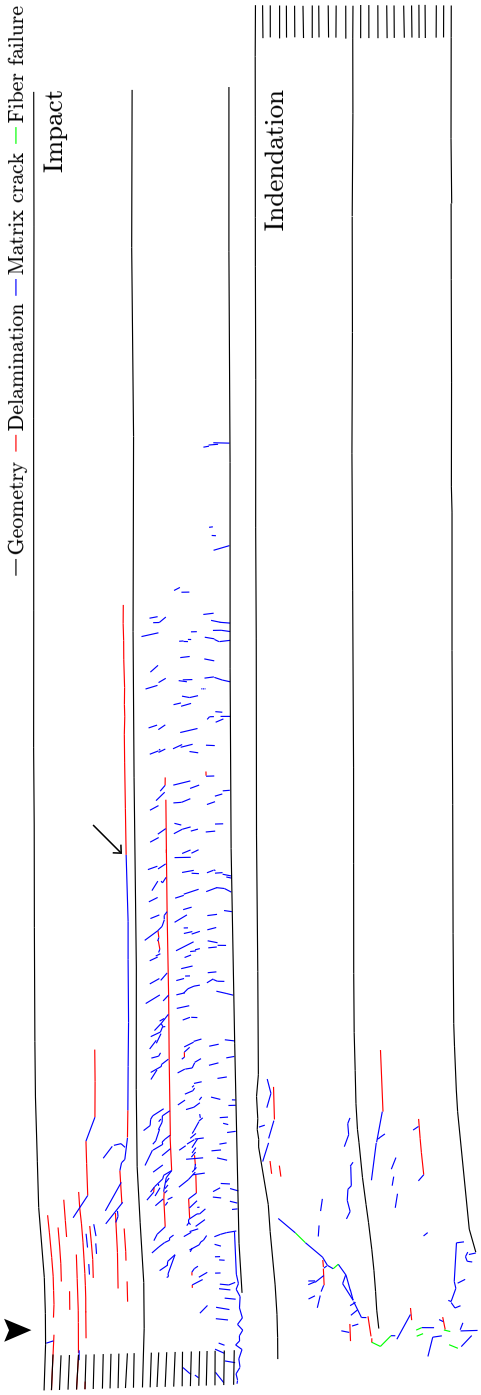

Figure 9.13. Damage characterized from stitched micrographs of G/PA-6 QI after LVI from 1.2 m *(top) and its corresponding QSI specimen (bottom). Both images are set to the same scale and aligned at impact, indicated with an arrowhead. The arrow points to a delamination that connects to an in-plane matrix crack.*

Validation of ultrasound measurements

The results from optical microscopy can be used to validate in-plane damage dimensions found along the lateral and longitudinal centrelines using C-scanning. Three damage lengths per microscopically investigated specimen are compared with the transmission C-scans, see figure 9.14. One transversal cut and one subsequent longitudinal cut is made, resulting in a cross-section from one crack tip to the other and one that reaches only up to the impact zone, respectively. The distance of the outermost delamination to the impact point is taken for comparison. Other types of damage are not included, since it is assumed that low concentrations of damage not perpendicular to the travel direction of the sound do not contribute to significant reductions of transmitted ultrasound. The results are summarised in figure 9.15. The solid bars indicate optical measurements, the data for the chequered bars is produced using the ultrasound technique. The three shades of grey correspond to the different directions in which the comparison is made, the darkest is linked to the longitudinal direction, the two lighter ones to the two transverse directions. Figures 9.12 and 9.13 contain damage characterisations of the right transverse direction of four specimens. The drawings in figure 9.12 represent the lightest bars of specimens 1 and 5. The sections in figure 9.13 are linked to the lightest bars of specimens 4 and 8.

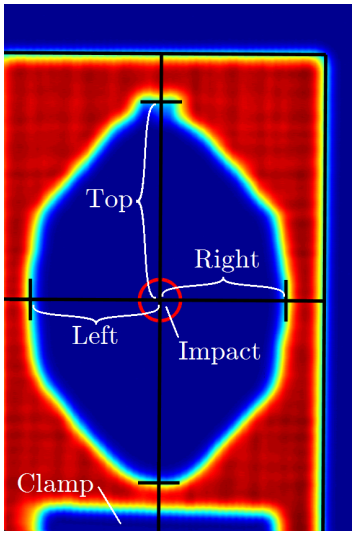

Figure 9.14. Description of the different delamination lengths mentioned in the legend of figure 9.15

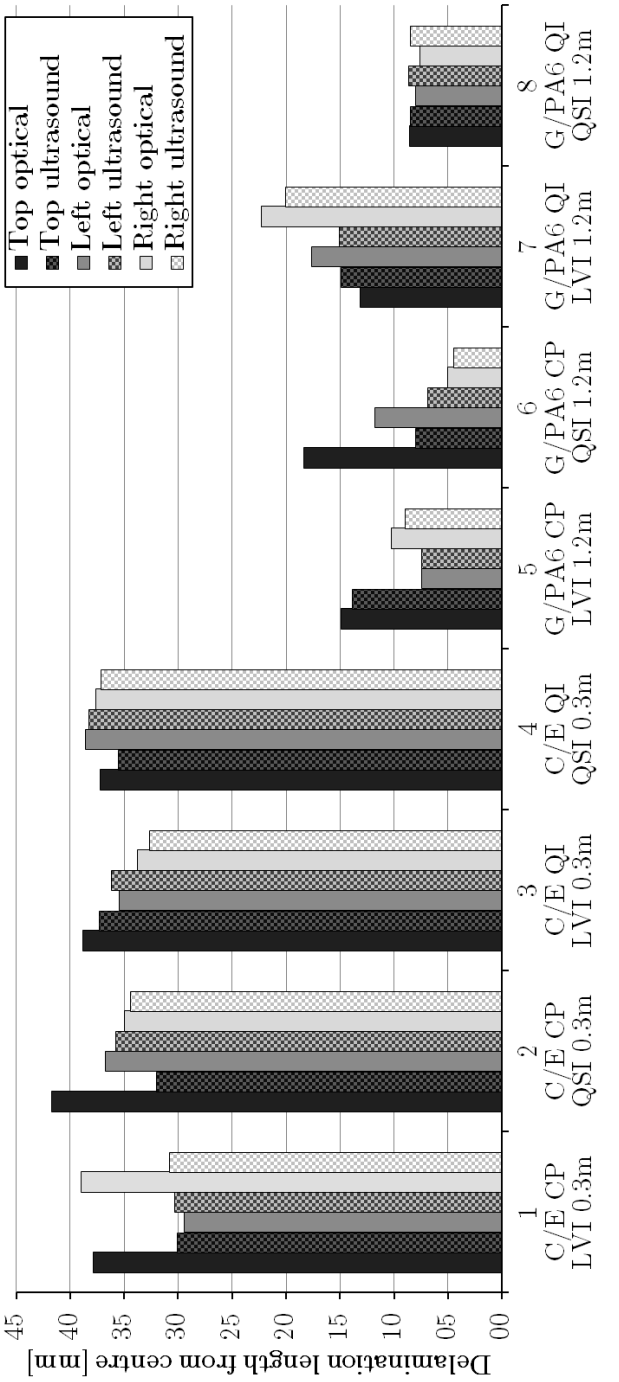

Figure 9.15. Comparison of in-plane delamination lengths measured using different techniques.

On average, the absolute difference between optical and ultrasound delamination length is $2.5\,\mathrm{mm}$. This makes it seem that the threshold value mentioned in section 8.8.1 is a good choice. In all but five cases, the optically measured length surpasses the ultrasonically obtained value. In the five cases for which the optical value is surpassed, the difference is only small. There are two possible explanations for this phenomenon. First, as can be seen by comparing the bottom image in figure 9.12 with figure 8.36, the delaminations are hardly visible. Especially towards their tips they have been reduced to a very thin line. In case two crack surfaces are held strongly together by the surrounding material, it could be that the crack does not appear on a C-scan, because sound is still efficiently transmitted over the crack. Second, it is also possible that the specimen cutting process induced extra damage, although the materials were supported along their entire length during cutting, and were only advanced at a relatively slow rate (as described in section 8.8.2).

All in all, it is concluded that transmission C-scanning is capable of accurately capturing the delamination length.

9.5 Conclusion

The dependency on rate of the response and the post-test damage has been evaluated for carbon/epoxy and glass/polyamide-6 composites. Cross-ply and quasi-isotropic layups were investigated in both a woven and a unidirectional configuration. A total of 120 impact tests from three drop heights per material system have been carried out, accompanied by 60 quasi-static indentation tests up to the same maximum displacements. Three different C-scanning techniques and microscopy were used to investigate the type and extent of damage caused.

For glass/polyamide-6, the influence of the constituent rate-dependency on the out-of-plane behaviour is too large to be able to characterise low-velocity impact behaviour using quasi-static indentation. The force-displacement response is completely different at the higher displacement values. Other characteristics (dissipated energy, area of delamination, dent depth) are relatively similar and could lead to a false sense of equivalence between the two test types. Optical microscopy brings the different damage mechanism clearly to light. The higher strength and strain to failure at high strain rate cause a much larger area to cooperate in the energy dissipation during impact by widespread matrix cracking, in contrast to the local damage zone created by indentation.

The results show, perhaps surprisingly, that carbon/epoxy also behaves different in quasi-static indentation compared to low-velocity impact. The differences, however, are considerably smaller than for glass/polyamide-6. The force-displacement curves show an underestimation of the load prior to the first significant stiffness loss for quasi-static indentation. Maximum force and (again)

dissipated energy are hardly affected. The C-scans show that the damaged area and dent depth are overestimated when using quasi-static indentation. Optical microscopy reveals that quasi-static indentation creates virtually no damage directly underneath the impactor for the carbon/epoxy cross-ply laminate investigated, contrary to low-velocity impact, and a reduced concentration of matrix cracks is seen. Hence, it is concluded that for accurate validation of finite-element models that intent to capture the impact damage, one needs to consider the rate-effects. From a design perspective, though, quasi-static indentation can be used to obtain a conservative estimation of the damage area due to low-velocity impact for carbon/epoxy.

The laminates with a woven architecture behave similarly to the UD laminates in terms of rate-dependency of out-of-plane behaviour. Typically the same conclusions could be drawn for both types of fibre architecture.

Finally, it is concluded that the energy dissipation of a laminate is not a suitable value to characterise the rate dependency of laminates under out-of-plane loading.

References

[1] R. Olsson. *Mass criterion for wave controlled impact response of composite plates*. Composites Part A: Applied Science and Manufacturing, 31(8):879–887, August 2000.

[2] A. Gilat, R. K. Goldberg, and G. D. Roberts. *Strain Rate Sensitivity of Epoxy Resin in Tensile and Shear Loading*. Technical report, National Aeronautics and Space Administration (NASA), March 2005.

[3] Z. Wang and Y. Xia. *Experimental evaluation of the strength distribution of fibers under high strain rates by bimodal Weibull distribution*. Composites Science and Technology, 57(12):1599–1607, January 1998.

[4] G. Shan, W. Yang, M.-b. Yang, B.-h. Xie, J.-m. Feng, and Q. Fu. *Effect of temperature and strain rate on the tensile deformation of polyamide 6*. Polymer, 48(10):2958–2968, May 2007.

[5] I. Benaceur, R. Othman, P. Guegan, A. Dhieb, and F. Damek. *Sensitivity of the flow stress of nylon 6 and nylon 66 to strain-rate*. International Journal of Modern Physics B, 22(09n11):1249–1254, April 2008.

[6] ASTM International. *ASTM Standard D7136, 2015, "Measuring the Damage Resistance of a Fiber-Reinforced Polymer Matrix Composite to a Drop-Weight Impact Event"*. Technical report, American Society for Testing and Materials, West Conshohocken, PA, 2015.

10 Conclusions and future research

In this chapter, conclusions are drawn for the research on rate dependency of composite laminates, after which recommendations for further work follow.

10.1 Conclusions

The dependency of the material properties with testing speed of two automotive composite material systems, carbon/epoxy and glass/polyamide-6, has been researched. Experimental methodologies were developed for three load cases: tension, mode-I delamination and out-of-plane impact. Dynamic tensile tests were carried out using a hydraulic pulse test bench. The impact experiments were conducted on a drop tower which had been specially redesigned in-house for the current experimental programme. Dynamic delamination was performed using both the drop tower and the hydraulic pulse machine.

A large and consistent set of test data was obtained. The results are reliable, because the testing limits of the various methods have been quantified and the data is limited to the valid range. The two material systems cover a wide variety of responses, allowing researchers to determine which aspects of material behaviour need to be included in predictive models. Furthermore, both basic materials and more complicated laminates have been tested, allowing the data to be used for model development as well as validation. All this leads to the conclusion that the goals set in the introduction have been mostly met.

10.1.1 Dynamic tension

Around 500 specimens of several lay-ups were subjected to dynamic tension. The hydraulic pulse test bench proved a very suitable piece of equipment to investigate composite material properties from quasi-static up to $200\,\mathrm{s}^{-1}$. A new dumbbell specimen type was designed for the pure $90°$, the quasi-isotropic and the woven cross-ply layups, which resulted in successful failures, consistently away from the clamps. Digital image correlation using a high-speed camera proved to produce useful results up to the maximum rate for even the brittlest material, although the full-field aspect of the strain data is lost because of the low resolution of the images. The computed strain corresponded well with that acquired from the readout of strain gauges using a high-speed signal conditioner. The data could be presented without the use of any filtering. Only for the calculation of the piston velocity the data required filtering to ensure the numerical differentiation would produce useful results.

It was shown that the synchronization of the various data streams, one load and two strain channels, is of utmost importance at the higher rates. This synchronization was successfully realized by careful analysis of all the measurement chains and taking into account all delays that occur in the various subsystems. Manual alignment of stress and strain on *e.g.* the initial signal rise or the failure point is not accurate and can even result in an apparent rate-dependency which does not occur in reality. In literature, though, there is very little discussion on the data synchronization. Only one group of researchers admit to manually align stress with strain, though the results in other works suggest this method was applied more often.

At high strain rate, care should be taken not to mistake dynamic test effects for material behaviour. This aspect is also very often overlooked in literature and test results are not rarely blatantly presented up to rates which far exceed the valid range. The causes of all the observed aspects of the test results have been identified, with the help of finite-element analyses. The numerical simulation of the experimental procedure is the only tool that allows to gain such a clear insight into the validity of the applied method. Five limits on the upper strain rate have been encountered and quantified: (1) the test bench capabilities, (2) ringing of the load cell, (3) the frame rate for DIC acquisition, (4) the bandwidth of the strain gauge amplifier and (5) the approximate equilibrium within the sample. Although they do not constitute 'hard' limits, results at higher rates should be interpreted with caution as they will no longer solely represent actual material behaviour. Most of the limits depend directly on the duration of the test, which in turn is dominated by the strain to failure of the material under investigation. The lower the strain to failure, the lower the maximum strain rate at which that material can be tested.

With the limits on maximum strain rate quantified, invalid results could be removed, resulting in a reliable database of dynamic tensile stress-strain curves and corresponding material parameters. Nowhere in literature is such a large and con-

sistent data set available, especially for glass/polyamide-6 composites, for which practically no dynamic data can be found, even though the material system is gaining more interest for applications in the automotive industry.

The strongest rate-dependency is seen in the pure polymers. The absence of rate-dependency in the pure carbon fibre properties causes the overall dependency on test speed of any fibre-dominated carbon/epoxy laminate, woven or unidirectionally layered, to be practically absent. The 0° unidirectional glass/polyamide-6 shows a clear rate-dependency which stems from the glass fibres, and it propagates into the other laminates, though the percentile change with rate is reduced. The macroscopic rate-dependency of woven composites with cross-ply or quasi-isotropic lay-ups mostly follow the behaviour of the 0° unidirectional laminates (or fibres) of the same material system, albeit that the differences become even smaller. For laminates with fibres only oriented in the ± 45 directions, woven or unidirectionally layered, the rate-dependency is strongest on maximum stress and Young's modulus while the strain to failure remains untouched: the stress-strain curves appear to be 'pulled upwards.'

In most cases the fracture surfaces look alike for the specimens tested at different velocities, though the dynamically tested specimens often have multiple cracks and more paint has fallen off. The fact that there is more than one failure point shows that stress wave effects are indeed significant, and that local interactions of stress waves can produce peak stresses which surpass material strength. The loss of more paint, moreover, indicates a more violent rupture, which means the accelerations were higher and/or more energy was released upon failure.

10.1.2 Dynamic mode-I delamination

Two test methods were applied to conduct dynamic mode-I delamination on the two material systems: the drop tower and the hydraulic pulse machine. In both cases, a double cantilever beam specimen was mounted horizontally and the lower arm was actuated while the upper arm was constrained in displacement and could only rotate in the vertical plane parallel to the side of the specimen.

The drop tower set-up proved capable to delaminate the specimens at different speeds depending on the drop height: the inertia of the bottom block is thus enough to conduct a delamination test. The experimental set-up is, however, limited to rather stiff composites due to its dimensions, and to interfaces with a rather low value for the fracture toughness due to the limited amount of energy that can be transferred to the bottom block. It is therefore not suitable to test G/PA-6 for dynamic delamination. Optical measurement of the bottom block displacement worked well, though the recording needs to be carried out at frame rates (far) exceeding the applied $20\,000$ frames per second to ensure that the double numerical differentiation of the data results in useful acceleration values. Extracting the dy-

namic fracture toughness using a combined experimental-numerical approach was not successful. The steel-to-steel impact between the impactor tip and the bottom block namely caused the problem to be ill-conditioned and no mesh convergence was obtained.

Dynamic delamination using the hydraulic pulse test bench worked better. The test bench is capable of measuring useful loads up to speeds of about $1\,\mathrm{m\,s^{-1}}$. Filtering of the load signal, however, is necessary, because the crack never progresses fully smoothly and the shape of the specimen causes the time needed to damp out the stress waves, resulting from a sudden crack jump, to be rather long. Stiffening the specimen reduces this time and is therefore beneficial for dynamic delamination tests. Stiffening, moreover, causes the number of crack steps for the woven specimens to increase, thus resulting in more reliable fracture toughness measurements.

Automatic crack front tracking at high speeds is not straightforward, as the usually limited resolution of high speed cameras at high frame rates reduces the accuracy to an unacceptably low level. Some authors resort to estimating the crack length from the displacement of the two halves and the quasi-static bending stiffness. The possible rate dependency, however, of the bending stiffness makes that also such a method is likely not accurate enough. Manually reading out the crack length from the high speed footage proved the only currently viable option, which is relatively time-consuming for large test programmes, but was proven to result in reliable data.

The experiments and a finite-element model show that the curvature of both legs is not equal during high speed mode-I delamination tests using a set-up where only one end of the specimen is loaded. This is especially the case in the initial part of the test. This means that the bending moment is not equal in both legs, resulting in a crack propagation which is not pure mode-I. The only way pure mode-I high speed delamination can be realised with the use of a double cantilever beam specimen, is by loading both halves simultaneously.

Using the finite element model, it was also shown that the test speed of the current experimental set-up is limited to about $3\,\mathrm{m\,s^{-1}}$, above which the equations used for the quasi-static tests are no longer valid due to the absence of equilibrium. The materials investigated show a decrease in the fracture toughness with rate in the valid range of actuation speeds from quasi-static to $1\,\mathrm{m\,s^{-1}}$. This rate-dependency might be caused by a change in the amount of bridging with testing speed, though more research is necessary to prove this claim.

10.1.3 Out-of-plane impact

A new drop tower was developed to conduct low-velocity impact tests on the composites of interest. Compared to the original drop tower, a largely increased consis-

tency in impact velocity was achieved, and thus the resulting force-displacement curves of multiple specimens for the same scenario show a much better agreement. The impactor was milled from a single solid piece of steel, which resulted in a doubling of the lowest frequency of the noise picked up in the load signal. The placement of the accelerometer in the centre of the impactor resulted in a strong reduction of noise on the acceleration measurements.

A contactless optical tracking method was applied to measure the displacement during the impact tests. It proved to be accurate enough to reproduce the load using a double differentiation of the measured displacement, something which is not at all possible using the displacement measured using the transducer mounted on the impactor. This agreement validates the measurement method. The amount of detail in the optically measured load is limited, though, due to the limited frame rate of the optical acquisition with respect to the direct measurement of the load using a load cell.

The rate-dependency of the materials during impact can be investigated only by clear load reduction events before the maximum displacement is reached. The ultimate values namely depend on the impact energy rather than the velocity of the impactor. The sudden reductions are connected to major damage events which have a stiffness reduction as a result. Only the carbon/epoxy had sudden jumps in load in its impact loading history. The load at which the sudden reductions occur lies above quasi-statically obtained values and increases with testing speed, suggesting a rate-dependency of the carbon/epoxy material.

As mentioned above, quasi-static indentation was applied as well. This test method was used to indent specimens to the same depth as was measured during the impact tests. In this way, a quasi-static reference was obtained for each impact scenario. An equality of results for either test method then points to rate-independency of a certain material. The force-displacement response, the absorbed energy and the resulting damage was compared for specimens of the same lay-up that were subjected to equivalent test situations. The damage was quantified using the dent depth and the area over which a reduction in ultrasound transmission strength was seen. A small selection of specimens was cut, polished, and inspected using an optical microscope.

For glass/polyamide-6, the influence of the constituent rate-dependency on the out-of-plane behaviour is large. The force-displacement response during low-velocity impact is completely different from that during quasi-static indentation at the higher displacement values. Other characteristics (dissipated energy, area of delamination, dent depth) are relatively similar and could lead to a false sense of equivalence between the two tests. It is thus concluded that these quantities alone are not suitable to characterise the rate dependency of laminates under out-of-plane loading.

It was shown that carbon/epoxy also behaves differently in quasi-static inden-

tation compared to low-velocity impact. The differences are considerably smaller than for glass/polyamide-6, but still significant. The force-displacement curves show that the load prior to the first significant stiffness loss increases with testing speed. Maximum force and (again) dissipated energy are hardly affected by the speed. The ultrasonic C-scans show that the damaged area and dent depth are larger for the indentation tests than for the impact tests. The microscopic investigation shows a different distribution of damage, notably a laminate which is almost intact underneath the indenter for quasi-static indentation, while the damage in the impacted specimen continues underneath the impact zone.

Quasi-static indentation is therefore not a suitable substitute for low-velocity impact if an accurate damage characterization is required. From a design perspective, though, indentation can be used to obtain a conservative estimation of the damage area due to low-velocity impact for carbon/epoxy.

In conclusion, the goals of the research have been met. Experimental methodologies have been developed and their ranges of reliability quantified. The methodologies have been applied to the two material systems in an experimental programme in which in total over a thousand tests have been executed. This programme has resulted in a large, consistent database of dynamic test results, capable of supporting the development of composite material models that predict impact with both input and validation data.

10.2 Recommendations for further research

Regrettably, time is a limited resource. Several opportunities were encountered along the way which deserve a further investigation, but for which there was simply not the time during the course of this research. The topics mentioned below are recommended for further research.

10.2.1 Pushing the limits for dynamic tension

Ringing of the load cell is currently responsible for the most stringent limit on maximum strain rate for dynamic tensile tests. Two possible solutions in literature evade the use of a piezoelectric load cell entirely, since the ringing frequency cannot be increased significantly.

The first option is to measure the load on-specimen using a dynamometer section on the specimen [1, 2], which means to give a portion of the specimen a larger width in order for it not to fail there, and attaching a second strain gauge in this zone of the specimen. This second gauge can then be used to indicate the load by measuring quasi-statically the strain levels which occur at certain loads. The challenge here is, however, that a rate-dependent response of the material's Young's modulus invalidates the quasi-static calibration. Two options remain. The first is

to take the rate-dependency of the modulus into account in the calibration, making use of the fact that the strain rate in a wider portion will lie below that of the gauge section, thus always allowing the modulus of the dynamometer section to be determined by a slower test. Another option is to manufacture the dynamometer section out of a material with a rate-insensitive modulus to enable quasi-static calibration again, though the challenge is to produce a reliable joint between the specimen and this section. In both cases, it also needs to be verified whether the dynamic stress field still matches what is seen in quasi-static conditions. The speed at which stress waves start to interact in such a way that this is no longer the case, could be an upper limit of the dynamometer method.

The downside of the aforementioned method is a required increase in length of the specimen, because a uniform stress state should exist in both the gauge length and the dynamometer section, and for both of them a certain minimum amount of specimen length is required. Another option to remove the necessity of a piezoelectric load cell is perhaps the application of the Virtual Fields Method to extract the local constitutive behaviour based on displacement alone [3]. Using the high-speed displacement field, both the local strains as the accelerations can be extracted. However, a combination of resolution and frame rate is required which lies beyond the capabilities of a 'regular' high-speed camera: a new type is needed which can capture full frames at maximum frame rate owing to a different arrangement of the memory. The challenges with the method are (1) to select a virtual field which can cover the behaviour of non-quasi-isotropic laminates and perhaps more importantly (2) obtaining a constant strain rate. Currently the method is namely typically applied by shooting a projectile on a specimen which therefore first undergoes a compressive stress wave and subsequently breaks in tension, thereby inevitably seeing a large spectrum of different strain rates.

If one were to find a suitable load cell, the absence of equilibrium is the next issue. It appears to be rather easily solved by the use of a shorter specimen, though there is a limit to how short one can take the specimen because the stress field can only be assumed uniform at some distance from the clamps. Still, the execution of dynamic tensile tests with varying specimen lengths is advised to gain further insight into the minimum requirements for approximate equilibrium in this case.

10.2.2 Dynamic pure mode-I delamination

The biggest challenge encountered during this thesis is the dynamic delamination study. Neither of the two applied methods results in a pure mode-I loading, owing to the asymmetric actuation of the double cantilever beam specimen. Perhaps a (mixed-mode) fracture toughness could be extracted from current tests at speeds exceeding the equilibrium condition, though the initial goal was to obtain a pure mode-I loading. The only way this can be ensured at high speeds is by simultane-

ous actuation of both halves of the specimen. The most promising method to do so seems to be some form of wedge-insert method [4], though the friction between the wedge and the specimen adds a large unknown to the equation.

A recent article was published where this friction is minimized because the wedge is not directly pushing on the fracture planes of the specimen, but rather on bearing axles in loading blocks [5]. This method seems promising, and they seem to be able to obtain reliable values for the dynamic fracture toughness. The maximum speed seems to be limited to about $1.4\,\mathrm{m\,s^{-1}}$ though. Above that speed, namely, strong oscillations appear in the load signal. The authors of that work attributed this to an observed discontinuous crack growth, though it seems from the presented results that this is an effect rather than the cause of the periodic load signal. Vibrations seem yet again to cause difficulties for the load acquisition, and, in this case, limit the results to what can still be accurately tested by actuating only one of the two halves. Perhaps a different speed profile with a smooth velocity increase of the wedge could reduce the excitation of natural frequencies. Such a profile could perhaps be applied by testing in a hydraulic pulse test bench rather than a drop tower.

10.2.3 Dynamic mode-II delamination

Although the mode-I delamination is important, perhaps the mode-II delamination is even more critical. Looking at the material behaviour during the impact test programme, namely, the entire laminate deforms in the same direction. The delamination growth is thus likely caused by a shear loading at the crack tip instead of the normal loading introduced in the mode-I tests. Articles dealing with dynamic mode-II are even less common than those treating dynamic mode-I delamination. Typical quasi-static mode-II tests comprise the end-loaded split (ELS) and the end-notched flexure (ENF) tests [6].

Some authors test the mode-II rate dependency using the ENF test, where the actuator pushes into the middle of a simply supported specimen with a precrack at one end, though typically actuation rates are very low, i.e. up to $0.1\,\mathrm{m\,s^{-1}}$ [7]. At these speeds, the actuation can still be actively controlled in a standard hydraulic test bench, and thus there is no need for a separate system to stop the piston. Doing this test with an open-loop system is problematic, because the piston will inevitably hit the load cell at full speed if no precautions are taken. Perhaps the set-up can be adapted such that the piston can perform the test by moving away from the specimen, by using a set-up that is also capable to apply fully reversed three point bending loads [8].

In any case, ENF seems a better candidate than ELS, because in the latter case the specimen is again asymetrically loaded, likely resulting in a loading which is not pure mode-II.

10.2.4 Finite-element modelling of composite impact damage

The goal of the M3 program is to enable a reduction of the number of tests needed to develop composite parts by replacing a large portion of the necessary test programme with efficient and accurate simulations. The important next step of this research is, therefore, to use the dynamic test data as an input for high-fidelity finite-element models that try to predict the damage resulting from an out-of-plane impact similar to what was tested in the low-velocity impact programme. This way, the outcome can be validated using the test data generated in this research.

It seems most fruitful to use explicit 3D solid elements with cohesive interlayers (or cohesive surface behaviour) to tackle this problem, much like is applied by Lopes et al. [9]. The solids are capable of handling the large variety in loading, which is necessary because an important part of the specimen is loaded by out-of-plane compression underneath the impactor. Classical or continuum shell elements are not expected to handle this loading well. The cohesive interlayer can be used to model the progressing delamination. Since tracking each and every crack in the composite layers would be far too computationally heavy, it is likely best to use a continuum damage approach for the solid elements, where a constitutive law needs to be chosen or formulated that allows modelling of the various damage modes that might occur (fibre failure in tension or compression, matrix cracking in tension or compression or shear).

The challenge will lie in making the model sophisticated enough to create an accurate representation of reality, but still to include only those elements that significantly contribute to the global behaviour of the impacted composite and not more. Applying a very sophisticated model *e.g.* as devised by Camanho et al. [10] on a model with cohesive behaviour between every lamina and full details of the surrounding will likely only lead to unrealistically long runtimes of the model. Instead, it seems most beneficial to include details only in a smart way by lumping sublaminates together where no delaminations are expected, replacing contact conditions with surrounding structure by simple boundary conditions where applicable, and simplifying the material model as much as possible so that it only checks for local damage modes which are actually expected in those locations.

10.2.5 Environmental influence on mechanical properties

Automobile structures experience a great variety of temperatures and relative humidity levels. To design reliable composite cars thus requires the investigation of the influence of temperature and relative humidity on the mechanical properties of the used composites. Especially for glass/polyamide-6, where research indicates that temperature and relative humidity influence its behaviour with the same mechanism and order of magnitude as strain rate, it is recommended that the combined influence of these effects be studied.

References

[1] International Organization for Standardization. *ISO 26203-2:2011. Metallic materials – Tensile testing at high strain rates – Part 2: servo-hydraulic and other test systems. German version DIN EN ISO 26203-2:2011.* Technical report, International Organization for Standardization, 2011.

[2] ESIS TC 5, Subcommittee on Dynamic Testing at Intermediate Strain Rates. *ESIS P7-00: Procedure for Dynamic Tensile Tests*. Technical report, European Structural Integrity Society, 2000.

[3] F. Pierron and M. Grédiac. *The Virtual Fields Method*. Springer New York, New York, NY, 2012. DOI: 10.1007/978-1-4614-1824-5.

[4] M. May. *Measuring the rate-dependent mode I fracture toughness of composites – A review*. Composites Part A: Applied Science and Manufacturing, 81:1–12, February 2016.

[5] S. I. Thorsson, A. M. Waas, J. Schaefer, B. Justusson, and S. Liguore. *Effects of elevated loading rates on mode I fracture of composite laminates using a modified wedge-insert fracture method*. Composites Science and Technology, 156:39–47, March 2018.

[6] B. R. K. Blackman, A. J. Brunner, and J. G. Williams. *Mode II fracture testing of composites: a new look at an old problem*. Engineering Fracture Mechanics, 73(16):2443–2455, November 2006.

[7] J. J. M. Machado, E. A. S. Marques, R. D. S. G. Campilho, and L. F. M. da Silva. *Mode II fracture toughness of CFRP as a function of temperature and strain rate*. Composites Part B: Engineering, 114:311–318, April 2017.

[8] I. De Baere, W. Van Paepegem, and J. Degrieck. *On the feasibility of a three-point bending setup for the validation of (fatigue) damage models for thin composite laminates*. Polymer Composites, 29(10):1067–1076, October 2008.

[9] C. S. Lopes, S. Sádaba, C. González, J. Llorca, and P. P. Camanho. *Physically-sound simulation of low-velocity impact on fiber reinforced laminates*. International Journal of Impact Engineering, 92:3–17, June 2016.

[10] P. Camanho, M. Bessa, G. Catalanotti, M. Vogler, and R. Rolfes. *Modeling the inelastic deformation and fracture of polymer composites – Part II: Smeared crack model*. Mechanics of Materials, 59:36–49, April 2013.

A

Dynamic tensile specimen dimensions

Table A.1 contains the measured dimensions of type 1 specimens, tables A.3, A.4, A.5 and A.6 the type 2 specimens, and tables A.2, A.7 and A.8 the type 3 specimens, respectively. The description of the variables and specimen types used in the tables can be found in figure 4.11.

Table A.1. Average dimensions and coefficients of variation of pure matrix specimens, see also figure 4.11.

	Epoxy Type 1		PA-6 Type 1	
	Avg [mm]	C.V. [%]	Avg [mm]	C.V. [%]
L	119.84	0.14	151.79	0.06
W_c	19.99	0.08	19.90	0.21
W_g	6.05	0.57	10.05	0.57
H_g	2.98	3.82	3.99	0.79

Table A.2. Average dimensions and coefficients of variation of narrow rectangular G/PA-6 specimens, see also figure 4.11.

	$[0]_4$ Type 3		$[90/0]_{2s}$ Type 3	
	Avg [mm]	C.V. [%]	Avg [mm]	C.V. [%]
L	93.76	0.07	93.85	0.03
H_g	0.965	4.99	2.219	2.73
W_c	9.91	0.61	9.96	0.11

Table A.3. Average dimensions and coefficients of variation of dogbone-shaped UD-layered C/E specimens, see also figure 4.11.

	$[90]_8$ Type 2		$[45/0/-45/90]_s$ Type 2	
	Avg [mm]	C.V. [%]	Avg [mm]	C.V. [%]
L	93.68	0.10	93.75	0.04
W_c	20.02	0.17	19.76	0.08
W_g	15.38	0.63	15.18	0.43
H_g	1.868	2.24	1.841	1.34

Table A.4. Average dimensions and coefficients of variation of dogbone-shaped woven-layered C/E specimens, see also figure 4.11.

	$[\#(0/90)]_{4s}$ Type 2		$[\#(90/0)]_{4s}$ Type 2	
	Avg [mm]	C.V. [%]	Avg [mm]	C.V. [%]
L	93.93	0.02	93.95	0.03
W_c	19.92	0.06	19.97	0.08
W_g	15.35	0.43	15.40	0.46
H_g	1.76	0.92	1.74	1.36

Table A.5. Average dimensions and coefficients of variation of dogbone-shaped G/PA-6 specimens, see also figure 4.11.

	$[90]_8$ Type 2		$[\#(0/90)]_{2s}$ Type 2		$[\#(90/0)]_{2s}$ Type 2	
	Avg [mm]	C.V. [%]	Avg [mm]	C.V. [%]	Avg [mm]	C.V. [%]
L	93.35	0.15	93.94	0.03	93.93	0.03
W_c	20.06	0.30	19.98	0.09	19.97	0.08
W_g	15.51	0.49	15.44	0.39	15.49	0.66
H_g	2.352	6.00	2.03	1.20	2.04	0.88

Table A.6. Average dimensions and coefficients of variation of dogbone-shaped woven QI specimens, see also figure 4.11.

	C/E $[\#(\pm 45)/\#(0/90)]_{2s}$ Type 2		G/PA-6 $[\#(\pm 45)/\#(0/90)]_{s}$ Type 2	
	Avg [mm]	C.V. [%]	Avg [mm]	C.V. [%]
L	93.86	0.21	93.78	0.18
W_c	19.95	0.09	19.85	0.42
W_g	15.38	0.49	15.33	0.58
H_g	1.74	1.24	1.99	3.28

Table A.7. Average dimensions and coefficients of variation of ± 45 C/E specimens, see also figure 4.11.

	$[\pm 45]_{2s}$ Type 3		$[\#(\pm 45)]_{4s}$ Type 3	
	Avg [mm]	C.V. [%]	Avg [mm]	C.V. [%]
L	93.85	0.05	93.86	0.03
W_c	19.91	0.16	19.86	0.09
H_g	1.832	2.01	1.739	1.46

Table A.8. Average dimensions and coefficients of variation of ± 45 G/PA-6 specimens, see also figure 4.11.

	$[\pm 45]_{2s}$ Type 3		$[\#(\pm 45)]_{2s}$ Type 3	
	Avg [mm]	C.V. [%]	Avg [mm]	C.V. [%]
L	93.82	0.07	93.86	0.03
W_c	19.97	0.16	19.97	0.08
H_g	2.193	3.89	2.031	0.88

B

Tensile mechanical properties versus strain rate

In this appendix, the first section contains three tables which show a selection of engineering properties at the various actuator speeds tested. It is decided to display the maximum stress (table B.1), the maximum strain (average of both DIC and SG data, table B.2) and the Young's modulus (table B.3). It is explained in section 4.7 how the engineering properties and the strain rate are obtained from the raw data. The subsequent sections contain a graphical representation of the rate-dependency of the engineering properties.The reader is referred to table 5.2 for an overview of up to which strain rate the data acquisition has led to valid results.

The current order of the displayed engineering properties is based on acquisition difficulty. Stress and strain can be measured independently from each other and are, therefore, relatively straightforward to measure. The Young's modulus is more challenging to obtain at high rates, as it requires an accurate synchronization of stress with strain. A small delay between the two quantities can namely have significant influence at high rates (see section 4.7.4). The inaccuracy on the modulus, moreover, is influenced by the inaccuracies on both stress and strain. Finally, while the force and the strain can still be measured when there is no longer equilibrium in a specimen, the measurement of the Young's modulus fails. Typically, the force and strain are measured in different locations, and an absence of equilibrium invalidates the computation of the modulus from the division of strain by stress.

B.1 Tabular overviews of engineering properties versus testing speed

The tables are organised in the same way as in chapter 5: the top half shows the results for C/E, while the bottom half displays G/PA-6 values. For each material system, the lay-ups are organised to increasing 'complexity.' The results are presented versus testing speed in the tables, because the measured strain rate varies between laminates (table 5.2).

Typically, the coefficients of variation for failure strain and Young's modulus are larger at the two highest speeds. Those tests were namely carried out with a very small resolution for DIC, which is deemed partially responsible for the elevated amount of noise in the results.

Table B.1. Average maximum stress [MPa] *and coefficient of variation* [%] *(in grey) for the various tested configurations. A green value means that load cell ringing is expected to influence the results, see table 5.2.*

	Material	**Test speed** $[\mathbf{m\,s^{-1}}]$					
		0.0001	0.005	0.05	0.5	5	15
C/E	Pure epoxy	61.3	44.4	46.1	51.3	53.9	58.4
		14.6	26.9	18.7	31.4	21.7	16.4
	$[90]_8$	32.7	32.8	36.3	37.1	54.6	63.2
		10.4	7.12	6.13	8.34	4.49	14.5
	$[\pm45]_{2s}$	113	114	126	132	149	167
		0.214	1.68	2.15	1.53	3.1	4.35
	$[45/0/-45/90]_s$	668	-	-	-	618	-
		8.43	-	-	-	4.92	-
	$[\#(0/90)]_{4s}$	659	651	683	638	688	704
		4.42	3.71	8.75	6.89	4.13	2.42
	$[\#(90/0)]_{4s}$	608	597	551	623	651	652
		7.31	7.64	10.2	3.06	9.42	6.7
	$[\#(\pm45)]_{4s}$	192	195	200	202	210	220
		3.28	2.72	2.2	4.56	1.64	1.98
	$[\#(\pm45)/\#(0/90)]_{2s}$	513	514	478	492	547	634
		5.43	3.86	11.5	4.93	3.6	3.39
G/PA-6	Pure PA-6	67.2	76	85.3	66	70.8	89.1
		1.12	4.74	1.26	13.4	2.88	15.9
	$[0]_4$	755	1160	1260	1390	1530	1420
		12.2	7.45	7.5	7.29	13.2	4.2
	$[90]_8$	65.8	53.1	60.2	65.1	74.9	93.3
		5.33	18.3	28.7	3.03	12.8	7.31
	$[90/0]_{2s}$	426	-	-	627	722	-
		16.9	-	-	8.26	4.78	-
	$[\pm45]_{2s}$	194	248	302	306	298	295
		22.1	8.69	1.57	1.32	9.56	14
	$[\#(0/90)]_{2s}$	483	575	625	642	602	652
		2.81	3.07	1.26	5.99	1.86	5.08
	$[\#(90/0)]_{2s}$	444	523	574	595	669	638
		3.27	5.02	3.76	4.73	3.92	10.3
	$[\#(\pm45)]_{2s}$	173	203	224	241	255	254
		5.21	2.34	3.03	3.01	1.16	2.78
	$[\#(\pm45)/\#(0/90)]_s$	355	418	473	471	533	535
		4.69	4.42	3.84	4.82	5.73	3.04

Table B.2. Average strain to failure [%] and coefficient of variation [%] (in grey) for the various tested configurations. A red value means that the test speed superseded strain acquisition limits (DIC and/or signal conditioner bandwidth), see table 5.2.

	Material	**Test speed** $[\mathbf{m\,s^{-1}}]$					
		0.0001	0.005	0.05	0.5	5	15
C/E	Pure epoxy	2.19	1.5	1.56	1.67	1.48	1.19
		31.4	34.1	21.1	33.8	32.5	26.7
	$[90]_8$	0.421	0.41	0.437	0.44	0.512	0.569
		11.3	6.94	11	12.3	18.4	24.1
	$[\pm45]_{2s}$	1.86	1.87	2.18	2.14	2.34	2.19
		10.3	21	21.8	26.5	22.5	31.9
	$[45/0/-45/90]_s$	1.72	-	-	-	1.47	-
		7.55	-	-	-	8.72	-
	$[\#(0/90)]_{4s}$	1.16	1.16	1.21	1.14	1.21	1.32
		5.92	4.24	7.17	6.49	9.77	4.27
	$[\#(90/0)]_{4s}$	1.08	1.06	0.992	1.11	1.08	1.15
		6.79	6.85	9.09	6.09	7.1	6.96
	$[\#(\pm45)]_{4s}$	11	10.1	10	9.26	6.77	6.98
		5.23	10.3	11.8	18.7	0	6.79
	$[\#(\pm45)/\#(0/90)]_{2s}$	1.32	1.29	1.26	1.22	1.37	1.45
		5.21	6.4	7.75	8.48	5.48	5.25
G/PA-6	Pure PA-6	41.8	23.7	11.5	2.3	2.55	2.33
		37.3	24	76.9	16.3	6.24	7.21
	$[0]_4$	2.45	3.08	3.42	3.7	4.07	3.69
		17.8	4.06	4.28	4.69	13.7	13.2
	$[90]_8$	1.13	0.707	1.21	0.853	0.797	0.881
		12.3	10.2	3.44	12.4	19.1	23
	$[90/0]_{2s}$	2.75	-	-	4.44	4.56	-
		11.6	-	-	4.3	5.56	-
	$[\pm45]_{2s}$	20.2	19.6	22.9	23.2	23.5	20
		24.5	21.6	4.62	4.87	15	27.7
	$[\#(0/90)]_{2s}$	2.64	3	3.3	3.4	4.29	4.34
		7.53	4.03	2.69	2.53	9.95	4.11
	$[\#(90/0)]_{2s}$	2.53	2.96	3.26	3.4	4.03	4.38
		5.18	5.89	2.68	4.56	7.16	8.48
	$[\#(\pm45)]_{2s}$	19.1	18.9	20.3	20	20.4	18.1
		10.1	3.75	10.3	3.87	5.59	8.8
	$[\#(\pm45)/\#(0/90)]_s$	2.86	3.29	3.83	4.21	4.94	4.85
		8.62	5.82	4.1	5.99	8.1	6.69

Table B.3. Average Young's modulus in longitudinal direction [GPa] *and coefficient of variation* [%] *(in grey) for the various tested configurations. A green value means that load cell ringing is expected to influence the results. A blue value means that the test was also too fast to achieve approximate equilibrium during the test. A red value means that the test speed superseded strain acquisition limits (DIC and/or signal conditioner bandwidth). See also table 5.2.*

	Material	**Test speed** $[\mathbf{m\,s^{-1}}]$					
		0.0001	0.005	0.05	0.5	5	15
C/E	Pure epoxy	3.14	3.24	3.27	3.79	5.65	3.51
		16.5	4.57	13.6	18.7	27.6	50.1
	$[90]_8$	8.89	9.54	9.85	10.8	9.86	7.3
		14.5	4.2	5.31	6.94	21.7	14.6
	$[\pm45]_{2s}$	11.4	12.5	13	13.7	13.8	14.9
		5.55	3.45	5.28	9.97	1.9	3.19
	$[45/0/-45/90]_s$	48.8	-	-	-	49.8	-
		5.59	-	-	-	13.4	-
	$[\#(0/90)]_{4s}$	53.8	53.4	54.6	54.8	53.1	38.1
		4.23	4.39	4.32	7.71	11	33.3
	$[\#(90/0)]_{4s}$	51.8	55.3	53.4	53.1	54.6	39.1
		7.27	9.06	8.27	3.96	12.3	14.3
	$[\#(\pm45)]_{4s}$	10.6	11.2	11.5	11.5	11.8	9.88
		4.99	6.13	5.12	3.91	5.31	7.35
	$[\#(\pm45)/\#(0/90)]_{2s}$	38.1	38	40.3	39.3	36.2	29.2
		11.4	7.53	9.18	8.45	9.09	12.7
G/PA-6	Pure PA-6	2.93	2.93	3.26	3.26	4.26	6.21
		4.04	5.74	11.4	8.01	5.64	73
	$[0]_4$	36.1	42.9	42.7	44.2	41.5	50.5
		7.76	10.9	11.6	10.3	19.1	17
	$[90]_8$	9.24	8.95	8.26	9.53	9.49	8.74
		13	2.44	4.76	7.29	28.1	29.7
	$[90/0]_{2s}$	19.4	-	-	20	22.2	-
		12.4	-	-	6.45	13.4	-
	$[\pm45]_{2s}$	6.88	9.31	9.91	8.94	8.88	8.76
		11.4	7.08	8.62	8.09	9.28	20.9
	$[\#(0/90)]_{2s}$	21.6	21.9	22.3	22.4	20.5	17.7
		13.1	9.34	6.16	8.23	13.8	15.7
	$[\#(90/0)]_{2s}$	19.9	21	21.5	22.3	23.4	14.7
		3.46	6.95	4.83	8.64	12	20.8
	$[\#(\pm45)]_{2s}$	5.82	7.36	7.89	8.11	8.58	7.35
		6.19	6.37	3.86	3.94	4.22	17.4
	$[\#(\pm45)/\#(0/90)]_s$	15.9	16.1	15.8	17.2	17.8	15
		8.45	11.2	8.12	9.91	8.82	13.9

B.2 Strain-rate dependency of carbon/epoxy

B.2.1 Pure epoxy

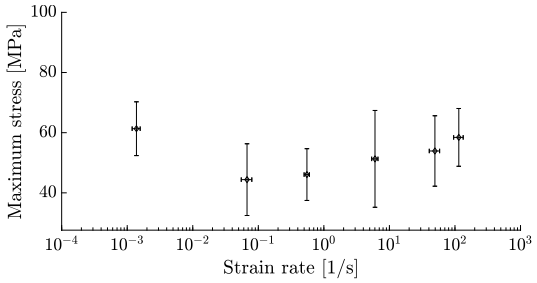

Figure B.1. Maximum stress versus strain rate for pure epoxy.

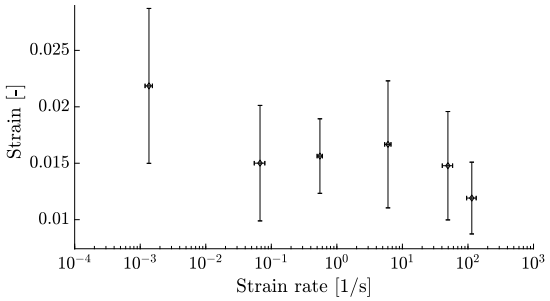

Figure B.2. Maximum strain versus strain rate for pure epoxy.

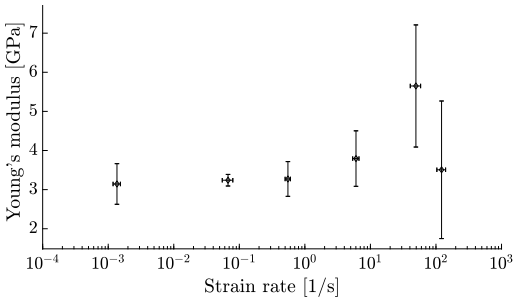

Figure B.3. Young's modulus versus strain rate for pure epoxy.

B.2.2 C/E pure 90° UD

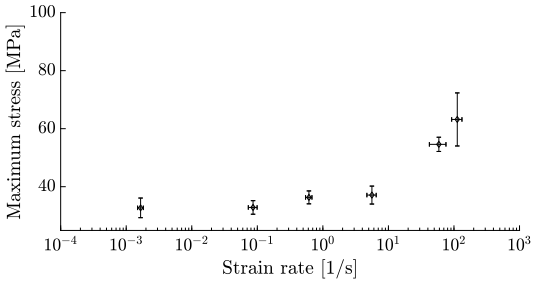

Figure B.4. Maximum stress versus strain rate for C/E $[90]_8$.

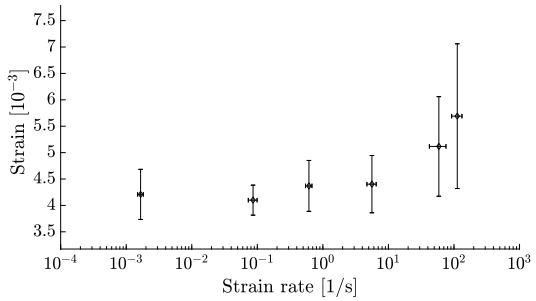

Figure B.5. Maximum strain versus strain rate for C/E $[90]_8$.

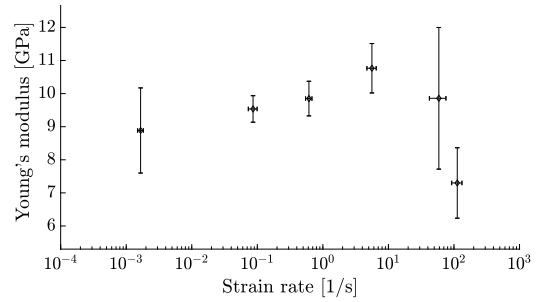

Figure B.6. Young's modulus versus strain rate for C/E $[90]_8$.

B.2.3 C/E ±45

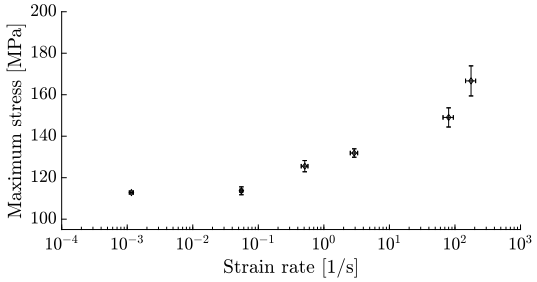

Figure B.7. Maximum stress versus strain rate for C/E $[\pm 45]_{2s}$.

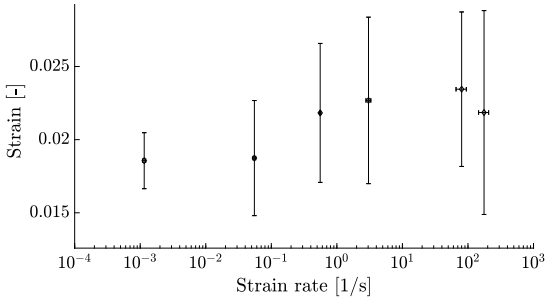

Figure B.8. Maximum strain versus strain rate for C/E $[\pm 45]_{2s}$.

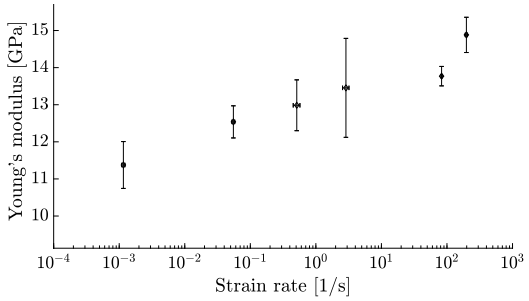

Figure B.9. Young's modulus versus strain rate for C/E $[\pm 45]_{2s}$.

B.2.4 C/E quasi-isotropic

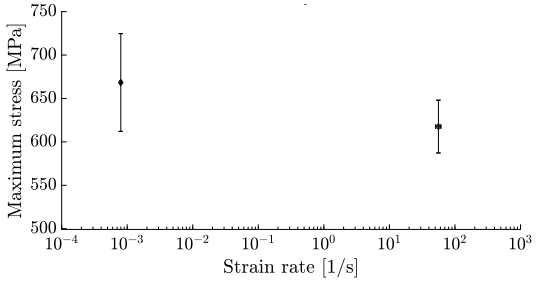

Figure B.10. Maximum stress versus strain rate for C/E $[45/0/-45/90]_s$.

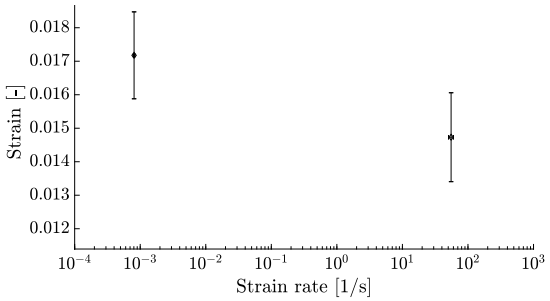

Figure B.11. Maximum strain versus strain rate for C/E $[45/0/-45/90]_s$.

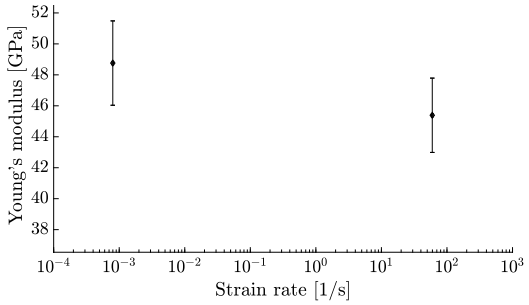

Figure B.12. Young's modulus versus strain rate for C/E $[45/0/-45/90]_s$.

B.2.5 C/E woven cross-ply - 0°

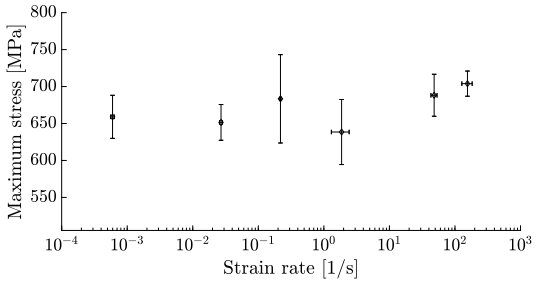

Figure B.13. Maximum stress versus strain rate for C/E $[\#(0/90)]_{4s}$.

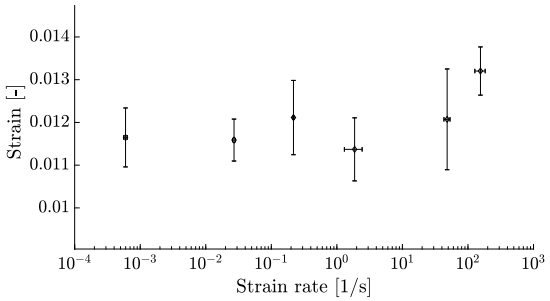

Figure B.14. Maximum strain versus strain rate for C/E $[\#(0/90)]_{4s}$.

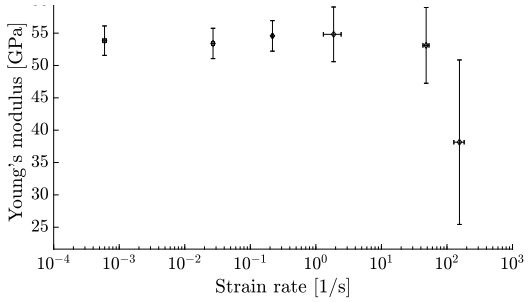

Figure B.15. Young's modulus versus strain rate for C/E $[\#(0/90)]_{4s}$.

B.2.6 C/E woven cross-ply - 90°

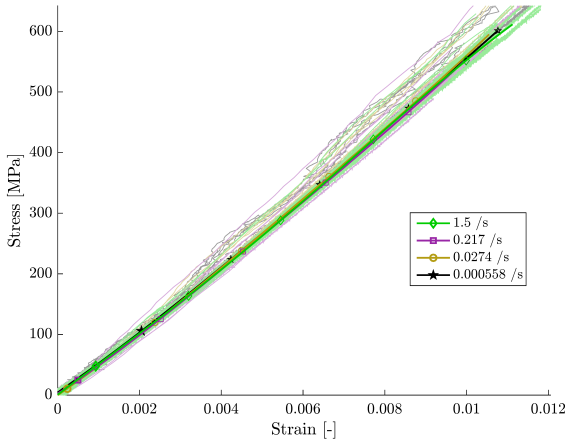

Figure B.16. Stress-strain curves of C/E $[\#(90/0)]_{4s}$ *at various strain rates.*

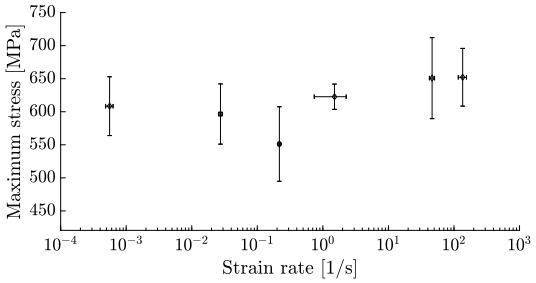

Figure B.17. Maximum stress versus strain rate for C/E $[\#(90/0)]_{4s}$.

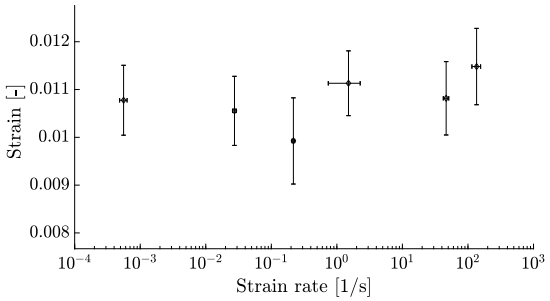

Figure B.18. Maximum strain versus strain rate for C/E $[\#(90/0)]_{4s}$.

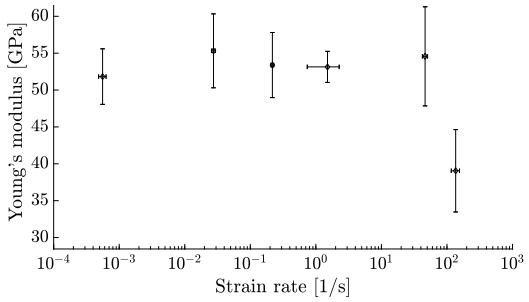

Figure B.19. Young's modulus versus strain rate for C/E $[\#(90/0)]_{4s}$.

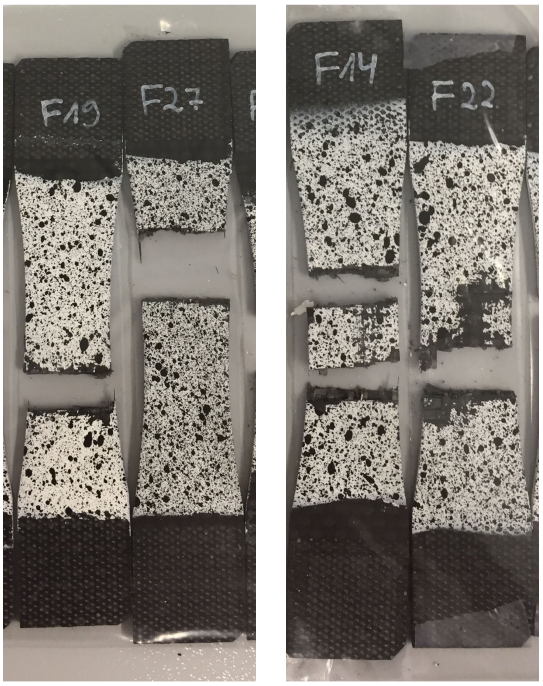

a. $v = 0.0001\,\mathrm{m\,s^{-1}}$. *b.* $v = 15\,\mathrm{m\,s^{-1}}$.

Figure B.20. Failed C/E $[\#(90/0)]_{4s}$ *specimens.*

B.2.7 C/E woven ±45

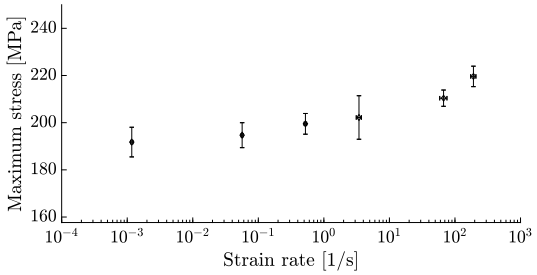

Figure B.21. Maximum stress versus strain rate for C/E $[\#(\pm 45)]_{4s}$.

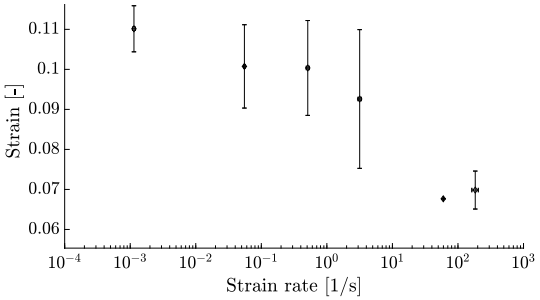

Figure B.22. Maximum strain versus strain rate for C/E $[\#(\pm 45)]_{4s}$.

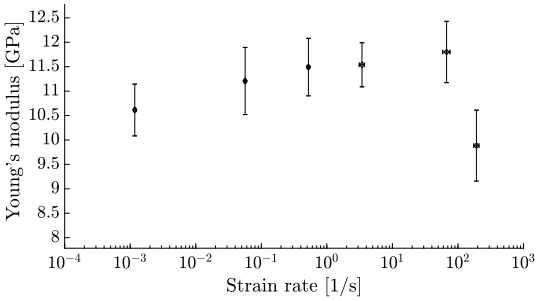

Figure B.23. Young's modulus versus strain rate for C/E $[\#(\pm 45)]_{4s}$.

B.2.8 C/E woven quasi-isotropic

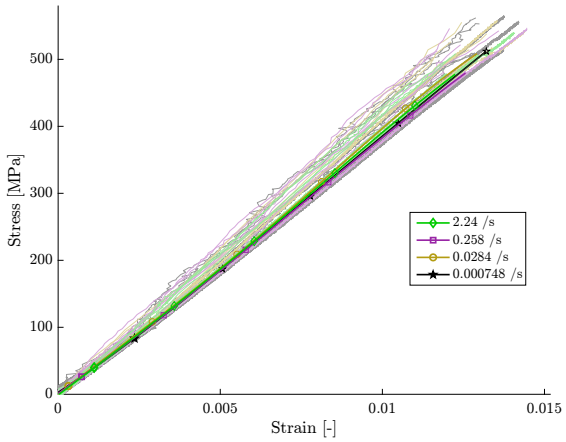

Figure B.24. Stress-strain curves of C/E $[\#(\pm 45)/\#(0/90)]_{2s}$ *at various strain rates.*

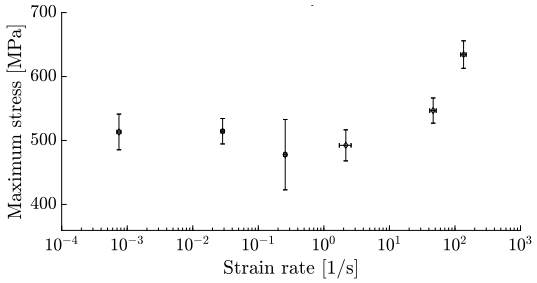

Figure B.25. Maximum stress versus strain rate for C/E $[\#(\pm 45)/\#(0/90)]_{2s}$.

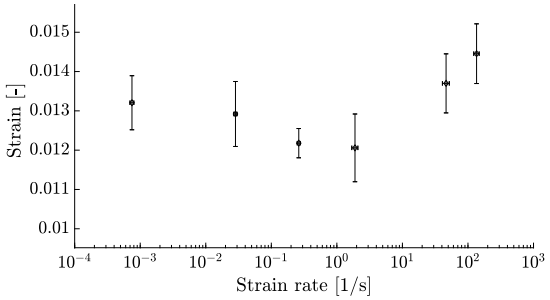

Figure B.26. Maximum strain versus strain rate for C/E $[\#(\pm 45)/\#(0/90)]_{2s}$.

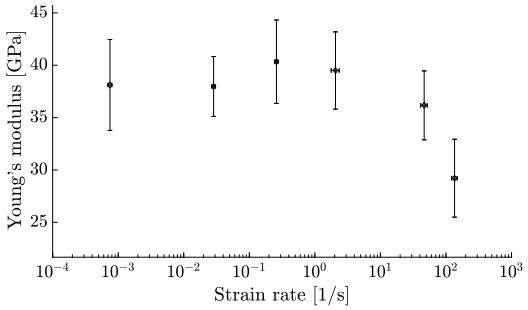

Figure B.27. Young's modulus versus strain rate for C/E $[\#(\pm 45)/\#(0/90)]_{2s}$.

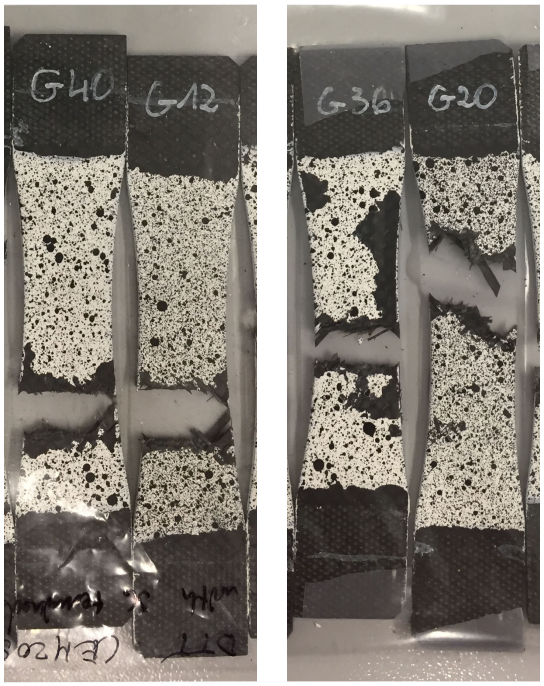

a. $v = 0.0001\,\mathrm{m\,s^{-1}}$. *b.* $v = 15\,\mathrm{m\,s^{-1}}$.

Figure B.28. Failed C/E $[\#(\pm 45)/\#(0/90)]_{2s}$ *specimens.*

B.3 Strain-rate dependency of glass/polyamide-6

B.3.1 Pure polyamide-6

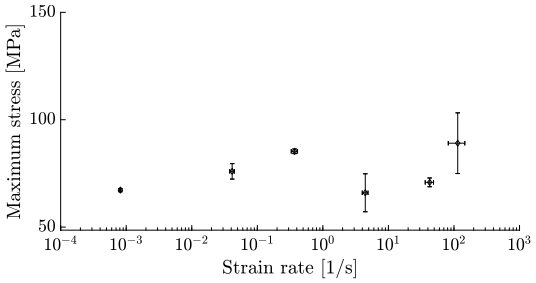

Figure B.29. Maximum stress versus strain rate for pure PA-6.

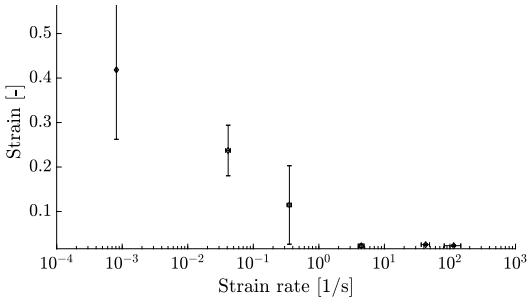

Figure B.30. Maximum strain versus strain rate for pure PA-6.

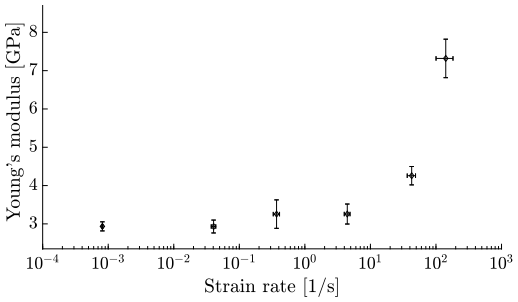

Figure B.31. Young's modulus versus strain rate for pure PA-6.

B.3.2 G/PA-6 pure 0° UD

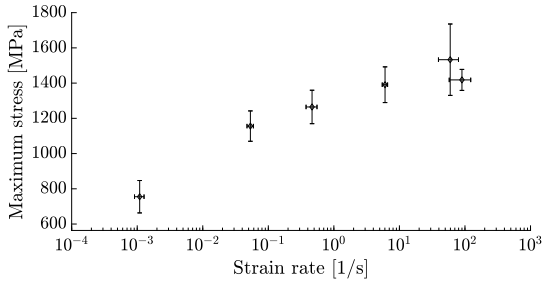

Figure B.32. Maximum stress versus strain rate for G/PA-6 $[0]_4$.

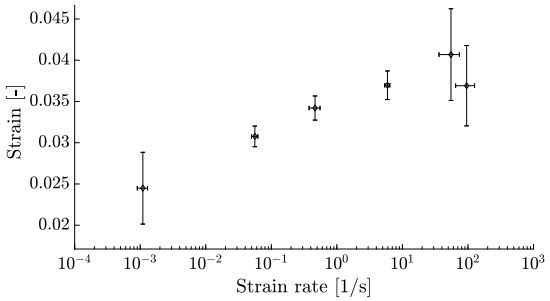

Figure B.33. Maximum strain versus strain rate for G/PA-6 $[0]_4$.

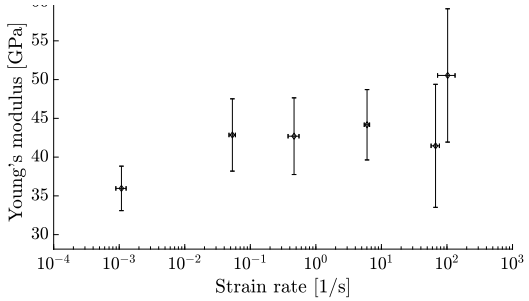

Figure B.34. Young's modulus versus strain rate for G/PA-6 $[0]_4$.

B.3.3 G/PA-6 pure 90° UD

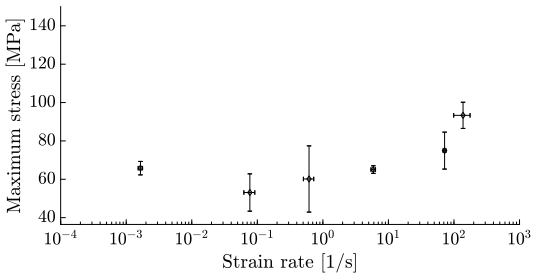

Figure B.35. Maximum stress versus strain rate for G/PA-6 $[90]_8$.

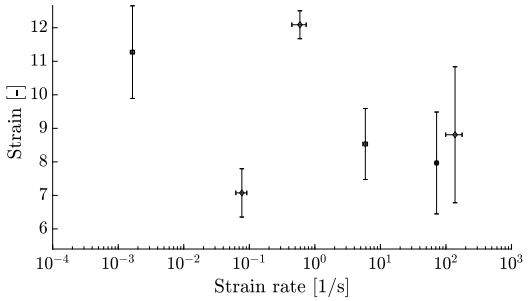

Figure B.36. Maximum strain versus strain rate for G/PA-6 $[90]_8$.

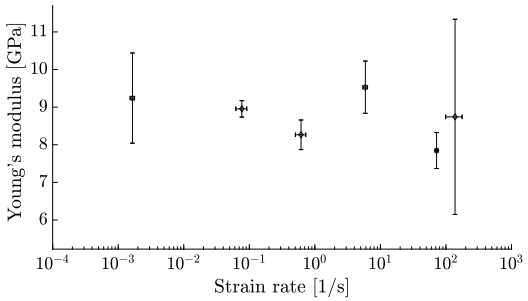

Figure B.37. Young's modulus versus strain rate for G/PA-6 $[90]_8$.

B.3.4 G/PA-6 cross-ply

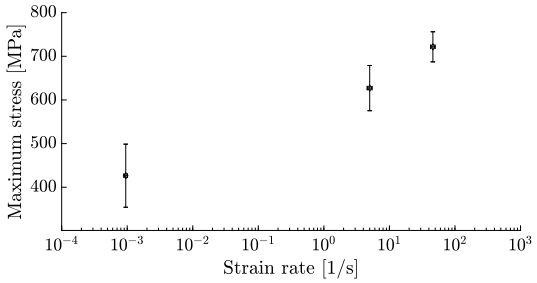

Figure B.38. Maximum stress versus strain rate for G/PA-6 $[90/0]_{2s}$.

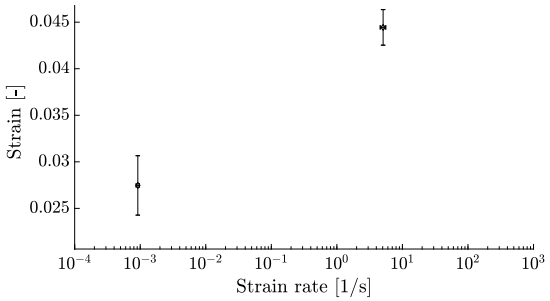

Figure B.39. Maximum strain versus strain rate for G/PA-6 $[90/0]_{2s}$.

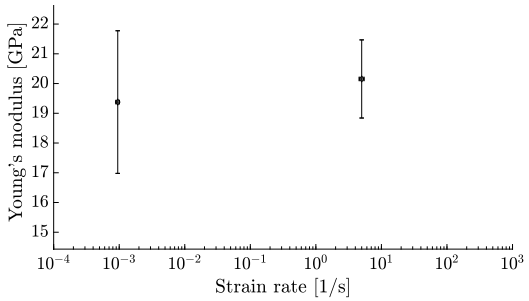

Figure B.40. Young's modulus versus strain rate for G/PA-6 $[90/0]_{2s}$.

B.3.5 G/PA-6 ±45 UD

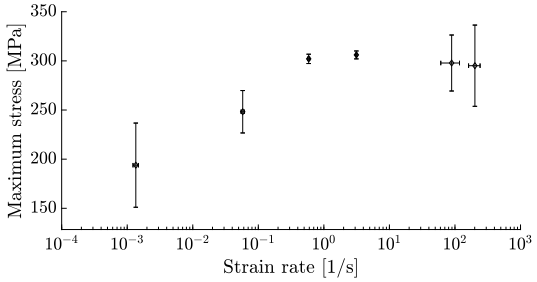

Figure B.41. Maximum stress versus strain rate for G/PA-6 $[\pm 45]_{2s}$.

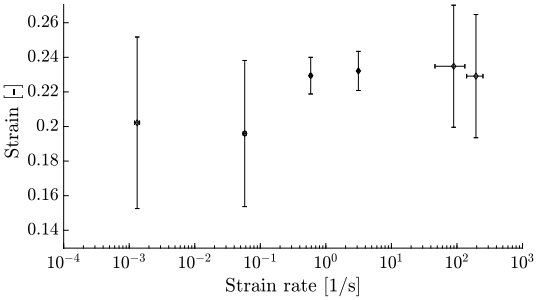

Figure B.42. Maximum strain versus strain rate for G/PA-6 $[\pm 45]_{2s}$.

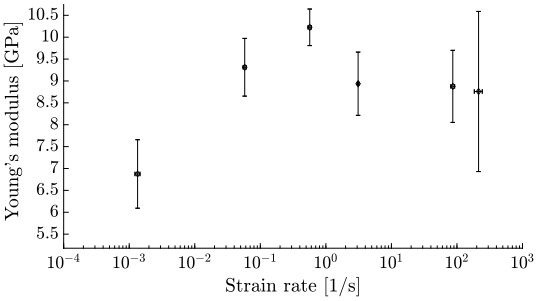

Figure B.43. Young's modulus versus strain rate for G/PA-6 $[\pm 45]_{2s}$.

B.3.6 G/PA-6 woven cross-ply - 0°

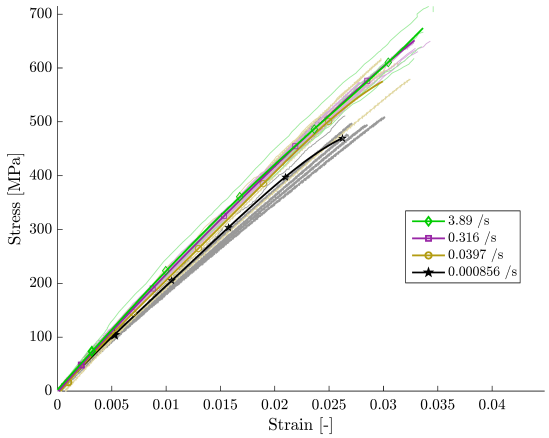

Figure B.44. Stress-strain curves of G/PA-6 $[\#(0/90)]_{2s}$ *at various strain rates.*

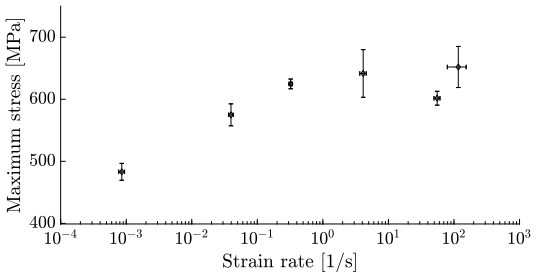

Figure B.45. Maximum stress versus strain rate for G/PA-6 $[\#(0/90)]_{2s}$.

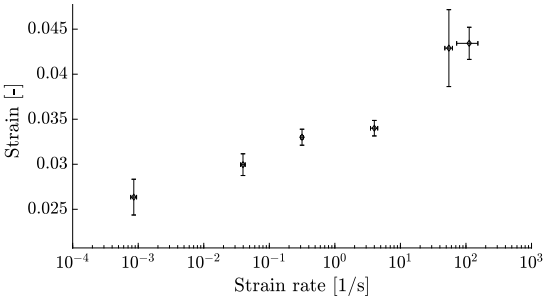

Figure B.46. Maximum strain versus strain rate for G/PA-6 $[\#(0/90)]_{2s}$.

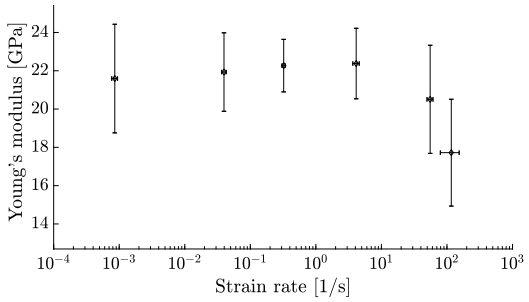

Figure B.47. Young's modulus versus strain rate for G/PA-6 $[\#(0/90)]_{2s}$.

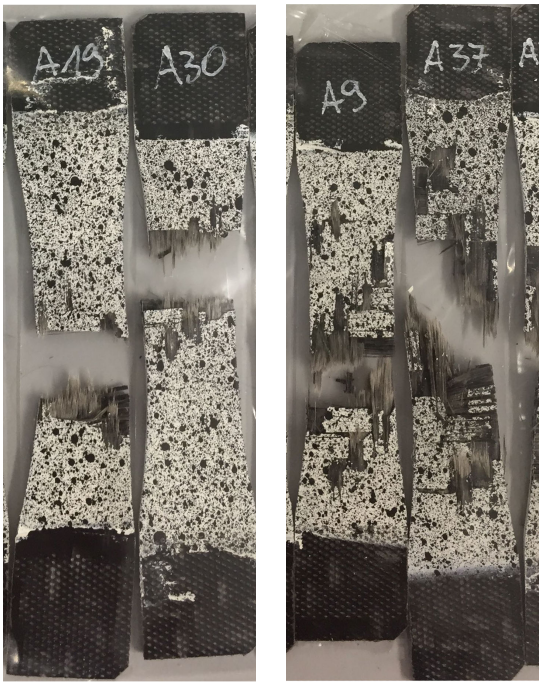

a. $v = 0.0001\,\mathrm{m\,s^{-1}}$. *b.* $v = 15\,\mathrm{m\,s^{-1}}$.

Figure B.48. Failed G/PA-6 $[\#(0/90)]_{2s}$ *specimens.*

B.3.7 G/PA-6 woven cross-ply - 90°

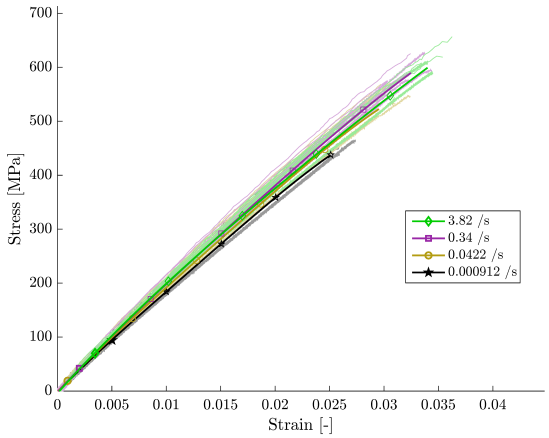

Figure B.49. Stress-strain curves of G/PA-6 $[\#(90/0)]_{2s}$ *at various strain rates.*

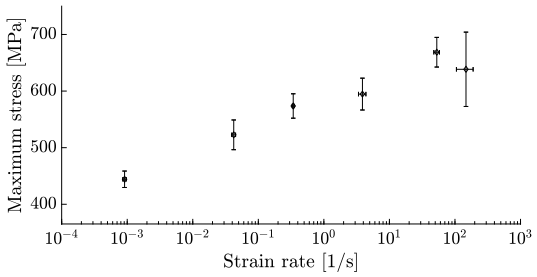

Figure B.50. Maximum stress versus strain rate for G/PA-6 $[\#(90/0)]_{2s}$.

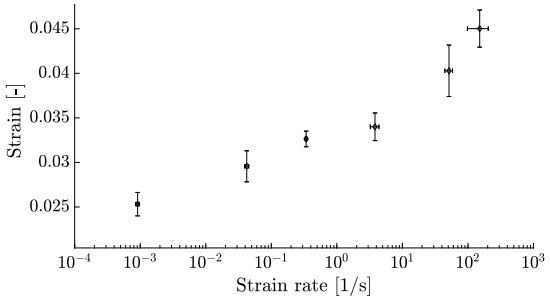

Figure B.51. Maximum strain versus strain rate for G/PA-6 $[\#(90/0)]_{2s}$.

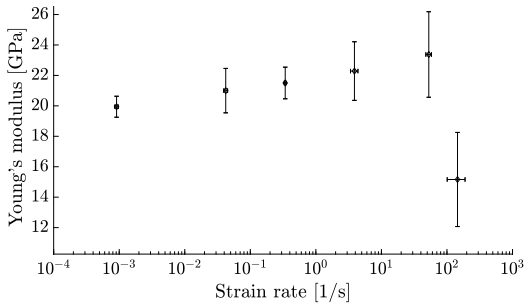

Figure B.52. Young's modulus versus strain rate for G/PA-6 $[\#(90/0)]_{2s}$.

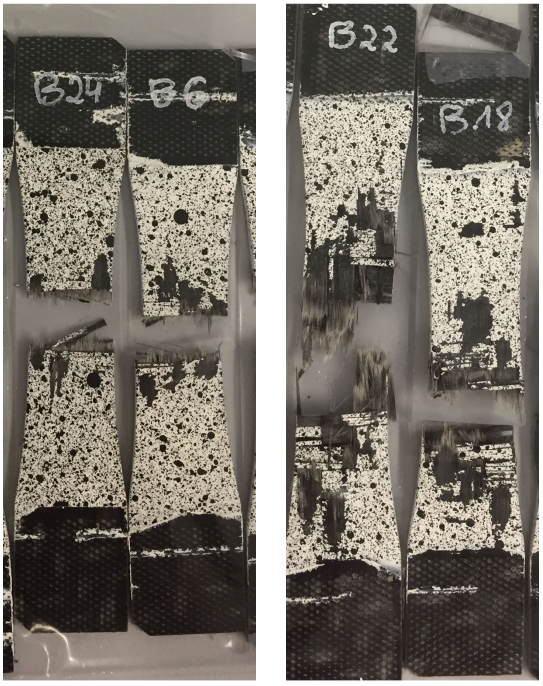

a. $v = 0.0001\,\mathrm{m\,s^{-1}}$. *b.* $v = 15\,\mathrm{m\,s^{-1}}$.

Figure B.53. Failed G/PA-6 $[\#(90/0)]_{2s}$ *specimens.*

B.3.8 G/PA-6 woven ±45

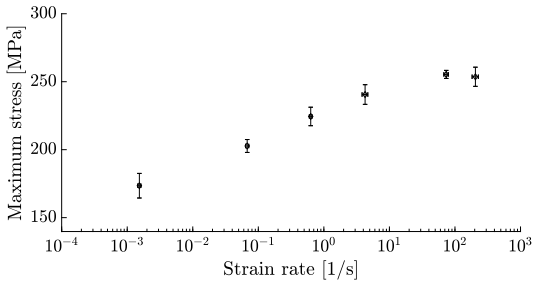

Figure B.54. Maximum stress versus strain rate for G/PA-6 $[\#(\pm 45)]_{2s}$.

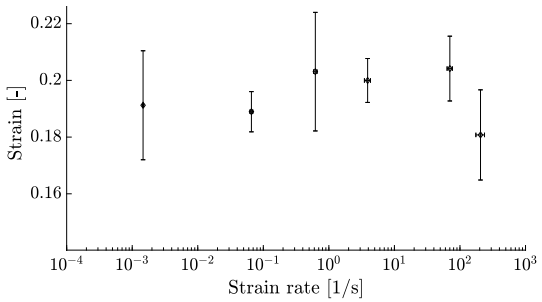

Figure B.55. Maximum strain versus strain rate for G/PA-6 $[\#(\pm 45)]_{2s}$.

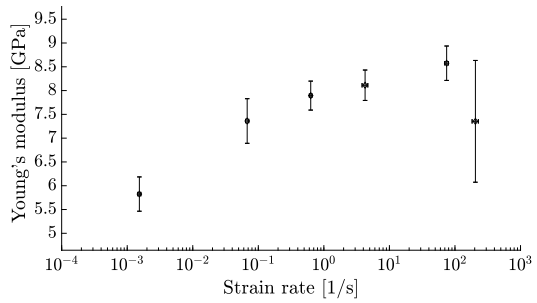

Figure B.56. Young's modulus versus strain rate for G/PA-6 $[\#(\pm 45)]_{2s}$.

B.3.9 G/PA-6 woven quasi-isotropic

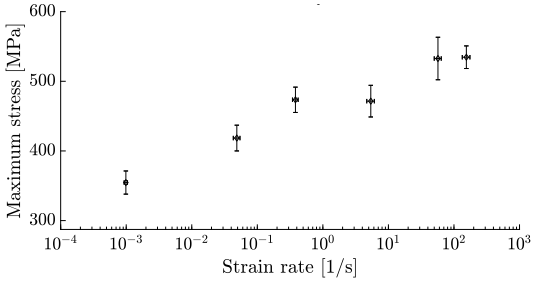

Figure B.57. Maximum stress versus strain rate for G/PA-6 $[\#(\pm 45)/\#(0/90)]_s$.

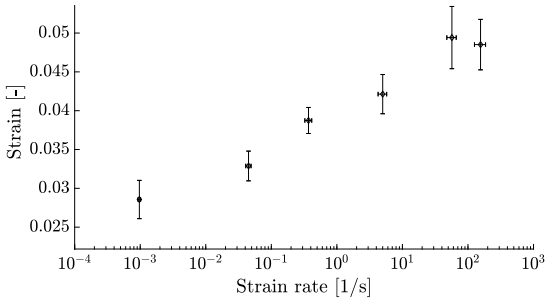

Figure B.58. Maximum strain versus strain rate for G/PA-6 $[\#(\pm 45)/\#(0/90)]_s$.

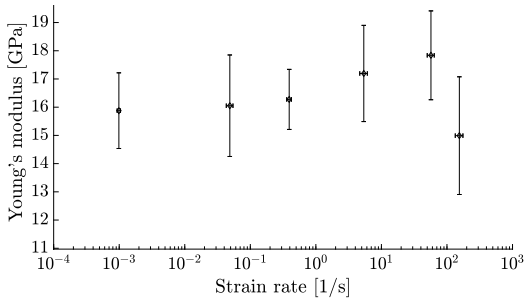

Figure B.59. Young's modulus versus strain rate for G/PA-6 $[\#(\pm 45)/\#(0/90)]_s$.